



Porous calcium phosphate based nanovectors for growth factor release

Janina Möller

► To cite this version:

Janina Möller. Porous calcium phosphate based nanovectors for growth factor release. Other. Université de Haute Alsace - Mulhouse, 2010. English. NNT : 2010MULH3224 . tel-00685006

HAL Id: tel-00685006

<https://theses.hal.science/tel-00685006>

Submitted on 3 Apr 2012

HAL is a multi-disciplinary open access archive for the deposit and dissemination of scientific research documents, whether they are published or not. The documents may come from teaching and research institutions in France or abroad, or from public or private research centers.

L'archive ouverte pluridisciplinaire **HAL**, est destinée au dépôt et à la diffusion de documents scientifiques de niveau recherche, publiés ou non, émanant des établissements d'enseignement et de recherche français ou étrangers, des laboratoires publics ou privés.

Année 2010



N° d'ordre

Université de Haute Alsace

THÈSE

Presentée en vue de l'obtention du grade de

DOCTEUR

SPÉCIALITÉ : CHIMIE DES MATÉRIAUX

Porous calcium phosphate based nanovectors for growth factor release

par Janina MÖLLER

Soutenue le 20 décembre 2010 devant la commission d'examen :

Président	Jean-Marie NEDELEC	Professeur, Université Blaise Pascal, Clermont-Ferrand II
Rapporteurs	Christèle COMBES	Maitre de Conférences HDR, Institut Polytechnique de Toulouse
Examineurs	Olivier GALLET	Professeur, Université de Cergy-Pontoise
	Karine ANSELME	Directeur de Recherche, IS2M, Mulhouse Directrice de thèse
	Cathie VIX-GUTERL	Directeur de Recherche, IS2M, Mulhouse Co-directrice de thèse

Entfalte du die alten Pergamente,
Nach Vorschrift sammle Lebens Elemente
Und füge sie mit Vorsicht eins ans andre.
Das Was bedenke, mehr bedenke Wie.

J.W. von Goethe, Faust II

Unfold all your ancient parchments,
Then, by rote, collect life's elements,
And place them together with due care,
Consider What, more deeply consider How.

Acknowledgements

This thesis would not have been possible without the support and advice of many of my colleagues and friends, and I want to thank them. A scientific work is never the result of individual efforts but always the result of teamwork.

I want to thank my supervisors Karine Anselme and Cathie Vix for welcoming me in their institute and their teams and for giving me the opportunity to work at the interface between materials and proteins. I am indebted to the national research agency (ANR) for generous funding of this project. I want to thank all our collaborators in the ANR project for insights into the various aspects of regenerative bone medicine and pleasant meetings all along this thesis. I especially thank Jean-Marie Nédélec and Olivier Raissle from the LMI in Clermont-Ferrand for providing the powders A, B, and C for the protein studies.

I want to thank Denis Spitzer and Benny Siegert from the ISL in Saint Louis for providing access to the Zetasizer at the last minute. I thank Patrice Laquerriere and Ali Ouadi for the opportunity to work with them on the radiotracing of proteins in order to complete these studies. I am grateful to Jean-Luc Rehspringer from IPCMS Strasbourg for providing the silica opal sample that was used as macroporous template.

I am grateful for having had the opportunity to work with Conchi Ovin Ania from the INCAR-CSIC in Oviedo, Spain, during the last months of this thesis. I want to thank her not only for scientific advice and numerous experiments on the TPD of proteins, but also for her enthusiasm and friendship.

I'm indebted to all the scientific, technical and administrative staff at the IS2M that have made this work possible. In particular, I want to thank

- Joseph Dentzer for technical support, the construction of the TPD device and for keeping the lab running;
- Karine Anselme, Cathie Vix, Julien Parmentier, Luc Delmotte, Camelia Ghimbeu and Roder Gadiou for scientific advice;
- Loïc Vidal and Hugues Bonnet for electron microscopy images and EDX;
- Marie-Paule Hirn for assistance with nitrogen physisorption measurements that are key techniques for the characterization of my ceramic powders;
- Gauthier Schrodj for thermogravimetric analyses;
- Fabien Schnell and Simon Grée for the introduction to X-ray diffraction;
- again Simon Grée for repairing electronic devices every time they failed (which happened quite often);
- all the girls (and boys !) from the bioteam for answering stupid questions without laughing;

-
- Cyrille Geney and Patrick Lamielle for the construction and maintenance of our ovens and the CVD;
 - Stephan Knopf for providing everything we needed and more than occasional laughs;
 - Luc Delmotte for his support and his eagerness to help and for teaching me how to identify edible mushrooms;
 - Sylvie Forget for her moral support and encouragements,
 - Louisa Idiri, Natalina Muller, Joelle Dagny, Nathalie Castelein, Christian Daniel and Fabienne Sorgato for allowing us to concentrate on science and for keeping the institute running;
 - again Natalina for teaching me how to cook a *caponata siciliana* and the best tomato sauce ever;
 - Judith Böhmler for being my friend and ally in this strange world which is France, and for teaching me how to prepare Spätzle the right way ;)

Among all the people that have welcomed me at the IS2M, several have marked the three years I had the pleasure to stay with them. Thank you all for being much more than just colleagues.

I also need thank the members of the jury for their time and patience with me and this manuscript and for having accepted to give their expertise on this work.

Von ganzem Herzen danke ich meiner Familie, meinen Eltern und meinem Bruder Joscha dafür, dass sie meine Karriere immer unterstützt und gut geheißen haben. Ohne ihre Hilfe und fortwährenden Zuspruch hätte ich es nie soweit gebracht. Ganz lieben Dank auch an meine Großeltern, dafür, dass ihr glaubt, ich könnte die Welt verändern.

Mein ganz besonderer Dank gilt auch dem Mann an meiner Seite, der meinen Rücken stärkt und meine Manuskripte korrigiert. Ohne dich, mein Herz, wäre ich jetzt nicht hier.

Abstract

This thesis is part of the ANR project PNano NANOBONEFILLER. The aim of this project is the development of a new injectable bone filling system based on mesoporous calcium phosphates associated with growth factors. The thesis is composed of two main parts: the synthesis of mesoporous calcium phosphates by hard templating techniques and the adsorption and release of growth factors on these porous ceramics. This work is the first association of growth factors with mesoporous calcium phosphates for bone regeneration.

Calcium phosphates are extensively used for bone regeneration due to their biocompatibility and good resorption. Their performance can, however, be improved if these materials are associated with growth factors. Growth factors are soluble proteins that stimulate cell activity, such as proliferation and differentiation. In order to control the release of growth factors from ceramic materials, the aim of this work has been the synthesis of calcium phosphates with controlled mesoporosity. Hard templating approaches have been developed for the synthesis of porous hydroxyapatites: mesocellular silica foam is obtained by the condensation of tetraethyl orthosilicate in presence of surfactant micelles. These silica foams have higher pore volumes and a pore structure that is more suitable for the replication than hexagonal type SBA-15 silica which was used as a reference material. Carbon replicas of these silica foams are obtained by chemical vapor infiltration (CVD) of propylene at 750 °C or by liquid infiltration with acidic sucrose solution. Depending on the carbon precursor, the replicas have different porosities and surface chemistries. The effect of these differences on the replication with hydroxyapatite was investigated systematically. The dissolution of the silica matrix by etching with hydrofluoric acid frees the porosity of the carbon replica. Hydroxyapatite is then produced inside the porosity both of silica and carbon templates by the infiltration of precursor solutions. The template elimination method depends on the nature of the template: in the case of silica templates, the matrix is dissolved by sodium hydroxide etching, whereas the carbon template is eliminated by selective oxidation in air.

The resulting ceramics are characterized by different electron microscopy techniques as well as by X-ray diffraction and nitrogen physisorption. These techniques show that the properties of the ceramics vary with the synthesis conditions such as the calcination temperature, the nature of the template and the infiltration conditions. The hydroxyapatites are composed of strongly agglomerated nanoparticles with specific surface areas from 30 to 160 m²/g, depending on the synthesis conditions. Their crystallinity depends on the temperature during the heat treatment. Nitrogen physisorption experiments prove that the ceramics are mesoporous.

Depending on their physico-chemical properties, six ceramics have been chosen for protein adsorption experiments. Three of these samples have been obtained from a project

partner. At first, two less expensive model proteins, BSA (bovine serum albumin) and Cytochrome C, are used to develop an adsorption and release protocol. The adsorption and release kinetics are evaluated by a depletion method: the supernatant of the powders is analyzed by UV/Vis absorption either directly (Cytochrome C) or after staining with Bradford reagent (BSA). Adsorption and release experiments using the growth factors TGF- β 1 and VEGF followed. TGF- β 1 is a cytokine able to stimulate bone regeneration whereas VEGF improves vascularisation. The combination of both factors is promising for the regeneration of bone defects. As the quantification by UV/Vis absorbance is not possible for the growth factors because they are too diluted, immunoassay techniques with specific antibodies have been chosen for quantification. These experiments show which are the most efficient powders for the adsorption and controlled release of growth factors.

During the thesis, we synthesized a number of calcium phosphate samples with different physico-chemical properties and evaluated their growth factor retention capacities. This study allows to connect the physico-chemical properties of calcium phosphates to their ability to store and to release proteins progressively.

Résumé

Les travaux de cette thèse s'inscrivent dans le projet ANR PNano NANOBONE-FILLER, qui a pour but le développement d'un nouveau système de comblement osseux à base de phosphates de calcium mésoporeux associés à des facteurs de croissance. La thèse comprend deux grandes parties : la synthèse de phosphates de calcium mésoporeux par des techniques de réplique et l'adsorption et le relargage de facteurs de croissance sur ces céramiques poreuses.

Les phosphates de calcium sont les céramiques les plus utilisées dans la régénération osseuse grâce à leur biocompatibilité et leur bonne résorption. Pourtant, leur performance peut être améliorée s'ils sont associés à des facteurs de croissance. Les facteurs de croissance sont des protéines solubles qui peuvent stimuler les activités cellulaires comme la prolifération et la différenciation. Afin de contrôler le relargage des facteurs de croissance, l'objectif de la thèse a été de synthétiser des phosphates de calcium avec une mésoporosité contrôlée. Ce travail représente la première association des phosphates de calcium mésoporeux avec les facteurs de croissance TGF et VEGF.

Pour obtenir des phosphates de calcium mésoporeux, des nouvelles techniques de réplique ont été mises en place : des mousses de silices mésoporeuses sont obtenues par condensation des tétraéthyle orthosilicate (TEOS) en présence de micelles de surfactant. Les mousses de silices représentent une surface spécifique plus importante et une géométrie poreuse plus adaptée à la technique de réplique que les silices hexagonales de type SBA-15 qui sont utilisées en tant que référence. Des répliques carbonées de ces mousses siliciques sont réalisées par infiltration en phase vapeur de propylène à 750 °C ou par infiltration liquide de sucrose en solution acide. En fonction du précurseur de carbone, les répliques carbonées présentent une porosité et une chimie de surface différente dont l'effet sur la réplique est analysé de manière systématique. La dissolution de la si-

lice par un traitement par l'acide fluorhydrique libère la porosité de la matrice carbonée. L'hydroxyapatite est ensuite synthétisée dans la porosité des templates siliciques ou carbonés par infiltration de précurseurs en solution aqueuse. L'élimination de la matrice s'effectue par dissolution chimique par de la soude dans le cas du template silicique et par oxydation sélective sous air dans le cas du template carboné. La caractérisation de la céramique effectuée par différentes techniques de microscopie électronique, par diffraction des rayons X et par adsorption d'azote montre que les caractéristiques finales de l'hydroxyapatite dépendent des conditions de synthèse ainsi que de la température de calcination, de la nature du matériau hôte et du procédé d'infiltration. Elle se compose de nanograins agglomérés présentant des surfaces spécifiques allant de 30 à 160 m²/g en fonction des paramètres de synthèse. La cristallinité de la céramique dépend de la température de traitement thermique. L'adsorption d'azote révèle que la céramique est mésoporeuse.

En fonction de leurs propriétés chimiques et physiques, six céramiques (dont trois provenant d'un partenaire du projet ANR) ont été choisies pour une analyse de leurs capacités d'adsorption et de relargage de protéines. Dans un premier temps, un protocole est mis en place en utilisant des protéines modèles, la BSA (bovine serum albumin) et le Cytochrome C, qui ont un coût moins important que les facteurs de croissance. Les cinétiques d'adsorption et de relargage des céramiques sont caractérisées par une méthode de déplétion : le surnageant des poudres est analysé par adsorption UV/Visible directe (pour le Cytochrome C) ou après révélation colorimétrique de type Bradford (pour la BSA). Des essais d'adsorption et de relargage avec les facteurs de croissance TGF- β 1 et VEGF ont ensuite été effectués. Le TGF- β 1 est un facteur de croissance capable de stimuler la régénération osseuse et le VEGF améliore la vascularisation. La combinaison de ces deux facteurs de croissance avec les phosphates de calcium est prometteuse pour améliorer la régénération osseuse dans des défauts osseux. Le dosage des facteurs de croissance n'étant pas possible par UV/Vis vue leur faible concentration, des méthodes d'essais immunologiques par des anticorps spécifiques (ELISA) ont été choisies. Ces travaux ont permis de déterminer les poudres les plus efficaces en terme d'adsorption et de relargage contrôlé de ces facteurs de croissance.

Pendant les travaux de cette thèse, nous avons synthétisé un certain nombre de phosphates de calcium avec des propriétés physicochimiques différentes et évalué leurs capacités de rétention de facteurs de croissance. Cette étude permet de relier les propriétés physicochimiques des phosphates de calcium avec leur aptitude à stocker des protéines et à les relarguer progressivement.

Contents

1	Introduction and context	1
1.1	Biomaterials	1
1.1.1	Definition	1
1.1.2	An ideal material for implanting	2
1.1.3	Tissue engineering	3
1.1.4	Calcium phosphate based biomaterials for bone regeneration	5
1.2	Description of the ANR project	8
1.2.1	Short description of the project	8
1.2.2	Bibliographic context and skills of the project partners	11
1.2.3	This work in the setting of the ANR project	12
1.2.3.1	Preparation of nanoporous calcium phosphate	12
1.2.3.2	Analysis of cytokine adsorption	16
2	Hydroxyapatite by hard templating techniques	19
2.1	Bibliography	19
2.1.1	Synthesis of hydroxyapatite	19
2.1.1.1	Precursors	19
2.1.1.2	Synthesis methods	20
2.1.1.3	Product treatment: hydrothermal, sintering, SPS	24
2.1.2	Templating	25
2.1.3	Mesoporous hydroxyapatite - State of the art	30
2.1.3.1	Hard templating of macroporous hydroxyapatite	30
2.1.3.2	Hard templating of mesoporous hydroxyapatite	34
2.1.3.3	Soft templating of mesoporous hydroxyapatite	37
2.1.3.4	Summary: templating of HA	49
2.2	Experimental	52
2.2.1	Template synthesis	52
2.2.1.1	Silica templates	52
2.2.1.2	Carbon templates	53
2.2.2	Hydroxyapatite synthesis	54
2.3	Results	57
2.3.1	Synthesis and optimization of templates	57
2.3.1.1	Mesoporous silica templates	57
2.3.1.2	Mesoporous carbon templates	68
2.3.2	Infiltration with hydroxyapatite	82
2.3.2.1	Influence of the HA precursor	82

2.3.2.2	Influence of the infiltration process	88
2.3.2.3	Evolution of the properties of the product with the size and the shape of the pores of the template	98
2.3.2.4	Product properties depending on the surface chemistry of the template	103
2.3.3	Products depending on the densification treatment	108
2.4	Discussion	113
2.5	Conclusion	116
3	Protein adsorption by porous hydroxyapatite	119
3.1	Bibliography	119
3.1.1	Adsorption of proteins on ceramic materials	119
3.1.1.1	Protein adsorption on calcium phosphate materials . . .	119
3.1.1.2	Protein adsorption in (meso)porous materials	121
3.1.2	Growth factor release systems based on calcium phosphate	124
3.1.3	Techniques for protein quantification	126
3.1.3.1	Colorimetry	127
3.1.3.2	Fluorometry	128
3.1.3.3	Radio-labeling	129
3.1.3.4	ELISA	129
3.1.3.5	Automated methods	129
3.1.3.6	Quantification of adsorbed proteins in porous materials .	129
3.1.4	Proteins used for the study	130
3.1.5	Materials used for the protein adsorption and release experiments	131
3.2	Experimental	133
3.2.1	Characterization of the ceramics in view of the protein experiments	133
3.2.1.1	ζ -Potential	133
3.2.1.2	Dissolution kinetics of the ceramics	134
3.2.2	Model proteins: BSA and Cytochrome C	135
3.2.3	Growth factors TGF-beta and VEGF	136
3.2.4	Thermo-programmed desorption	137
3.3	Results	138
3.3.1	Characterization of the ceramics in view of the protein experiments	138
3.3.1.1	ζ -Potential	138
3.3.1.2	Dissolution kinetics of the ceramics	138
3.3.2	Model proteins	144
3.3.3	Growth factors	144
3.3.4	Protein quantification by TPD	154
3.3.4.1	TPD of the ceramics	154
3.3.4.2	Quantification of protein traces by TPD	154
3.4	Discussion	160
3.4.1	Model proteins	160
3.4.2	Growth factors	162
3.5	Conclusion	164

3.5.1	Model proteins	164
3.5.2	Growth factors	164
4	General conclusion and perspectives	165
4.1	Conclusion	165
4.2	Perspectives	166
4.2.1	Biological evaluation	166
4.2.2	Possible further improvements of the synthesis of mesoporous hydroxyapatite	167
5	Appendix	169
5.1	Fundamentals of physisorption	169
5.1.1	Determination of pore size distribution	173
5.2	Mass Spectrometer coupled Thermoprogrammed Desorption (TPD-MS) .	174
5.3	ELISA	175
5.4	List of samples prepared	177

List of abbreviations

\varnothing_p	mean pore diameter
AAO	Anodic Aluminum Oxide
AFM	Atomic Force Microscopy
ANR	Agence Nationale de Recherche (national research agency)
ATR	Attenuated Total Reflection
BCA	BiCinchonic Acid
BET	Brunauer, Emmett and Teller (theory for the determination of the specific surface area from physisorption experiments)
BJH	Barrett, Joyner, Halenda (theory for the determination of porosity parameters from physisorption experiments)
BMP	Bone Morphogenic Protein
BRT	Biomatériaux et régénération tissulaire (Biomaterials and tissue repair)
BSA	Bovine Serum Albumin
Ca	calcium
CaP	Calcium Phosphate
CAT	Calcium di(hexafluoro-2,4-pentadione)(tetraglyme)
CMK-3	Carbon Mesostructured by Kaist: sucrose replication of SBA-15
CTAB	Cetyl TriAmmonium Bromide
CVD	Chemical Vapor Deposition
DLVO	Derjaguin, Landau, Verwey, and Overbeek. Theory describing the interaction of charged surfaces and particles in solution and dispersion.
DMEM	Dulbecco's Modified Eagle's Medium: culture medium containing amino acids, proteins, vitamins, sugars and salts.
DPM	DiPivaloyl Methane
DSC	Differential Scanning Calorimetry
E_1	heat of adsorption of the first layer during physisorption experiments

E_L	heat of liquefaction of the gas used for physisorption experiments
ECM	Extracellular Matrix
EDX	Energy Dispersive X-ray Spectroscopy
ELISA	Enzyme Linked Immunosorbent Assay
FA	Fluorapatite
FDA	Food and Drug Administration
FGF-2	Fibroblast growth factor 2
FSM	Folded Sheet Material
FTIR	Fourier Transform InfraRed spectroscopy
GC	Gas Chromatography
HA	Hydroxyapatite
HF	hydrofluoric acid
IBTH	Interaction Biomatériaux/Tissus Hôtes (Interaction bio-materials and host tissues)
ICP	Inductively Coupled Plasma (Ionization method for MS)
IGF-1	Insulin-like Growth Factor 1
IS2M	Insitut de Science des Matériaux de Mulhouse (Insitute for Materials Research in Mulhouse)
ISO	International Standard Organization
IUPAC	International Union of Pure and Applied Chemistry
K_c	solubility constant (equilibrium constant of dissolution reaCtion)
LC	Liquid Chromatography
LCT	Liquid Crystal Templating
LMI	Laboratoire des Matériaux inorganiques (Laboratory for Inorganic Materials)
LPC	Laboratoire de Physique Corpusculaire (Laboratory for Particle Physics)
M/P	Mesitylene/Pluronic ratio
MCF	Meso Cellular Foam: mesoporous silica with foam-like porosity
MCM-41/48	Mobile Composition of Matter: class of mesoporous silica materials
MMP	Matrix Metalloprotease (enzyme used by cells in order to degraded the extra cellular matrix, and to release proteins that are contained in the ECM)

MOCVD	Metal Organic Chemical Vapor Deposition
MS	Mass spectrometry/spectroscopy
MTAB	Myristyl Trimethyl Ammonium Bromide
NMR	Nuclear Magnetic Resonance
OCF	Octa Calcium Phosphate
OPA	O-phthaldialdehyde (fluorochrome)
P	phosphorus
p/p_0	relative pressure in physisorption experiments
PBS	Phosphate Buffered Saline
PDGF-BB	Platelet Derived Growth Factor composed of two B chains
PIXE	Particle Induced X-ray Emission
PSS	Poly-(Sodium 4-Styrene sulfonate)
QCM	Quartz Crystal Microbalance
rpm	rotations per minute
S_{BET}	specific surface area determined after the BET theory from nitrogen physisorption
SAXS	Small Angle X-ray Diffraction
SBA-15	Santa Barbara 15: mesoporous silica material
SDA	Structure Directing Agent
SDS	Sodium Dodecyl Sulfate
SEM	Scanning electron microscopy
SPS	Spark Plasma Sintering
TCP	Tri Calcium Phosphate
TEM	Transmission electron microscopy
TEOS	Tetraethyl Orthosilicate
TGF	Transforming growth factor
TLCT	True Liquid Crystal Templating
TMB	TriMethylBenzene (mesitylene)
TPD	Thermo Programmed Desorption
UV/Vis	UltraViolet and Visible light spectroscopy
V_{ads}	adsorbed volume (in physisorption experiments)
V_m	volume of the monolayer (in physisorption experiments)
V_{micro}	micropore volume (volume of pores <2 nm)
V_{meso}	mesopore volume (volume of pores between 2 and 50 nm)
V_p	total pore volume
VEGF	Vascular Endothelial Growth Factor
WAXS	Wide Angle X-ray Diffraction
XRD	X-ray diffraction

1 Introduction and context

1.1 Biomaterials

1.1.1 Definition

The development of biomaterials has started in the late 60's, with the first international meeting on Biomaterials held at the university of Clemson in South Carolina. Since then, it has become an important field of research that keeps growing every year. The definition of biomaterials is more difficult to find than one could think as the definition strongly depends on the field that we are working in. A definition from the late 1990s that still achieves high consensus from biologists and material scientists is the following:

A biomaterial is a non viable material intended to interface with biological systems to evaluate, treat, augment or replace any tissue, organ or function of the body [1]. It is important to note that a biomaterial is defined by its interface to biological systems, a hermetically closed pacemaker is therefore not a biomaterial. In the Leading Opinion paper published in Biomaterials in 2009, David F. Williams [1] gives an even more general definition, leaving the possibility of further developments and research wide open: *A biomaterial is a substance that has been engineered to take a form which, alone or as part of a complex system, is used to direct, by control of interactions with the components of living systems, the course of any therapeutic or diagnostic procedure, in human or veterinary medicine.*

Additionally, the focus of research on biomaterials has shifted from the search of *bioinert* materials towards *bioactive* materials. "Bioinert" is a term that should be used with care: every material implanted into the body will trigger a response. Bioinert can therefore only be a material that causes the minimal reaction from its surrounding tissues. The implant becomes covered with a non-adherent fibrous tissue layer, but is not bonding with its environment.

Bioactive materials on the other hand bond to their surrounding tissues. In 1991, Hench [2] proposed the bioactivity index in order to evaluate the bioactivity of a given material in vivo:

$$I_B = \frac{100}{t_{50bb}} \quad (1.1)$$

The bioactivity index is given by equation 1.1, with t_{50bb} being the time needed for half of the implant surface to be bonded.

Additionally, Hench divided bioactive materials for bone regeneration into two classes: Class A bioactive materials lead to osteoconduction (bone growth along the implant/bone interface) and osteoproduction (formation of bone on the surface of the implant due to

rapid chemical reactions), whereas class B bioactive materials are restricted to osteo-conduction [2].

Today, biomaterials are used in every part of the human body: artificial heart valves, stents in the blood vessels, implants to replace shoulder, knee or hip joints, ears and teeth. The replacement of hips and knees are the most frequent applications for biomaterials as degenerative diseases like arthritis degrade the mechanical properties of the bone [3].

1.1.2 An ideal material for implanting

In order to achieve the desired response from the body to the implant and not to trigger a foreign body response, a material used for implantation has to fulfill several criteria. These requirements have been summarized by Hench and Jones [4] as follows:

1. The material must be biocompatible and non-cytotoxic.
2. The implant should provide a template for three dimensional tissue ingrowth.
3. Interconnected macropores with diameters exceeding 100 μm allow cell penetration, tissue ingrowth and vascularization; the transport of nutrients and the evacuation of waste from the regenerating tissue can be achieved.
4. Osteoconductive materials bond to the surrounding tissue without the formation of scars and fibrous interphases.
5. The surface texture of the material should allow the adsorption of biological metabolites and promote cell adhesion.
6. An ideal implant influences the genes of surrounding cells in such a way that differentiation and proliferation are favored.
7. Ideally, the material should be resorbed at the same rate as new tissue is formed. When the implant is resorbing, metabolites should be non-toxic and easy to excrete from the body, for example via the respiratory or via the urinary system.
8. The production of irregular shaped implants must be possible with the chosen fabrication technique in order to adapt the implant to the form of the defect.
9. Especially in load-bearing application in bone, the implant must provide sufficient mechanical stability to allow tissue regeneration.
10. Ideally, for commercialization, the material must meet the standards of the International Standards Organization (ISO) or the Food and Drug Administration (FDA).

Whereas the first points are universally applicable to most implant types, the later ones are more specific and refer not only to the materials itself, but to its fabrication process as well. In some cases, compromises must be made between several requirements: for example, polymers have a lower Young's modulus than bone, but they can easily be manufactured with porous structures and three dimensional architecture. This is why they have been used for drug delivering applications [5], but cannot be used for the regeneration of load-bearing bone.

1.1.3 Tissue engineering

Tissue Engineering is the association of the principles of engineering and the principles of life sciences in order to create *biological substitutes that restore, maintain or improve tissue function* [6]. The resulting materials are characterized by the combination of artificial materials with biological components. Three main fields can be distinguished in tissue engineering:

1. Isolated cells or cell substitutes.

Replacing only the type of cells that generate the function of the tissue can help to avoid complications during the intervention. Cells can be treated before the infusion. On the other hand, cells might lose their function during treatment and injection or may be rejected by the patient's body.

2. Tissue inducing substances.

Signaling molecules such as growth factors must be produced or purified in large scale for this approach. The development of appropriate delivery systems remains a challenge.

3. Cells on or within matrices.

The association of cells with matrices includes cells isolated from the body via a membrane that allows nutrition and waste elimination but prevents immunological entities (antibodies and immune cells) from destroying the implant and cells attached to implanted matrices.

The subject of this thesis can be classified into the second category: the aim of this work is the association of calcium phosphate based ceramics with bone inducing growth factors.

In the United States, only ten percent of the patients with liver failure (30,000 in 1991) have access to a donor organ. Artificial substitutes cannot fulfill all of the functions of a living tissue. This is why tissue engineering has gained increasing attention over the past decades. Additionally, it offers the possibility for considerable savings for the health care system, as current methods of transplantation and reconstruction are one of the most costly interventions in today's medicine. [6]

Operation site	procedures
Spine	45 400
Knee joint	39 000
Hip joint	15 000
Hand	5500

Table 1.1: Number of interventions per year separated by site. Trauma patients in Japan 2006/2007. From [8].

Bone tissue engineering. In England and Wales, more than 700,000 joint and bone replacements were accomplished between 2003 and 2007. The most frequent operations were hip (71,000) and knee (76,000) implants [7]. Most of these interventions were primary, i. e. the first surgical intervention at the implantation site. In Japan, 226,000 patients underwent orthopedic surgery in 2006 and 2007. Among these, 104,000 were trauma patients, whereas the remaining were treated for degenerative diseases. Cancer patients counted within the trauma group [8]. Table 1.1 shows the number of interventions within the trauma patients separated by intervention site.

Most of these interventions are autogenous bone grafts (bone from the same patient is transferred to the implantation site) or allogenic bone donations (bone from a donor with similar genetic profile, often a family member, is used for implantation). These interventions are limited by the quantity of bone that can be retrieved from the donor site, by donor site morbidity and by contour irregularities. [6]

Artificial materials for bone tissue engineering include metals, polymers and ceramics. Pure metals are bioinert and offer good mechanical properties. The most frequently used materials are stainless steel, cobalt/chromium alloys, titanium and its alloys. Unfortunately, the bond between bone and implant tends to degrade over time if metals are used for implantation. Abrasion, corrosion and limited biocompatibility are other reasons for implant failures [3,9]. In order to improve the bone/implant interface, calcium phosphate coatings can be applied to the metal surface [10,11].

Polymers have been used for bone substitution. In general, it is difficult to adapt a polymeric material to natural bone in terms of mechanical strength and optimal degradation properties [6]. On the other hand, polymers are suitable materials for the release of biologically active molecules on the implantation site.

Ceramic materials can be bioinert (such as alumina) or bioactive (bioglasses and hydroxyapatite). They are generally used as porous implants (calcium phosphates). Porous materials with pore sizes above 200 μm (macropores) allow bone ingrowth into the porosity. By this mechanism, the union between bone and implant is stronger than for bulk materials [6]. Mesopores (2 to 50 nm in diameter) can be present on the surface of the implant. They favor protein adsorption from biological fluids and can be used for the encapsulation of biomolecules [12]. The presence of both porosities enhanced the performance of porous implants as compared to non-porous ones.

1.1.4 Calcium phosphate based biomaterials for bone regeneration

Table 1.2 gives an overview over biocompatible calcium orthophosphates [10]. Along with the common name and the chemical formula, the Ca/P atomic ratio is given. This value greatly defines the behavior of the material and is a useful tool to classify calcium orthophosphates. For instance, calcium orthophosphates with a Ca/P ratio below unity are unsuitable for implantation due to their high solubility.

Calcium phosphates are often used for bone substitution because of their chemical similarity to the mineral component of hard tissues (bone and teeth). They are non-toxic and biocompatible. Upon implantation, they are not recognized as foreign to the body and therefore not rejected. Calcium phosphates are bioactive and form a strong bond with the surrounding bone tissue. They integrate into living tissue and induce the remodeling of natural bone [14].

Calcium phosphates have been shown to promote osteoblast adhesion and proliferation. Their main drawbacks are a poor resistance to mechanical stress and the brittle behavior with a poor fatigue resistance. The brittleness is emphasized when porous scaffolds are produced in order to favor vascularisation and cell colonization. This is why they are mainly used as fillers or coatings but not in load-bearing applications [15].

Apatites are a mineral family defined by the general formula: $\text{Ca}_5(\text{XO}_4)_3(\text{Y})$, where M represents a bivalent cation, PO_4 represents a tetragonal bivalent anion (mostly phosphate) and Y represents a monovalent anion. As the unit cell contains two formula units, the formula is often written as $\text{Me}_{10}(\text{XO}_4)_6(\text{Y})_2$. The most abundantly found family member is hydroxyapatite $\text{Ca}_{10}(\text{PO}_4)_6(\text{OH})_2$.

Apatites crystallize in the hexagonal system and have the space group $P6_3/m$. The unit cell parameters a , b and c depend on the nature of the anions. For pure hydroxyapatite they are $a = b = 9.418 \text{ \AA}$ and $c = 6.875 \text{ \AA}$ [16]. The theoretical density of HA is 3.16 g/cm^3 .

The phosphate groups form a rigid system with no substitutions [16]. On the other hand, two types of tunnels can be described inside the phosphate structure: type I tunnels are of about 2.5 \AA in diameter and host the four Ca(I) atoms per unit cell. Each calcium atom is coordinated by nine oxygen atoms. Type II tunnels are between 3 and 4.5 \AA in diameter and are occupied by the six Ca(II) atoms. The Ca(II) atoms form two triangles at $c = 1/4$ and $c = 3/4$ of the unit cell. The triangles are rotated by 60° around the c axis. Figure 1.1 shows a projection of unit cell of hydroxyapatite.

The Y anions occupy several positions along the c axis (see figure 1.2). They can change sites easily and are the first to be solvated when the hydroxyapatite is placed into aqueous media [16]. Substitutions both of anions and the calcium cations are frequently observed in hydroxyapatite. Biological apatite for instance is carbonated: CO_3^{2-} groups replace some of the PO_4^{3-} and OH^- positions. In biological samples, half of the substitutions occur on the surface of the sample whereas the remaining carbonate replaces phosphate and hydroxy groups in the core of the ceramic. The concentration of carbonate in the hydroxyapatite constituting human bone is 3 to 6% in weight. Additionally, biological apatite contains hydrogenophosphate HPO_4^{2-} and alkaline cation substitutions. The presence of these ions often distorts the crystallographic system.

Ca/P ratio	Compound	Chemical formula	Solubility at 25°C -log(K_c)	Solubility at 37°C -log(K_c)	25 °C, stable at pH
0.5	Monocalcium phosphate monohydrate (MCPM)	$\text{Ca}(\text{H}_2\text{PO}_4)_2 \cdot \text{H}_2\text{O}$	1.14		0.0-2.0
0.5	Monocalcium phosphate anhydrous (MCPA)	$\text{Ca}(\text{H}_2\text{PO}_4)_2$	1.14		^a
1.0	Dicalcium phosphate dihydrate (DCPD) ^c	$\text{CaHPO}_4 \cdot 2\text{H}_2\text{O}$	6.59	6.63	2.0-6.0
1.0	Dicalcium phosphate anhydrous (DCPA) ^d	CaHPO_4	6.90	7.02	^a
1.33	Octacalcium phosphate (OCP)	$\text{Ca}_8(\text{HPO}_4)_2(\text{PO}_4)_4 \cdot 5\text{H}_2\text{O}$	96.6	95.9	5.5-7.0
1.5	α -Tricalcium phosphate (α -TCP)	$\alpha\text{-Ca}_3(\text{PO}_4)_2$	25.5	25.5	^b
1.5	β -Tricalcium phosphate (β -TCP)	$\beta\text{-Ca}_3(\text{PO}_4)_2$	25.5	25.5	^b
1.2-2.2	Amorphous calcium phosphate (ACP)	$\text{Ca}_x\text{H}_y(\text{PO}_4)_z \cdot n\text{H}_2\text{O}$ n=3-4.5	^e		5-12
1.5-1.67	Calcium deficient hydroxyapatite (CDHA)	$\text{Ca}_{10-x}(\text{HPO}_4)_x(\text{PO}_4)_{6-x}(\text{OH})_{2-x}$, 0>x>1	85.1	85.1	6.5-9.5
1.67	Hydroxyapatite (HA)	$\text{Ca}_{10}(\text{PO}_4)_6(\text{OH})_2$	116.8	117.2	9.5-12 ^f
1.67	Fluorapatite (FA)	$\text{Ca}_{10}(\text{PO}_4)_6\text{F}_2$	120.0	199.2	7-12
2.0	Tetracalcium phosphate (TTCP) ^g	$\text{Ca}_4(\text{PO}_4)_2$	38-44	37-42	^b
^a stable above 100°C, ^b these compounds can not be precipitated form aqueous solution, ^c mineral name: brushite, ^d mineral name: monetite, ^e cannot be measured precisely, ^f other sources indicate 4.2-8.0 [13], ^g mineral name: hilgenstonite.					

Table 1.2: Calcium orthophosphates and their major properties, reproduced from [10].

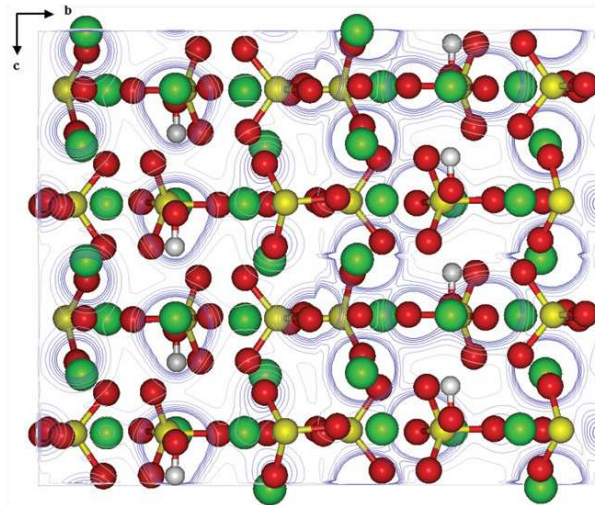


Figure 1.1: Projection of the unit cell of hydroxyapatite showing oxygen in red, calcium in green, phosphorus in yellow and hydrogen in white. All atoms are reduced to $1/4$ of their van der Waals radius. From [17].

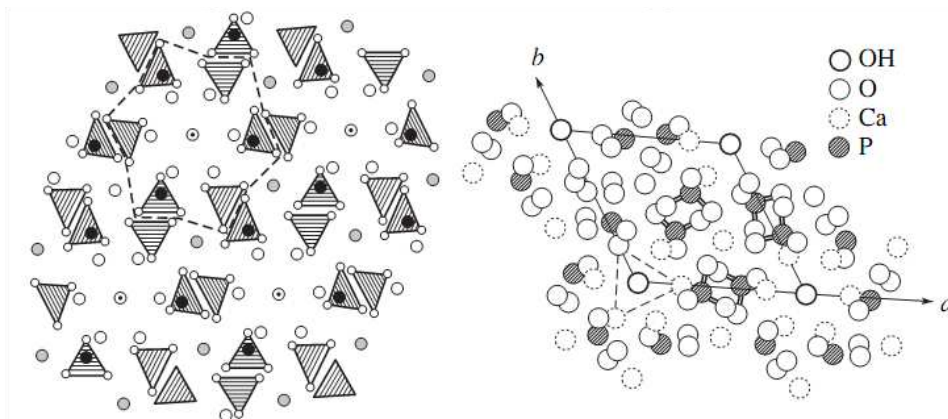


Figure 1.2: On the left: Atomic structure of HA. On the right: projection of HA unit cell along the c-axis. From [18].

The distortion of the crystallographic system due to ionic substitution is of prime importance: the modification of the cell parameters causes the crystallinity and the thermal stability to decrease, whereas the solubility rises.

Hydroxyapatite osteointegration The bonding mechanism of HA materials to bone is not yet completely understood [19]. Roughly, the integration steps are the following: First, osteogenetically competent cells adhere on the HA surface. The HA induces these cells to differentiate into osteoblasts. Progressively, a bone matrix is formed on the implant surface. In this state, the interface between the implant and the bone is amorphous, but contains small apatite crystals. As maturation occurs, the bonding zone shrinks and finally disappears. Finally, the HA is attached to the bone by a thin epitaxial layer. With HA, a fibrous interphase is not formed. Bone formation occurs from the implant surface towards the porosity of the bone.

1.2 Description of the ANR project

The present work is part of the ANR project Nanobonefiller (ANR-06-PNANO-22) submitted by six research teams in 2006 (see table 1.3) and coordinated by Dr Karine Anselme who is also one of the supervisors of this thesis. The aim of the project is the development of an injectable bone filling system based on calcium phosphate materials associated with growth factors for improved bone regeneration. It is intended to inject the material into bone cavities to allow the progressive release of growth factors during its biodegradation and thus favor the bone regeneration.

The project associates six research groups with different research interests and competences: Chemists as specialists for nanoporous materials and calcium phosphate sol-gels, biochemists for the release of growth factors, biologists, specialists for in vitro and in vivo studies of biomaterials and physicists able to analyze the degradation and integration of materials in tissues.

1.2.1 Short description of the project

In a first step, nanoporous calcium phosphate materials will be produced by different techniques: Molecular or supramolecular entities can be mixed into the synthesis mixture. They are occluded in the growing solid and give rise to a pore system upon their removal. For this approach the term “endotemplating” is proposed. Alternatively, the template can be a material with structural pores in which another solid is created, thus providing a scaffold for the synthesis. Such a template is referred to as “exotemplate”. A more profound explanation of the terms “endo-” and “exotemplate” can be found in section 2.1.2 on page 25.

These different templating techniques will lead to materials having mesoporous textures with pore sizes depending on the choice of the templating procedure. The synthesis of mesoporous calcium phosphates by templating is a technological limitation to be overcome by the project as few papers on the preparation of CaP by templating have been

Laboratory name		research unit	town	researcher	task
IS2M	Institute for Material Science in Mulhouse	CNRS LRC 7228	Mulhouse	K. Anselme	coordination
IBTH	Interactions between Biomaterials and Host Tissues	INSERM ERM 0203	Reims	P. Laquerriere	synthesis and characterization of nanovectors by templating, protein adsorption study of the inflammatory potential, cell/material interactions
LPC	Laboratory of Particle Physics	CNRS UMR 6533	Clermont	E. Jallot	nano-PIXE
LMI	Laboratory of Inorganic Materials	CNRS UMR 6002	Clermont	J-M. Nedelec	synthesis of nanovectors by soft chemistry approaches, XRD, XPS characterization of the materials
BRT	Biomaterials and Tissue Repair	INSERM U 577	Bordeaux	J. Amedee	in vitro and in vivo evaluation of the materials.

Table 1.3: The teams participating in the ANR project NANOBONEFILLER.

published. Additionally, the quality of the calcium phosphate obtained after calcination has to be controlled in order to control the degradation kinetics. The two laboratories in Mulhouse (IS2M) and in Clermont (LMI) have both confirmed expertise in the field of the chemistry of ceramics and have special equipment at their disposition. The first phase of the project will therefore be the following: Synthesis of mesoporous calcium phosphate ceramics by exotemplating (Mulhouse) and endotemplating (Clermont).

Secondly, the mesoporous scaffolds will be impregnated with growth factors. Vascular Endothelial Growth Factor (VEGF) and Transforming Growth Factor beta 1 (TGF- β 1) have been chosen for the association with the ceramic. The former favors the formation of blood vessels, the latter stimulates bone formation. The control of the impregnation of these porous structures by the different molecules is the second technological limitation to overcome since the size of the considered biomolecules is close to the size of mesopores (2-50 nm). Various techniques will be used to characterize the biomolecule adsorption inside the porosity. In particular, an innovative mass spectrometry technique has been adapted in Mulhouse for the quantification of proteins trapped inside porous materials [20, 21].

The LPC team has developed a specific protocol to determine the distribution of growth factors in the ceramic at nanometer scale with a focused ion beam. Chemical maps (Ca, P, S) across the ceramic are performed by nano-PIXE (Particles Induced X-ray Emission). Other techniques based on ELISA (Enzyme-linked Immunosorbent Assay) or colorimetry will be used for release experiments.

Thirdly, the cytocompatibility of the nanovectors will be tested in vitro in direct or indirect contact with osteoblasts by the IBTH teams. The eventual inflammation and cellular alterations induced by the nanoporous ceramics will be investigated in Reims using an original cryo-method: cryo-sections of human monocytes and osteoblasts cultured in contact with the ceramics are analyzed with electron microscopy coupled with X-ray spectroscopy. This technique allows to analyze the potassium to sodium ratio in the cell and thus the characterization of the inflammatory potential of pure and loaded calcium phosphates.

The final step of the ANR project will be the validation of the efficacy of osteogenesis by the doped ceramics in in vitro and in vivo experiments. The evaluation will be carried out in Bordeaux by the BRT team. The effect of the release of bone regenerating growth factors on human endothelial and osteoprogenitor cells will be observed in vitro. For the in vivo validation, both a bone site implantation and a subcutaneous implantation (ectopic site) will be done in small animal models. Osteoinductive properties will be analyzed by the implantation under the skin of the animals. In order to study the osteoconductive properties of the ceramics, a bone cavity will be created in femoral condyles of mice. The bone cavity will be closed and filled across the cortical wall to validate the injectability of the material. The creation of closed bone cavities and their filling through a syringe is another technical limitation to overcome. Indeed, the nanovectors must be in powder form composed of nanoparticles with diameters below 200 nm. A liquid or gel vector must be developed to assure the even distribution of the ceramic inside the bone cavity. For these purpose, Hydroxypropylmethylcellulose, xanthan or hyaluronate have been shown to form slurries with controlled injectable

properties [22, 23].

1.2.2 Bibliographic context and skills of the project partners

Orthopedic surgeons are frequently confronted with bone loss following trauma, infections or tumors. Many synthetic or natural bone substitutes have been proposed for bone replacement but up to now their efficacy remains lower than the one of autologous bone grafts which are still considered as the ‘gold standard’. Tissue engineering strategies have been developed as alternative solutions to autologous bone grafts. Hybrid materials associating autologous bone marrow stem cells with macroporous calcium phosphate substrates have been proposed for these applications. The biologist teams from IS2M [24, 25] and BRT [26, 27] have a strong experience in these hybrid materials.

However, a lot of problems still remain for increasing either osteogenesis or angiogenesis in these hybrid materials. For several years, several teams have searched to develop scaffolds allowing the covalent grafting or the entrapping of osteogenic or angiogenic growth factors but the perfect control of the quantity of growth factors entrapped in the scaffolds, of their release and of the degradation kinetics of the material is still not achieved [28–30]. Additionally, because of the aging of the population in the developed countries, the clinical need of injectable materials for bone filling is more and more critical for decreasing the cost and health risks of surgical operations. This has led to the development of injectable calcium phosphate cements [31]. These materials have been used for the release of antibiotics or growth factors because of their resorption capacity [32]. The possibility to release biomolecules from hydroxyapatite microspheres or particles has been also considered [33]. These materials can be injected when associated with an appropriate vector [22]. The controlled release from mesoporous silica or carbon of biomolecules like albumin, lysozyme, interleukin-1 or hemoglobin has been recently demonstrated [34–37]. Thus, it appears that mesoporous structures could be adequate materials to control the release of active biomolecules. Consequently, it appears very promising to develop calcium phosphate materials with a controlled mesoporous texture for the release of osteogenic growth factors. The team Carbon and Hybrid Materials from IS2M is recognized for its expertise in carbon and silica ceramics materials. This team has gathered an considerable know-how in the synthesis of ordered porous carbon materials used as selective adsorption or energy storage medium [38–41]. The LMI laboratory from Clermont-Ferrand is well known in the field of calcium phosphate sol-gels [42–44]. The association of the competences of these two laboratories will permit the development of perfectly innovative calcium phosphate materials with controlled mesoporous architecture since, to our knowledge, an equivalent material for entrapping and releasing biomolecules in a controlled way does not exist yet. The release of biomolecules from the mesoporous materials is investigated first by using model molecules cheaper than growth factors like BSA and Cytochrome C. Then, release experiments are performed using commercial TGF- β 1 and VEGF. The *in vitro* and *in vivo* biological validation of doped and non-doped materials is carried out by the different biologist teams involved in this project (IS2M, IBTH, BRT). These teams are internationally recognized as specialists of cellular and tissue reaction to bone biomaterials. They will associate their

competences for validating the in vitro behavior of various cell types concerned during the implantation of the doped mesoporous materials like monocytes, osteoblasts and endothelial cells [45–51]. Moreover, the IBTH and LPC teams will use original physico-chemical techniques they have developed for characterizing the material degradation and the cell response [52–54].

1.2.3 This work in the setting of the ANR project

1.2.3.1 Preparation of nanoporous calcium phosphate

Two different methods can be distinguished when templates are used for the synthesis of porous solids. By analogy to the terms 'endoskeleton' and 'exoskeleton' in biology, we propose to distinguish between 'endotemplate' and 'exotemplate'. Section 2.1.2 gives an overview on these terms. *In the frame of the project, these two synthesis strategies are adopted to prepare nanoporous calcium phosphate (CaP) with a controlled and interconnected porosity.*

Endotemplating with supramolecular surfactant aggregates. Ordered mesoporous silica materials such as MCM-48, SBA-15 etc. are commonly prepared by this approach [55]. They result from the lyotropic liquid-crystal arrangement of surfactant molecules, around which silicate ions condense to form the silica framework. The condensation of an inorganic phase into these supramolecular assemblies allows the preparation of various architectures depending on the composition of the water/organic phase/surfactant. Using this pathway, it is possible to synthesize ordered porous materials with pore sizes in the range of 2-10 nm. For this study, organized mesoporous silica materials of the SBA-15 and MCF type are prepared following the procedures described in the literature [56, 57]. The silica will be used as host material for the preparation of CaP by an exotemplating pathway (see 1.2.3.1).

However, the main motivation to mention this supramolecular templating pathway is our wish to adapt this approach developed for silica to the synthesis of CaP. It has been shown that this method could be applied to other materials than silica [58]. The synthesis is however more difficult to succeed than for silica. To our knowledge, no paper was so far devoted to the preparation by this way of CaP. Only one paper related to the synthesis of mesoporous hydroxyapatite was found [59]. It describes the synthesis of HA using a cationic surfactant (CTAB) as template. The channels have dimensions around 3.5 nm and the spaces between the nano-channels are filled with an ordered crystalline HA structure. Our objective is to prepare pure HA or biphasic CaP material (mixture of HA and TCP) with pore size ranging between two and a few nm and with a specific surface area of few hundred m²/g. Several parameters must be studied, among them the synthesis conditions and the type of surfactant which is the dominating factor for directing the formation of a specific structure.

Experiments following the endotemplating pathway were carried out by Olivier Raissle, PhD student in the LMI and LPC team in Clermont-Ferrand. Some of his methods and results will be presented in section 3.1.5.

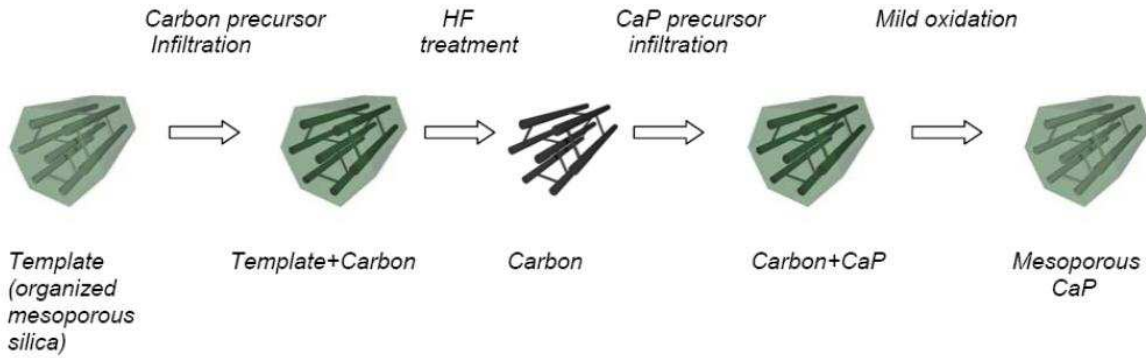


Figure 1.3: Synthesis of porous hydroxyapatite by double replication from silica

Exotemplating with ordered porous carbons. The concept of exotemplating has been developed only over the last few years, when it was realized that it was possible to obtain structure replication on a length scale of nanometers. Two approaches will be adopted in this project to prepare mesoporous and macroporous CaP:

- the nanocasting of an ordered porous carbon material and
- the synthesis of inverse opals.

For the nanocasting approach, a 3-D-connected ordered mesoporous material is filled with a precursor for another solid material. The product is obtained in pure form as the negative of the template after removal of the template. By this way, different types of ordered porous carbons can be prepared which in turn will be used again as exotemplates. In our case, CaP will be prepared by nanocasting of ordered porous carbon materials which themselves will be prepared by templating of organized mesoporous silica. The synthesis pathway is schematically represented in figure 1.3.

The preparation of ordered porous carbons is well controlled by the Carbon and Hybrid Materials group at IS2M, which has given many new developments in this topic [38,39,41]. By this way, carbon materials with an organized interconnected porous texture, a high specific surface area (between 1000 and 2000 m²/g), a uniform pore size distribution (pore sizes between 2 and 10 nm) and a micro/mesoporous character can be obtained. The texture of the carbon can be controlled by the choice of the template, the carbon precursor and the impregnation method [40,41].

Numerous strategies have been proposed to prepare calcium phosphates ceramics. The most widely known and used is the precipitation method. However, this method is not compatible with exotemplating. An alternative method is the sol-gel process. The ordered porous carbon material will be impregnated by a CaP precursor prepared by a sol-gel technique. This process offers a molecular mixing of the calcium and phosphorus precursors capable of improving the chemical homogeneity [60–62] and allows to obtain bioceramics with different physico-chemical characteristics (composition, porosity and crystallinity, ...). The success of the impregnation will depend on several factors – among them the impregnation conditions (atmosphere, temperature, concentration of

the sol, wettability of the carbon template, ...) – that will be studied in a systematic way. The impregnated carbon material will then be heat-treated at high temperature to convert the sol-gel into a CaP material and to remove the carbon (see figure 1.3). The characteristics of the CaP material must comply with the following criteria:

- The porous texture must be adapted to an efficient cytokine adsorption. Efficient cytokine adsorption has been observed in a mesoporous organic silica material (pore size around 6 nm) [37].
- The porous texture must be adapted for controlling the biodegradation rate. In fact, the solubility and resorption rate are strongly influenced by the texture (e.g. the solubility increases with the pore size [63]). Combined use of sol-gel chemistry and template synthesis will allow controlling the texture (specific surface area, pore size, pore volume, ...) which are predominant parameters for the control of the biodegradation rate.
- The crystallinity and/or crystal size must be appropriate. Indeed, they are also important parameters to control since they play an important role in the dissolution of the ceramics [54, 63–65].

To meet these criteria, synthesis conditions such as the preparation conditions of the sol-gel (concentration, aging temperature, ratio of the CaP precursors), the duration and sintering temperature are taken into account and optimized.

To summarize, CaP materials can be prepared by nanocasting of ordered porous carbon materials. They display a mesoporous and interconnected network with pore sizes between 2 and 10 nm and a narrow pore size distribution. By changing the texture of the carbon template, the final characteristics of the CaP can be modified. Therefore, this exotemplating pathway represents an interesting means to prepare model CaP materials with a controlled and organized porosity.

The originality of the project can be summarized by the following points:

- Preparation of porous model materials to study the mechanism of formation of a CaP material in a confined medium.
- Determination of the optimum properties of calcium phosphates regarding high protein loadings and controlled release.
- Development of a drug delivery system that can be injected into closed bone cavities through the cortical bone wall.

The synthesis of calcium phosphate materials by exotemplating based on ordered mesoporous carbon and silica is the core of this work. In chapter 2.3.1, the choice and the optimization of the template material are detailed. In addition to ordered mesoporous carbon, silica foam materials will be used for the synthesis of CaP materials.

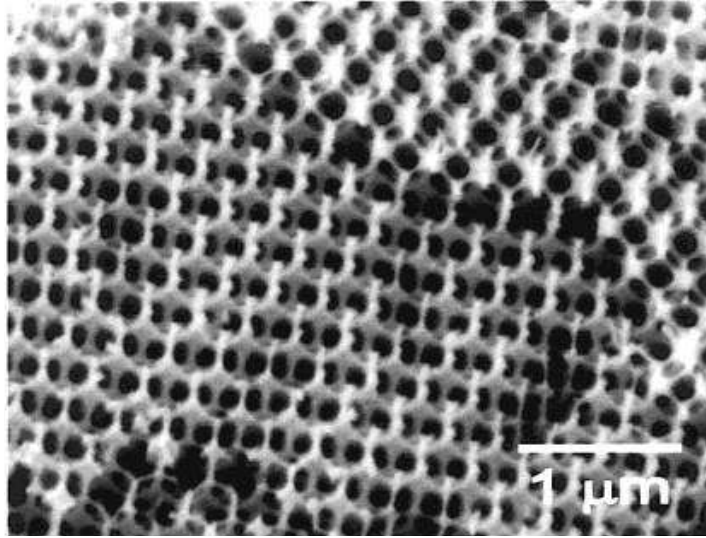


Figure 1.4: Porous hydroxyapatite obtained by opal replication. From [68]

Exotemplating with opals. The second exotemplating way studied in this project will be the synthesis of inverse opals. While templating with supramolecular aggregates, such as liquid crystals, or the nanocasting process results in the formation of pores in the mesopore range, ordered macroporous materials are accessible by templating with colloidal crystals formed from monodisperse spherical particles with diameters of several hundred nanometers [66]. The synthesis of inverse opals will be achieved by filling the voids in close sphere packings with a desired solid (in our case the CaP sol-gel) and subsequent removal of the original spheres. Several decisive steps in the synthesis process of an inverse opal will be studied such as the assembly of the opal template, the wetting of the opal template, the filling degree of the voids of the initial opals and the condensation and template removal conditions. The choice of the initial size of the spheres in the template will control the size of the pores in the final material. Contrary to the nanocasting approach, the final CaP material obtained by this system would be rather macroporous (pores >50 nm). This method has been successfully used to prepare hydroxyapatite as described by Stein et al. [67,68] (see figure 1.4). However so far, no biological studies of this material were presented in the literature.

Even if the material is macroporous, the comparison of its performance with those of the mesoporous CaP will be of great interest. Another interest to develop this approach is the possibility to combine it with the endotemplating approach.

Although the exotemplating with opals was mainly studied in Clermont-Ferrand, some preliminary experiments on the replication of silica opals will be also carried out in Mulhouse. The reader may find information to these in chapter 2.3.2.3.

Characterization of the CaP materials. Whatever the synthesis pathways selected, the obtained CaP materials are characterized by X-ray diffraction, IR spectroscopy and nitrogen adsorption at 77K to determine the pore size distribution of the material. Mi-

Microscopic observations by SEM and TEM are also performed. X-ray diffraction patterns allow the determination of the crystalline phases that compose the material and can detect impurities. In addition to this chemical characterization, the width of the diffraction peaks is related to the size of the crystallites. From this value, conclusions on the crystallinity of the material can be drawn. IR spectroscopy gives complementary information on the chemical composition of the ceramic: Contrary to X-ray diffraction, the technique can analyze amorphous phases that do not diffract X-rays. The combination of both techniques gives a complete picture of the chemical composition of the ceramic.

Nitrogen physisorption is the most widely used technique for the characterization of nanoporous materials. The shape of the isotherm and the amount of adsorbed gas allow the determination of the specific surface area, the pore size and volume and the pore size distribution. A more detailed description of the technique and the theories that allow the calculation of the characteristic values of the porous material can be found in appendix 5.1 on page 169.

Microscopic observation with SEM and TEM complete the description of the ceramics. They allow the visualization of the surface of the material (SEM) and of its structure and porosity (TEM). In TEM, the pores of the material appear in white as they do not hinder the transmission of the electron beam.

To summarize, two approaches are proposed to prepare CaP: an endo- and/or an exotemplating pathway. For endotemplating, the use of supramolecular surfactant aggregates with a calcium precursor allows to obtain mesoporous ceramics with pores between 2 and 10 nm. The exotemplating pathway corresponds to the nanocasting of ordered porous carbon materials or of inverse opals. For the nanocasting process, a mesoporous CaP is expected with a pore size ranging between 2 and 10 nm. Since the porous texture of the final material can be controlled, this way appears as an excellent method to prepare model CaP material. These model materials are useful to perform a fundamental study on the mechanism of CaP formation in a confined medium and to determine the optimal textural characteristics that the CaP material must display to be efficient in regard to the proteins adsorption.

The second exotemplating approach concerns the synthesis of an inverse opal. Even if the synthesis process is less innovative and leads to a macroporous material, no systematic study of the proteins adsorption on this type of material was already found in the literature. However, by reducing the size of the spheres composing the opal, smaller pores can be created in the CaP material, improving the material's capacity of growth factor retention.

1.2.3.2 Analysis of cytokine adsorption

Adsorption of model biomolecules will be studied in order to adapt the pore volume, the structure and the surface chemistry of the CaP to molecular weight and charge of the growth factors we chose to study in this project. Concerning the growth factors, osteogenic factors like Bone Morphogenic Proteins (BMPs) have been extensively studied in association with various carriers for bone induction and bone regeneration. Particularly, BMP-2 has shown its efficiency for bone regeneration but as Malafaya et al.

underline in their review paper, little has been reported on the release profile of other bone regenerating growth factors like FGF-2, PDGF-BB, IGF-1, TGF- β 1 or VEGF [69]. We have chosen in our project to focus our attention on two of these last bone regenerating factors: TGF- β and VEGF. We preferred TGF- β to BMP-2 since BMP-2, in spite of many studies in ectopic and bone sites in various animal species and in association with various carriers, has not yet overtaken the experimental stage and appears to be less promising for bone engineering than ten years ago.

TGF- β has interesting properties for tissue engineering applications. It is a multifunctional protein that regulates many aspects of cellular function. On bone, TGF- β has a pivotal role in the bone remodeling process since it affects both bone resorption and formation [70]. All three TGF- β isoforms are detected in bone but the TGF- β 1 isoform is the most abundant. TGF- β 1 increases in vitro bone formation mainly by recruiting osteoblast progenitors and stimulating their proliferation. On the other hand, it blocks later phases of differentiation and mineralization. Moreover, TGF- β 1 promotes fracture healing and bone formation in vivo. However, no clinical application of TGF- β 1 has been developed yet. The half-life of TGF- β 1 is short (about 2 min) implying the need for a scaffold for a slow release of the growth factor and its confinement in bone tissue [70].

VEGF (Vascular Endothelial Growth Factor) is not really a bone regenerating factor. Its main action concerns angiogenesis. It has a mitogenic potential for endothelial cells but has been shown to be synthesized by human bone marrow stromal cells and to have a mitogenic action on these cells [71]. It appears also to be a main signaling molecule between osteoblast cells and endothelial cells. As vasculature plays an important role in bone regeneration, it appears pertinent to associate a factor stimulating angiogenesis and a factor stimulating bone formation in the same drug release system. It has been shown that VEGF coupled with bioactive glass enhanced angiogenesis and bone maturation [71]. This approach of association of growth factors for clinical application is still in infancy whereas the complementary functions of several growth factors are promising. The development of multiple growth factor delivery systems that control the temporal availability of the factors has shown utility in angiogenesis, and this concept may be useful for application in bone regeneration [72].

Members of each growth factor family have similar structural features regarding their chain length, their oligomeric and 3D structure and their overall charge at a given pH (isoelectric point). More details on the growth factors that have been selected for this study can be found in section 3.1.4 on page 130.

Mesoporous carriers with cavities around 10 to 15 nm would be most suited for this type of small protein molecules.

Given the prices of commercially available growth factors, we will use basic proteins with low molecular weight as models to set up our first series of experiments. Cytochrome C for example is a favored candidate since it has been previously used as model molecule for TGF- β [73]. We will also use BSA, which has been studied previously by TPD at our institute [21]. It can easily be quantified by UV/Vis adsorbance after staining with Bradford reagent.

A quantitative evaluation of protein binding to calcium phosphate scaffolds and the

kinetics of release will be studied in various experimental conditions (pH, concentration, etc). The precise amount of protein will be easily determined by ELISA assays using anti-VEGF and anti-TGF- β 1 antibodies and by colorimetry for the model proteins.

An innovative technique will be used to characterize the biomolecule adsorption directly inside the pores. It associates mass spectrometry with temperature programmed desorption (TPD). This technique has been recently adapted in IS2M to quantify the proteins entrapped inside nano-porosity [20, 21]. It is based on the emission of a H₂S peak during the heat treatment process of the nanoporous material impregnated with proteins. This H₂S formation is linked to the degradation of disulphur bonds which are numerous in proteins like albumin, fibronectin or in growth factors of the TGF- β family.

The release of growth factors must be progressive on several days and the activity of the growth factors must be maintained during all the release. For the determination of the correct doses to release, we will base ourselves on previously published papers describing release of growth factors from calcium phosphate materials [29, 48, 71, 74–77] and on the expertise of the BRT team in Bordeaux. *Adsorption and release experiments with both model proteins and growth factors constitute the second part of this thesis (see chapter 3.1.)*

2 Hydroxyapatite by hard templating techniques

2.1 Bibliography

This chapter first gives an overview of the synthesis methods and precursors that are commonly used for the synthesis of hydroxyapatite. In a second part, the concept of templating will be introduced. Finally, the attempts to make mesoporous hydroxyapatite by templating methods published to date are reviewed.

2.1.1 Synthesis of hydroxyapatite

2.1.1.1 Precursors

Inorganic salts. Inorganic calcium salts are one of the most frequently used precursors in the synthesis of HA. Simple salts such as calcium chloride CaCl_2 [59, 78], hydroxide $\text{Ca}(\text{OH})_2$ [79–83], sulfate CaSO_4 [18], carbonate CaCO_3 [18] and nitrate $\text{Ca}(\text{NO}_3)_2 \cdot 2\text{H}_2\text{O}$ [84–88] can be used for the synthesis both in sol/gel and in precipitation techniques. Table 2.1 gathers the solubility and the pH of salt solutions for important calcium precursors for the synthesis of calcium phosphates for biological application.

In addition to simple salts, some calcium phosphates can be used as precursors for hydroxyapatite. For example, α -TCP [18] hydrolyzes into calcium deficient HA. When starting from calcium phosphates, it is important to choose one precursor with a Ca/P ratio less than 1.67, the Ca/P ratio of HA, and the other one with a higher Ca/P ratio. Calcium phosphates can act both as calcium and as phosphate sources.

Inorganic phosphorus precursors include phosphoric acid H_3PO_4 [78, 81, 89], triammonium phosphate $(\text{NH}_4)_3\text{PO}_4$, diammonium hydrogenophosphate $(\text{NH}_4)_2\text{HPO}_4$ [80, 84, 85], ammonium dihydrogen phosphate $\text{NH}_4\text{H}_2\text{PO}_4$ [9, 73, 82, 83] and phosphorus pentoxide P_2O_5 [90, 91]. Ammonium components are of particular interest as they can be decomposed under gas development. They can therefore act as porogenes, creating intrinsic porosity in the ceramic during sintering. Unfortunately, this porosity is seldom interconnected, and its size is difficult to control.

Metalorganic precursors. Metalorganic calcium precursors are calcium compounds with organic ligands. Typical examples are alkoxides $\text{Ca}(\text{OR})_2$, such as ethanlates $\text{Ca}(\text{OEt})_2$, and acetate $\text{Ca}(\text{OAc})_2$. Organophosphorus compounds commonly used for

Name	Formula	Solubility in water	pH of aqueous solution
Calcium chloride	CaCl_2	740 g/L	8-10 ¹
Calcium nitrate tetrahydrate	$\text{Ca}(\text{NO}_3)_2 \cdot 4 \text{H}_2\text{O}$	2710 g/L	5-7 ²
Calcium hydroxide	$\text{Ca}(\text{OH})_2$	1.7 g/L	12.6 ³
Calcium acetate	$(\text{CH}_3\text{CO}_2)_2\text{Ca}$ or $\text{Ca}(\text{OAc})_2$	400 g/L	7.2-7.4 ²
Calcium dihydrogen phosphate monohydrate	$\text{Ca}(\text{H}_2\text{PO}_4)_2 \cdot \text{H}_2\text{O}$	31.5 g/L	0-2
Tricalcium phosphate	$\text{Ca}_2(\text{PO}_4)_3$	1.2 g/L	0-2

¹ 100 g/L at 20°C, ² 50 g/L at 25°C, ³ saturated solution.

Table 2.1: Calcium precursors for the synthesis of calcium phosphates.

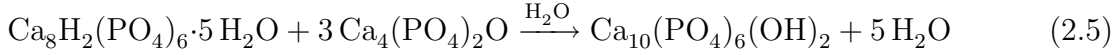
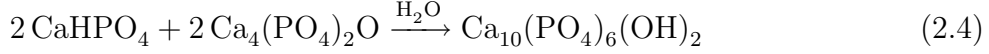
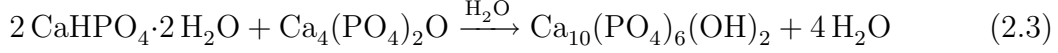
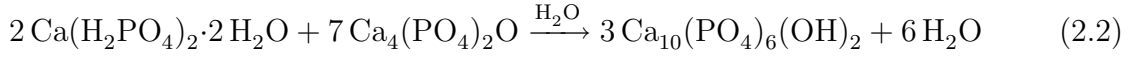
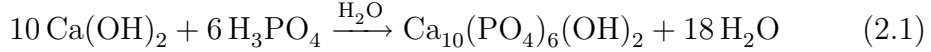
the preparation of calcium phosphates are organophosphates $(\text{RO})_3\text{PO}$ and organophosphites $(\text{RO})_3\text{P}$. These are esters of phosphoric and phosphorous acid respectively. Additionally, organophosphorous compounds can be used. In contrast to organophosphates and -phosphites, these compounds are characterized by a direct phosphorus/carbon bond. Among these, triethyl phosphine $\text{P}(\text{Et})_3$ [92] and (dichloro)phenyl phosphine [87] have been used for the synthesis of HA. Both compounds are air- and moisture-sensitive and must be handle under protective atmospheres.

Compared to simple inorganic precursors, metalorganic compounds are soluble in organic solvents and hydrolyze at different velocities. The velocity of the hydrolysis can be controlled by choosing the right ligands. By this way, the kinetics of the reaction can be controlled by the choose of the precursor and the hydrolysis conditions.

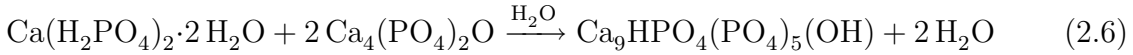
2.1.1.2 Synthesis methods

Precipitation techniques or wet chemistry approaches involve the precipitation of HA from solutions that contain Ca^{2+} and PO_4^{3-} ions in basic conditions. The most commonly used calcium sources are CaCl_2 , $\text{Ca}(\text{NO}_3)_2$, $\text{Ca}(\text{OH})_2$, CaCO_3 , $\text{CaSO}_4 \cdot 2 \text{H}_2\text{O}$, $(\text{CH}_3\text{COO})_2\text{Ca}$. Phosphorus sources include H_3PO_4 , $\text{NH}_4\text{H}_2\text{PO}_4$, $(\text{NH})_2\text{HPO}_4$, and K_3PO_4 . The pH of the solutions can be adjusted by ammonia (gaseous or in solution) and NaOH [18]. In order to obtain pure hydroxyapatite by precipitation, simple acid/base reactions are used. In this case, one precursor is more acidic, the other one more basic than HA. The acidic reactant should have a Ca/P ratio below the one of HA,

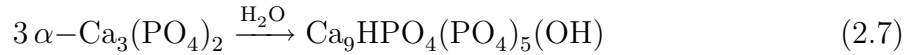
the basic one a higher Ca/P ratio. Some possible reactions are [18]:



These are just some examples of many possible synthesis routes. By changing the ratio of the reactants, non-stoichiometric compounds can be produced:



This reaction uses the same precursors as reaction (2.3) but produces calcium deficient HA due to the modified ratio between the reactants. Calcium deficient HA can also be formed by direct hydrolysis from α -TCP:



Independently from the precursor, these reactions form calcium phosphates via dissolution/precipitation mechanisms. The driving force of the reaction is therefore the difference in solubility of the product and the reactants (see table 2.1 for values). According to the Ostwald-Gay Lussac law of progressive crystallization, some products will form through metastable intermediates. For example, reactions 2.3 and 2.7 will give rise to calcium hydrogen phosphate dihydrate $\text{CaHPO}_4 \cdot 2 \text{H}_2\text{O}$ that decomposes into HA.

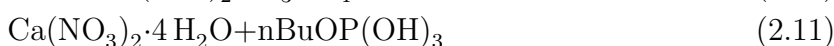
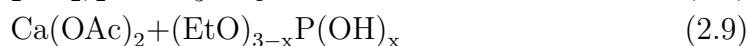
Precipitation reactions and direct hydrolysis of α -TCP can occur at 37°C. The reaction conditions are unlikely to damage adjacent tissue: they proceed at pH values and ionic strengths close the one of extracellular fluids and do not change the temperature. Additionally, the formation of HA in physiological environment can be directed epitaxially by the proteins present. These are the reasons why precipitation reactions are the basis of self-setting calcium phosphate cements: they can be injected into the body without further damaging the implantation site and give rise to HA in situ.

For the application in the synthesis of mesoporous HA, precipitation reactions are unsuitable. The reaction occurs immediately and the kinetics are generally fast. For templating, it is necessary that the precursors react slowly and preferably upon external stimulation (for example heating) to allow the arrangement around surfactant micelles or inside the porosity of a hard template.¹ Thus, sol-gel approaches must be preferred.

¹see section 2.1.2

Sol/gel. The sol/gel synthesis of ceramics involves at least three steps: the preparation of a sol, gelation of this sol into a gel and the removal of the solvent. A *sol* is the colloidal suspension of particles in a liquid. The inertia of the suspended phase is sufficiently small that the solid exhibits Brownian motion and does not sedimentate. When further reaction of the precursors takes place, the sol is transformed into a gel by polycondensation and reticulation: a *gel* is an integrated network that entraps its solvent. The kinetics of the formation of the gel are governed by two processes: the hydrolysis of the precursors and the polycondensation. By carefully choosing the right combination of precursors and the right synthesis conditions (pH, solvent, temperature), the kinetics of the reaction can be controlled.

Typically, sol-gel approaches for the synthesis of ceramics involve organometallic precursors – such as alkoxides – and metal chlorides. In the case of calcium phosphates, organophosphorus or organocalcium compounds can be used. Some typical precursor combinations are [67]:



Although all these examples contain at least one organometallic component, sol/gel systems can also be achieved from the all inorganic combination of $\text{Ca}(\text{NO}_3)_2 \cdot 4\text{H}_2\text{O}$ with phosphoric acid or phosphorus pentoxide [67].

Sol-gel syntheses are perfect candidates for the application in templating: by adjusting the synthesis parameters and by using the right combination of precursors, the kinetics of the reaction can be controlled. Additionally, reticulation and gel forming often requires an external stimulus (heating) so that the precursor can penetrate the porosity of the template before the system solidifies.

Vapor phase deposition. Chemical vapor deposition (CVD) is a technique that involves gaseous precursors that decompose on the surface of a substrate or within a template, giving rise to the desired compound. In contrast to physical vapor deposition (PVD), where the product is deposited by simple sublimation, the precursor(s) undergo(es) a chemical reaction that gives rise to the desired product. In tissue engineering, CVD techniques are often used in the field of biomaterials in order to apply coatings to metallic implants. Plasma spray coating is however more popular. If metalorganic precursors are used, the term MOCVD (Metal-Organic Chemical Vapor Deposition) is adopted.

The first papers on the MOCVD of hydroxyapatite were published as early as 1994 by Spoto et al. [93]. Spoto et al. deposited HA coatings to alumina surfaces using calcium dipivaloylmethane chelate ($\text{Ca}(\text{DPM})_2$, see figure 2.1) and phosphorus pentoxide as precursors. The precursors were evaporated separately and introduced into a hot wall

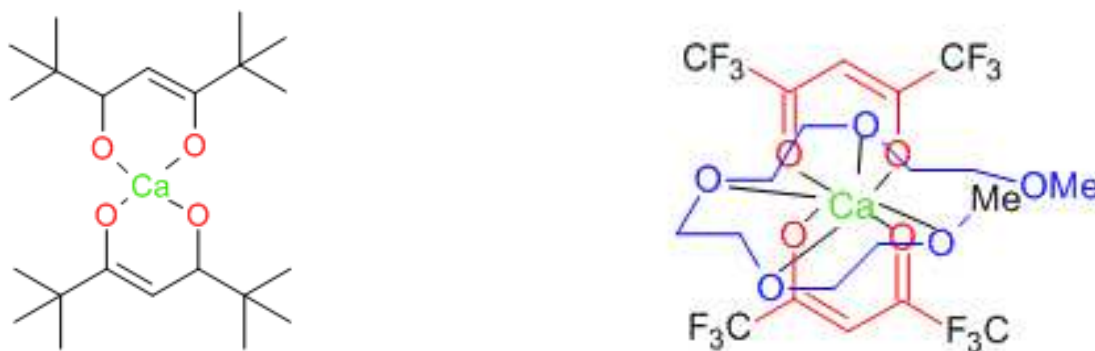


Figure 2.1: $\text{Ca}(\text{DMP})_2$ and CAT: typical MOCVD precursors for calcium phosphates.

reactor at 850°C . The HA was deposited at the coldest spot in the reactor which was the alumina surface. The authors obtained a dense layer of microparticles with diameters ranging from 5 to $10\ \mu\text{m}$. After calcination of these layers at 1350°C , the side products $\beta\text{-Ca}_3(\text{PO}_4)_2$, $\beta\text{-CaP}_2\text{O}_7$ and AlPO_4 , which were found initially, disappeared.

A comparable method was patented in 2001 for the preparation of a fiber-containing composite material [94]. Fluorine containing calcium- β -diketonates and alkylphosphates and phosphites as well as phosphorus pentoxide are cited as possible precursors.

Darr et al. use a similar type of calcium precursor [95]: calcium di(hexafluoro-2,4-pentadione)(tetraglyme) (CAT) as shown in figure 2.1. These compounds are volatile calcium complexes that can be reacted with tributylphosphate in the gas phase in order to deposit HA coatings. The obtained coatings are composed of carbonated HA and found to be very similar to bone mineral in composition.

MOCVD is an elegant method for the synthesis of coatings and can be used for the replication of porous templates as well. The gaseous precursors can reach the pores easily if they are not too large. The surface of the template represents spots of high surface energy, which will favor the deposition of the product. On the other hand, big precursors occupy a lot of space and give only small amounts of product. In this case, the dead volume effect (volume occupied by the precursor or the solvent that will not be filled with product) is important and prevents the complete filling of the porosity. It is a challenge to develop precursors that are volatile, sufficiently stable to be sublimated without decomposing, give the desired product and are not too bulky.

Solid state reactions involve the reaction of powders without a solvent. Compared to sol/gel and precipitation methods, they are rarely used for the synthesis of HA. Normally, high temperatures or mechanical activation are required in order to permit the reaction over the grain border.

R. Ramachandra Rao and coworkers [96] describe the solid state reaction between calcium phosphate and calcium hydroxide leading to different calcium phosphate species. The composition of the resulting phase depends on the stoichiometric relation between

the reactants and on the heat treatment. In most cases, a mixture of different calcium phosphate species is obtained.

Yeong and Wang present a mechanochemical synthesis of hydroxyapatite starting from calcium oxide and calcium hydrogenophosphate [97]. The dry powders are ball milled for 20 h, resulting in nanocrystalline hydroxyapatite powder with high interparticular surface.

Using the same kind of reaction, but starting from calcium pyrophosphate and calcium carbonate, Chang et al. [98] managed to create porous hydroxyapatite implants. The milling was performed in the presence of water. The porosity was generated by the use of folded sheets made from polyester templates. Burning of the polymer template gives interconnected cylindrical pores with diameters in the micrometer range. See figure 2.4 on page 27 for an illustration on how sheets are transferred into cylindrical pores.

This last example is one of the rare cases where templating has been combined with mechanosynthesis and it only created macropores. For the synthesis of mesoporous hydroxyapatite, more fragile templates are used, which would withstand the mechanical or thermal stress during the synthesis.

2.1.1.3 Product treatment: hydrothermal, sintering, SPS

Not only the precursors influence the properties of the final material, the treatment plays an equally crucial role. In order to transform the precursors into the desired product, energy must be provided. In some cases, if the precursors are unstable, an external energy source is unnecessary, and the reaction occurs spontaneously. In the majority of reactions, thermal activation is nevertheless required.

Sintering. The term “sintering” describes the densification of a ceramic green body due to heat treatment. Often, the term is used as a synonym for heat treatment or calcination. If the heat treatment is directly applied to the precursor, solid state reactions can transform two (or more) precursors into the desired product. But also for sol/gel and precipitation techniques, sintering often follows the wet chemical step of the formation of the product. In these cases, the sintering transforms intermediate products into HA, eliminates by-products and residues of the precursor, and improves crystallization.

Calcination is carried out in furnaces, often with control of the atmosphere. Reactive gases such as oxygen, water or carbon dioxide can be used. In other cases, inert gases such as nitrogen and argon are preferred. They do generally not interact with the products and act only as a carrier to eliminate gaseous by-products.

Heat treatments at high temperatures are always accompanied by structural reorganization of the product, improving its crystallinity. As nanoparticles have a high surface energy, the system will try to minimize this energy by grain growth [99]: small particles will fuse and form bigger ones, having less specific surface and thus leading to a system with less energy. This grain growth effect is undesired and can be reduced by adding magnesia [100], calcium hydroxide [101] or other sintering additives that wrap the particles and inhibit the grain growth. It is however favorable to remove the additive after calcination in order to isolate the pure product after the treatment.

Hydrothermal treatments are carried out in a sealed container at moderate temperatures (40 to 200°C) in the presence of a solvent. Due to the conjugate action of temperature and pressure, crystalline products can be obtained without calcination [88, 102]. After hydrothermal treatment, nanocrystalline powders are obtained, as the temperature is normally not sufficient to induce excessive grain growth. Nanoparticles with high specific surface areas can be synthesized [102].

Spark plasma sintering (SPS) is a sintering technique that uses pulsed direct current that is directly passed through the sample. By this means, heat can be generated directly inside the sample. High heating rates (up to 1000 K/min) can be obtained and the process is fast. Due to the short reaction time, no grain growth takes place. By SPS, dense nanostructured or porous samples can be obtained [103]. The mechanisms of densification and whether plasma is generated has not been confirmed yet, especially when non-conductive ceramic powders are compacted. It has, however, been experimentally verified that densification is enhanced by the use of a current or field.

2.1.2 Templating

According to the IUPAC [104], porous solids can be classified into three categories by their pore size: materials with pores inferior to 2 nm are referred to as *microporous*, pore sizes between 2 and 50 nm characterize *mesoporous* materials and materials with pores larger than 50 nm are called *macroporous*. It is important to note that scientists from other fields, e.g. biology might refer to macroporous materials as “microporous”, when the pores are in micrometer range as opposed to “macropores” measuring several dozens of micrometers. In the present work, the IUPAC nomenclature is used exclusively.

Mesopores correspond to the size of big bio-organic molecules such as proteins and lipids. Macropores are big enough to host cells and bacteria. Hence, applications vary greatly with the pore size: Mesoporous materials are used for drug and protein delivery, as catalyst support, as membranes and for the synthesis of quantum structures. Macroporous materials are used as scaffolds for bone regeneration and for photonic applications.

In the following, we will focus on the synthesis of mesoporous materials. Mesoporous materials can be obtained by different templating approaches. In general, templating implies the addition of a species to the reaction mixture that will give rise to a porous structure upon removal after condensation of the system. It is important to differentiate *hard* and *soft* templating – which refers to the nature of the template used – and *endo* and *exotemplating* – which refers to the position of the product compared to the template.

Soft templating is based on the micellar arrangement of surfactant molecules in solution. Surfactants are amphiphilic molecules with an polar head group and an apolar tail. In solution, when the concentration is high enough (critical micellar concentration), these molecules will form micelles. Figure 2.2 shows examples for the three main classes of surfactant molecules: cationic, anionic and nonionic. Zwitterionic surfactants

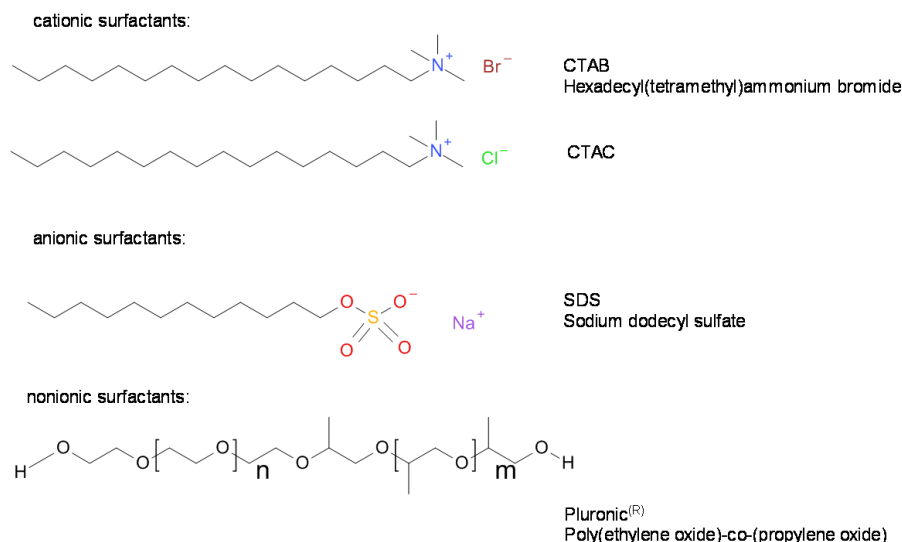


Figure 2.2: Some examples of frequently used surfactants.

are rarely used for soft templating. A more comprehensive list of surfactants can be found in [105].

In addition to the concentration of the surfactant solution and its shape, the concentration of salts, the pH and the temperature influence micelle formation. The shape and size of the micelles in solution will determine the pore shape of the mesoporous material. Spherical pores can be obtained by using spherical micelles as in MCFs² [57], SBA-15 type materials with channels can be obtained from rod-like micelles [56].

Micelles can adopt a long range order in solution. These solutions are then referred to as *liquid crystals* or *mesophases*. Due to this mesophase formation, ordered mesoporous materials can be obtained by soft templating. Three mechanisms are proposed [106]:

1. True liquid crystal templating (LCT or TLCT)
2. Cooperative Mechanism
3. Folded Sheet Mesoporous Materials (FSM)

Figure 2.3 and 2.4 show schematics of the three mechanisms. In true liquid crystal templating, micelles form a stable mesophase around which the inorganic precursors condensate and freeze the structure. In the cooperative mechanism, the mesophase is formed due to the condensation of the precursor. The micelles do not adopt long range order without the addition of the inorganics. In most real systems, a combination of the LCT and the cooperative mechanism is observed.

Folded sheet materials are another class of mesoporous materials derived from the layered silicate kameinite ($\text{Na}(\text{H}_2\text{O})_3[\text{Si}_2\text{O}_4(\text{OH})]$) [107]. The synthesis principle is the intercalation of surfactant micelles into the layers of the material followed by calcination.

²Mesocellular foam: silica material with big spherical mesopores interconnected by large windows.

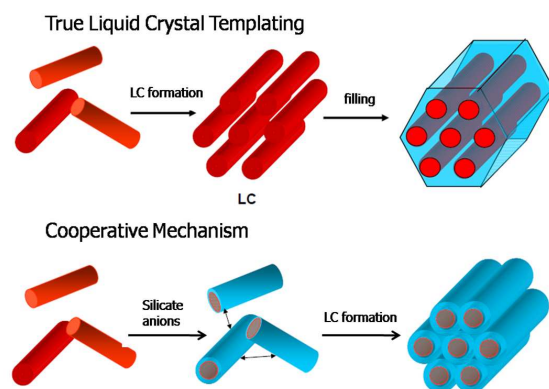


Figure 2.3: Schematic representation of the LCT and the cooperative mechanism for the formation of mesoporous silica.

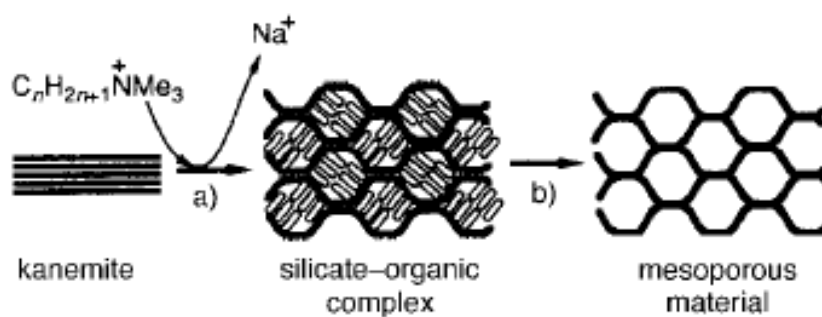


Figure 2.4: Synthesis of folded sheet mesoporous materials from kamnite. a) Ion exchange, b) calcination. From [108].

Consequently, the material contains rodlike pores. A schematic representation of the synthesis mechanism is given in figure 2.4. For the moment, the FSM mechanism is restricted to layered silicates.

Soft templating techniques have been developed for mesoporous silicas, but they can be used for the synthesis of non-siliceous materials as well: mesoporous zirconium oxophosphate, titania, aluminum phosphates and platinum have been synthesized using surfactant templating [106].

In order to liberate the porosity, the template has to be eliminated. Most of time, this is achieved by a heat treatment under oxidative atmosphere in which the organic template is burned. Simultaneously, the calcination completes the condensation of the precursor. The disadvantage of this method is the shrinking of the structure due to the high temperature ($T > 600^\circ\text{C}$). In the case of low molecular weight surfactants, extraction with a solvent can be an alternative. However, ionic surfactants cannot be extracted by solvents as they build up strong interactions to the pore walls.

Hard templating or *nanocasting* uses mesoporous silicas, carbons or microporous zeolites obtained by soft templating as reaction vessel for other materials. In 1986, Knox and coworkers [109] reported on the synthesis of mesoporous carbon materials in the porosity of silica. Upon removal of the silica, mesoporous carbon was obtained. Depending on the pore structure of the template, porous carbons with a wide range of porosities can be obtained. Figure 2.5 shows the general principle of hard templating and some example of substance classes. As illustrated by these examples, the shape of the silica directs the porosity of the carbon replica: the replication of microporous zeolites with thin pore walls gives microporous carbon replicas. If mesoporous carbon replicas are to be synthesized, mesoporous silicas such as SBA-15 or MCM-41 can be used as templates. Macroporous systems such as silica opals or anodized alumina oxide membranes give rise to macroporous carbon replicas.

However, the porosity of the carbon replica does not depend on the geometry of the silica porosity alone: the carbon precursor plays an important role, too [38, 111]: Parmentier et al. investigated the carbon replicas of SBA-15 silica with sucrose, thermally cracked propylene and pitch. They found that the use of sucrose led to carbon replicas with micro- and mesopores whereas the replication with propylene (same process as used in the present work) gave mesoporous replicas [111].

Endotemplating. The definitions of endo- and exotemplating are close to those of soft and hard templating and can, in some cases, be used interchangeably. For endotemplating, a templating species is added to the reaction mixture in order to be occluded by the forming solid. Upon removal of this species during calcination or by solvent extraction, the voids are freed and a pore system develops. The size of the pores can range from the molecular scale when molecules are used as templates, to the macroscopic scale where for example latex particles give rise to a macropore system. If the pores do not have the same size and shape as the template, the term *structure directing agent (SDA)* should be preferred to the term *template* [112].

Exotemplating. An exotemplate is a porous structure providing voids which are filled during replication. Upon removal of the template, either small particles with high surface area or a porous solid are generated, depending on the three-dimensional connectivity of the pore structure of the template [112].

In the case of templating with silica spheres, the process can be referred to as “exotemplating” if the spheres are interconnected and form a rigid solid, if on the other hand, the spheres are present in a colloidal solution, the term “endotemplating” is more adequate.

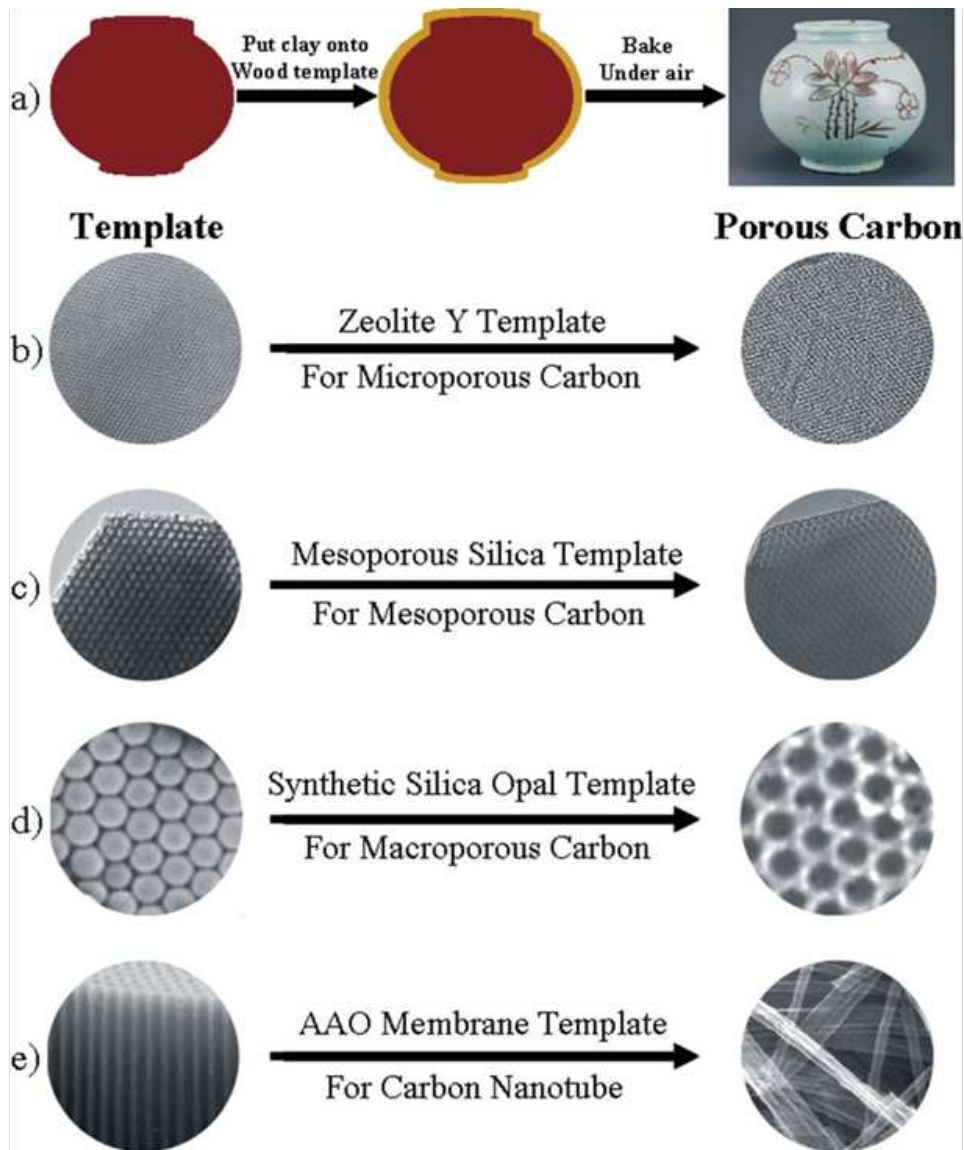


Figure 2.5: a) Schematic representation showing the templating concept. b) Microporous, c) mesoporous and d) macroporous carbons and e) carbon nanotubes are obtained by the replication of zeolites, mesoporous silica, silica opals and AAO membranes respectively. From [110].

2.1.3 Mesoporous hydroxyapatite - State of the art

In the attempts to make porous HA materials, both endo- and exotemplating approaches have been used. The following section gives a literature review on methods and results, and localizes this work within the bibliographic context.

2.1.3.1 Hard templating of macroporous hydroxyapatite

Porogenes, gel casting, ceramic foaming and polymer sponge techniques are not really hard templating approaches. In most cases, they are applied to preformed commercial HA powders and are therefore considered a shaping technique, not a synthesis method. Nevertheless, they lead to porous calcium phosphates and should at least be mentioned briefly here.

Porogenes are volatile particles that burn away during sintering [113]. These agents include paraffin, naphthalene, carbon, starch, flour, hydrogen peroxide and synthetic or natural polymers, e.g. agarose [114]. These agents are mixed into the ceramic slurry and eliminated in the subsequent sintering step. After calcination, a porous ceramic structure is obtained.

Ceramic foaming consists in foaming ceramic slurries or swelling uncalcined ceramic bodies with chemical reactions that liberate gaseous products. Some foaming agents are hydrogen peroxide, carbonates and baking powder (sodium hydrogen carbonate) [113]. These products generate O_2 or CO_2 when heated and lead to porous ceramics with pore sizes between 30 and 600 μm in diameter.

Gel casting is a related process and consists in dispersing ceramic particles in a monomeric solution. After polymerization of the monomer, the ceramic particles are trapped in a rigid polymer network. The composite is then calcined which results in the elimination of the polymer. The resulting ceramic is porous as the space occupied by the polymer is liberated [115].

The *polymer sponge technique* consists in the infiltration of HA slurries into polymer sponges. Contrary to the gel casting method, the polymerization of the sponge is carried out before the addition of the ceramic. Upon calcination, HA materials with well-interconnected pores and good control of the pore size are obtained [113].

Polymer sphere opals. Latex and other polymers that are obtained by emulsion polymerization can be synthesized with good control of their diameter and are commercially available, e.g. in aqueous dispersion. These spheres have narrow monomodal size distribution and arrange in close packing when centrifuged or filtered. After short heat treatment above the glass transition temperature (*annealing*), the resulting opals are one of the most frequently used hard templates for the synthesis of macroporous calcium phosphates. An example of a colloidal crystal is shown in figure 2.6. When the spheres are burned, a porous network is freed in the HA material. The pores are interconnected at the spots where the spheres of the template touched one another or where they were connected due to annealing.

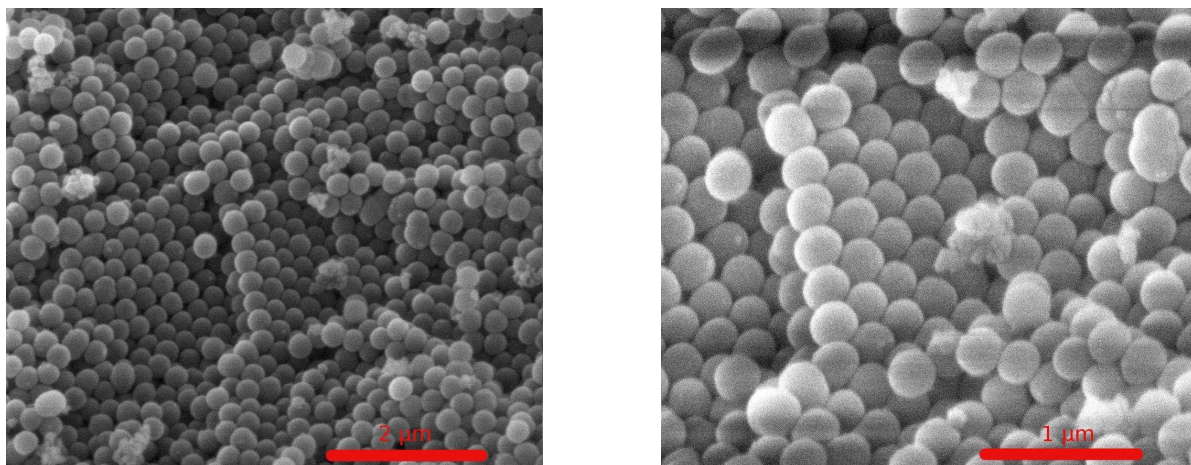


Figure 2.6: SEM images obtained for a colloidal silica crystal annealed at 945°C for 2 h. The diameter of the spheres is 200 to 300 nm. Own work.

Many groups have reported the synthesis of macroporous calcium phosphates using latex beads. The method proposed by Melde and Stein is the following [67]: Poly-(methylmethacrylate) (PMMA) spheres were produced with 256 ± 5 nm and 375 ± 4 nm in diameter. Colloidal crystals were prepared by centrifugation at 1000 rpm and annealing at 130°C for 10 min. The interstitial porosity was infiltrated under reduced pressure with a solution containing calcium nitrate and phosphoric acid in the molecular ratio of 1.67. After filtration and drying in air, the product was calcined at 300°C in air to remove the polymer and then sintered at higher temperature.

Figure 2.7 shows some typical scanning electron microscopy images of the obtained products sintered at different temperatures. The higher the calcination temperature the more likely is the three dimensional pore structure destroyed by uncontrolled grain growth. The products remain however visibly porous even after sintering.

This basic synthesis can be adapted in several ways to achieve products with the desired properties: variation of the sphere size and therefore the pore size of the resulting HA [116, 117], different precursors or even HA nanoparticles [117, 118]. Instead of latex (PMMA), other polymers such as poly(vinyl butyral), PVB, can be used [117]. By adapting the precursor and the synthesis conditions, other calcium orthophosphate phases can be obtained [119].

Polymer spheres can be replaced by other shapes, e.g. polymer fibers can be used as a template for the synthesis of macroporous HA, resulting in different pore morphologies. To quote just one example, Chang and coworkers used polyester fiber sheets to cast macroporous HA with interwoven channel-like pores [98].

Silica sphere opals. The method described above is not restricted to polymers. Wang et al. demonstrated in 2009 that silica spheres can be used as a template for macroporous HA materials [120]. Silica spheres with diameters around 300 nm were prepared by the hydrolysis and condensation of TEOS in basic solution. Surface modification with H_2O_2

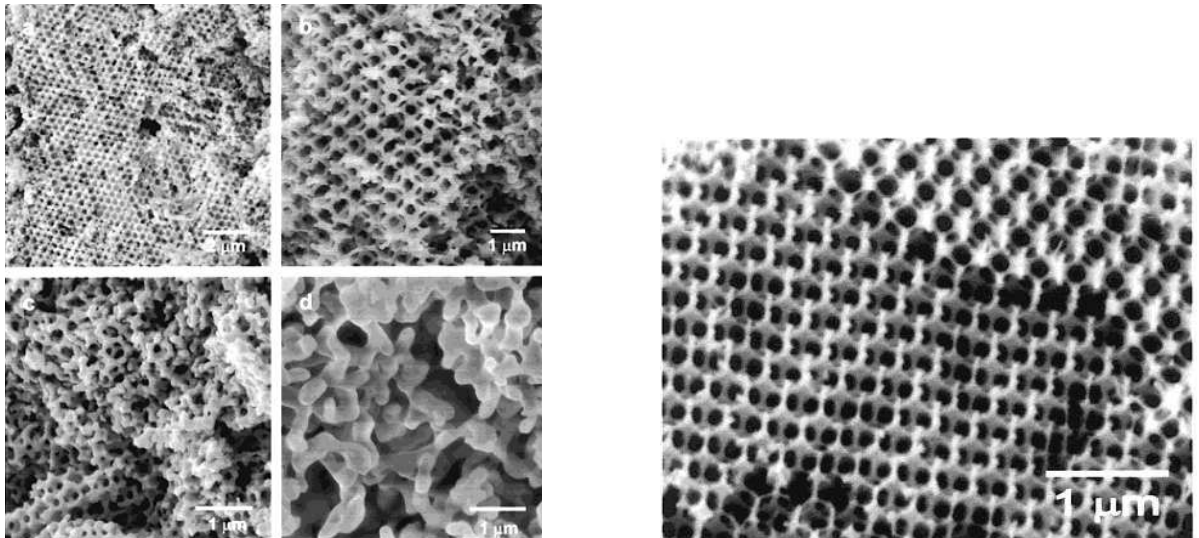


Figure 2.7: SEM images obtained for latex templated HA sintered at different temperatures: a)475, b)600, c)800 and d)1000°C. On the right: HA calcined at 700°C obtained by the replication of a latex crystal without annealing by Melde and Stein. From [67].

led to self-assembly into a close-packed structure. The particles were not annealed before impregnation with the HA precursor solution. SEM images of the product obtained after calcination and dissolution of the silica template with NaOH are shown in figure 2.8. The highly ordered structure and the interconnection between the pores are clearly visible.

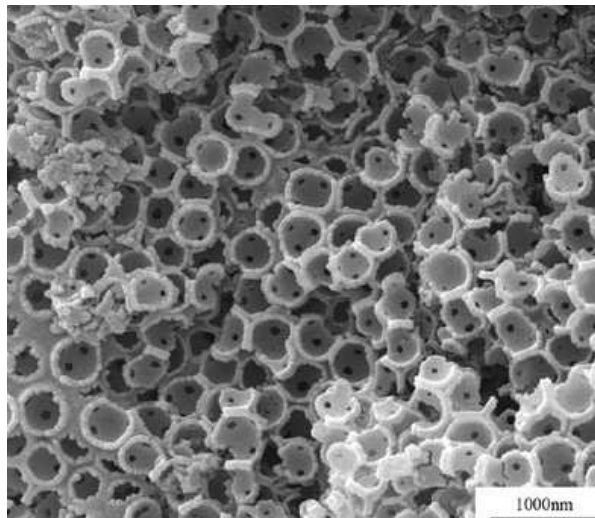


Figure 2.8: SEM images of macroporous HA obtained by silica sphere templating. Interconnecting windows between the spherical macropores are clearly visible. From [120].

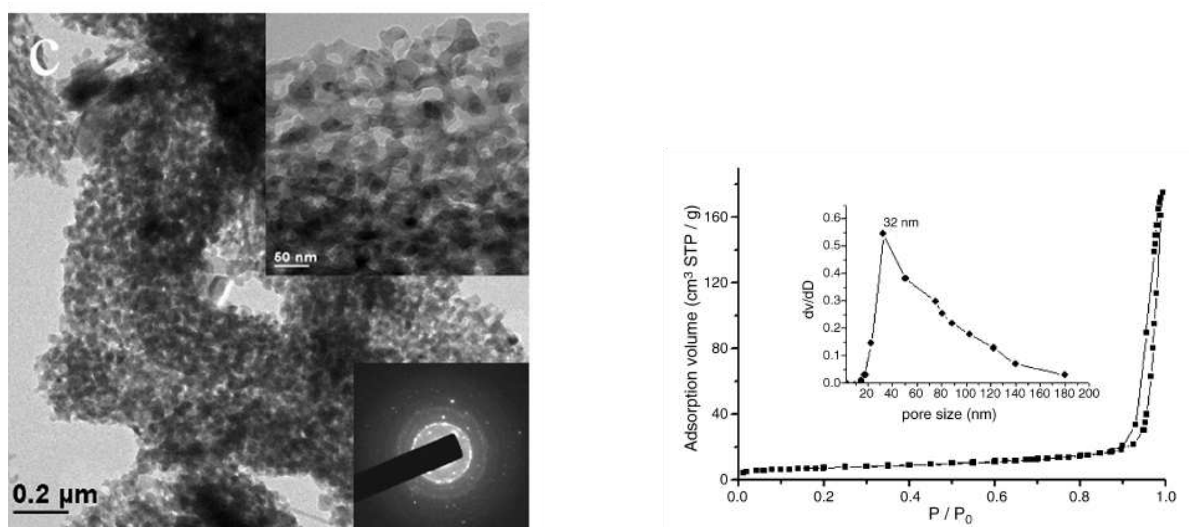


Figure 2.9: Transmission electron micrographs and nitrogen physisorption isotherm obtained for hydroxyapatite replica of CMK-3 by Fan and coworkers. From [121].

2.1.3.2 Hard templating of mesoporous hydroxyapatite

So far, to our knowledge, only two papers have been published that describe the synthesis of mesoporous hydroxyapatite through a hard templating approach, both starting from CMK-3 materials. CMK-3 is the sucrose replica of SBA-15 that after calcination and silica removal gives rise to rod shaped carbon interconnected by smaller pillars. The interstitial pores are about 3 nm in diameter.

In 2007, the team around J. Fan and D. Zhao published results on the attempt to replicate mesoporous CMK-3 materials with HA [121]. Their method was the following: CMK-3 mesoporous carbons were obtained by sucrose infiltration into SBA-15, carbonization at 900°C and subsequent etching with HF solution. The carbon was then infiltrated with calcium chloride and trimethoxyphosphate ((MeO)₃PO) in ethanol. The infiltration was carried out in atmospheric pressure under vigorous stirring for 2 h, the liquid was then evaporated at 40°C. After aging at 100°C, the composite was calcined at 500°C in air for 6 h to remove the carbon template.

Transmission electron micrographs and the nitrogen physisorption isotherm are reproduced in figure 2.9. As can be seen from the TEM image, the sample is composed of agglomerated nanoparticles with gaps around 20 to 30 nm in diameter. The particles are rod shaped and approximately 20 to 30 nm long. Both the pore size and the particle size exceed by far the values expected from the measurements of the carbon template: As the walls of the carbon template are in the range of 3 nm, the product was expected to have pores in the same range. Likewise, as the template presents pore walls that are about 3 nm thick, the size of the hydroxyapatite particles was expected to be below that value. A control experiment carried out without template showed bulk HA with large crystals. This observation evidences that the carbon template can partially inhibit the

grain growth of calcium phosphate and can liberate some porosity upon combustion, but the product is not a replication of the carbon porosity. It might be more appropriate to talk about *structure directing* instead of *templating*.

On the other hand, given the shape of the isotherm, which is type II with type H3 hysteresis³, the porosity is not accessible. For a truly mesoporous material, a type IV or V isotherm with H1 or H2 hysteresis is expected. The BJH theory should not be applied to the observed kind of isotherm. The position of the hysteresis at high pressures can be attributed to textural porosity. Contrary to what Fan et al. concluded, the material is not mesoporous. The pores shown in the TEM image are not interconnected and inaccessible. This is the reason why a small surface area of only 27 m²/g is measured.

Two years later, Xia and coworkers reported on a similar approach [122]. The synthesis of the template was the same as in the previous paper, but the silica dissolution was carried out with NaOH instead of HF. The CMK-3 carbon was then infiltrated by calcium chloride and diammonium hydrogen phosphate (NH₄)₂HPO₄ in water under reflux at 120°C for 24 h. After aging at room temperature, the composite was dried at 100°C and calcined at 600°C for 8 h in air to remove the carbon.

The authors describe the product as “fluffy”, which indicates a high surface area. Figure 2.10 shows the transmission electron micrographs obtained for the HA. The product is composed of elongated nanoparticles (about 100 nm x 20 nm) that are agglomerated. There seems to be some porosity inside the grains, but no interconnection or aperture to the outer surface of the grains is visible.

From the shape of the nitrogen physisorption isotherm, shown in figure 2.11, it can be concluded that the product possesses only textural porosity, but no mesoporosity. The isotherm is type II, with small hysteresis at high relative pressures. Again, real mesoporosity is not evidenced. The application of the BJH theory to this kind of isotherm is not advised, giving rise to unreliable results as the formation of the meniscus inside the pores of this size is not governed by capillary forces only. Again, the surface area is smaller than expected for a mesoporous material and was measured to be 42.4 m²/g.

An original approach was proposed by He and coworkers in 2010: instead of using mesoporous carbon materials, they used living yeast cells as template for the synthesis of hydroxyapatite. As the cells are burned during the calcination step, they fulfill the same role as the carbon materials in the two previously described approaches. On the other hand, the cells are bigger than mesopores, their elimination would lead to macropores. The mesoporous structure that He et al. observed is due to the unique synthesis method: Yeast cells were cultured in glucose solution at room temperature. After 30 min, calcium hydroxide was added slowly. Upon complete addition, diammonium hydrogen phosphate was added dropwise to the solution. The mixture was allowed to age at room temperature for one day, was centrifuged and dried at 80°C for another day. The composite was calcined at 700°C for 2 h.

Figure 2.12 shows the physisorption isotherm and the pore size distribution obtained from the calcined sample. Contrary to the previous syntheses, real mesoporosity can be

³See section 5.1 for description and graphic representation of the isotherms and their interpretation.

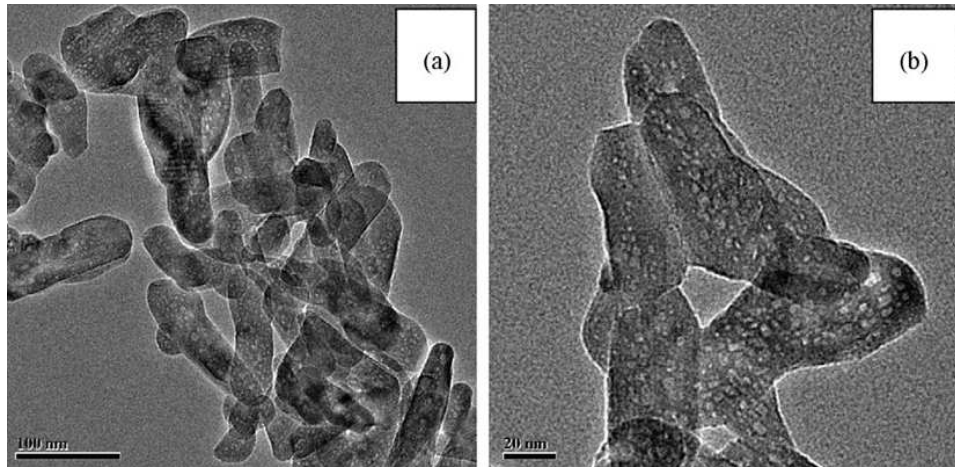


Figure 2.10: Transmission electron micrographs obtained for the HA replication of CMK3 materials by Xia and coworkers. From [122].

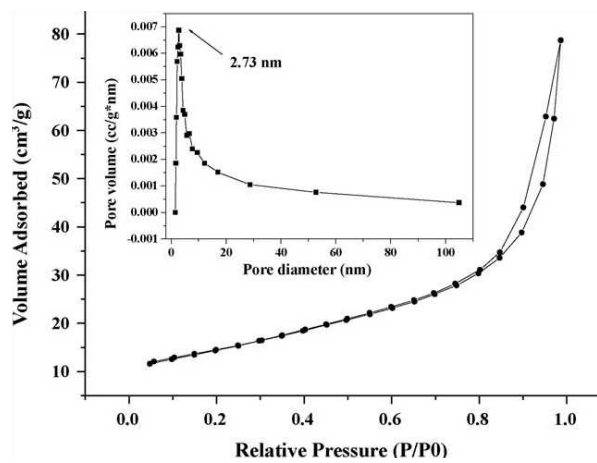


Figure 2.11: Nitrogen physisorption isotherm and pore size distribution by BJH obtained for the HA replication of CMK3 materials by Xia and coworkers. From [122].

concluded from the isotherm shape which is type IV with H3 hysteresis. The BJH analysis indicates a wide pore size distribution between 2 and 40 nm with a maximum centered around 4.5 nm. The specific surface area was 86 m²/g.

A reproduction of the TEM images for the sample is given in figure 2.12. The templated product is composed of nanoparticles, strongly agglomerated. For comparison, in the upper part of the graphic, two images are shown for HA obtained without yeast cells. The particles in these samples are less agglomerated, showing no porosity.

The product templated by yeast cells presented by He and coworkers is the only one described where a real mesoporosity is observed. It is possible that this porosity is not due to the addition of yeast cells to the synthesis mixture, but due to the presence of glucose. Organic molecules have been shown to influence grain growth and crystallization [124]: Organic molecules absorb preferentially on specific crystal planes, blocking their growth. Thus, they influence both size and shape of the growing crystal.

The use of mesoporous carbon templates has been shown to be less effective, but the synthesis can be improved; Neither Xia et al. nor Fan et al. have tried to work under reduced pressure in order to force the precursors into the porosity. When pore filling is attempted under atmospheric pressure, the pores of the template are filled with air, making the penetration of the porosity more difficult. Xia et al. have observed that only 33% of the pore volume of their template were filled during infiltration. This may be a possibility to improve the yield of the synthesis and to achieve better replication of the pore structure of the template.

Both papers use CMK-3 carbon templates, a template with relatively small porosity. In this work, templates with bigger pores will be used in order to improve the penetration of the precursor into the porosity. The shape of the pores in CMK-3 is elongated and narrow. When infiltrated by a solidifying sol, pore blocking can easily occur. For this reason, we have decided to use silica foam structures as a template, presenting spherical pores with large windows, easier to fill with HA precursors.

Additionally, the syntheses carried out by Xia and Fan are based on carbon templates. In order to remove them, heat treatments are necessary. During the calcination, grain growth occurs, and the mesoporous structures can collapse [125, 126]. In this work, additionally to carbon template, silica templates are used. They can be eliminated at lower temperature by refluxing NaOH at 100°C. Thus, grain growth during calcination can be avoided.

2.1.3.3 Soft templating of mesoporous hydroxyapatite

Soft templating with surfactant micellar structures as templates seems to be a promising way to synthesize mesoporous HA in larger quantities. Contrary to hard templating, most of the syntheses are single step and one pot methods, allowing rapid production of the ceramic.

Cationic surfactants. Several groups have attempted to create mesoporous hydroxyapatite with the help of the cationic surfactant *cetyl trimethyl ammonium bromide*

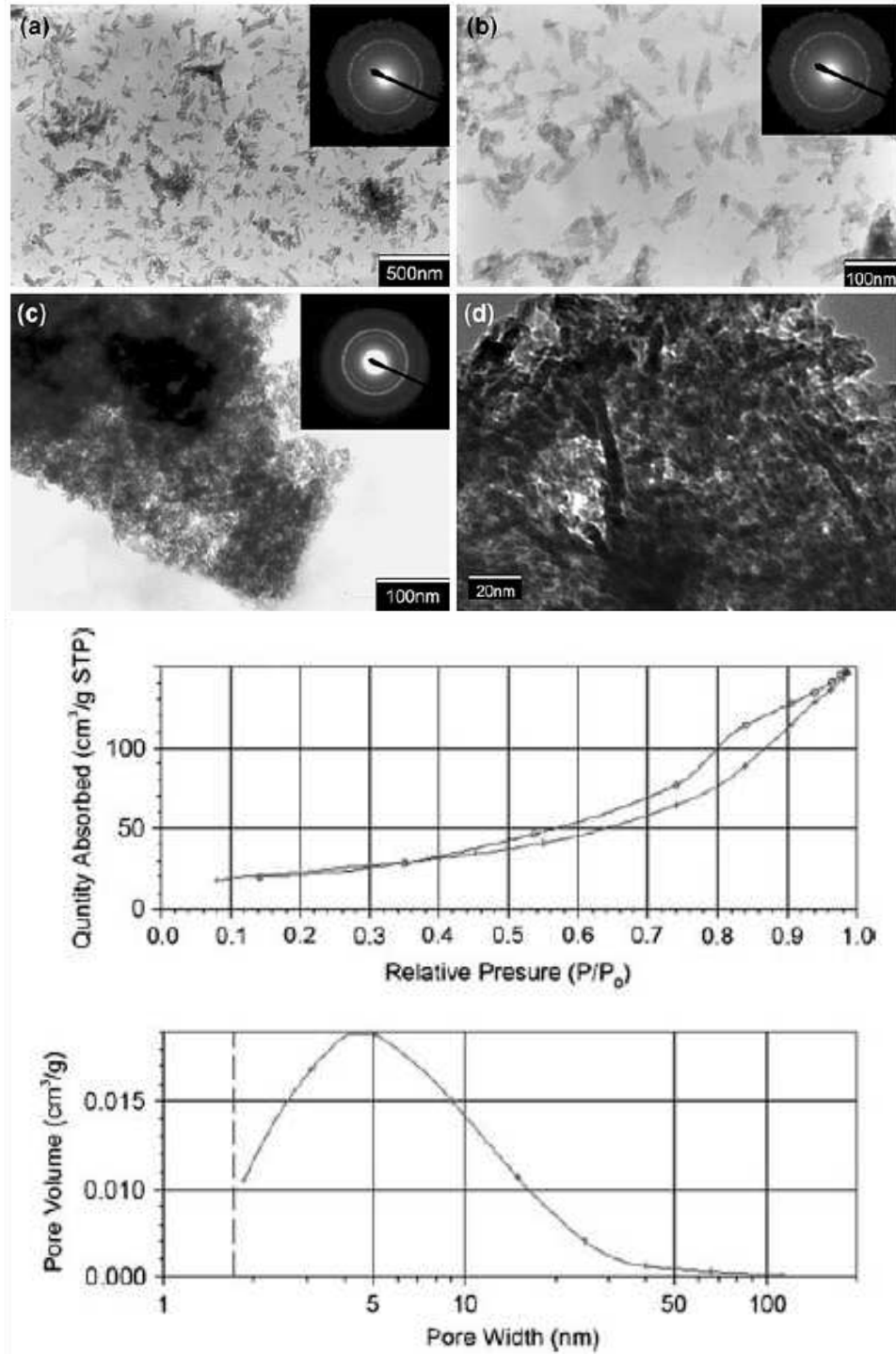


Figure 2.12: Left: Transmission electron micrographs obtained for the HA synthesis in presence of yeast cells by He and coworkers. a) and b): HA obtained without template, c) and d): HA obtained with yeast cells. On the right: Nitrogen physisorption isotherm and pore size distribution by BJH obtained for the HA. From [123].

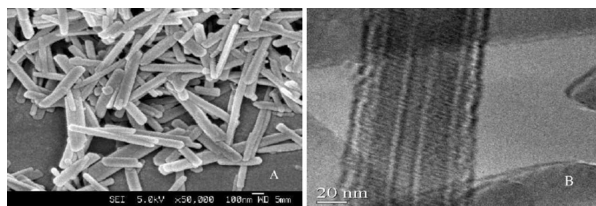


Figure 2.13: Scanning and transmission electron micrographs of HA nanorods synthesized with CTAB by Yao et al. From [59].

(CTAB, see figure 2.2, page 26). One of the first articles on this approach was published in 2003 by Yao and coworkers [59]. They obtained hydroxyapatite materials by the following method: Calcium chloride solution in water was added dropwise to an aqueous solution containing potassium hydrogen phosphate ($\text{K}_2\text{HPO}_4 \cdot 3\text{H}_2\text{O}$) and CTAB, the pH adjusted to 12 with sodium hydroxide. The mixture was refluxed for 24 h, then filtered. The gel-like paste was dried at 100°C and then calcined at 550°C for 6 h.

The product is composed of nanometric rods, as shown in scanning electron microscopy images in figure 2.13, on the left. Transmission electron micrographs (on the right of the same figure) show channel shaped mesopores inside the grains along the longer axis of the particles, which the authors attribute to hexagonally arranged surfactant micelles during the synthesis.

Unfortunately, the authors fail to give the nitrogen physisorption isotherm and indicate only the pore size distribution. A specific surface area is not indicated, neither. It is therefore difficult to judge if real mesoporosity was obtained. From the value for the mesoporous volume ($0.0113 \text{ cm}^3/\text{g}$) we can conclude that there are only few mesopores, if any.

On the other hand, Yao et al. propose a mechanism for the formation of HA around positively charged surfactant molecules: It is suggested that CTA^+ molecules form rod shaped micelles covered by PO_4^{3-} ions. When Ca^{2+} is added to the mesophase, the formation of $\text{Ca}_9(\text{PO}_4)_6$ -clusters is preferred due to the conformation compatibility between the cluster and the hexagonal arrangement of the micelles. The micelles therefore act as nucleation point for the HA crystals. During aging, the HA crystal seeds coalesce and form a three dimensional structure.

In 2008, Yang and coworkers produced europium doped HA with CTAB templating [127]. The europium was contained in the final product to an extent of 5% in mol and provokes the ceramic to be luminescent, rendering visualization after implantation easier. The synthesis method was adapted from Yao and coworkers as described above. Europium nitrate was used as Eu source and was added with the calcium chloride. The Eu is incorporated into the HA crystal without changing its X-ray diffraction pattern. The product is composed of rod shaped nanoparticles with aligned mesopores as shown in figure 2.14. The mesoporosity is better developed than for the product obtained by the original paper from Yao. The surface areas obtained range from $58 \text{ m}^2/\text{g}$ for the europium free HA to $55 \text{ m}^2/\text{g}$ for the doped HA. The difference might be caused by a

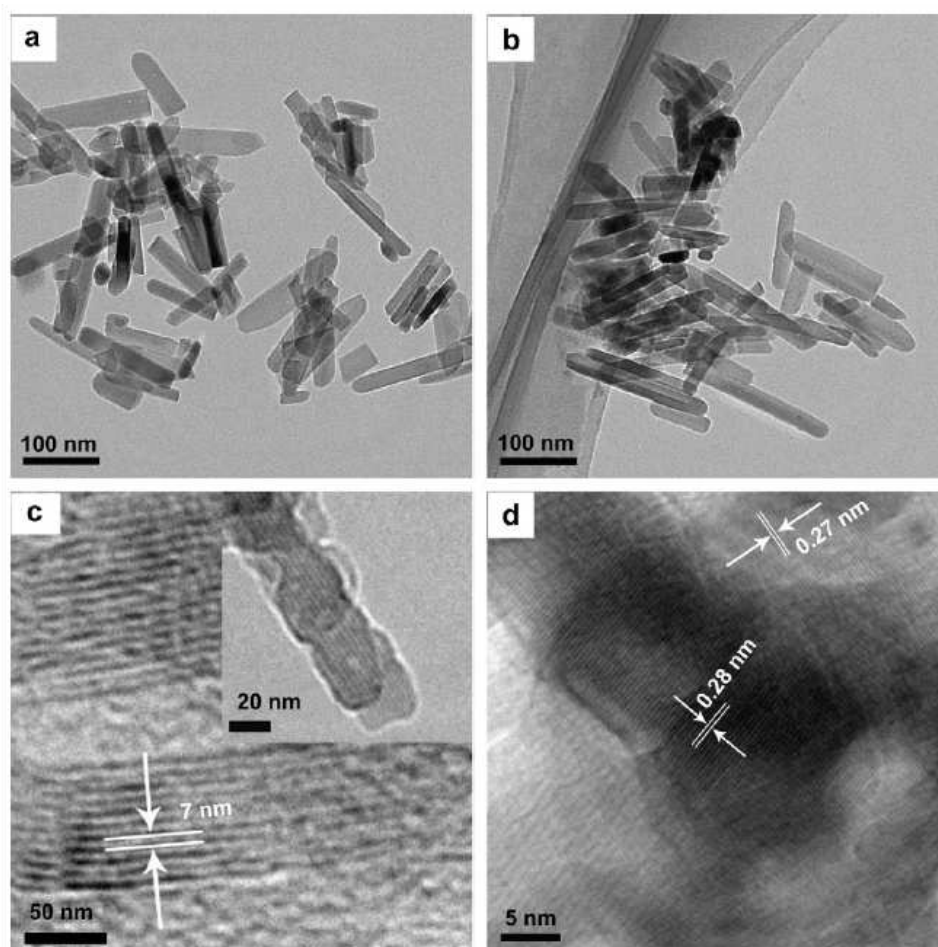


Figure 2.14: Transmission electron micrographs of a) pure HA, b) Eu doped HA. Images c) and d) show enlarged images and HRTEM of the europium containing HA. From [127].

slight change in the product density by the incorporation of a heavier cation.

The nitrogen physisorption isotherms are type II, but the hysteresis onset is situated at relatively low pressures, indicating some mesoporosity. Figure 2.15 shows the isotherms for pure and doped HA, and doped HA filled with ibuprofen before and after release experiments.

The product shows real mesoporosity, contrary to the product published in the paper from which the synthesis was inspired. Apparently, no change was made to the synthesis conditions. As the europium free product is mesoporous as well, the addition of europium to the HA structure cannot be the origin of the improved results.

In 2006, Schmidt and coworkers combined long tail organic phosphate precursors and CTAB with the co-solvent ethanol [128]. The organic phosphate fulfilled the double role of phosphate precursor and structure directing agent. CTAB was added as a co-surfactant and ethanol used as a co-solvent to the aqueous reaction mixtures. Briefly, the

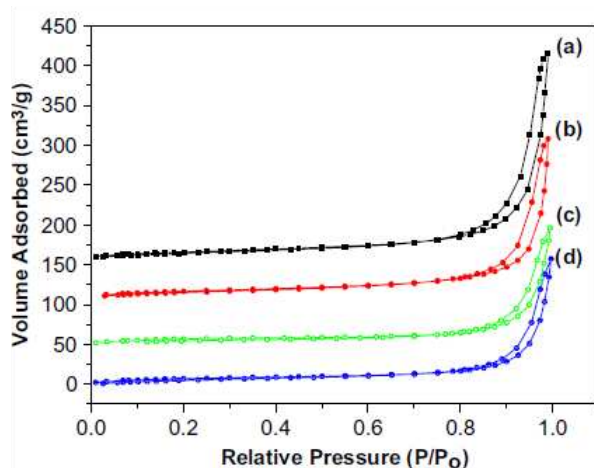


Figure 2.15: Nitrogen physisorption isotherms for a) pure HA, b) Eu doped HA, c) Eu doped Ha charged with ibuprofen, d) Eu doped HA after ibuprofen release. From [127].

method was the following: Mono-n-dodecyl phosphate ($(C_{12}H_{25}O)P(O)(OH)_2$, MDP) was transformed into its potassium salt with potassium hydroxide and dissolved in water by gentle heating. Calcium chloride powder was added to the solution. CTAB dissolved in water was added at last with vigorous stirring and the mixture was reacted for 12 h. In one case, 10% of ethanol were added to all solutions. Surfactant elimination was achieved by anion exchange with sodium acetate as proposed by [129].

The products obtained appear to be mesoporous microparticles as shown in the TEM images in figure 2.16. However, an interconnection between these pores is not apparent. Nitrogen physisorption results in flat type II with wide hysteresis as shown in the same figure. The hysteresis seems to be a combination of H3 and H4, indicating that additionally to the mesopores, textural porosity is present. It must be noted however, that the desorption branch does not join the adsorption at 0.2 relative pressures as expected for nitrogen physisorption experiments. This is an indication of very small pores with obstruction where the nitrogen molecules leave the porosity with difficulty. The isotherm does not represents an equilibrium state. Considering the small amount of nitrogen adsorbed, the powders have to be considered as non-porous. This is in agreement with the TEM images that show only closed porosity.

Although several authors have claimed that they have achieved mesoporous materials due to cationic templating with CTAB, the only product with mesoporosity is the one proposed by Yang et al. [127]. Even for the undoped HA, the isotherm shows mesoporosity. In all other cases, mesoporosity was not evidenced, even when calcination was omitted as in the paper proposed by Schmidt et al. [128]. It seems that the mesostructure is not destroyed during calcination, but that a mesostructure is not formed in the first place. This may be due to fast condensation mechanisms that do not leave enough time for mesostructured arrangements [125].

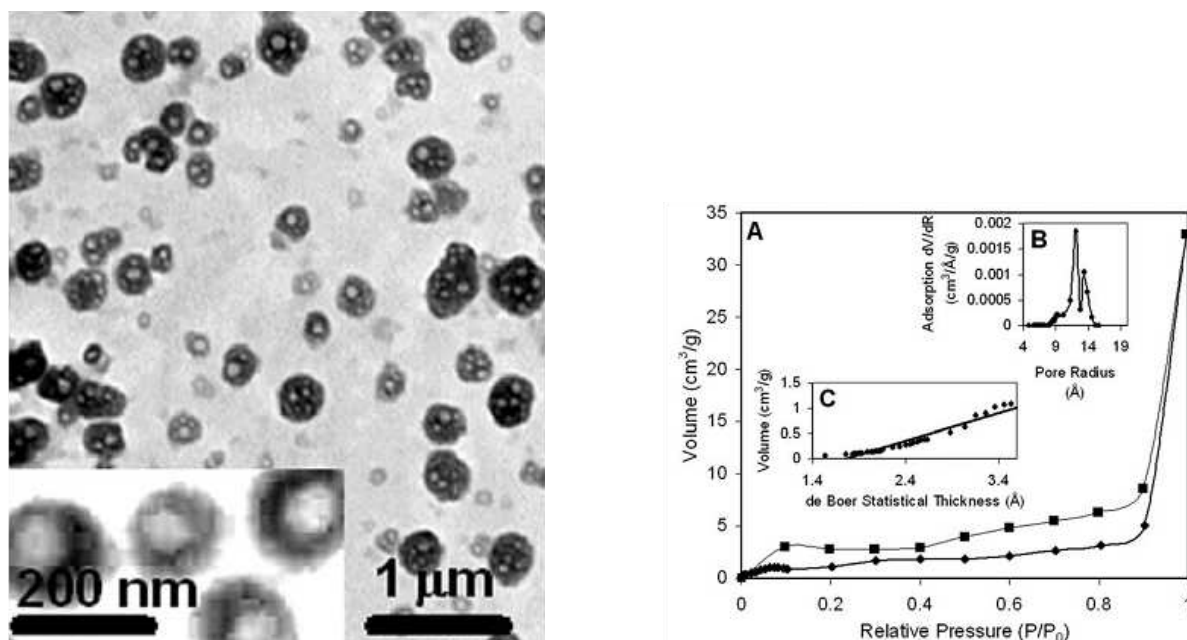


Figure 2.16: Transmission electron micrographs and nitrogen physisorption isotherm for calcium phosphate microspheres obtained with MDP and CTAB by Schmidt et al. From [128].

Anionic surfactants. In 2008, Zhang and coworkers published a method to synthesize mesoporous calcium phosphates (α - $\text{Ca}_2\text{P}_2\text{O}_7$) with anionic sodium dodecyl sulfate (SDS) and phenylphosphonic acid ($\text{C}_6\text{H}_5\text{P}(\text{O})(\text{OH})_2$) [130]. The synthesis was the following: phenylphosphonic acid and SDS were dissolved in water and added to NaOH solution. An aqueous solution of calcium chloride was added dropwise. The resulting precipitate was hydrothermally treated in a sealed autoclave at 150°C for 24 h. The product was cooled down, filtered, washed with water and dried at 100°C. The authors varied the time and the temperature of calcination up to 12 h and up to 500°C.

Figure 2.17 shows the nitrogen physisorption isotherms obtained for the different products. Both the samples calcined at 300 and 400°C show remarkable hysteresis of type H4 that can be attributed to slit like pores. From the isotherm, the authors calculated a mean pore size of 15.9 nm for the 400°C sample. The specific surface area was determined to be 76 m²/g for the calcination at 300°C and 72 m²/g for the calcination at 400°C. The combination of a bulky organic group of the phosphorus precursor with the SDS leads to layered structures with increased pore volumes compared to the use of phenylphosphonic acid alone. The pore formation mechanism the group proposed is reproduced in figure 2.18. Briefly, the phenylphosphonic acid forms bilayers that upon addition of calcium chloride and after calcination result in a layered calcium phosphate. When SDS is present in the reaction mixture, additional porosity is formed due to the intercalation of SDS micelles into the phenylphosphonic acid bilayers. The transmission electron micrographs (figure 2.19) show that additionally to the higher porosity, the pore network is better connected when SDS is present in the reaction mixture. Calcination

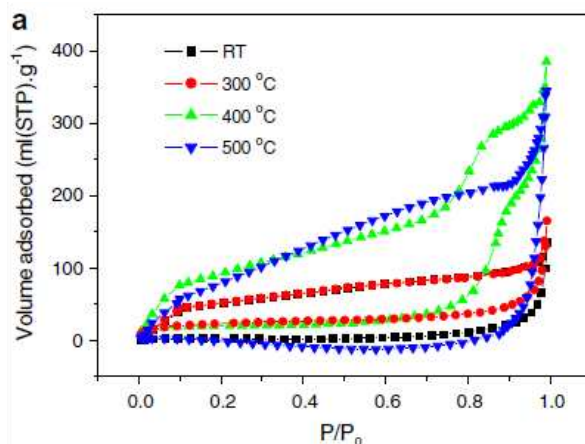


Figure 2.17: Nitrogen physisorption isotherms obtained for calcium phosphates synthesized from phenylphosphonic acid in presence of SDS after calcination at different temperatures. From [130].

at high temperatures (exceeding 400°C) leads to the destruction of the layered structure and to low surface areas (6 m²/g after calcination at 500°C).

For the products obtained without the addition of SDS, surface areas of 20 m²/g were measured. These samples do not exhibit mesoporosity, the nitrogen physisorption isotherms show no hysteresis. It is therefore possible to conclude, that only the combination of phosphonic acid with a bulky organic group with SDS leads to mesoporous calcium phosphates.

This year, Xiao et al proposed to use the polyelectrolyte poly(sodium 4-styrene sulfonate) PSS as soft template for the synthesis of hydroxyapatite in hydrothermal conditions. They did not attempt to create mesoporosity, but observed the control of the grain size and the crystal growth by the surfactant. It seems that the surfactant acts as an impurity, attaching to positively charged crystal surfaces and blocking the crystal growth. In fact, smaller nanoparticles were produced when PSS was added to the reaction mixture as evidenced by the transmission electron micrograph reproduced in figure 2.20. The change in morphology is due to the preferential adsorption of the PSS on the calcium rich crystal surfaces [100] and [010].

The addition of PSS to the reaction mixture can inhibit the grain growth considerably, but does not give rise to mesoporous products. The combination of bulky phosphorus sources with SDS leads to real mesoporosity. Anionic surfactants are rarely used for the synthesis of mesoporous HA. It seems that mesoporosity cannot be obtained from anionic surfactants alone, as their micelles are coordinated by calcium ions. In HA, it is the phosphate ions that build up the crystal structure. It is therefore easier to obtain templated products from cationic surfactants which favor the arrangement of phosphate ions on their surface. These considerations have been examined in a comparative study published by Ikawa [132]:

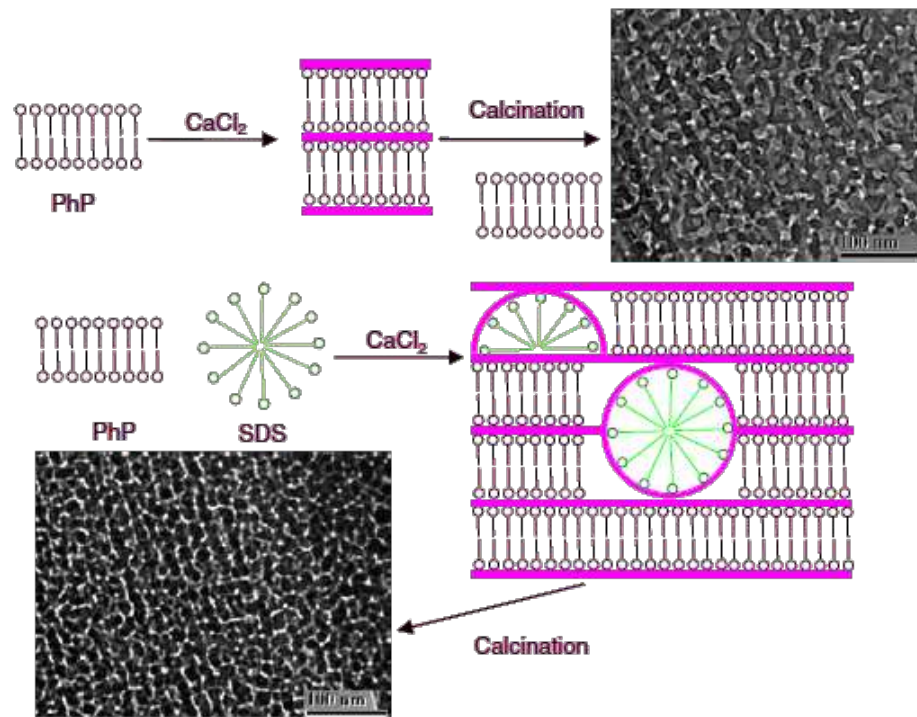


Figure 2.18: Pore formation mechanism by the combination of phenylphosphonic acid and SDS. From [130].

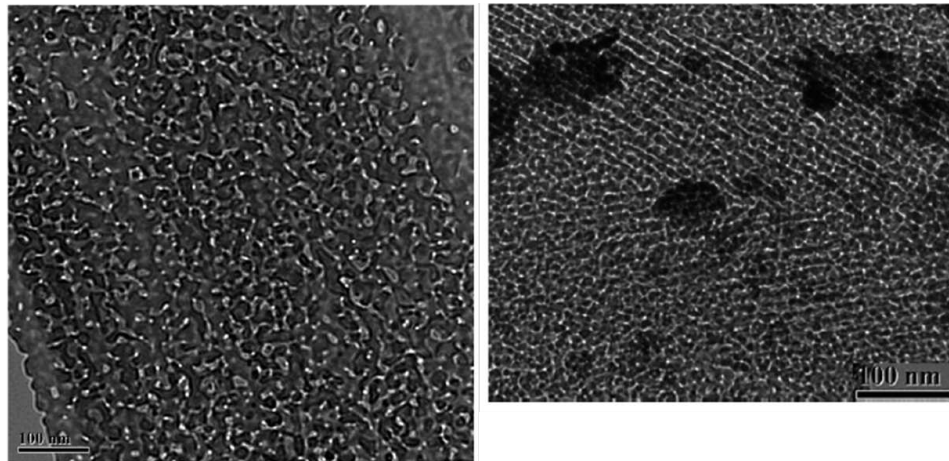


Figure 2.19: Transmission electron micrographs obtained for calcium phosphates synthesized from phenylphosphonic acid alone (right) and with SDS (left). From [130].

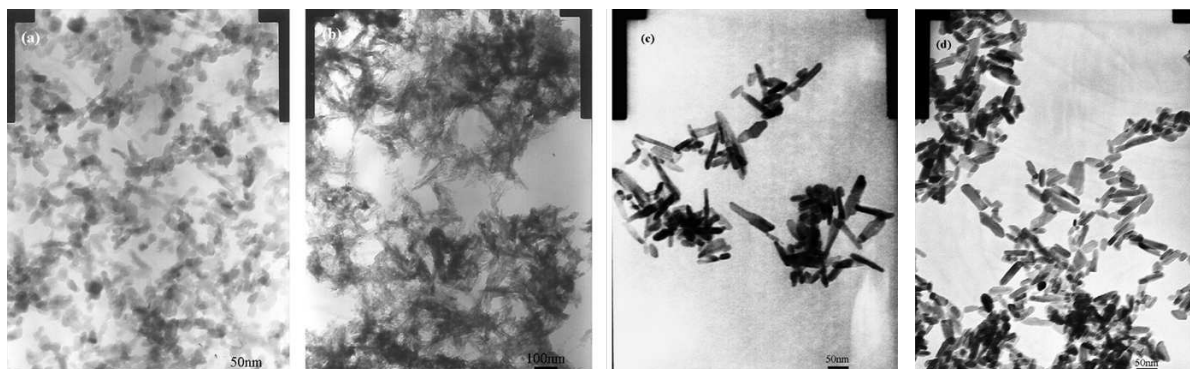


Figure 2.20: Nanoparticles of HA obtained with the addition of a) 0 wt% b) 0.1 wt% c) 0.2 wt% and d) 0.3 wt% PSS. From [131].

Comparison of ionic surfactants. Recently, Ikawa and coworkers published a comparative study on the use of anionic and cationic surfactants for the synthesis of mesoporous calcium phosphates [132]. They used dodecyl diethylene triamine ($C_{12}H_{25}N(C_2H_4NH_2)_2$, C_{12} DETA) as cationic amine type surfactant and N-lauroyl-L-glutamic acid ($C_{12}H_{23}CONHCH(CO_2H)C_2H_4CO_2H$, C_{12} GLU) as anionic, carboxylic acid type surfactant. For the synthesis with C_{12} DETA, the method is the following: Tetramethyl ammonium hydroxide $(CH_3)_4NOH$ and C_{12} GLU were mixed in ethanol for 2 h until a white slurry was obtained. A calcium acetate solution in water was added and stirred for 30 min. The precipitate was filtered, washed with ethanol and dried in air. Calcination was carried out at $400^\circ C$ for one hour in nitrogen flow, then for 5 more hours in oxygen flow.

For the synthesis with C_{12} GLU, the method was the following: the surfactant and calcium isopropoxide were stirred in a water/ethanol solution for 2 h. Diammonium hydrogen phosphate $(NH_4)_2HPO_4$ was added and stirred for another 2 h. The precipitate was filtered, washed with ethanol and dried in air. Calcination was carried out at $400^\circ C$ for 1 h in nitrogen flow, then for another hour in oxygen flow.

The authors found that the chemical composition of the two products varied considerably: In the product templated with C_{12} GLU, the Ca/P atomic ratio was 0.95, for the product templated with C_{12} DETA, it was 1.92. The calcium rich product did not show any effect of templating, the worm-like mesostructure observed before calcination in form of a small angle XRD diffraction peak did not withstand the calcination, probably because the phosphate ions could not build a dense framework in the Ca rich composition. The P rich product obtained with C_{12} DETA on the contrary maintained its structure upon calcination. NMR results show that the phosphate framework condensed during calcination. The nitrogen physisorption isotherm obtained for this product is shown in figure 2.21. The hysteresis at low relative pressure indicates the presence of mesopores. The specific surface area was determined to be $140 m^2/g$ and the mean pore size 7.1 nm. The pore volume was $0.47 cm^3/g$.

Ikawa and co-workers have shown that for the synthesis of mesoporous calcium phosphate, cationic surfactants are more suitable as they allow the formation of a condensed

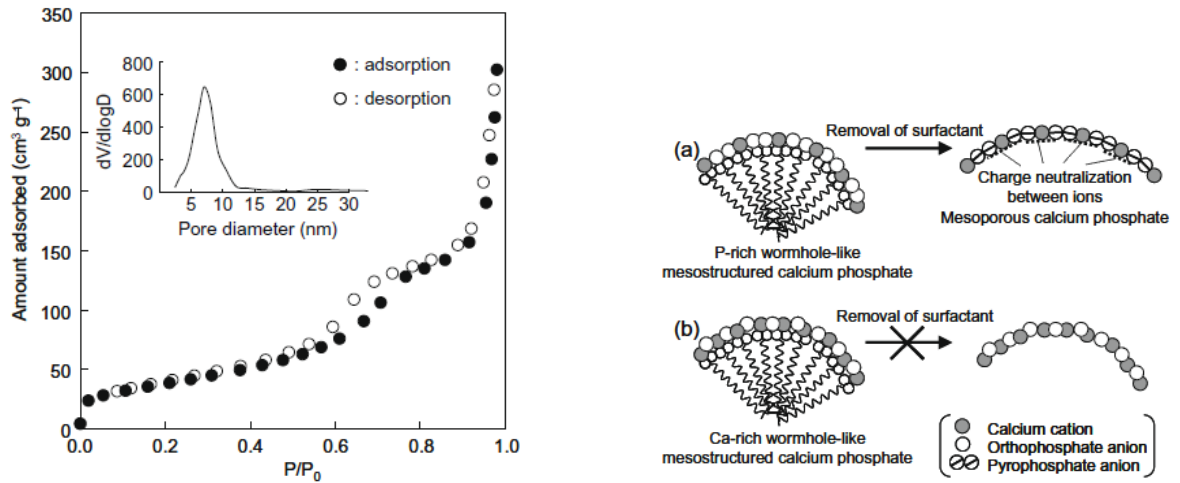


Figure 2.21: Left: Nitrogen physisorption isotherm for mesoporous P rich calcium phosphates obtained by Ikawa et al. Right: Formation mechanism for mesoporous calcium phosphates with $C_{12}GLU$ and $C_{12}DETA$. From [132].

phosphate framework that can withstand calcination. Anionic surfactants on the other hand lead to Ca rich frameworks that collapse during heat treatment (see figure 2.21).

Interestingly, the pores observed in transmission electron micrographs and the nitrogen physisorption experiments are bigger than the surfactant micelles and are enlarged during heat treatment. The authors explain this behavior by fusion of initially formed mesopores during calcination. The mechanism is detailed in figure 2.22.

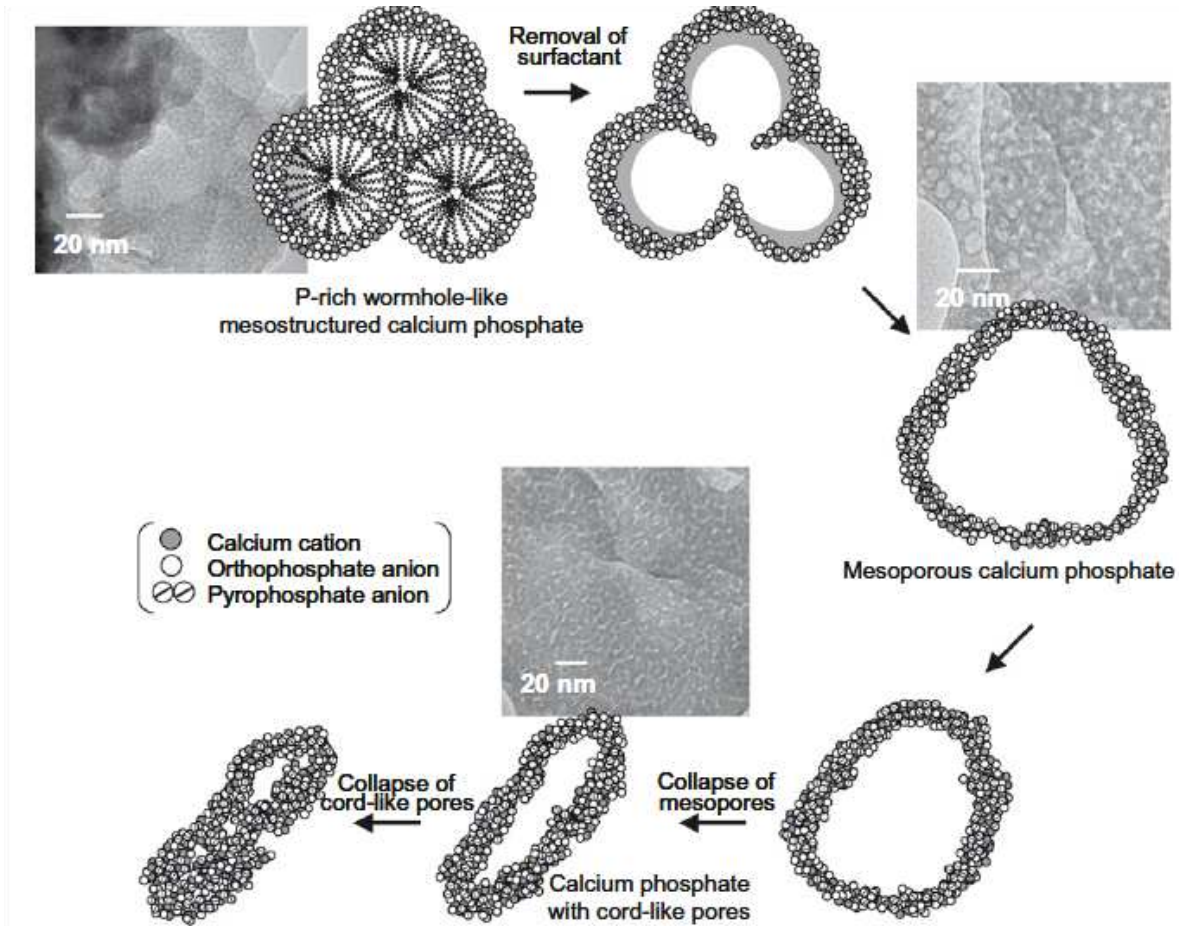


Figure 2.22: Formation mechanism for large mesopores in P rich mesoporous calcium phosphates proposed by Ikawa et al. . Initially, worm-like mesopores are formed by the surfactant and occupied by ionized C_{12} DETA molecules. During calcination at 400°C , the removal of the surfactant causes the pores to fusion. The resulting large mesopores are first shrunk and then collapsed by calcination for longer time (>6 h) or at higher temperatures (500°C). From [132].

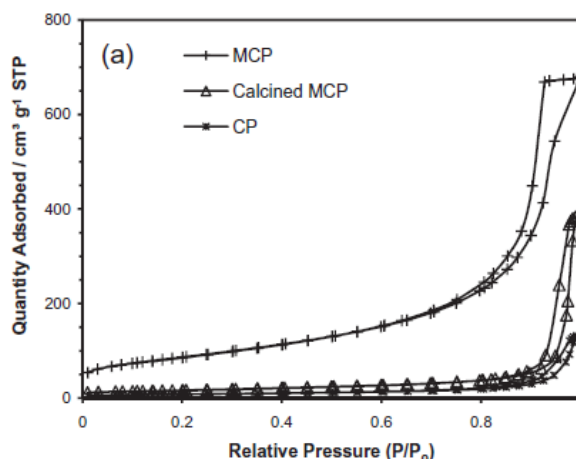


Figure 2.23: Nitrogen physisorption isotherms for the HA obtained with 80% F127 after surfactant elimination by washing (MCP) and by calcination (calcined MCP). For comparison, a commercial product (CP) is represented as well. From [133].

Non-ionic surfactants. In 2010, Ng and coworkers published a paper on the use of the nonionic surfactants P123 and F127 [133]. Both surfactants are poly(ethyleneoxide)-co-Poly(propyleneoxide) triblock polymers: $\text{EO}_{20}\text{PO}_{70}\text{EO}_{20}$ - P123 and $\text{EO}_{99}\text{PO}_{65}\text{EO}_{99}$ -F127. The method was adapted from a paper published by Zhao and coworkers [134] combining organic calcium precursors and F127 in order to achieve mesoporous calcium phosphates. Contrary to this first paper, Ng and coworkers used high surfactant amounts. For the synthesis, calcium-D-pantothenate $\text{Ca}(\text{C}_9\text{H}_{17}\text{NO}_5)_2$ solution in water was added to the surfactant solution in water. The pH was adjusted to 1 using hydrochloric acid. Dipotassium hydrogen phosphate K_2HPO_4 was added slowly while stirring. The pH of the resulting solution was raised to 12 using NaOH. The mixture was stirred for 24 h before it was centrifuged and the precipitate was washed five times.

The authors used high amounts of surfactant, from 10 up to 80 % in weight. Under these conditions, both surfactants gave rise to mesoporous products, with bigger pores for the F127 surfactant due to the longer chain. If calcination is omitted, nitrogen physisorption results in a type IV isotherm with H1 hysteresis, indicating the presence of real mesopores as shown in figure 2.23. On the other hand, when the product is calcined, the mesoporosity is destroyed and nitrogen physisorption results in the type II isotherm which is typical of a non-porous solid. The specific surface area for the washed calcium phosphate was found to be $263 \text{ m}^2/\text{g}$, but the surface area decreases to $43 \text{ m}^2/\text{g}$ after calcination at 550°C for 6 h.

The TEM images in figure 2.24 support the results of the nitrogen physisorption, showing mesoporous calcium phosphate materials with elongated pores in hexagonal arrangement. These images are only obtained for the sample that has not been subjected to heat treatment.

It seems that the combination of organic calcium precursors with high surfactant

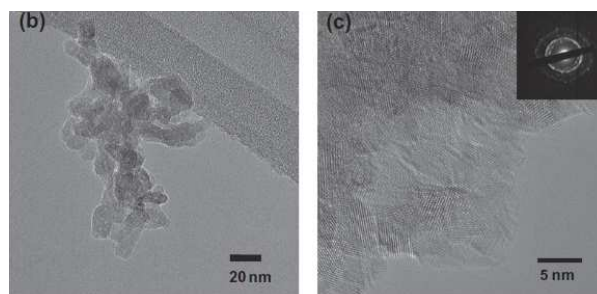


Figure 2.24: Transmission electron micrographs for the mesoporous calcium phosphate obtained with 80% F127 after surfactant washing. The insert shows an EDX diffraction pattern. From [133].

amounts can give rise to really mesoporous products if calcination is omitted and the surfactant is eliminated by washing with water or ethanol. Additionally, Ng et al started their synthesis in acidic solution to slow down the reaction [135]. In conclusion, high surfactant concentration and slowly hydrolyzing precursors can lead to mesoporous structures. These structures are destroyed if high temperatures are used to burn the surfactant. It is therefore preferable to eliminate the surfactant by extraction with an appropriate solvent.

2.1.3.4 Summary: templating of HA

Table 2.2 summarizes the synthesis methods that have been reviewed in the previous chapter. As we have seen, both hard and soft templating approaches have been used for the synthesis of mesoporous hydroxyapatite. As soft templating of mesoporous hydroxyapatite is addressed in the scope of the ANR project by the team in Clermont-Ferrand, we have focused our efforts on the hard templating of calcium phosphates.

The only studies published on the hard templating of mesoporous hydroxyapatite use CMK-3 (carbon replicas of SBA-15) as a template. This material has two main drawbacks: the first one are its tubular pores with low diameter. This porosity is prone to pore blocking when infiltrated with an aqueous precursor solution. The second one is the elimination method: the carbon template has to be burned in order to be removed. During this heat treatment, the hydroxyapatite experiences grain growth that partially destroys its structure and causes a low specific surface area. We have therefore chosen different templates that are more suitable for the replication: mesoporous silica foams have higher pore volume than SBA-15 and spherical pores with wide interconnections. The replication of these silicas with carbon leads to carbon templates with higher pore volume and a widely open pore geometry that are more suitable for replication.

As an alternative, we developed a direct method for replication of the silica foam with hydroxyapatite. This method addresses both drawbacks of the CMK-3 materials: The silica foam has a higher pore volume and spherical pores that are easier to infiltrate than the tubular pores of the CMK-3 materials. Additionally, the silica can be eliminated by a low temperature treatment using sodium hydroxide, thus reducing heat induced grain

growth as the calcination can be omitted.

Table 2.2: Summary: methods for the synthesis of porous HA

template	removal	aimed porosity	ordered? interconnected?		pros and cons
Soft templating					
Ionic surfactants [59, 127, 128, 130, 132, 136]	calcination	meso	yes	yes	- Calcination destroys porosity. - So far, few mesoporous products reported. - Low surface areas. + Mesoporous materials can be obtained. + Anionic surfactants can lead to mesoporous materials. + One pot synthesis, easy scale up.
Non-ionic surfactants	calcination [133]	meso	yes	yes	as before
Non-ionic surfactants	extraction [122]	meso	yes	yes	+ Mesoporosity can be maintained due to absence of calcination + ordered mesoporous structures - low surface areas - few successful syntheses reported
Hard templating					
polymer spheres [67, 116–118]	calcination	macro	yes	depends on annealing	- macroporous - often poorly interconnected + porosity withstands calcination + pore size and shape are adjustable
silica spheres [120]	NaOH etching	macro	yes	depends on annealing	- macroporous - often poorly interconnected + no calcination required + pore size and shape are adjustable
mesoporous [121, 122]	carbon calcination	meso	yes	yes	+ mesoporous - calcination destroys porosity - small pores, pore infiltration difficult
mesoporous silica	NaOH etching	meso	yes	yes	+ mesoporous + no calcination required + bigger pores compared to CMK materials ± no synthesis reported yet

2.2 Experimental

This chapter describes the synthesis methods that have been used during the work on this thesis. The first part of the chapter describes the synthesis of two silica and three carbon templates. Commonly used SBA-15 materials were synthesized as described in the literature and will be used in the following as a reference material. The synthesis of mesoporous foam (also: mesocellular foam - MCF) was adapted from the literature and several parameters were changed in order to obtain the optimum template material. The effect of these parameter changes is discussed in detail in the following chapter.

The second part of this chapter describes the synthesis methods that have been used for the preparation of mesoporous hydroxyapatite.

2.2.1 Template synthesis

2.2.1.1 Silica templates

SBA-15 silica. is obtained by the condensation of TEOS (tetraethyl orthosilicate $\text{Si}(\text{OEt})_4$) in the presence of Pluronic® 123 micelles. The method was adapted from [137] but the amounts were increased. The synthesis was carried out as follows: 100 mL of concentrated hydrochloric acid (1.2 mol, Riedel de Haën, p.a.) are diluted with 525 mL of distilled water. Under agitation at 40 °C 20 g of Pluronic 123 (3.4 mmol, Aldrich) are dissolved. 42.5 g of TEOS (tetraethyl orthosilicate, 0.2 mol, Aldrich) are added. Stirring is continued for another 4 h. For aging, the sealed pyrex bottle is transferred into a Teflon beaker and put into the drying oven at 110 °C for 72 h. Alternatively, a steel autoclave is used for the aging process. After cooling and filtration, the product is dried at 80 °C overnight and then calcined at 550 °C for 4 h with a heating rate of 1 K/min in an air flow of 20 L/h. The template was characterized by nitrogen physisorption, small angle X-ray diffraction and transmission electron microscopy.

MCF silica. When incorporated into the micellar solution of Pluronic, mesitylene molecules add to the hydrophobic part of the micelles. This leads to swelling of the micellar size and to the formation of spherical micelles instead of rod-shaped ones. The synthesis method was presented by Schmidt-Winkel and coworkers [138]. A typical method was the following: 10 g Pluronic are dissolved in 375 mL of diluted hydrochloric acid of 1.6 mol/L. 10 g of mesitylene are added, the mixture is heated to 40 °C. After 30 min of agitation, 22 g of TEOS are added. Agitation is pursued for 20 h. The solution is then aged for 24 h. The precipitate is filtered and dried overnight at 80 °C. The powder is calcined at 500 °C for 8 h with a ramp of 2 K/min and an air flow of 20 L/h.

According to another publication from the same group [139], the pore size can be tuned by varying the mesitylene/pluronic (M/P) ratio. In the aim of achieving the biggest pore size, the mass ratio is varied from 0.18 to 2.15. Another study is carried out to find the best parameters for the calcination: as the heating ramp is time and energy consuming, the heating rate is varied from 1 to 10 K/min. The experiments for the calcination study

are carried out on a silica product with $M/P = 0.38$. The temperature dwell at 500°C for 8 h is maintained.

2.2.1.2 Carbon templates

SBA-15 carbon replica by CVD. Chemical vapor deposition is carried out at 750°C with propylene in argon. For all CVD experiments, a vertical quartz reactor is used. The reactor is equipped with a fused silica frit at mid-height on which the silica rested during the deposition. Argon and later argon mixed with propylene are introduced from the top of the reactor. The gas flow is chosen and monitored using mass flow controllers. The deposition method is the following: 0.67 g of silica are introduced into the furnace and heated under argon flow (10 L/h) to 750°C . The heating rate is 10 K/min. Once the temperature reached, the argon flow is increased to 20 L/h and 0.5 L/h propylene are added. After 8 h, the propylene flow is interrupted and the composite is allowed to cool down in argon flow.

MCF carbon replica by CVD. The synthesis is similar to the synthesis of the SBA-15 replica. The mass of the silica template used is about 1.2 g per deposition. Deposition time is varied in order to find the best duration: short depositions lead to products without structural cohesion, too long deposition times lead to products with low pore volumes.

MCF carbon replica by sucrose infiltration. The sucrose replication is adapted from the method described by Ryoo and coworkers in [140]. The amount of sucrose that can be infiltrated into the porosity of the silica template depends on the pore volume of the latter. Two successive infiltrations are carried out, the first using an incipient wetness approach based on the complete pore volume, the second infiltration with half the amount. For a silica template with a pore volume of $1\text{ cm}^3/\text{g}$, the method is the following: 0.18 g concentrated sulfuric acid H_2SO_4 are diluted in 6.4 mL of distilled water. 1.6 g of sucrose (α -D-fructofuranosyl-(2-1)- β -D-glucopyranoside, $\text{C}_{12}\text{H}_{22}\text{O}_{11}$, also called saccharose) are dissolved in the acid and the silica is added to the solution. The mixture is stirred for 8 h at room temperature and then dried at 100°C overnight. Precalcination is carried out at 150°C for 6 h in air. After grinding by hand in a mortar, the solid is infiltrated a second time with 0.96 g of sucrose in 6.4 mL and 0.1 g H_2SO_4 for 8 h. The composite is dried overnight at 100°C and then precalcined at 150°C for 6 h. Calcination is carried out at 900°C for 5 h under argon flow (20 L/h). The heating ramp is 3 K/min.

Silica template elimination. At the end of the infiltration process (CVD or liquid infiltration with sucrose), a carbon/silica composite is obtained. In order to dissolve the silica and to liberate the carbon porosity, etching with hydrofluoric acid HF^4 is carried out: 1.5 g of composite are placed into a Teflon beaker equipped with a magnetic stirring

⁴HF is extremely dangerous. For the etching, Teflon labware must be used and special precaution measures are necessary!

rod wrapped in Teflon. 40 mL of concentrated HF (30%) are added very carefully under slow stirring; the reaction is exothermic and can cause some material to be ejected from the beaker. The beaker is covered with a teflon watch glass and stirred overnight. The solid is filtered and washed several times with distilled water. The carbon product is dried at 80°C overnight.

Surface modification of CVD carbon by oxidation with NaOCl. The hydrophobic surface of the CVD carbon is unsuitable for the wetting with and the infiltration of aqueous precursor solutions. In order to improve the surface chemistry, we introduce oxygenated surface groups onto the carbon surface. Hypochlorite is a mild oxidizer and introduces mainly carboxylic acid groups [141]. We expect that the presence of these groups on the carbon surface facilitates the replication with HA.

400 mg of carbon template are stirred for 24 h or 5 days in 15 mL of diluted sodium hypochlorite solution (concentration: 6.7% free chlorine, obtained by dilution of the commercial 10 % solution with water 2:1) at room temperature in a round-bottomed flask. The treated carbon is filtered and dried at 80°C overnight.

2.2.2 Hydroxyapatite synthesis

Five precursor combinations are chosen for HA synthesis:

- Calcium nitrate $\text{Ca}(\text{NO}_3)_2 \cdot 4\text{H}_2\text{O}$ and triethyl phosphine $(\text{EtO})_3\text{P}$
- Calcium ethoxide $\text{Ca}(\text{OEt})_2$ and triethyl phosphate $(\text{EtO})_3\text{PO}$ or tributyl phosphate $(\text{BuO})_3\text{PO}$
- Calcium nitrate $\text{Ca}(\text{NO}_3)_2 \cdot 4\text{H}_2\text{O}$ and sodium metaphosphate $(\text{NaPO}_3)_n$
- CAT [calcium di(hexafluoro-2,4-pentadione)(tetraglyme)]⁵ and tributyl phosphite $(\text{BuO})_3\text{P}$.
- Calcium nitrate $\text{Ca}(\text{NO}_3)_2 \cdot 4\text{H}_2\text{O}$ and diammonium hydrogen phosphate $(\text{NH}_4)_2\text{HPO}_4$ solution in ethanol

The methods are the following:

$\text{Ca}(\text{NO}_3)_2 \cdot 4\text{H}_2\text{O}$ and $(\text{EtO})_3\text{P}$. Calcium nitrate is dissolved in water, and triethyl phosphite is hydrolyzed with water for at least 4 h. The amount of water is varied: for incipient wetness syntheses ("concentrated solution"), the minimum amount of water required for the dissolution of the nitrate was used (1 mL for 1.2 g), and 12.5 mol% water are used to hydrolyze the phosphite. The liquids are mixed at room temperature and stirred for 15 min until homogeneous. The solution is aged for 1 h at 60°C, evaporated and dried at 80°C overnight. Calcination is possible in air or in argon.

⁵see figure 2.1, page 23.

The infiltration into the template is either carried out after the aging of the sol at 60°C or the sol is prepared in presence of the template, that is the template is added to one of the precursor solutions before they are mixed. Infiltration can be done at atmospheric pressure or under reduced pressure. Multiple infiltrations (up to three) are carried out in order to study the effectiveness of the filling.

In the case of carbon templates, a heat treatment under air flow is necessary in order to remove the template. The temperature can be varied between 500°C and 750°C. The lower the temperature, the longer the treatment must be. It is possible to densify the composite material at 600 or 800°C in argon prior to the template removal. The densification can improve the structural stability of the ceramic.

In case of silica templates, the calcination can be omitted. The silica template is dissolved in 1 M sodium hydroxide solution in water and ethanol (1:1 in volume) at 100°C: For 1 g of composite, 40 mL of NaOH are added to the powder in a Teflon beaker. The mixture is heated to 100°C and allowed to reflux for 1 h. The supernatant liquid is decanted and fresh solution is added. The treatment is repeated for 1 h. The solid is filtered and dried at 80°C.

Ca(OEt)₂ and (RO)₃PO, R=Et, Bu. The precursors used for this approach are moisture-sensitive and must be stored in protective atmosphere, e.g. under argon. The synthesis was adapted from [142]: 0.02 mol of calcium ethoxide and 1 g of template are introduced into a 25 mL Schlenk flask in the argon flushed glove box and closed with a septum. The phosphate precursor and 5 mL of absolute ethanol are added dropwise via a syringe. The mixture is stirred at room temperature for 24 h and then at 40°C for another 24 h. The temperature is raised to 75°C for 10 h before the solvent is evaporated in air at 120°C for at least 12 h or until dry. The composite is calcined at 780°C for 4 h in air (silica template) or argon (carbon template). The heating rate is 5 K/min, and the gas flow is 20 L/h.

Ca(NO₃)₂ · 4 H₂O and (NaPO₃)_n. A first test is carried out in order to see if the calcium metaphosphate can be transformed into HA by heat treatment. For this, 18 mL of saturated (NaPO₃)_n solution (corresponding to 13.34 g (PO₃)_n) are mixed with 14.2 g of Ca(NO₃)₂ · 4 H₂O dissolved in 10 mL of water. The mixture is stirred for 1 h, during which a white gelatinous precipitate is formed. The solid is filtered, washed three times with 10 mL of distilled water and dried at room temperature for one week. (Drying at higher temperatures leads to liquefaction of the product). The sample is divided into five equal parts, which are calcined for 1 h at 200, 400, 600 and 800°C in air with 8 K/min.

For the infiltration into silica MCF template, 0.5 g of silica are degassed for 5 min in high vacuum. The valve towards the pump is closed and 9 mL of saturated polyphosphate solution⁶ are added through a syringe. The silica and the solution are stirred under static vacuum for 2 h. The mixture is allowed to come back to atmospheric pressure, then rinsed rapidly with water and dried for at least 4 h at 80°C. The impregnated silica is placed under vacuum again, the valve is closed and a solution of 7.1 g calcium nitrate in

⁶this corresponds to 6.67 g (PO₃)_n

5 mL water are added through a syringe. The mixture is stirred under static vacuum for 1 h before it is allowed to come back to atmospheric pressure. The composite is rapidly rinsed with water, then dried at 80°C overnight.

CAT and (BuO)₃P. 100 mg of template (silica or carbon) and 0.5 g of CAT (see figure 2.1, page 23) are mixed and introduced into a small steel container. The reactor is evacuated for 3 h. The vacuum valve is closed while the reactor is heated to 150°C at 10 K/min. The temperature is maintained for 30 min. The impregnated template is cooled down and allowed to come back to atmospheric pressure. 300 μ L of tributyl phosphite are added. The reactor is placed into liquid nitrogen and evacuated again. 27 mbar nitrogen are added back into the reactor. The reactor is directly placed into a hot furnace at 500°C for 4 h.

Ca(NO₃)₂ · 4 H₂O and (NH₄)₂HPO₄ in ethanol solution. This synthesis was adapted from [143]: 11.8 g of calcium nitrate tetrahydrate are dissolved in 160 mL to create a 0.5 molar solution. 3.93 g diammonium hydrogen phosphate are dissolved in 50 mL ethanol to create 0.5 molar solution. The calcium solution is heated to 85°C in a two-neck-flask fitted with a dropping funnel and a water cooled condenser on an oil bath. The phosphate solution is slowly dropped into the calcium solution. The pH of the solution is tested every 10 mL, and Ca(OH)₂ is added in small portions to raise the pH. The pH is maintained at about 10. In total, 1 g of calcium hydroxide are added. The mix is stirred and maintained at 85°C for 4 h. the temperature is lowered to 40°C and the mixture is stirred overnight. The solid is filtered, washed with ethanol and dried at 80°C overnight.

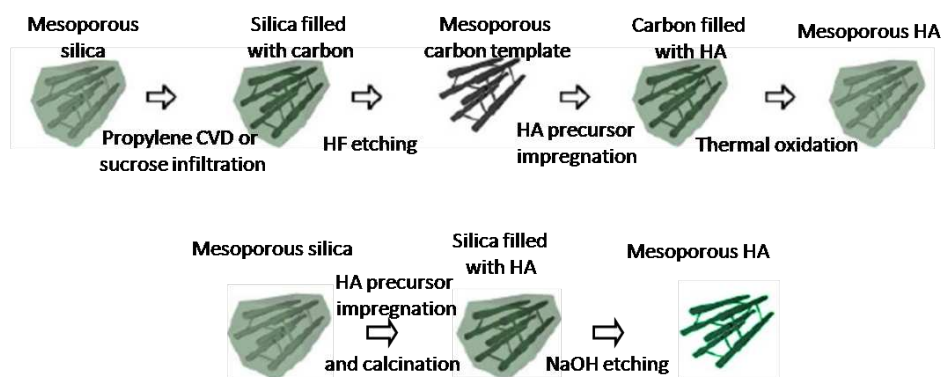


Figure 2.25: Two synthesis pathways for the synthesis of mesoporous hydroxyapatite: double replication (top) via mesoporous carbon templates and direct infiltration (bottom) of mesoporous silica templates.

2.3 Results

For the synthesis of mesoporous hydroxyapatite by hard templating, two synthesis pathways are proposed as shown in figure 2.25. Starting from mesoporous silica, we can either prepare mesoporous carbon and fill the carbon template with HA precursor or fill the silica template directly with HA. Depending on the pathway, the structure of the mesoporous hydroxyapatite is different: in the case of the double replication, the final ceramic should have a pore structure close to the one of the initial mesoporous silica. In the case of the direct infiltration into the silica, the hydroxyapatite is the negative replica of the silica pore structure.

In the following, we will discuss the synthesis of the mesoporous silica and carbon templates.

2.3.1 Synthesis and optimization of templates

2.3.1.1 Mesoporous silica templates

SBA-15. The product obtained is a white powder composed of particles with low apparent density. Figure 2.26 shows transmission electron micrographs of the silica. The material is highly porous, and on the TEM images, the hexagonal arrangement of the pores is clearly visible. The pores form elongated channels, several micrometers in length (the length of the particles). The pore diameter is about 7 nm. Interconnecting nanochannels cannot be seen on the TEM images, but the carbon replication proves their existence: if the channels were not interconnected, individual carbon rods would be formed instead of particles with three-dimensional porosity (see page 70).

Figure 2.27 shows the isotherm for nitrogen physisorption experiments. The insert shows the pore size distribution calculated from the physisorption data. The isotherm shape is typical of a type IV adsorption isotherm with type H1 hysteresis (see section 5.1 on page 169). The isotherm shows that the ceramic is mesoporous with monomodal

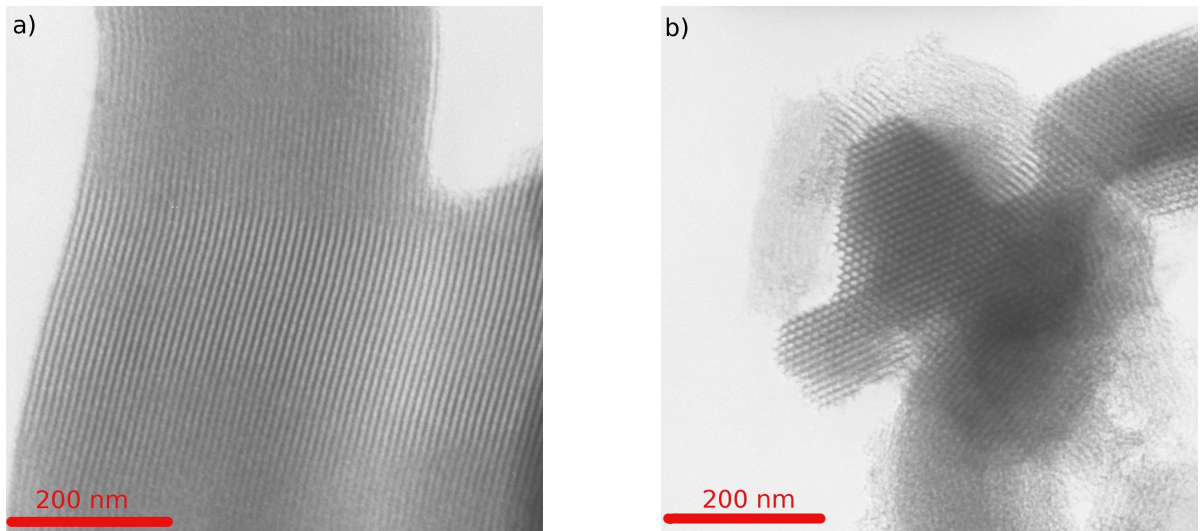


Figure 2.26: Transmission electron micrograph of the SBA-15 silica. a) alignment of elongated channels. b) cross section showing the hexagonal arrangement of the channel entries.

and narrow pore size distribution. The specific surface area, determined with the BET equation, is $619 \text{ m}^2/\text{g}$. Using the BJH model on the desorption branch of the isotherm, the mean pore diameter and the pore volume can be calculated: the pore diameter is 7.5 nm and the pore volume is $1.2 \text{ cm}^3/\text{g}$. The pore diameter corresponds well to the observations in TEM.

The synthesis was repeated a total of four times. The results of the physisorption experiments are compared in table 2.3. The mean value obtained for the surface area is $594 \text{ m}^2/\text{g}$. All the samples were obtained with the same parameters, and the standard deviation of the surface area is 8 %.

The results obtained by TEM and physisorption correspond to those described in the

SBA-15	specific surface [m^2/g]	pore size [nm]	total pore volume [cm^3/g]	mesopore volume [cm^3/g]	unit cell d [nm]
SBA15-1	620	7	1.2	0.9	
SBA15-2	580	8	1.2	0.9	5.1
SBA15-3	536	10	1.1	0.8	
SBA15-4	641	7	1.2	0.9	4.9
mean	595 ± 50	8.2 ± 1.2	1.2 ± 0.04		

Table 2.3: Nitrogen physisorption results for SBA-15 samples at 77 K. The unit cell parameter d was calculated from small angle X-ray scattering for those samples that have been analyzed by SAXS.

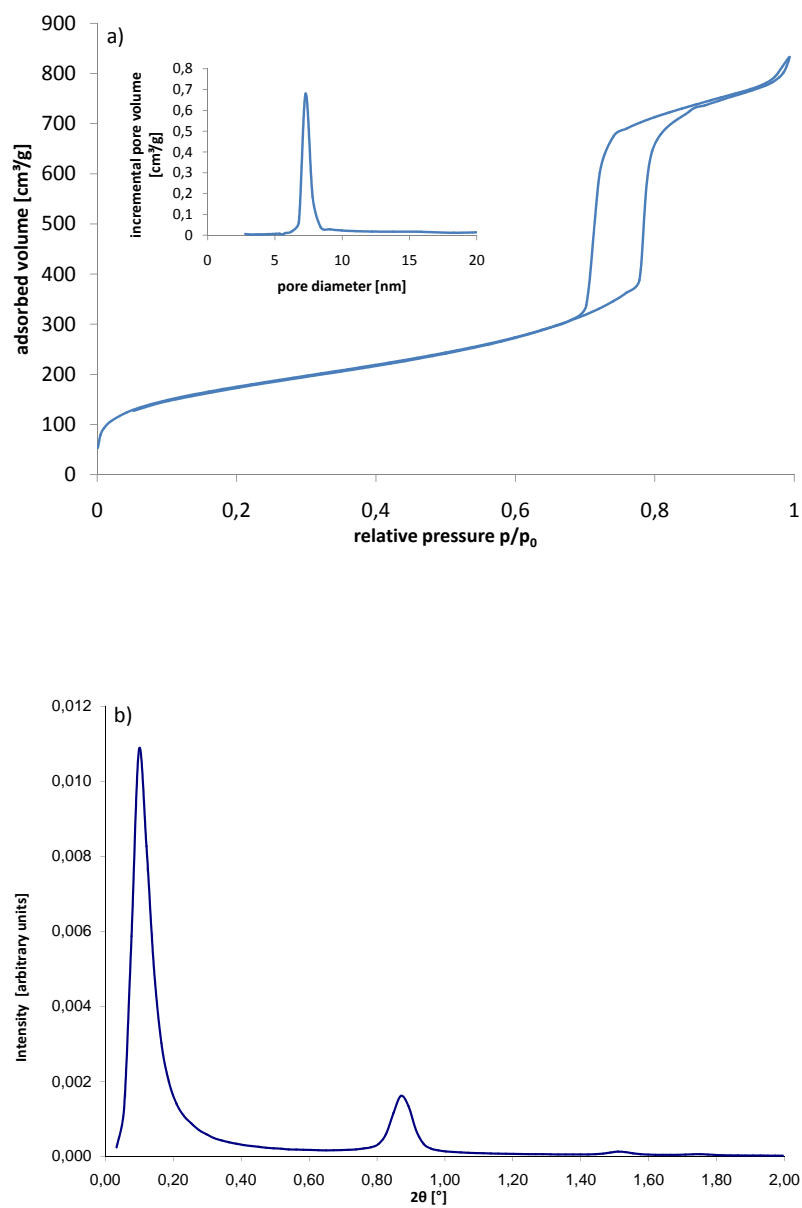


Figure 2.27: a) Nitrogen physisorption isotherm for SBA-15 silica. The insert shows the pore size distribution. b) Small angle X-ray diffractogram for SBA-15 silica.

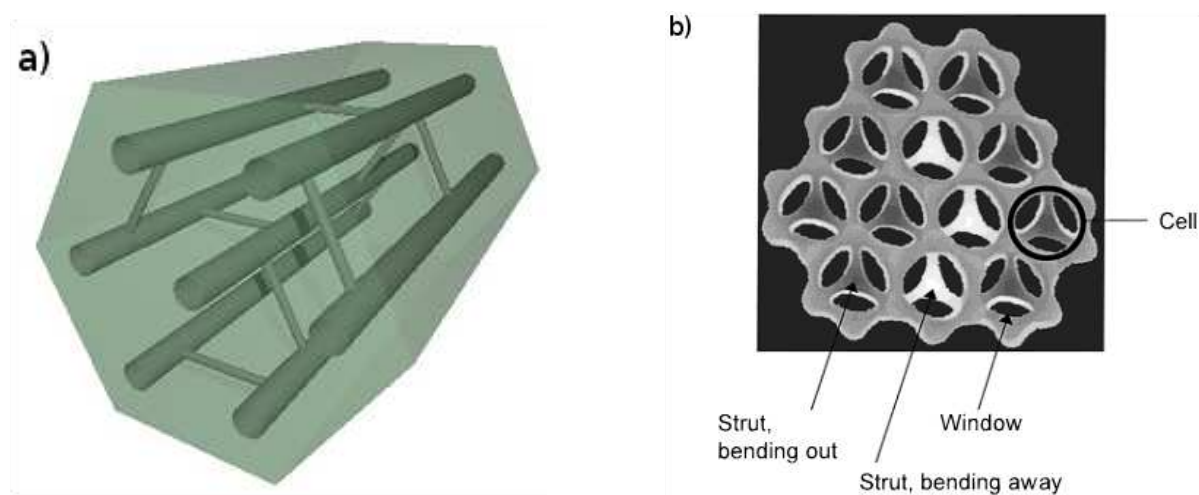


Figure 2.28: a) Schematic representation of the pore structure of SBA-15: elongated mesoporous channels interconnected randomly by micropores. b) Schematic representation of the pore structure of MCF: spherical mesopores interconnected by large windows. From [139].

literature [56, 137]. The high surface area and the pore volume of more than $1 \text{ cm}^3/\text{g}$ evidence that the silica is suitable for replication with carbon and hydroxyapatite.

Small angle X-ray scattering (SAXS) (see figure 2.27) shows a main reflex at 0.1° that corresponds to the (100) crystal plane. The first harmonic of this diffraction peak can be observed at 1.53° . The peak at 0.87° corresponds to the (110) plane. The shape of the diffractogram is typical of the hexagonal arrangement of the pores and has been observed before [56, 144].

Nevertheless, the pore structure is not appropriate for impregnation: The pores form long channels with small interconnections (see illustration in figure 2.28). This kind of porosity can easily be blocked when product is deposited at the entry of the channel and prevents the reactants from further penetrating the inner pore volume. For this reason, silicas with bigger mesopores and large interconnections were synthesized: mesocellular foams (MCFs). The pore structure of MCF materials are represented in the figure 2.28b.

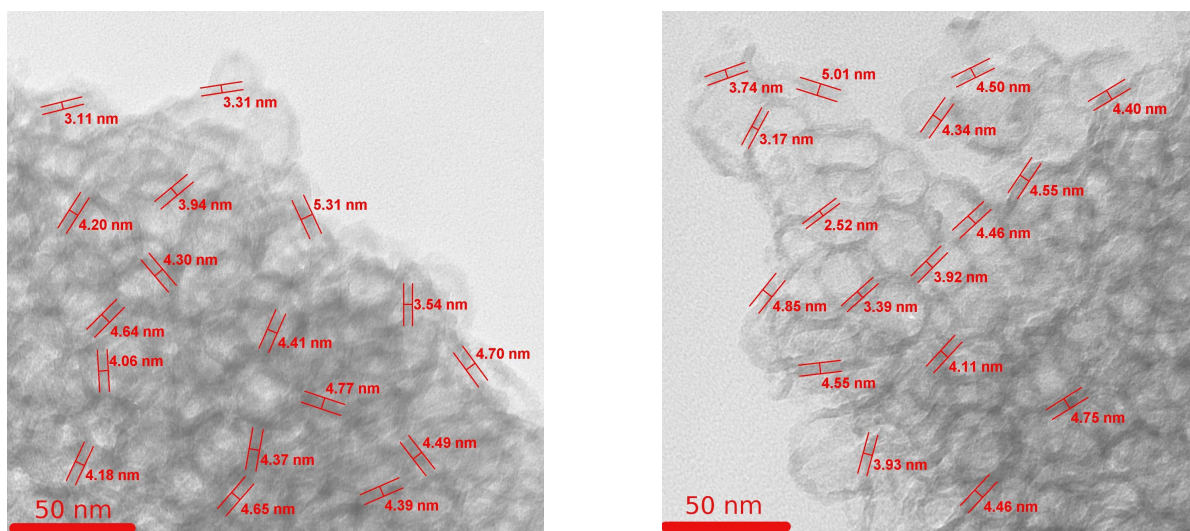


Figure 2.29: Transmission electron micrographs for a MCF silica. Measurements indicate the thickness of the pore wall.

MCF. After calcination, the MCF material appears as a white powder with low apparent density. Figure 2.29 shows transmission electron micrographs of the ceramic. The measurements indicate the thickness of the pore walls. The images show a highly porous structure with large spherical pores. The interconnecting windows are large and apparent on the image. The pore diameter is observed to be in the range of 10 nm and more. The pore walls are about 4 nm thick. The wall thickness is crucial: during replication, the walls of the template form the pores of the replica.

Figure 2.30a shows a typical nitrogen physisorption isotherm and the corresponding pore size distribution. The isotherm shape is type V with H1 hysteresis. The sample is highly mesoporous with big mesopores as the hysteresis is located at high relative pressures. The shape of the hysteresis indicates even pores with narrow pore size distribution.

Small angle X-ray diffraction pattern are shown in figure 2.30b. The represented pattern was obtained for a MCF material with a P/M ratio of 0.5. Variations of the pluronic to mesitylene ratios lead to different diffraction patterns (see figure 2.31). This is caused by the change in the shape of the surfactant micelles that is affected by the swelling agent concentration. In figure 2.30b, the main peaks are situated at 0.12° , 0.39° , and 0.63° . Harmonics can be distinguished at 0.92° and 1.22° . Except for the first peak, these peaks correspond to those observed by Schmidt-Winkel and coworkers [138, 139]. The first peak is covered by the primary beam in the quoted paper. The same pattern is obtained when a regular array of equi-sized spheres is simulated [139]. We can conclude that the pores are spherical, equal in size and arranged in a close packing.

The synthesis of the MCF silica was repeated four times with the same parameters. Table 2.4 summarizes the results of the physisorption experiments for these four samples. The mean surface area was determined to be $688 \text{ m}^2/\text{g}$. The standard deviation is 10.3 %. Figure 2.32 shows the corresponding nitrogen physisorption isotherms. Whereas the

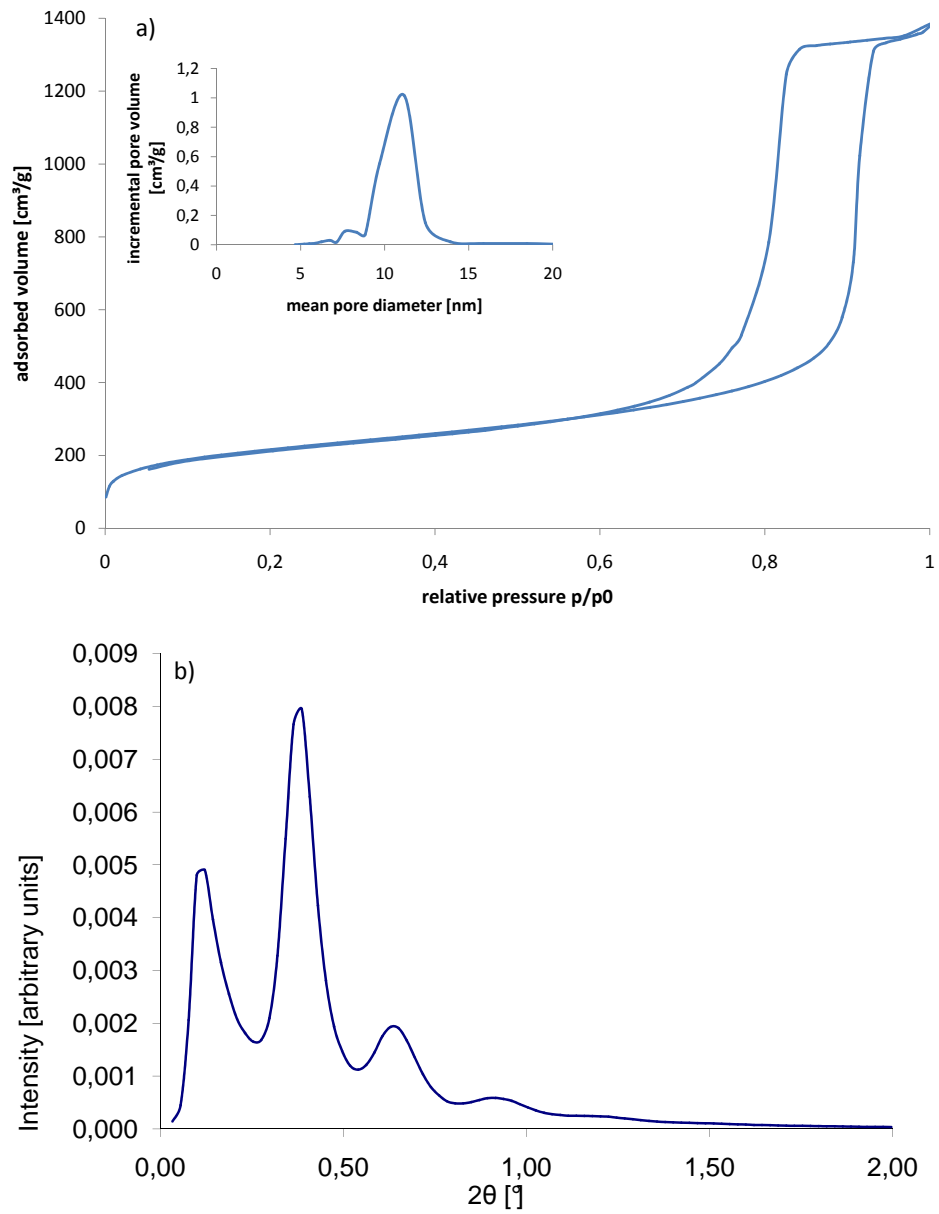


Figure 2.30: Typical nitrogen physisorption isotherm (a) and small angle X-ray diffraction pattern (b) for MCF-3 silica sample. The insert shows the pore size distribution derived from physisorption data.

Sample	Specific surface area [m ² /g]	Total pore volume [cm ³ /g]	Mesopore volume [cm ³ /g]	Pore size [nm]	unit cell [nm]
MCF-3	743	2.1	1.7	10.2	
MCF-4	741	2.1	1.7	10.0	11.3
MCF-5	594	2.0	1.7	13.3	10.8
MCF-6	674	2.2	1.4	11.0	11.3
mean	688 ± 70	2.1 ± 0.1	1.6 ± 0.1	11.1 ± 1.5	

Table 2.4: Nitrogen physisorption results and unit cell parameters calculated from small angle X-ray scattering (data not available for all samples) for MCF samples for the M/P ratio 0.5

samples MCF-3 and MCF-4 lead to identical isotherms, the isotherm for the sample MCF-6 is shifted down at low relative pressures, indicating a lower surface area. The hysteresis is shifted towards higher pressures, evidencing a larger pore diameter. The higher adsorbed volume at high pressures can be interpreted as a high pore volume. The isotherm of sample MCF-5 on the other hand is shifted down, and its hysteresis is situated at even higher pressures. The maximum adsorbed volume nevertheless is lower than for the other three samples. Sample MCF-5 has bigger pores but a lower pore volume and lower surface area than the other samples. The same observations can be made from the pore size distributions shown in the insert of the figure: MCF-3 and MCF-4 have identical pore size distributions, whereas MCF-5 and MCF-6 have larger pores. In the case of MCF-6, the pore size distribution is considerably larger, too.

The syntheses show considerable variations between the different batches even if the synthesis parameters remained unchanged.

Schmidt-Winkel et al. [139] claim that the pore sizes can be controlled by varying the mesitylene to pluronic ratio. They observe that with rising M/P ratio, the pore diameter follows a cube root law. Linear regression gave rise to the following equation:

$$d_p = \text{pore diameter [nm]} = \left(26.1 \cdot \left(\frac{m_{\text{Mesitylene}}}{m_{\text{Pluronic}}} \right)^{\frac{1}{3}} + 6.33 \right) \text{ nm} \quad (2.13)$$

The results of the nitrogen physisorption experiments for a series of synthesis with different M/P ratios is given in table 2.5 and in figure 2.33. Considering the variation between batches of the same silica sample, the variations must be considered insignificant. The effect of the varied surfactant/swelling agent ratio on the pore size that was described by Schmidt-Winkel et al. could not be reproduced. It has to be noted, that the pore sizes observed in the original paper are much higher than the pore sizes measured during our experiments (25 to 38 nm) whereas our silicas have pores ranging from 8 to 15 nm in diameter. This difference may be caused by the scale-up of the synthesis that has been carried out: In hydrothermal synthesis, the pressure inside the autoclave is governed by the vapor volume over the liquid phase during the synthesis. The smaller the available

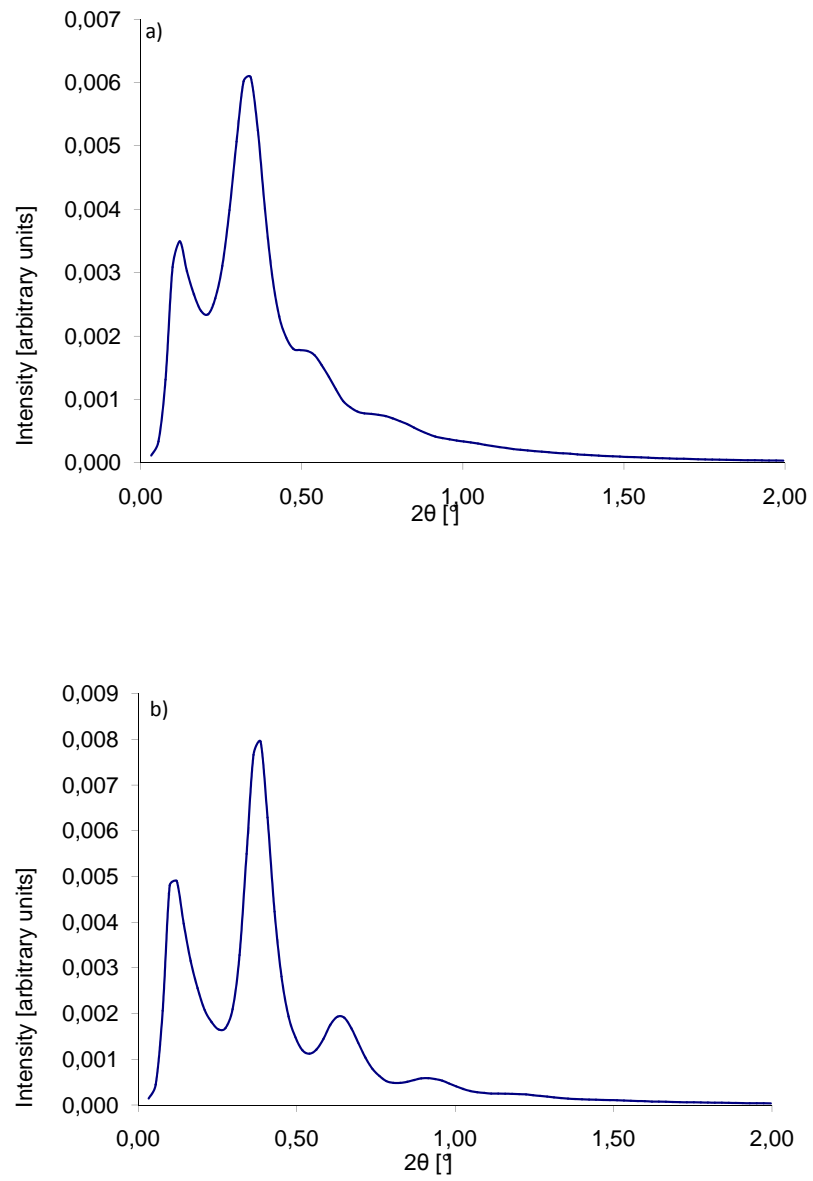


Figure 2.31: Small angle X-ray diffraction pattern for MCF material with a) P/M=1.0 and b) P/M=0.5. The pluronic/mesitylene ratio affects the shape of the micelles.

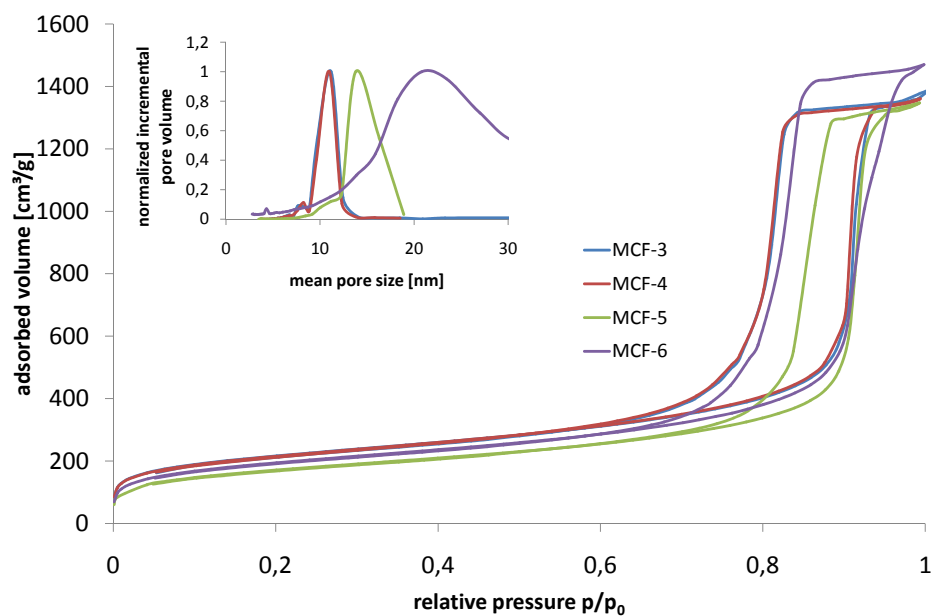


Figure 2.32: Comparison of nitrogen physisorption isotherms and pore size distributions (insert) of MCF materials obtained for M/P ratio 0.5.

space, the higher the pressure will rise. As the authors do not indicate the volume of the autoclave used [139], we cannot compare if the empty volume in our synthesis was the same or at least to scale. However, the authors produced smaller batches, indicating that they have probably used smaller autoclaves.

M/P ratio	Specific surface area [m ² /g]	Total pore volume [cm ³ /g]	Mesopore volume [cm ³ /g]	Pore size [nm]
0.18	611	1.1	0.7	9.1
0.5	743	2.1	1.7	10.2
0.68	656	1.6	1.1	10.4
1.0	708	2.4	2.1	11.0
1.5	662	2.3	1.8	10.4
1.53	626	2.7	1.4	14.8
1.73	622	1.7	1.2	10.0
2.15	781	2.8	2.4	13.3

Table 2.5: Nitrogen physisorption results for MCF samples for different M/P ratios.

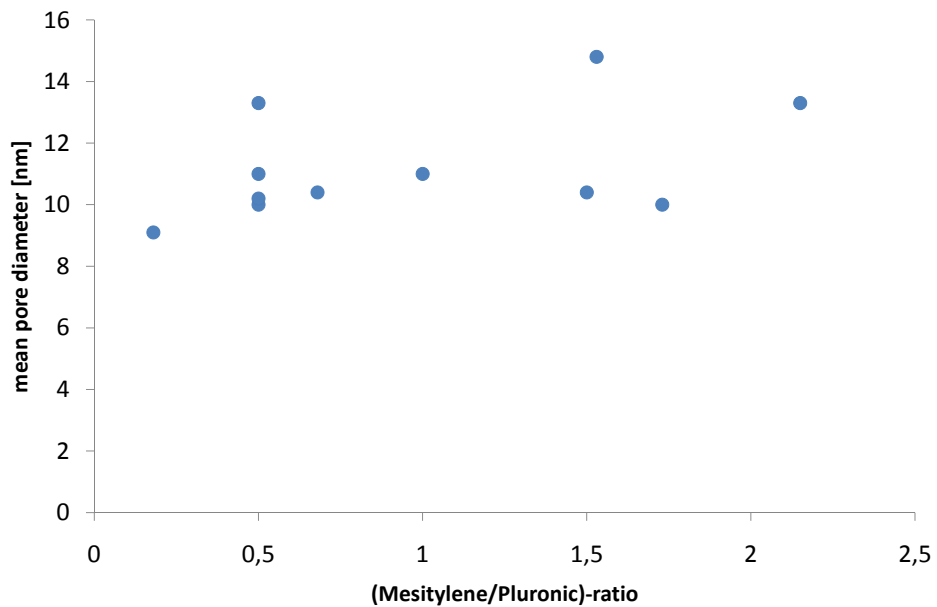


Figure 2.33: Scatter plot showing the mean pore diameter of the silica MCF in function of the (mesitylene/pluronic)-ratio used during their synthesis.

Heating ramp K/min	S_{BET} m ² /g	pore volume cm ³ /g	pore diameter nm
1	602	1.55	10.2
2	606	1.57	10.3
3	670	1.64	9.9
4	661	1.70	10.4
5	602	1.38	8.4
10	614	1.69	9.4

Table 2.6: Influence of the calcination ramp on the properties of MCF determined by nitrogen physisorption.

Influence of the calcination ramp on the properties of the MCF silica. Another study was carried out to determine the ideal heating ramp for the calcination. For a sample with constant M/P ratio, the heating ramp was varied between 1 and 10 K/min. Table 2.6 gathers the results of the nitrogen physisorption experiments on the samples after calcination. *Considering the variations of the surface area and the pore volume within different batches obtained with the same parameters (see above), the changes are not significant. In conclusion, it is possible to speed up the calcination process and heat up the sample with 4 K/min without significantly losing surface area or pore volume.*

2.3.1.2 Mesoporous carbon templates

Carbon replica of SBA-15 by CVD. After the deposition with propylene and before the treatment with hydrofluoric acid, a silica/carbon composite is obtained. Burning a small sample of this composite allows the determination of the yield of carbon during the deposition: a heat treatment in air at 700°C eliminates the carbon and only the silica remains. The mass of carbon is equal to the weight loss during the oxidation. For the replication of SBA-15 with propylene at 750°C for 8 h, 31.5% of the composite are carbon. From the pore volume of the silica and a theoretical carbon density of 2.26 g/cm³ (density of graphite), we can calculate that about 86.0% of the pore volume of the silica has been filled during the CVD. This simple calculation neglects carbon that has been deposited on the external surface of the silica template.

Figure 2.34 compares the physisorption isotherms and transmission electron micrographs of the SBA-15 silica and the carbon template obtained after silica removal with HF. Instead of a classical type IV isotherm with type H1 hysteresis as for the silica, the nitrogen physisorption on the carbon replica yields in an isotherm with H3 hysteresis. The shape of the isotherm seems to be a hybrid between type II and IV. This indicates that the pores have become more slit-like (thinner in diameter and with increased aspect ratio) and that the pore size distribution is broader. The surface area of the SBA-15 carbon replica was determined to be 718.4 m²/g, the pore volume is 0.93 cm³/g and the mean pore diameter 7.1 nm. The TEM images illustrate how the pore walls of the silica correspond to the pores of the carbon replica. On the transmission electron micrograph of the silica material, dark areas represent the silica walls. On the second picture showing the carbon replica, dark areas represent carbon. Dark and bright areas are inverted on the two pictures, however the pores of the carbon replica are slightly smaller than the silica pore walls. This shrinking effect can be attributed to the high temperature during the CVD.

These characterizations show that the carbon replica has pores that are, even narrower than the one of the original silica template. The infiltration of this porosity with HA is difficult (see section 2.3.2.3).

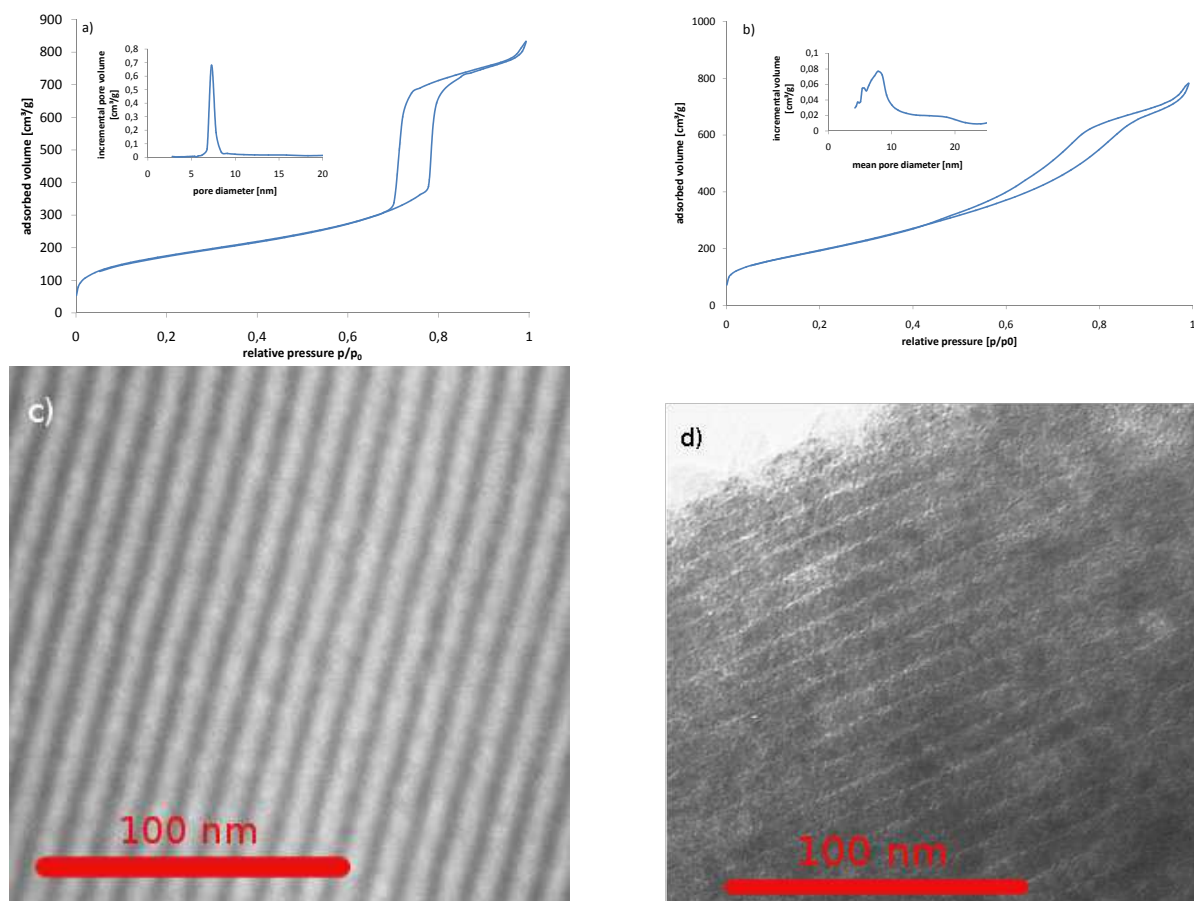


Figure 2.34: Comparison of the nitrogen physisorption isotherms (a and b) and the transmission electron micrographs (c and d) of the SBA-15 type silica (isotherm a and TEM image c) and its carbon replica (b and d). Both TEM images have the same scale. The inserts show the pore size distributions derived from physisorption data.

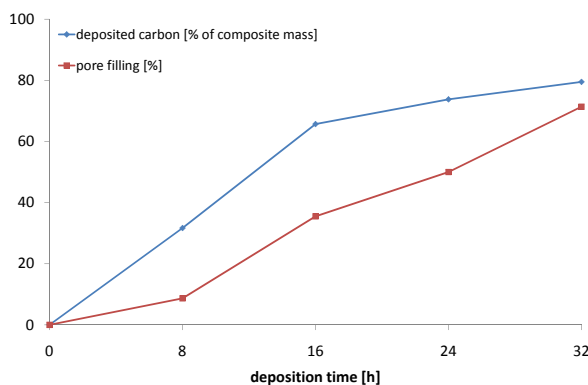


Figure 2.35: Evolution of mass and volume percentage of carbon in silica MCF templates during CVD with propylene at 750°C.

Carbon replica of MCF by CVD. Contrary to SBA-15, whose replication by CVD is well known and published, carbon replicas of the MCF materials have not been produced yet. For this reason, the right parameters for the deposition were determined first. Propylene cracking was carried out for 8 to 32 hours and the pore filling was determined. Table 2.7 gathers the results of this study. For the sample with only 8 hours of deposition, the product lacked structural stability and could not be filtered after HF etching. The pore filling grows steadily with the deposition time, contrary to the carbon mass deposited in the silica template (see figure 2.35). From this behavior it can be concluded that the carbon first deposits as a film on the silica walls and then progressively fills the porosity. The deposition of carbon on silica is favoured compared to the deposition of carbon on already deposited carbon. An illustration of this filling mechanism is given in figure 2.36a. The incomplete filling of the silica porosity leads to highly porous structures with two types of pores:

- big mesopores that are essentially incompletely filled silica pores
- and smaller mesopores that are liberated by the dissolution of the silica pore walls.

Figure 2.36b shows the pore size distributions of the carbon replicas after different deposition times. As expected, the amount of large mesopores decreases with deposition time, whereas the amount of small pores increases. For short deposition times (16 h), partial filling of small silica pores (windows) is evidenced by the peak at small pore diameters that is shifted to smaller values compared to longer deposition times.

Figure 2.37 shows a typical isotherm obtained for carbon replicas after 16 h and after 32 h of deposition. The isotherm for 16 h is type II shaped with type H3 hysteresis: this isotherm shape is typical of materials with multimodal pore size distribution and possible interconnections. For longer deposition times, the hysteresis shifts towards type H2 as the fraction of the smaller pores gradually overpower the big ones.

In favor of high surface areas and pore volumes, a deposition time of 16 h was chosen for all following experiments. Figure 2.38 shows transmission electron micrographs of the silica template and the carbon replica obtained after 16 h of CVD. The pore filling

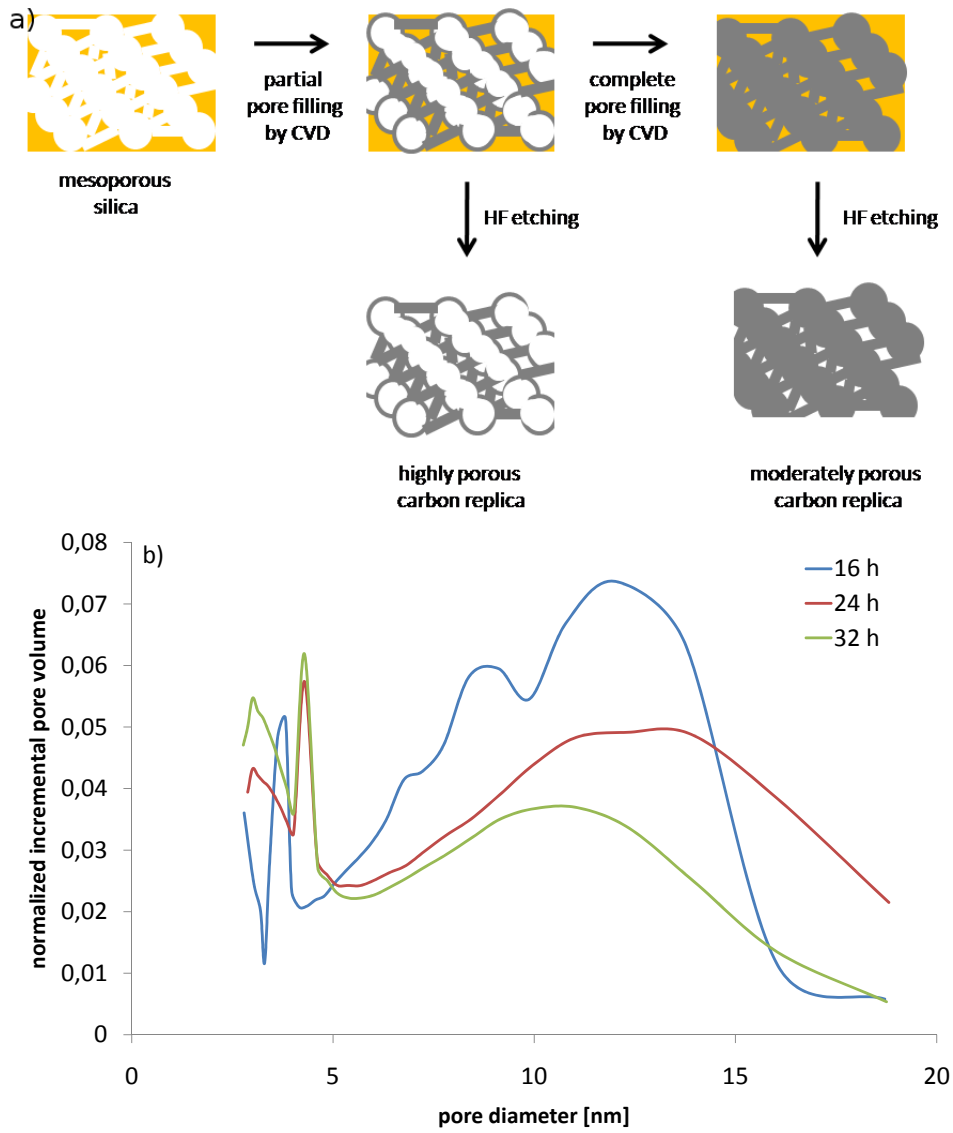


Figure 2.36: a) Formation of highly porous carbon replicas by incomplete pore filling. b) Pore size distributions for carbon replicas after different deposition times: increasing small pores and decreasing large pores with increased deposition time.

deposition time h	carbon mass in composite %	pore filling %	sp. surface area m^2/g	mean pore diameter nm	pore volume cm^3/g	total pore volume cm^3/g
8	31.7	8.67	<i>a</i>	<i>a</i>	<i>a</i>	
16	65.7	35.5	494	5.8	0.9	
24	73.8	50.0	364	4.2	0.5	
32	79.5	71.4	304	4.2	0.3	

^a Product could not be retrieved after HF treatment.

Table 2.7: Optimization of the deposition time for CVD replicas of MCF silica.

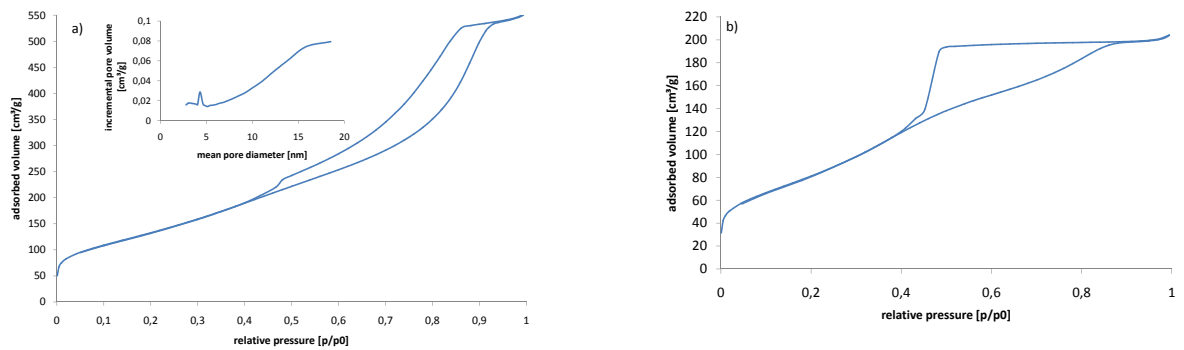


Figure 2.37: Nitrogen physisorption isotherms for MCF carbon replicas obtained after 16 h (a) and 32 h (b) of deposition.

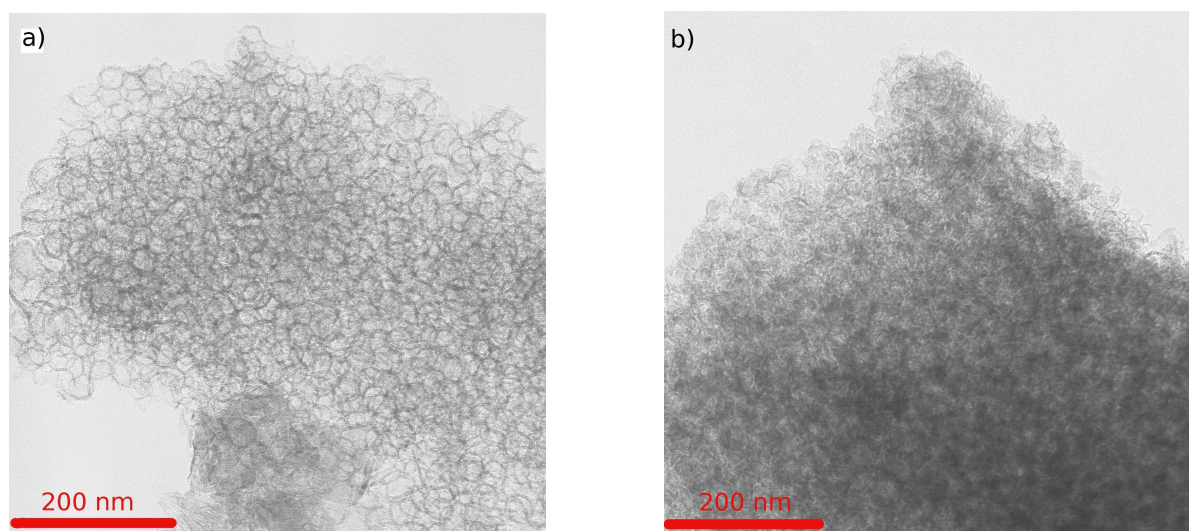


Figure 2.38: Transmission electron micrographs for MCF silica (a) and carbon replica (b) obtained after 16 h of propylene deposition.

is incomplete, the replication of the silica porosity is therefore imperfect. The carbon replication contains two types of pores: small mesopores that derive from the dissolution of the silica pore walls and bigger pores that are basically residual silica pores that have not been filled completely.

Comparable studies have already been carried out with SBA-15 silicas. It is generally accepted that a deposition time of 8 h is sufficient to fill the porosity [38,111]. The MCF silica requires longer deposition times due to its higher pore volume. Contrary to SBA-15 silicas, where a complete filling is desired, incomplete filling of the MCF silica leads to carbon replicas with higher pore volumes and higher specific surface areas, which are more suitable for the replication with HA. In this case however, the carbon replica is not well ordered and a larger pore size distribution is obtained.

A 16 h deposition was repeated a total of six times on different silica samples. Table 2.8 gathers the results of the nitrogen physisorption experiments on the silicas and the carbon replicas. Even with the same parameters of deposition, two experiments do not lead to the same amount of carbon deposited: the pore filling ratio (percentage of filled pores referring to the total pore volume) varies between 35 and 52.3 %. These differences might be related to inhomogeneities of the particle sizes of the silica.

The filling process of the silica porosity can be monitored by comparing the nitrogen physisorption isotherms of the silica template, of the composite made of silica and carbon, and of the carbon after template removal. Figure 2.39 shows the nitrogen physisorption isotherms and transmission electron micrographs of the three stages of deposition. A comparison of the first two isotherms (silica and composite) shows that the carbon has partially filled the porosity of the silica template: The surface area and the pore volume decrease from $744 \text{ m}^2/\text{g}$ and $2.1 \text{ cm}^3/\text{g}$ for the silica to $256 \text{ m}^2/\text{g}$ and $0.4 \text{ cm}^3/\text{g}$ for the composite, respectively. The hysteresis occurs over a larger range in the isotherm of the composite. This is due to partial pore filling that gives rise to smaller

Sample	Silica template					Composite		Carbon replica				
	M/P	S_{BET}	V_p	ϕ_p		%C	% V_p	S_{BET}	V_p	V_{micro}	V_{meso}	ϕ_p
CVD-1	MCF-1	1.0	709	2.4	11.0	65.7	35.5	494	0.6	0.1	0.5	5.8
CVD-2	MCF-5	0.5	579	2.0	13.2	68.2	47.5	382	0.6	0.1	0.5	5.2
CVD-3	MCF-3	0.5	744	2.1	10.0	62.5	35.0	527	0.8	0.2	0.6	5.2
CVD-4	MCF-4	0.5	741	2.1	10.0	66.0	41.5	466	0.2	0.05	0.15	4.6
CVD-5	MCF-4	0.5	741	2.1	10.0	71.8	52.3	no data				
CVD-6	MCF-6	0.5	674	2.3	11.0	66.2	38.7	493	0.3	0.1	0.2	7.0

Table 2.8: 16 h CVD on different silica samples: Comparison of the results of nitrogen physisorption for templates and replicas. M/P is the mesitylene/pluronic ratio used for silica synthesis, S_{BET} is the specific surface area determined by the BET equation, V_p and ϕ_p are the pore volume and the mean pore diameter determined by BJH on the desorption branch of the nitrogen physisorption isotherm, %C is the percentage of carbon in the composite after CVD and before etching with HF, % V_p is the percentage of filled pore volume.

pores with different pore diameters. The large hysteresis range evidences a large pore size distribution. On the other hand, the hysteresis is shifted towards lower relative pressures: in total, the pores are therefore smaller than for the pristine silica (4.9 nm instead of 10 nm). The isotherm for the silica is type IV with neat H1 hysteresis. This shape is typical of a highly mesoporous solid with small pore size distribution. The isotherm of the composite is type IV with an hysteresis that can be thought of as a mixture of H2 and H3. H2 or H3 hysteresis are observed for solids with pores of different sizes and hint towards interconnection. The shape of the isotherm and the larger hysteresis range both evidence that the silica pores are partially filled with carbon. We observe a bimodal pore size distribution with a larger peak centered around 7 nm and a smaller, narrow peak at 4 nm. The bigger pores correspond to partially filled pores of the template. The smaller pores correspond to porosity between carbon nanoparticles that are formed inside the template.

The isotherm obtained for the carbon replica after template removal shows higher surface area and pore volume again: 527 m²/g and 0.8 cm³/g respectively. The isotherm is type IV with large hysteresis somewhere between H2 and H3. The pore size distribution is large and bimodal: small pores (mean diameter about 3.7 nm) were developed during dissolution of the silica walls with HF. These pores have added to the small pores already observed in the composite that can attributed to interstices between carbon nanoparticles. Larger pores (large peak centered around 9 nm) are residual silica pores that have not been filled completely during CVD.

The CVD carbon templates have high surface areas and pore volumes that are suitable for the impregnation with HA precursors. On the other hand, CVD carbons are known for their hydrophobic surface chemistry that do not favor the impregnation of aqueous solutions [145]. The wetting of the template surface by the HA precursor is crucial [146]. When the interactions between the surface and the solution are unfavorable, even vacuum treatment will not allow the infiltration. Two ways are possible to modify the surface

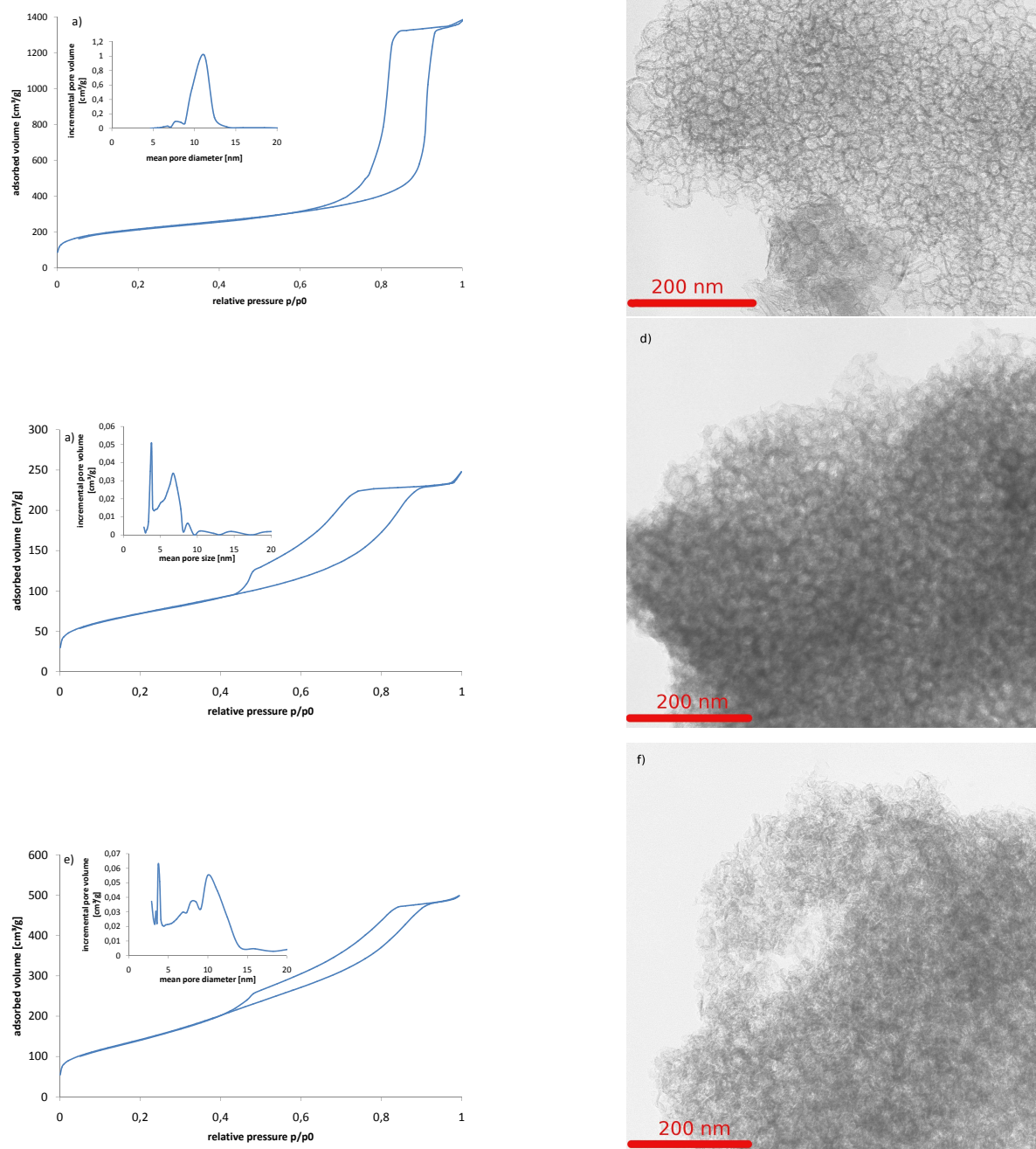


Figure 2.39: Nitrogen physisorption isotherms and transmission electron micrographs for the MCF silica (isotherm a and TEM image b), the silica/carbon composite obtained after CVD (c and d) and the carbon replica liberated by HF etching (e and f). Note the different scales on the ordinate of the isotherms. The inserts show pore size distributions obtained from physisorption data.

chemistry of the carbon template: modification of the surface by oxidation or the use of another carbon precursor which contains heteroatoms such as sucrose (contains oxygen).

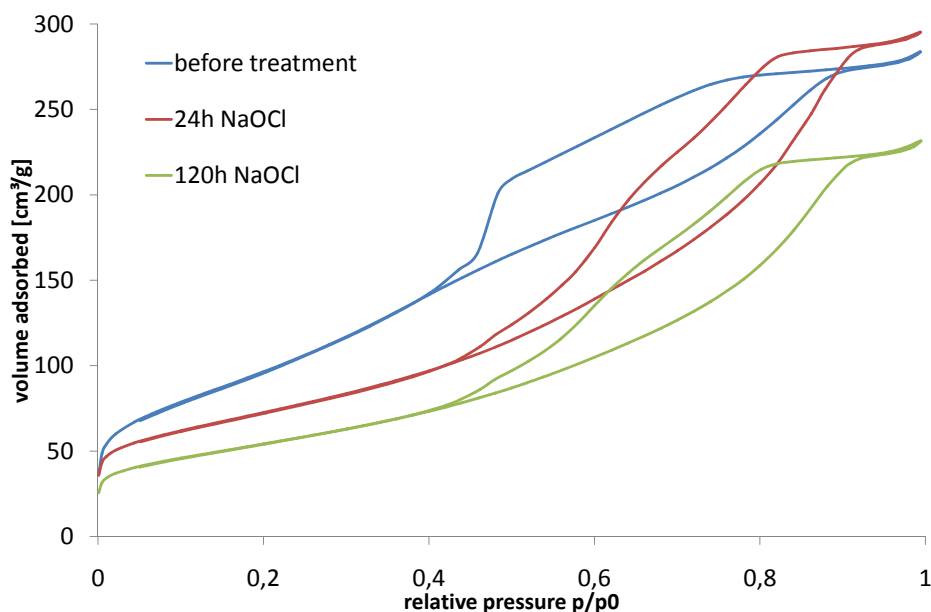


Figure 2.40: Nitrogen physisorption isotherms of carbon templates before (—) and after 24 h (—) and 5 day (—) NaOCl treatment.

Surface modification of mesoporous carbon replicas. Nitrogen physisorption experiments were carried out after the surface modification with NaOCl. The specific surface area was considerably decreased even after the shortest treatment. The initial surface area was $363 \text{ m}^2/\text{g}$, after 24 h it decreased to 259 and after 5 days to $195 \text{ m}^2/\text{g}$. Figure 2.40 shows the nitrogen physisorption isotherms of the untreated and the treated carbon samples. Within the first 24 h, the shape of the hysteresis shifts from type H2 towards type H1. As H2 hysteresis is obtained for solids with interconnected pores of different sizes, and H1 for unconnected pores without interconnections, we can conclude that the smaller pores that have been obtained by the dissolution of the silica walls are damaged during the oxidation treatment. It has been observed before that oxidative treatments destroy porous materials [145]. If the NaOCl treatment is prolonged, the shape of the isotherm does not further change, but the surface area continues to shrink.

Thus, the oxidative treatment with NaOCl damages the pore structure and reduces the surface area of the carbon template. Because both are crucial parameters for the replication of the carbon template with HA, surface modified carbon templates have been obtained in a different way, using sucrose as carbon source. This way, high surface area carbon materials could be produced.

Sample	S_{BET} [m ² /g]	V_p [cm ³ /g]	V_{micro} [cm ³ /g]	V_{meso} [cm ³ /g]	ϕ_p [nm]
CS-1	743	0.6	0.3	0.3	4
CS-2	608	0.6	0.3	0.3	4.5

Table 2.9: Results of nitrogen physisorption analysis on the sucrose replicas of MCF silica foams.

MCF silica replication by liquid infiltration with sucrose. Figure 2.41 shows transmission electron micrographs and the nitrogen physisorption isotherm of the sucrose replication of MCF silica. Contrary to the CVD replication, the sucrose replica is a true replication of the silica pore structure because the pore filling during the replication is more complete. The pore size distribution (figure 2.41d) shows a large and narrow peak at 3.68 nm. These pores are obtained from the dissolution of the silica walls. Pores with higher diameters and a large pore size distribution can be attributed to textural porosity between the carbon particles. This synthesis was repeated twice. Table 2.9 gathers the results of nitrogen physisorption on these two samples. The carbon samples have a high specific surface area, but the pore volume is less than for the CVD replicas due to the more complete filling of the silica porosity during their synthesis. In contrast to the CVD replicas that are mainly mesoporous, the sucrose replicas have a high micropore fraction (50%). For the replication with hydroxyapatite, the microporosity is less useful as it leads to micropores in the ceramic but not to the desired mesopores.

Comparison of the oxidation of CVD and sucrose replicas of MCF silica. While heated in oxidative atmosphere, the sucrose carbon and the CVD carbon show different behaviors. Figure 2.42 shows the mass loss of both samples as observed when heated in pure oxygen. We observe a first step of weight loss for the sucrose around 100°C that can be attributed to the evaporation of water on the surface of the carbon. The graph representing the CVD carbon on the other hand does not show this step, as its hydrophobic surface prevents the adsorption of water.

The second step of weight loss of the sucrose carbon can be attributed to the oxidation of the carbon material following the equation:



As we can see, the oxidation starts at lower temperature than for the CVD carbon (about 400°C instead of 500°C). We conclude that the elimination of the hydrophilic sucrose carbon is easier due to the already oxygen-rich surface chemistry. Both the surface chemistry and the oxidation are key characteristics of the templates for the replication with hydroxyapatite: the hydrophilic surface chemistry is more favorable for the infiltration with aqueous precursors, facilitating the penetration of the porosity by the aqueous precursor solution (see page 103). The oxidation in air is the method we use for the elimination of the template, it is thus important to know at which temperature the template can be eliminated. The lower the temperature of oxidation can be chosen, the less grain growth occurs during calcination. Heat induced grain growth is one of the

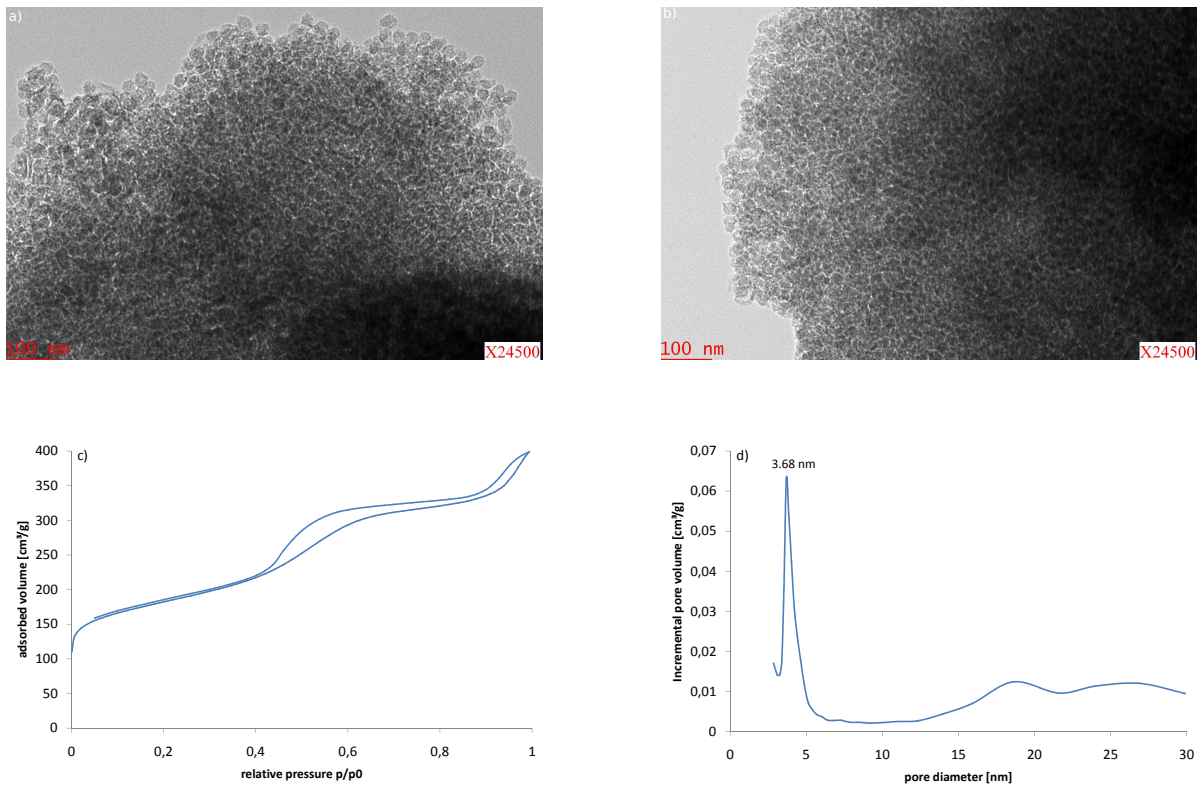


Figure 2.41: Transmission electron micrographs (a and b), nitrogen physisorption isotherm (c) and BJH pore size distribution (d) for the sucrose replica of MCF silica.

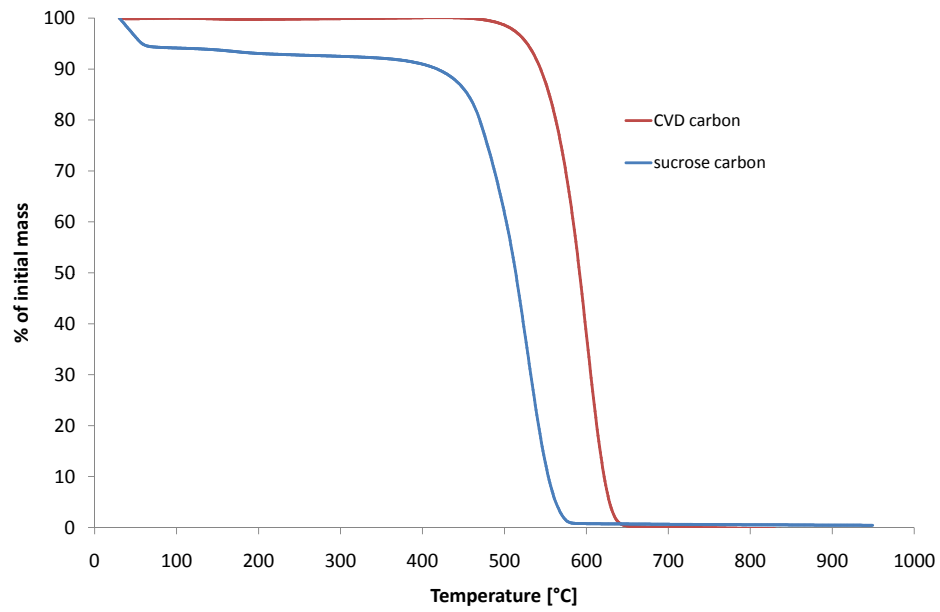


Figure 2.42: Thermogravimetric analysis of the CVD and sucrose carbon replica while heated in pure oxygen.

reasons that ceramics with low specific surface area are obtained from carbon template approaches. Both templates can be eliminated at 500°C. In section 2.3.2.4 on page 103 we will compare the ceramics obtained by the replication of these two carbon templates.

Summary: templates. In total, five different templates can be used for the replication with hydroxyapatite. The following table gathers their main characteristics:

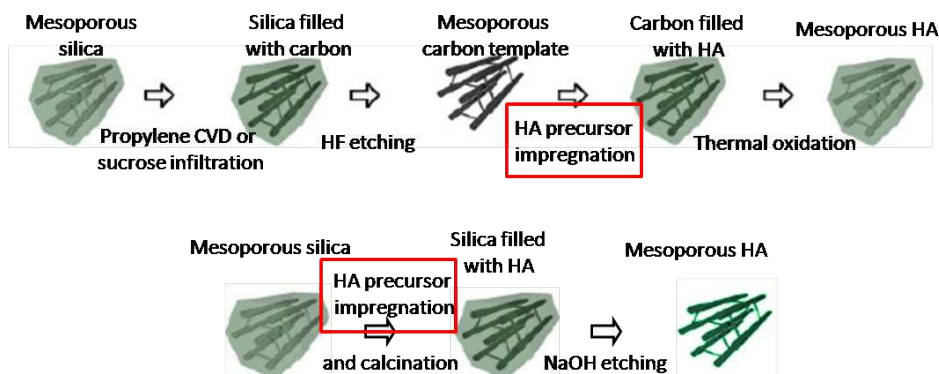
Template	S_{BET} [m ² /g]	pore shape	\varnothing_p	V_p [cm ³ /g]	V_{micro} [cm ³ /g]	V_{meso} [cm ³ /g]
Silica						
SBA-15	600	hexagonally arrange tubular pores, interconnected by smaller mesopores or micropores	8	1.2	0.3	0.9
MCF	690	spherical mesopores in close packing, with large windows	11	2.1	0.3	1.8
Carbon						
SBA-15 CVD replica	720	tubular mesopores	7	0.9		
MCF CVD replica "CVD"	700	spherical, irregular mesopores	11	0.6	0.1	0.5
MCF sucrose replica "CS"	740	irregular mesopores and micropores	4	0.6	0.3	0.3

Table 2.10: Main characteristics of the different mesoporous templates.

In addition to the textural properties that are represented in this table, the surface chemistry of the template plays a key role for the infiltration with aqueous hydroxyapatite precursors: in general, we can assume that the silica and the sucrose carbon have a hydrophilic surface chemistry, respectively with silanol and carboxylic acid groups at the surfaces. The carbon template obtained by CVD on the other hand is hydrophobic, and has only little surface functionalization.

In the following section, we will investigate different precursors and techniques for the synthesis of mesoporous hydroxyapatite starting from the templates that we just introduced.

2.3.2 Infiltration with hydroxyapatite



In the following, we will discuss the different steps of the infiltration and their effect on the final product. This chapter will show a comparison of hydroxyapatite samples obtained from different synthesis methods. A comprehensive list of the samples prepared during the work on this thesis can be found in section 5.4 on page 177.

The first part will deal with the choice of a precursor system that is compatible with both templates.

2.3.2.1 Influence of the HA precursor

$\text{Ca}(\text{NO}_3)_2 \cdot 4 \text{H}_2\text{O}$ and $(\text{EtO})_3\text{P}$ The synthesis was initially adapted from [147]. In a first experiment, the amount of water was chosen to be 13-fold in excess of the phosphite. The amount of water needed to dissolve the calcium nitrate was not given in the original paper and was chosen to be the same volume as for the phosphite hydrolysis. In total, precursors for 3.72 g HA were infiltrated into 0.5 g silica template. This corresponds to 8.75 g of calcium nitrate and 3.7 mL of phosphite. Considering the pore volume of the silica ($2.02 \text{ cm}^3/\text{g}$) and the theoretical density of HA ($3.8 \text{ g}/\text{cm}^3$) this amount is sufficient to fill half of the porosity of the template if the reaction is complete.

Figure 2.43 shows the wide angle X-ray diffractogram of the product after the template has been removed. Overall, the product is poorly crystalline. Most of the peaks can be attributed to a crystalline hydroxyapatite phase. The product however contains an additional calcium silicate phase that derives from a reaction between the template with the calcium precursor. These observations are in good agreement with the paper published by Liu et al. [147] : the authors observed the formation of HA without by-phases if the sol was aged at room temperature for more than 500 minutes. As they worked without a template, they did not observe a silicate phase. The broad peaks can be attributed to small crystallites; Scherrer calculations indicate between 8 and 17 nm in diameter. This is above the values expected from the size of the silica pores, which are only 14 nm in diameter. Crystallites with 17 nm in diameter cannot be contained in 14 nm porosity; at least some particles must have formed on the outside of the silica pores.

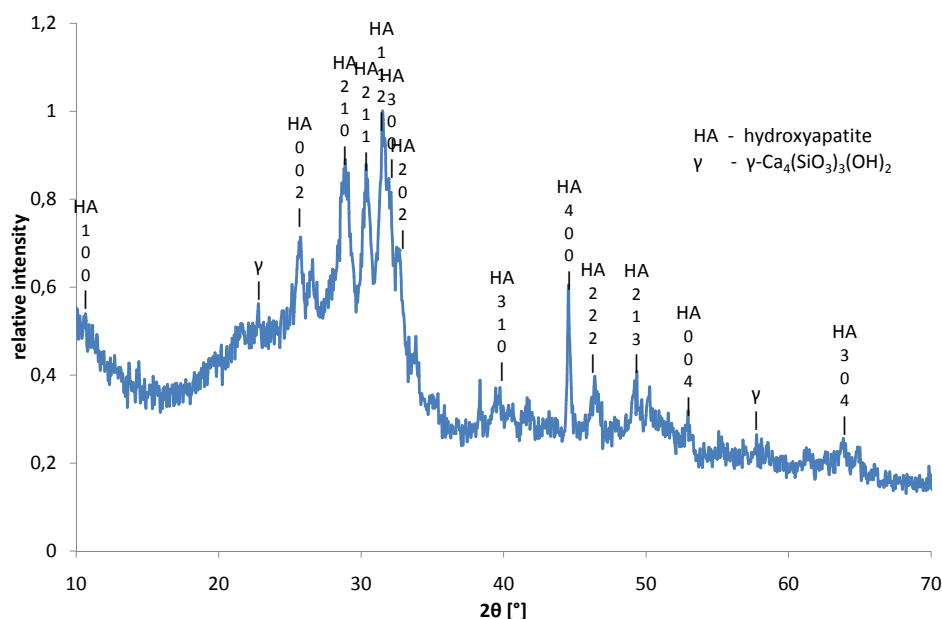


Figure 2.43: Wide angle X-ray diffraction pattern for silica templated hydroxyapatite synthesized from $\text{Ca}(\text{NO}_3)_2 \cdot 4\text{H}_2\text{O}$ and $(\text{EtO})_3\text{PO}$, calcined at 600°C . After template removal.

The reaction of calcium nitrate and pre-hydrolyzed triethyl phosphite is fast. It is conceivable that the reaction occurs so rapidly that the crystallizing product immediately blocks the pore entries of the template and prevents any further penetration of the porosity.

Organometallic precursors offer the possibility of controlled hydrolysis and can be reacted slowly, leaving enough time for the penetration of the porosity. It is advantageous to use a method that does not involve solvent or only little solvent: Solvents occupy a large part of the porosity of the template. This dead volume effect prevents the pores from being filled completely with the desired product.

CAT and $(\text{BuO})_3\text{P}$ The CAT precursor can be sublimated at moderate temperatures and used for MOCVD synthesis. But it can also be used for liquid infiltration as it melts at low temperature (about 40°C). In order to follow the infiltration of the molten complex into the porosity, thermogravimetric analysis was performed. The evaporation temperature of the calcium complex decreased from 310°C to 215°C , showing that the complex has penetrated the porosity: the interactions with the pore walls are unfavorable, making the evaporation energetically beneficial at lower temperatures.

Table 2.11 shows EDX results for the product after infiltration of the phosphate precursor. In addition to the carbon, oxygen, calcium and phosphorus that is expected in the sample, we found fluorine, non-negligible amounts of iron, manganese and other heavy metals. The fluorine is fixed on the carbon template surface and derives from the silica dissolution step in the synthesis. The metals come from the wall of the autoclave

Element	Atomic %	Attributed to
C	75.62	carbon template
O	18.49	
F	1.75	
P	2.09	calcium phosphate Ca/P=0.69
Ca	1.40	
Cr	0.04	autoclave
Mn	0.18	
Fe	0.35	
Cu	0.01	
Au	0.03	
Ni	0.04	

Table 2.11: EDX results for the carbon template infiltrated with CAT and $(\text{BuO})_3\text{P}$ before the removal of the template. All values are means over three measurements.

in which the reaction was carried out. The presence of heavy metals is particularly disturbing because these elements are toxic.

The low Ca/P ratio of 0.69⁷ shows that the calcium complex has not reacted with the phosphate precursor to form the desired calcium phosphates. It is possible that the phosphorus precursor has not reached the calcium complex trapped in the porosity of the template or that the calcium complex evaporated instead of reacting with the phosphorus.

⁷The expected value for HA is 1.67

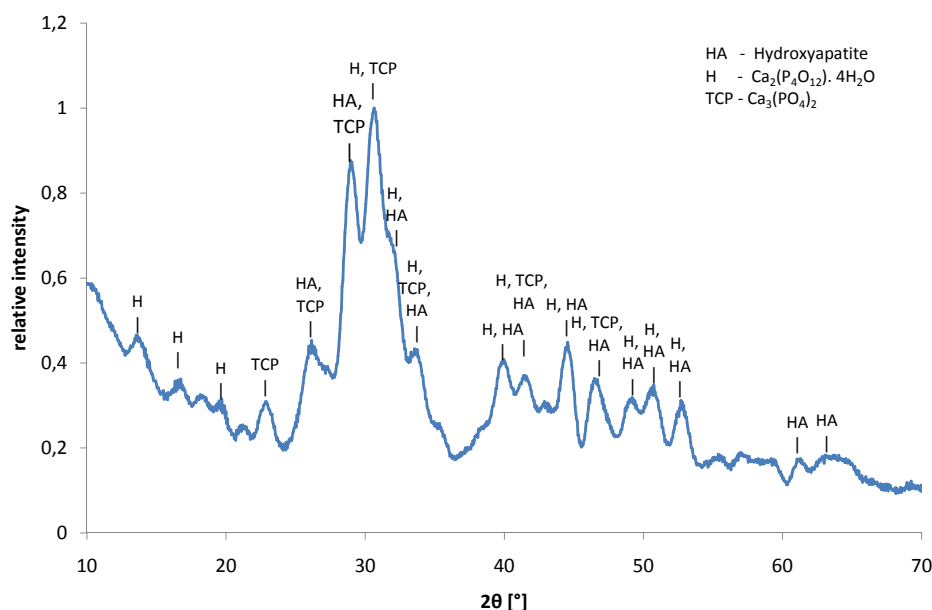


Figure 2.44: XRD pattern for the HA prepared from ethanolic solutions of $\text{Ca}(\text{NO}_3)_2 \cdot 4\text{H}_2\text{O}$ and $(\text{NH}_4)_2\text{HPO}_4$.

Ethanol-based sol: $\text{Ca}(\text{NO}_3)_2 \cdot 4\text{H}_2\text{O}$ and $(\text{NH}_4)_2\text{HPO}_4$. This synthesis was reproduced from [143] without a template. The results of X-ray diffraction of the powder obtained are shown in figure 2.44. Even if the product was not calcined, it shows a certain crystallinity. The mean crystallite size is between 9 and 17 nm. Not all the peaks could be attributed to hydroxyapatite; the product additionally contains calcium phosphate hydrate and tricalcium phosphate. It is possible that these secondary phases disappear when the powder is heat treated. *The main drawback of this method is however the high dilution of the precursors. In the case of the templating synthesis, this dilution would lead to a strong dead volume effect, preventing high pore filling.*

Solvent-free synthesis: $\text{Ca}(\text{OEt})_2$, $(\text{BuO})_3\text{PO}$ or $(\text{EtO})_3\text{PO}$. The synthesis was adopted from [142]. When the precursors are mixed under protective atmosphere, ethanol has to be added in order to obtain a mixture that can be stirred and in order to allow the infiltration into the template. During the reaction, the orange color of the calcium ethoxide remains. After calcination, the product is white. Table 2.12 shows results of EDX measurements of the sample after calcination. Unfortunately, the phosphorus content is very low. This shows that the precursors have not reacted and that no calcium phosphate has been formed.

Transmission electron micrographs (see figure 2.45) show an interesting structure resembling crushed paper sheets. These structure is not a replication of the silica porosity as the sheets are much bigger than the silica pores. This evidences that no templating effect occurred and that the template is consumed during the synthesis.

The synthesis was repeated with triethyl phosphite as P precursor without a template.

Element	Atomic %
C	30.65
O	51.01
Na	2.16
Si	9.2
P	0.06
Ca	6.85

Table 2.12: EDX results after calcination and template removal of solvent-free synthesis of HA. Values are averaged over five measurements.

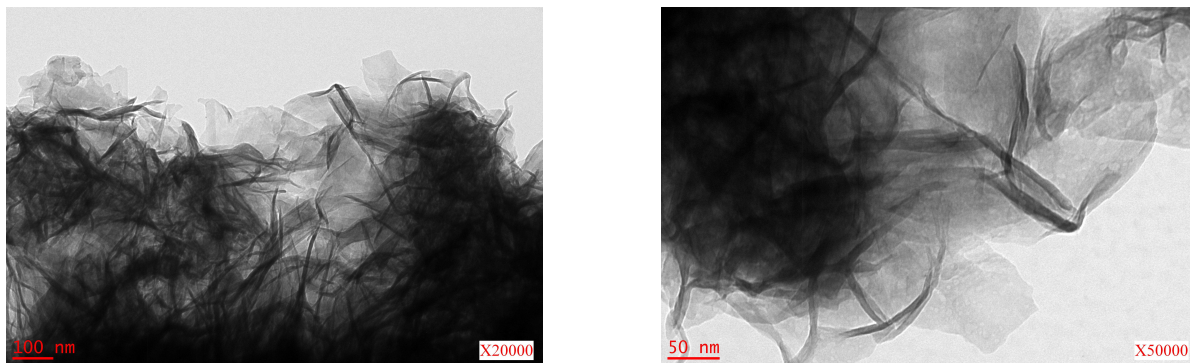


Figure 2.45: Transmission electron micrographs of the product obtained from solvent-free synthesis after calcination and template removal.

The observation were the same, the orange color of the calcium ethoxide remains during the reaction. After calcination, a white powder is obtained. EDX spectra again show a low phosphorus content and a Ca/P ratio of 16.2 on average (four measurements). This underlines that even triethyl phosphite does not react under the chosen conditions.

Calcium metaphosphates. For the previously described syntheses, pore filling was the main issue: As the infiltration of the porosity is incomplete, the grains lack structural cohesion once the template is removed. This way, three-dimensional porosity was not preserved, individual nanoparticles are obtained. A polymeric precursor would allow the connection between several pores and ensure the formation of a three-dimensional network. Metaphosphates, $(\text{PO}_3)_n$, are naturally occurring polymers with polyphosphate chains. Soluble polyphosphates have been used extensively as additive in detergents for dishes and laundry to trap Ca^{2+} ions that are part of the water hardness. The reaction between metaphosphates and alkaline earth metal ions is spontaneous and occurs at room temperature [148]. The infiltration of metaphosphate into the porosity of silica or carbon templates might be a new method for the synthesis of porous HA.

Mixing saturated $\text{Na}(\text{PO}_3)_n$ -solution with $\text{Ca}(\text{NO}_3)_2 \cdot 4 \text{H}_2\text{O}$ -solution results in a gelatinous precipitate. After drying, the product is brittle, translucent and of glass-like aspect. After calcination, white powders are obtained. As the calcination temperature is crucial for the transformation of the calcium metaphosphate into hydroxyapatite, we will discuss the results of this synthesis method in the section 2.3.3 on page 108.

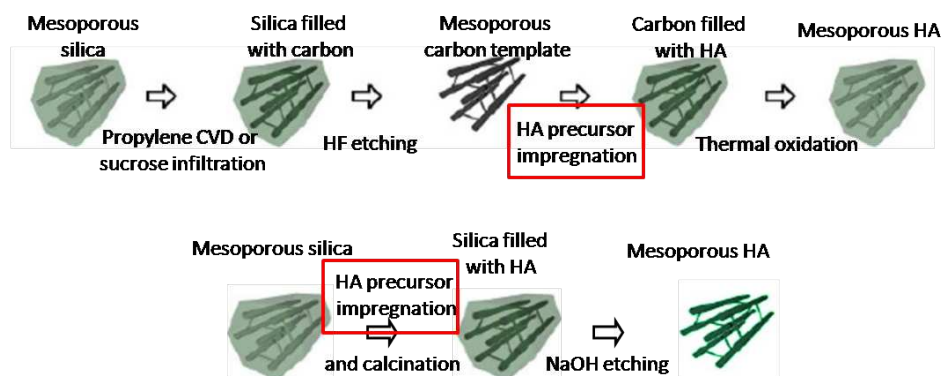
Summary: hydroxyapatite precursors. In total, five precursor combinations have been tested. All but one have several drawbacks that are summarized in table 2.13:

Precursor	Observations
$\text{Ca}(\text{NO}_3)_2 + (\text{EtO})_3\text{P}$	essentially HA, little or no silicon by-phases
$\text{CAT} + (\text{BuO})_3\text{P}$	heavy metal contamination from the autoclave, incomplete reaction (Ca/P ratio: 0.69)
$\text{Ca}(\text{NO}_3)_2 + (\text{NH}_4)_2\text{HPO}_4$ in ethanol	product contains byproducts, high dilution required
$\text{Ca}(\text{OEt})_2 + (\text{BuO})_3\text{PO}$	no reaction, maybe due to humidity
$\text{Ca}(\text{OEt})_2 + (\text{EtO})_3\text{PO}$	
$\text{Ca}(\text{NO}_3)_2 + (\text{NaPO}_3)_n$	reacts with the silica template

Table 2.13: The most important observations related to the choice of the HA precursor

The most suitable precursor is the combination of calcium nitrate with triethyl phosphite. This combination allows to work in high concentration and can be combined with the silica template without giving too much by-products. For most of the following experiments, this combination of precursors was used.

2.3.2.2 Influence of the infiltration process



Besides the nature of the precursors and the templates, the concentration of the precursor solutions and the volume of solvent infiltrated into the pores play an important role on the replication of porosity. The infiltration under reduced pressure is thought to allow better infiltration into the porosity of the template as well. Starting from the same precursor combination ($\text{Ca}(\text{NO}_3)_2 \cdot 4\text{H}_2\text{O}$ and $(\text{EtO})_3\text{P}$), different infiltration conditions were tested:

- diluted solutions
- concentrated solutions
- infiltration under atmospheric pressure and under vacuum
- multiple infiltrations

Diluted and concentrated solutions in MCF silica. For the infiltration with calcium nitrate ($\text{Ca}(\text{NO}_3)_2 \cdot 4\text{H}_2\text{O}$) and triethyl phosphite ($(\text{EtO})_3\text{P}$), two infiltration ways are tested. In the first approach (“diluted solution”), the amount of water was chosen to be 13 times the stoichiometric amount of the phosphite. For the calcium nitrate, about three times this volume is used for the dissolution. In total, the precursor amount is sufficient to fill half of the porosity of the silica template. These amounts have been adapted directly from the reference [147]. In the second approach (“concentrated solution”) a minimum amount of water is used to dissolve the calcium nitrate. The phosphite is hydrolyzed with 1/8 molar equivalent of water. The total amount of precursor is chosen so that the template porosity can be filled completely with the HA, assuming a yield of 80% during synthesis and calcination. Table 2.14 shows an example for the amounts of precursor for both methods in a template presenting 1 mL pore volume.

Figure 2.46 shows transmission electron micrographs for both approaches of the template filled with HA precursor and the HA remaining once the template is dissolved. In the case of the diluted solution approach, the template porosity is not completely filled, as shown on figure 2.46a. The porosity of the silica is still visible, and the HA

	diluted solution	concentrated solution
m_{HA} aimed [g]	1.6	3.2
$\text{Ca}(\text{NO}_3)_2 \cdot 4\text{H}_2\text{O}$ [g]	4.7	9.4
H_2O [mL]	10	8
$(\text{EtO})_3\text{PO}$ [g]	2.17	4.34
H_2O	3 mL	50 μL

Table 2.14: Amounts of precursor used for the filling of 1 mL pore volume in the case of “diluted solution” and “concentrated solution” approach.

has only coated the template pore wall. Consequently, upon template removal, the HA shows a high porosity. The unfilled porosity of the silica adds to the porosity that is formed when the silica walls are dissolved. Figure 2.36 on page 71 shows the formation mechanism. It has to be noted however that the foam-like structure - that is shown in the image of the HA after template removal - does not correspond to the same length scale as the silica pores. Whereas the silica pores measure about 15 nm in diameter, the pores formed in the HA are in the range of several dozens of nanometers. Consequently, there is no direct templating effect.

In the case of concentrated solutions, the template is completely filled and enclosed by the HA. On the transmission electron micrograph represented on figure 2.46c, the two phases (silica and HA) are indistinguishable, and no porosity is apparent. After template removal, the product is composed of strongly agglomerated nanoparticles several dozens of nanometers in length. Again, a templating effect could not be visualized.

We followed the filling of the template porosity by nitrogen physisorption experiments as well. Figure 2.47 shows isotherms of the template, the silica/HA composite and the HA resulting after template removal for both approaches. The isotherm of the template has been described in detail previously. In the case of the infiltration with the diluted solution, the isotherm obtained for the composite has the same shape as for the template. The surface area is reduced from 743 to 538 m^2/g and the pore volume has decreased from 2.33 to 1.93 cm^3/g . The pore size distribution remains monomodal, but the mean pore size is shifted towards higher values. This shows, along with the unchanged isotherm shape, that only little HA is deposited inside the porosity. At least a part of the HA has formed outside the pores of the template and has formed pores that exceed the size of the silica pores. After template removal, a type IV isotherm is obtained. This indicates that the HA contains real mesoporosity. The surface area is 105 m^2/g . The pore size distribution is monomodal and indicates large pores with diameters around 17 nm. These large pores exceed the pore size of the silica template, showing the ceramic has formed outside the porosity and has formed porous structures that are bigger than the template pores.

In the case of the concentrated solution approach, the composite isotherm shows a large hysteresis, indicating incomplete filling of the pores: At high relative pressures, the hysteresis shows an early onset, indicating that the biggest pores have been (partially) filled. The pore size distribution is monomodal and shifted towards smaller values

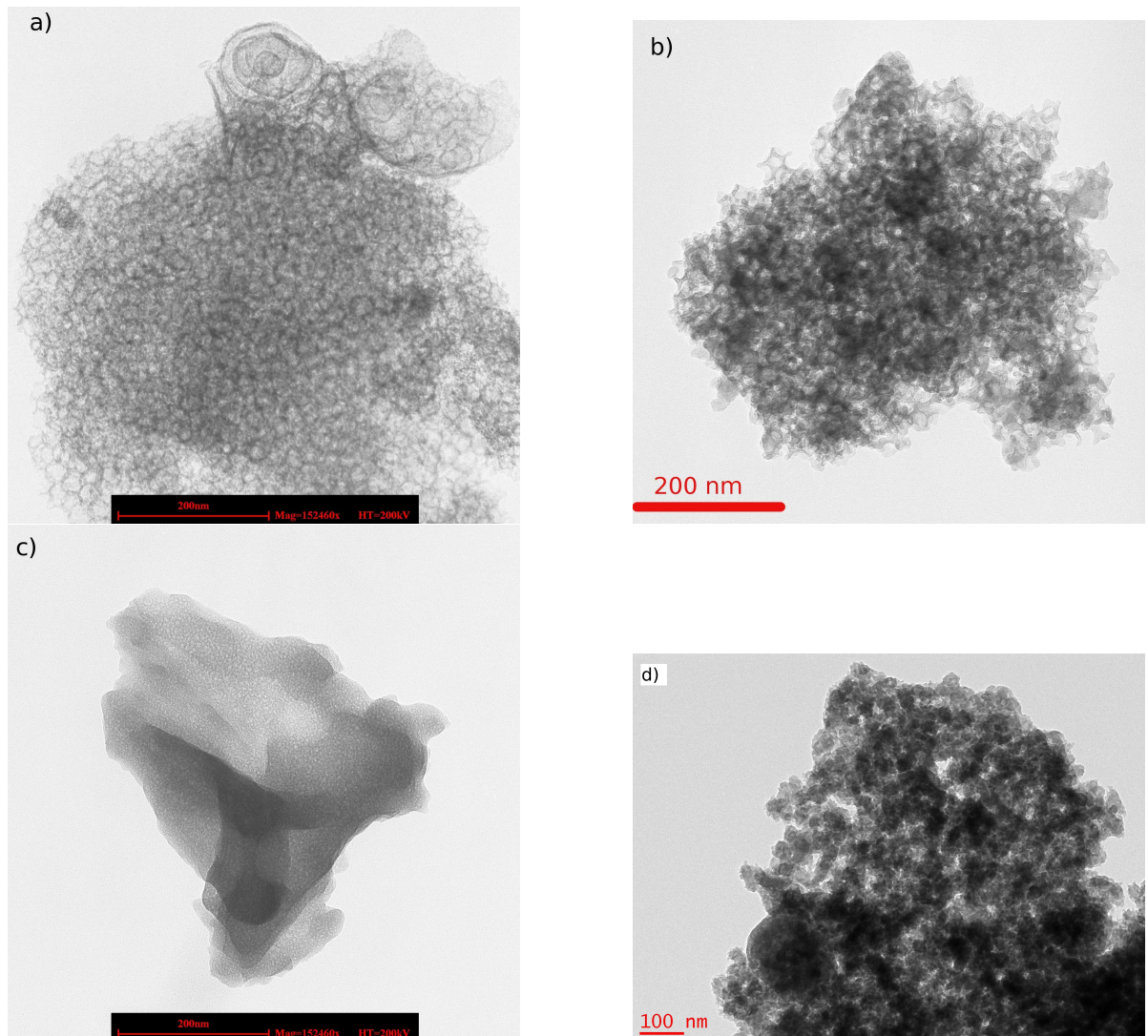


Figure 2.46: Transmission electron micrographs of the composite silica/HA and the HA after template removal for both the diluted and concentrated solution approach: a) composite obtained from diluted solution, b) HA obtained from diluted solution, c) composite obtained from concentrated solution, d) HA obtained from concentrated solution

compared to the template alone. This supports the hypothesis that the silica pores are partially filled. This leads to the appearance of smaller pores of various sizes, which are responsible for the large hysteresis range and the early onset of the hysteresis. The surface area is reduced to $8.4 \text{ m}^2/\text{g}$, indicating pore filling and blocking by the ceramic phase.

Once the template is removed, the isotherm is of type II and shows a H3 hysteresis. It seems that the product is mesoporous, but its surface area is lower than for the diluted solution approach: $87.5 \text{ m}^2/\text{g}$. The pore size distribution is very large, combining a small peak at low pore diameters – obtained from the dissolution of the silica walls – with larger pores. The larger pores correspond to partially filled pores from the template and to textural porosity between the ceramic particles.

The concentrated solution approach leads to ceramics with a lower surface area and less porosity, but the mass of HA that can be obtained from the same amount of template is twice the amount that can be obtained by using diluted solutions. The low amount of HA deposited by the diluted solution leads to decreased yields in HA from the same template mass (see table 2.14).

Infiltration under atmospheric pressure or in vacuum. The infiltration of mesoporous materials is often done in vacuum, assuming that the precursor penetrates the porosity more easily if the air that fills the porosity in the pristine state is evacuated. It is expected that the empty pores suck in the precursor solution by capillary effects. MCF silica template are impregnated with calcium nitrate and triethyl phosphite both in vacuum and in atmospheric pressure. The method chosen for these experiments is the diluted solution approach.

Figure 2.48 shows the nitrogen physisorption isotherm of the silica template after the filling with HA precursor in atmospheric pressure and under vacuum. For comparison, the isotherm of the template is included. From the isotherms, it seems that the infiltration in atmospheric pressure is more successful: the hysteresis range has decreased, indicating partial pore filling. The monomodal pore size distribution that has been observed for the template remains monomodal but the maximum is shifted from about 11.5 nm to 10.4 nm . The isotherm of the vacuum-infiltrated composite on the other hand seems not to have changed compared to the template. A closer look at the specific surface areas shows however that the initial surface area of $741 \text{ m}^2/\text{g}$ has decreased in the two cases: 465 in the case of vacuum infiltration and $538 \text{ m}^2/\text{g}$ for the infiltration in atmospheric pressure. As expected, the vacuum infiltration leads to a lower surface area, indicating a better infiltration into the porosity. The same trend is observed for the pore volumes, which decrease from 2.07 (template) to 1.9 in atmospheric pressure conditions and to $1.57 \text{ cm}^3/\text{g}$ under vacuum. The pore size distribution for the composite obtained by vacuum infiltration is shifted towards higher pore sizes. This indicates that a certain amount of HA has formed outside the pores of the template and arranged in porous structures with bigger pores.

In the case of the vacuum infiltration, the quantity of product retrieved after template removal was insufficient to allow nitrogen physisorption. The results obtained for

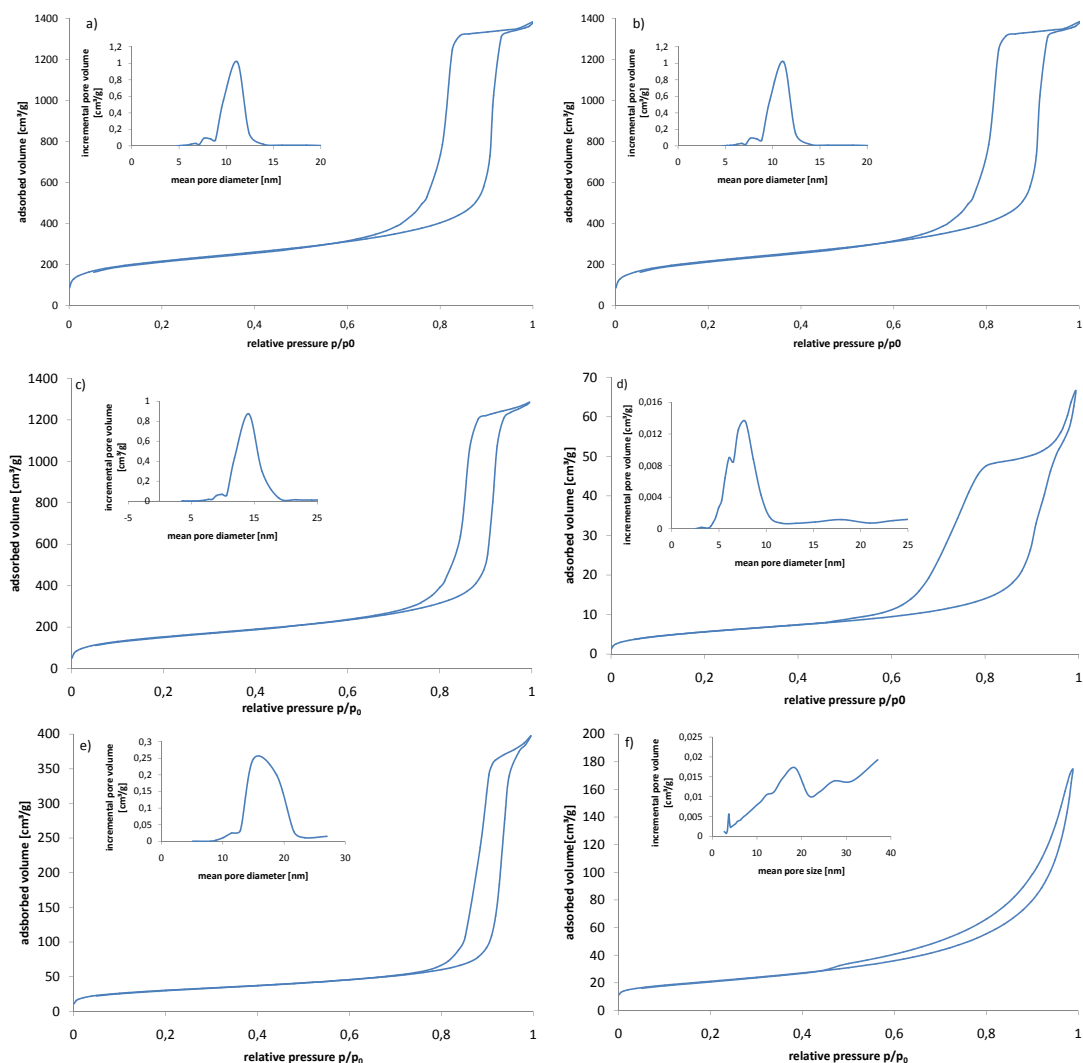


Figure 2.47: Nitrogen physisorption isotherms of the three steps of infiltration: template (top), composite material comprising the HA filled silica template (middle) and the HA obtained after template removal (bottom). Silica MCF template (a) and (b), composite obtained with diluted (c) and concentrated solution (d), HA obtained from concentrated (e) and from diluted solution (f).

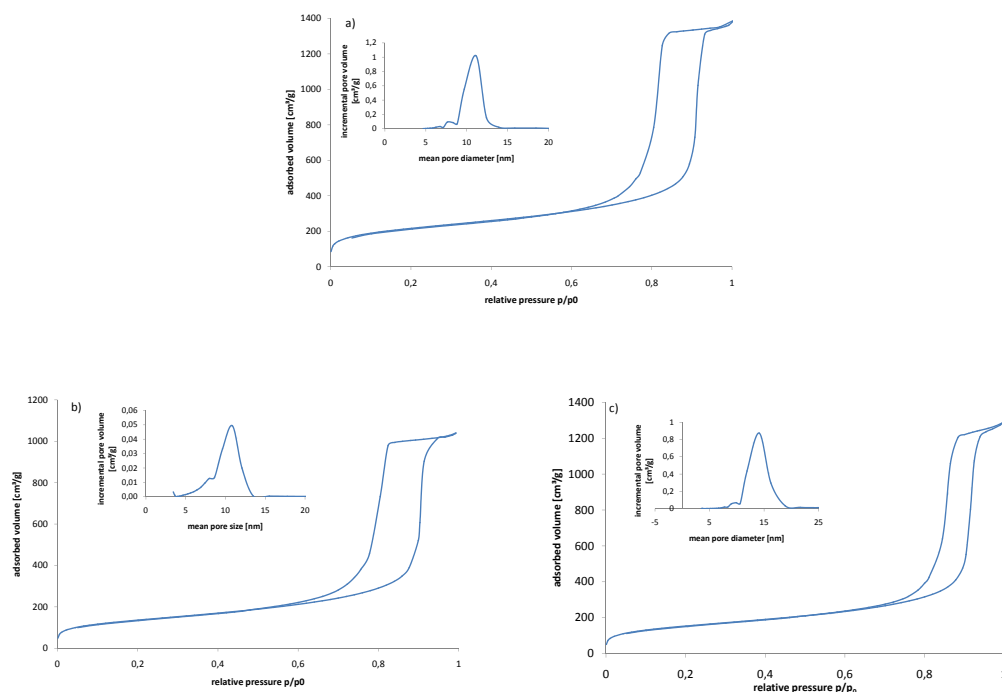


Figure 2.48: Nitrogen physisorption isotherms for the silica template (a) and the composite obtained after infiltration with the diluted solution approach under vacuum (b) and in atmospheric pressure (c). The inserts show the pore size distributions derived from the physisorption data.

the composite are nevertheless meaningful even without this result: *in the case of diluted solutions, the infiltration under vacuum improves the pore filling and therefore the replication of the template porosity.*

Multiple infiltrations. Every time a liquid sol is infiltrated into the porosity of a template, the porosity is filled with the precursor (that gives rise to the desired product) and the solvent. During drying and eventually during calcination, the volume occupied by the solvent is liberated again, resulting in incomplete pore filling. Incomplete pore filling is one of the reasons for imperfect replication of the porosity of the templates. The pore filling can be improved when infiltration steps are repeated.

A systematic study of multiple infiltrations was carried out both for MCF silica templates and for their carbon replicas. The method adopted was the diluted solution approach. 0.5 g of template are infiltrated with 6 mL HA sol, then filtered and dried. The infiltration and drying are repeated twice. In the case of silica templates, the composite is calcined at 500°C for 4 h. In the case of carbon templates, the composite is first calcined at 500°C for 1 h in air, then the carbon is burned completely at 750°C for 1 h. The silica template is dissolved by a NaOH treatment. Samples are prepared with

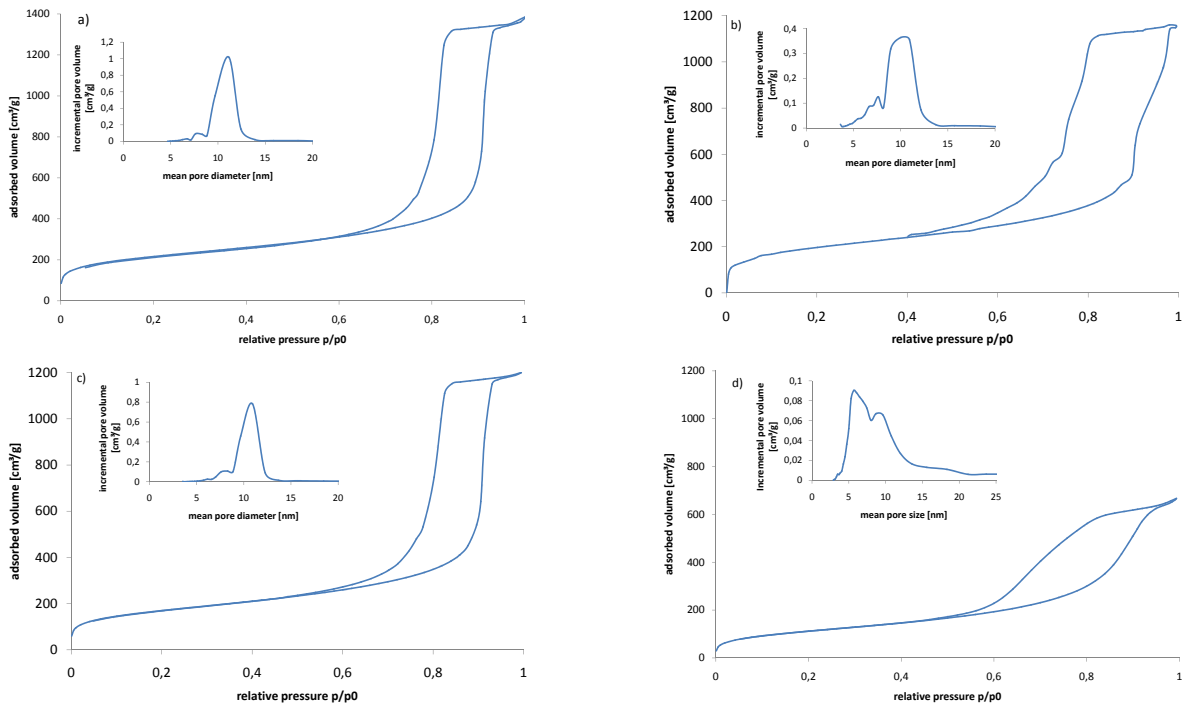


Figure 2.49: Nitrogen physisorption isotherms for the multiple infiltration series on MCF silica: the template before filling (a), filled once (b), twice (c) and three times (d) successively.

single, double and triple infiltration.

Figure 2.49 shows nitrogen physisorption isotherms of the silica template and the three composite materials. The inserts correspond to the pore size distribution calculated from the physisorption data. Figure 2.50 shows the same isotherms and pore size distributions for the carbon series. Table 2.15 summarizes the values for surface area and pore volume of the templates and the composites. In the case of the silica template, the shape of the isotherm changes more strongly than for the carbon template. After the first filling step, the isotherm (type IV with H1 hysteresis for the silica template) shows a wider hysteresis. The smaller pores evidenced by this observation are due to incomplete pore filling. The surface area and the pore volume decrease from 741 to 694 m²/g and from 2.1 to 1.8 cm³/g respectively. After the second infiltration step, the pore volume is not affected. The isotherm resembles the isotherm of the template, but the surface area has again decreased and is now 594 m²/g. The hysteresis range has shrunk indicating a narrower pore size distribution than after the first infiltration step. After the third infiltration step, the isotherm shape has changed considerably and now features a large range hysteresis with a sloping adsorption and desorption branch (H3). This hysteresis shape is an indication for a change in the pore morphology: the pores are now narrower and of different sizes. The pore volume has decreased to 1.0 cm³/g. Comparing the pore size distributions, we observe that the mean pore diameter shifts towards lower value during the filling process, indicating successive pore filling. In the final composite, the

Infiltrations	S_{BET} [m^2/g]	V_p [cm^3/g]
Silica series		
template	741.0	2.1
1	694	1.8
2	594	1.0
3	406	0.9
Carbon series		
template	494	0.75
1	403	0.74
2	354	0.69
3	383	0.64

Table 2.15: Surface area and pore volume after multiple infiltrations into silica and carbon templates.

pore size distribution is bimodal and dominated by small pores that are about 7 nm in diameter. We believe that they are obtained by partial filling of the porosity of the template. On the other hand, larger pores have appeared that are bigger than the original porosity of the template. From these isotherms, we can conclude that the pores of the template have not been filled completely even after three successive infiltrations. The isotherms are still dominated by the porosity of the template.

In the case of the carbon templates, the isotherm shape remains the same throughout the filling process. It has been described in detail in a previous section. The pore size distribution of the template is bimodal, with small pores that are derived from the dissolution of the silica template and large pores in between the carbon particles. The surface area however decreases from 494 to 404 m^2/g after the first infiltration and to 355 m^2/g after the second filling step. Curiously, the surface area increases again with the third infiltration step (383 m^2/g), probably due to the formation of pores inside the deposited HA. The pore volume however decrease steadily ($0.75 \rightarrow 0.74 \rightarrow 0.69 \rightarrow 0.64 \text{ cm}^3/\text{g}$), indicating progressive filling of the porosity of the templates. As in the case of silica, three deposition steps are not sufficient to complete the pore filling. The pore size distributions of the composites resemble one another throughout the filling process: they are bimodal with a sharp peak at below 5 nm and a larger peak centered around 12 nm.

The study of the isotherms shows that even with three infiltrations, the diluted solution approach does not fill the porosity of the templates. Figure 2.51 shows transmission electron micrographs of the templates after the third filling step. It is interesting to compare the carbon and the silica template: Whereas in the case of the carbon template the HA has formed outside the porosity, the silica template seems to allow the growth of HA inside its porosity. There is however some exocrystallization (shown in the upper right corner of the image) in the case of silica templating, too.

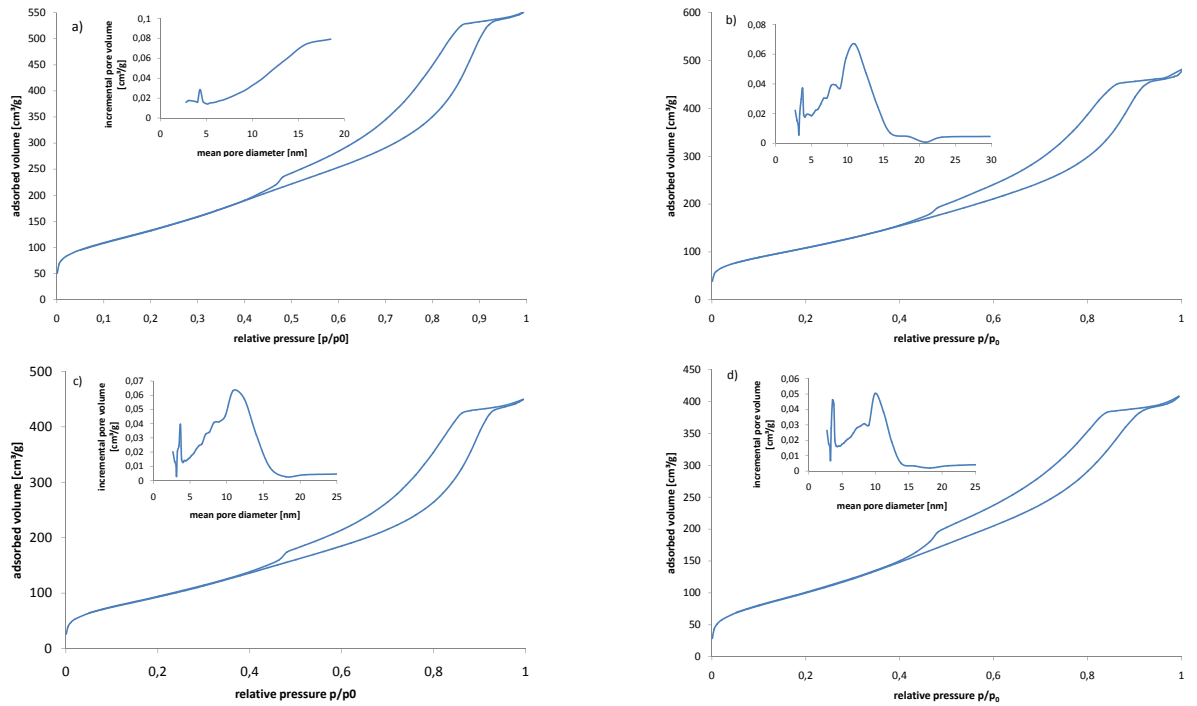


Figure 2.50: Nitrogen physisorption isotherms for the multiple infiltration series on carbon foam: the template before filling (a), filled once (b), twice (c) and three times (d) successively.

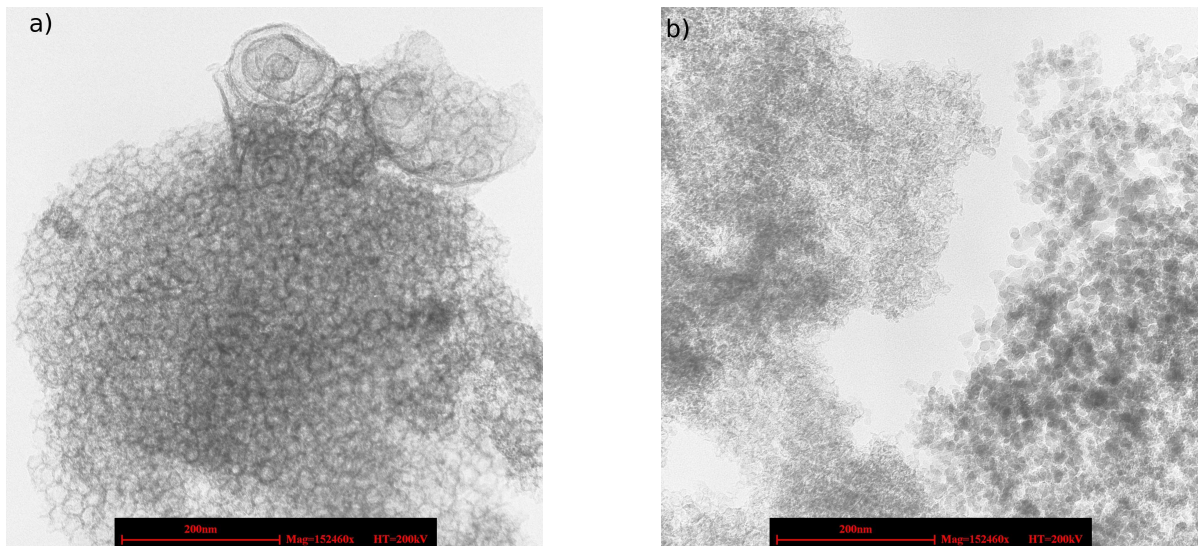


Figure 2.51: Transmission electron micrographs of the silica (a) and the carbon (b) template filled with HA in three successive steps.

After dissolution of the template, the obtained HA ceramics have similar characteristics to the ones obtained by the diluted solution approach after a single infiltration. It seems plausible that a part of the HA deposited in the first steps is redissolved during the following dissolutions, resulting in reduced effectiveness of the multiple infiltrations. The nitrogen physisorption isotherms indicate however that the porosity is progressively filled.

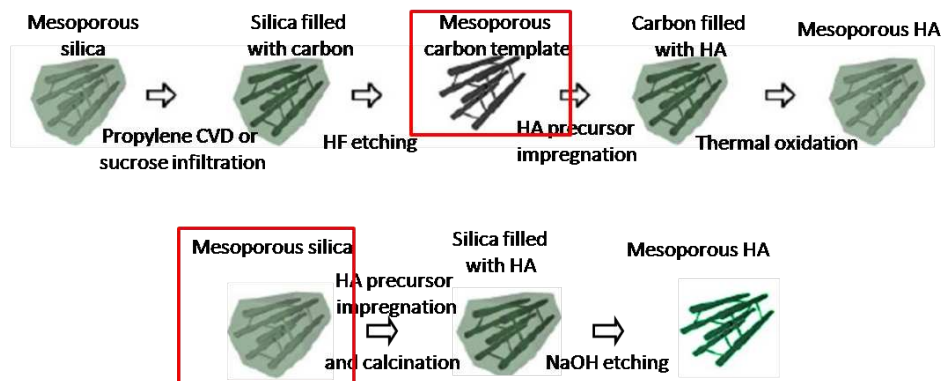
Summary: infiltration process The infiltration conditions can change the resulting ceramic considerably by allowing better or worse filling of the porosity of the template. Table 2.16 summarizes the observations that we made by varying the infiltration parameters.

The best conditions for the infiltration are the combination of concentrated solutions with vacuum. The use of concentrated precursor solutions represents a compromise between reasonable yields in hydroxyapatite from a given amount of template and a lower pore volume of the final ceramic.

Parameter	Observed effect
dilution of the precursors	Using a concentrated solution for the infiltration leads to higher yields in hydroxyapatite, but the ceramic is less porous and has a smaller specific surface area
infiltration under vacuum	better pore filling
multiple infiltrations with diluted solutions	Multiple infiltrations lead to a progressive filling of the porosity of the template, but are less effective than a single infiltration with concentrated solutions.

Table 2.16: Effects of the different infiltration parameters.

2.3.2.3 Evolution of the properties of the product with the size and the shape of the pores of the template



The aim of this section is to compare different templates that share the same surface chemistry, but have different pore sizes. For this purpose, two mesoporous and one macroporous silica templates have been compared.

SBA-15 and MCF are mesoporous silica templates prepared by the condensation of TEOS in the presence of surfactants. SBA-15 has tubular mesopores about 7.5 nm in diameter with small interconnecting channels in the micropore range. The aspect ratio⁸ of the tubes is about 10^4 . In contrast, MCF has spherical pores with large interconnections. The pore diameter is in the range of 9 to 15 nm, the aspect ratio is 1. Figure 2.52 compares TEM images of both mesoporous silicas, showing the different pore morphologies.

Silica sphere opals have the same chemistry as the mesoporous silica templates, but their porosity is not in the same range. The template is composed of silica spheres which are about 300 nm in diameter. Figure 2.53 shows scanning electron micrographs of the silica opal at different scales. It has to be noted that the length scale is higher than for

$$^8\text{aspect ratio} = \frac{\text{pore length}}{\text{pore diameter}}$$

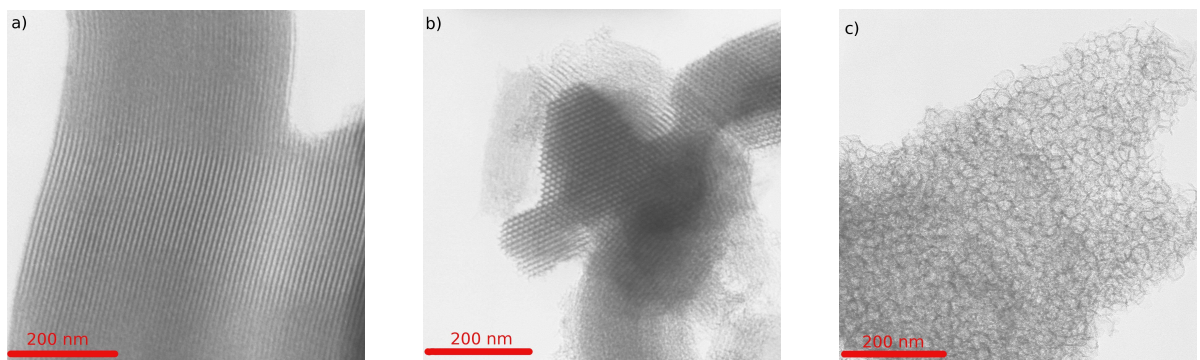


Figure 2.52: Transmission electron micrographs of the two mesoporous silica templates: SBA-15 with channels (a) and channel entries (b) and MCF (c).

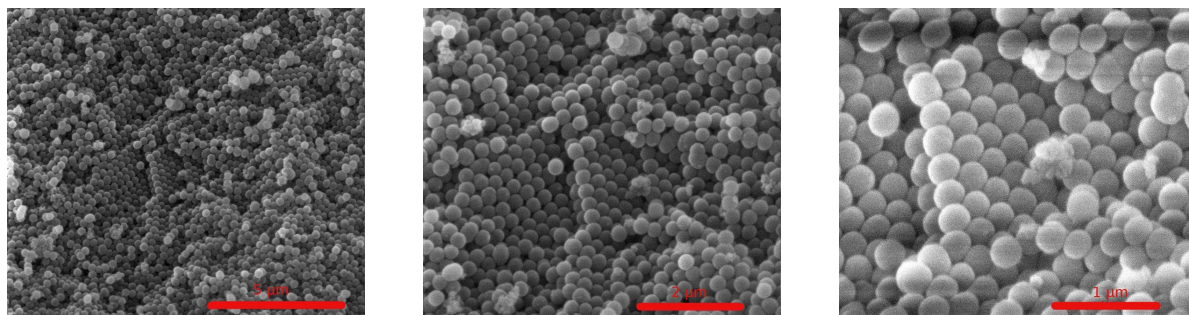


Figure 2.53: Scanning electron micrographs of the silica opal at different magnifications. The product was graciously provided by Dr. Rehspringer of IPCMS Strasbourg.

the TEM images.

The infiltrations were carried out with the $\text{Ca}(\text{NO}_3)_2 \cdot 4\text{H}_2\text{O}$ and $(\text{EtO})_3\text{PO}$ method in concentrated solutions.

Figure 2.54 shows transmission electron micrographs of the HA ceramics synthesized in the different silica templates after the template has been removed. The HA ceramic obtained by SBA-15 templating is highly porous. On the other hand, this porosity is not a replication of the porosity of the template. The pores are clearly larger than the pore size of the silica: the pores are in the mesopore range at the limit to macropores - about 50 nm in diameter - while the expected porosity was in the low mesopore range (about 4 nm).

For the ceramic templated by MCF silica, a similar observation is made: the product is composed of strongly agglomerated nanoparticles. The size of the nanoparticles is in the range of several dozens of nanometers. Here too, a direct relationship with the template porosity is not evidenced, the pore size of the silica (about 12 nm) is largely exceeded. The product is nevertheless highly porous.

The ceramic templated by the silica opal is a real replication of the opal structure: the HA has formed around the silica spheres and clearly shows the imprints of the spheres that have been dissolved. The porosity is in the range of the silica particles (300 nm) and the long range order of the spheres is preserved in the replication. This is illustrated even better by figure 2.55, which shows transmission electron micrographs of sections of the opal templated HA. For comparison, MCF templated HA was prepared in the same way. The resulting pictures are shown in the same figure. It is clearly visible that both ceramics are composed of similar nanoparticles but arranged differently: in the case of the MCF replication, the particles are randomly agglomerated. In the case of the replication of the silica opal, the nanoparticles have formed around the silica spheres and show spherical voids where the silica has been dissolved.

For all templates, nitrogen physisorption isotherms were taken of the ceramic after the template was dissolved by NaOH etching. The isotherms are shown in figure 2.56. The inserts show the pore size distributions. The multimodal pore size distributions for the products obtained from SBA-15 and from MCF templates are similar. A first

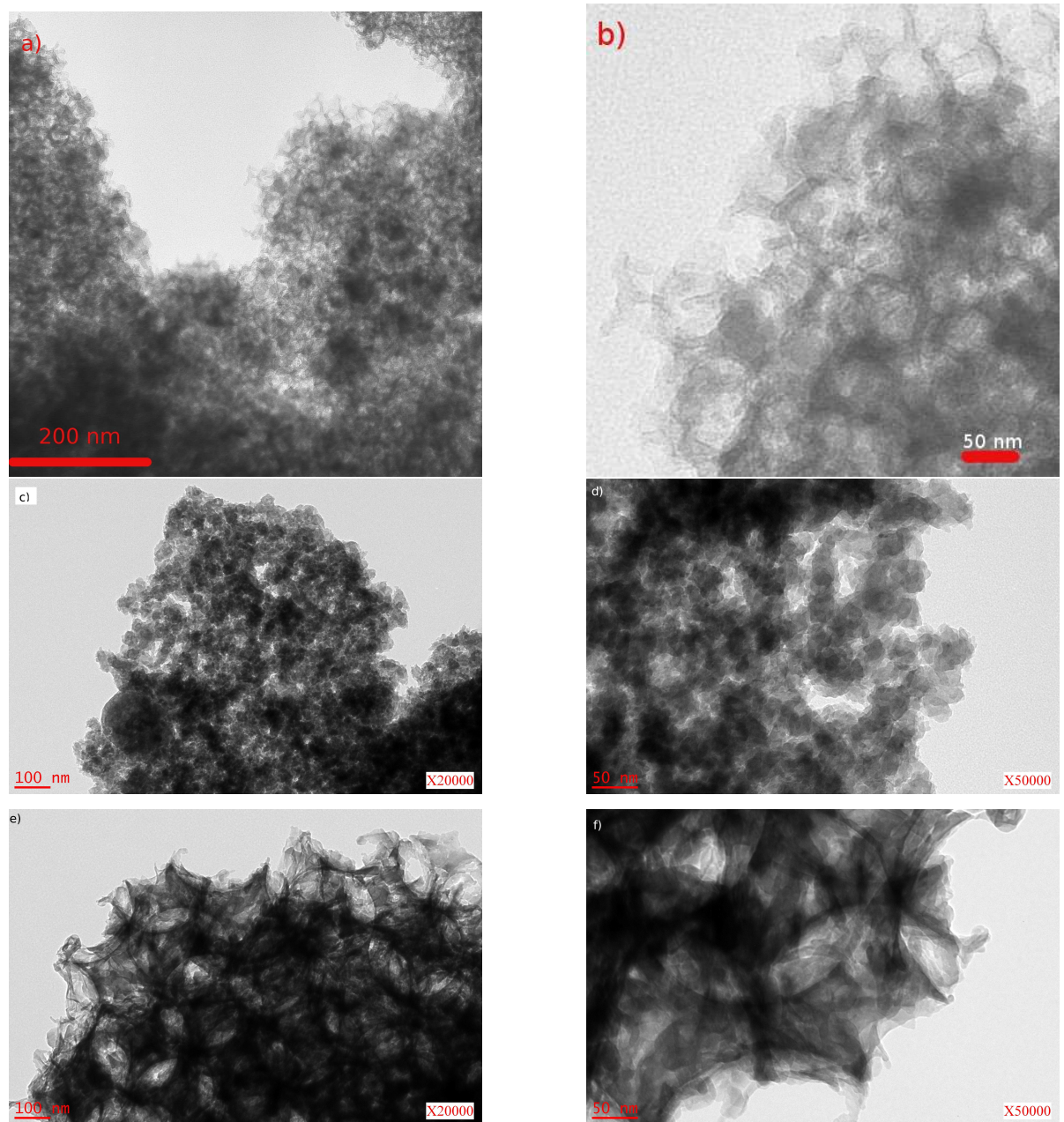


Figure 2.54: HA replication of SBA-15 (a,b), MCF (c,d) and opal (e,f) silica templates: transmission electron micrographs after template removal.

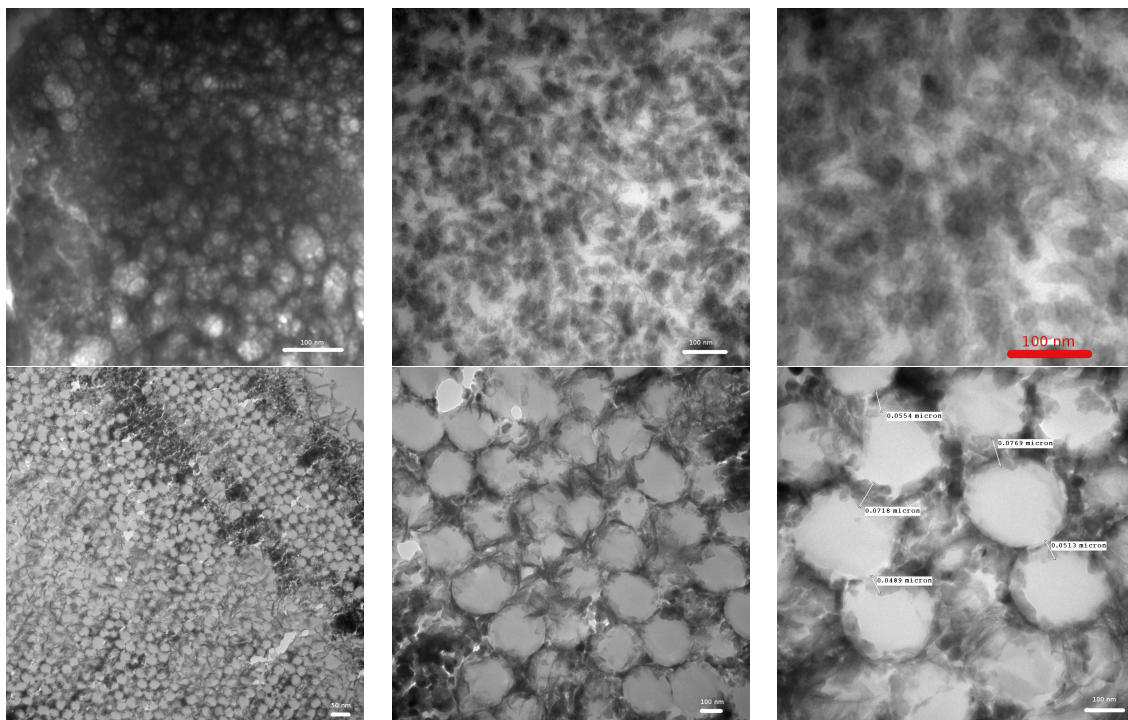


Figure 2.55: Transmission electron micrographs taken from sections of the HA replication of MCF (top) and of opal (bottom) silica templates. The images have been taken by Dr. Edouard Jallot of LPC Clermont.

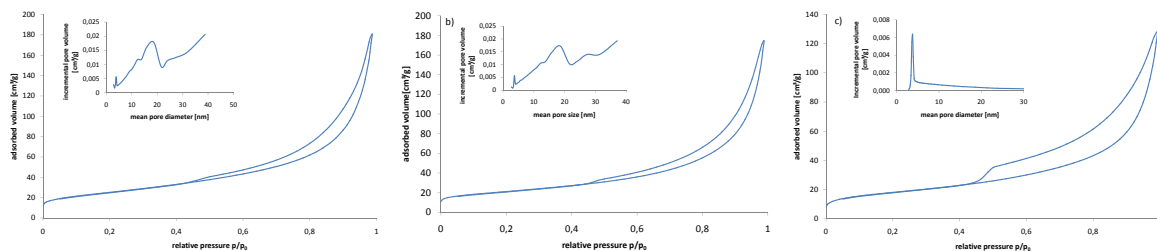


Figure 2.56: Nitrogen physisorption isotherms of the HA replication of the SBA-15 (a), MCF (b) and of opal (c) silica templates. Note the different scales on the y-axes. The inserts show the pore size distributions derived from the physisorption data.

sharp peak below 5 nm corresponds to the dissolution of the silica walls. The second, large peak envelopes all the pores that are obtained from partially filled template pores, and the last peak is caused by textural porosity between the ceramic particles. The similarity between these two ceramics – obtained from silica templates whose pores are very different in size and shape – indicate that no real templating effect occurs: the HA precursors condense outside the porosity of the template, forming porous structures that are independent of the template porosity. In the case of the opal template, a monomodal distribution is obtained, with a narrow peak at about 3.8 nm. these pores are too small to be caused by the silica template, they have formed between the particles.

For the MCF and the SBA-15 template, the filling process of the templates has further been monitored by nitrogen physisorption experiments: adsorption isotherms have been taken for the templates, the templates filled with the HA precursor and the HA ceramic after the template has been removed. For the MCF template, the isotherms are shown in figure 2.57. The template isotherm (shown in blue) is a typical type IV isotherm with H1 hysteresis. During the filling process, the surface area decreases from 674 m²/g to 20.7 m²/g. The initial pore volume of 2.24 mL/g is reduced to 0.08 mL/g. The isotherm of the composite is flattened compared to the template and the hysteresis is shifted towards lower relative pressures. This is an indication for a broader pore size distribution: some pores have been partially filled, resulting in smaller pore diameters. On the other hand, the biggest pores are partially filled, resulting in a hysteresis that closes earlier towards high relative pressures. The isotherm for the HA ceramic obtained after template removal has type II shape with H3 hysteresis. The early onset of the hysteresis indicates that real mesoporosity has been formed. The surface area is 74.2 m²/g. The pores of the template have not been filled completely; as a consequence, the ceramic is not a real replication of the porosity. The product is mesoporous, however, the porosity is not ordered as expected from the template porosity.

For the SBA-15 template, the shape of the isotherms does not change as much. All isotherms are type IV, but the position of the hysteresis shifts: the onset of the hysteresis is at low relative pressures (about 0.7), indicating small mesopores. While filling, the hysteresis shifts towards higher relative pressures, indicating bigger pore diameters. As these bigger pores cannot be assigned to partial pore filling – which would lead to

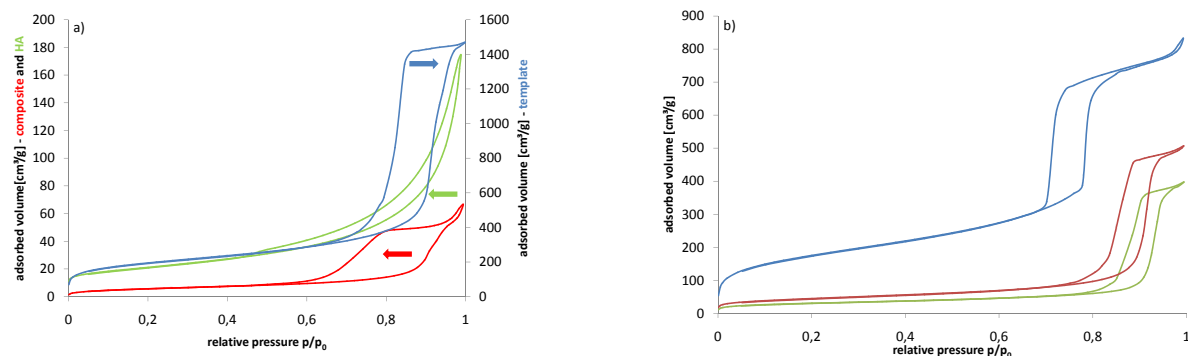


Figure 2.57: Nitrogen physisorption isotherms for the silica template (—), the template filled with HA (—) and the HA after template removal (—). Colored arrows indicate to which y-axis the isotherms have to be referred. a) MCF template, b) SBA-15 template.

smaller pores – they must have formed during the synthesis by the HA independently from the template porosity. This hypothesis is supported by the observation that the big pores are conserved when the template is removed. The hysteresis obtained for the HA after template removal is even more shifted towards higher relative pressures than for the composite. We can conclude that the composite isotherms represent a mix of the template isotherm, dominated by small mesopores, and the HA isotherm, obtained from large mesopores. The evolution of the surface area is the following: $674 \text{ m}^2/\text{g}$ for the template, $157 \text{ m}^2/\text{g}$ for the composite and $105 \text{ m}^2/\text{g}$ for the HA. The value for the surface area is high and indicates that real mesoporosity is formed. The same conclusion can be drawn from the shape of the isotherm. Nevertheless, the porosity is not a replication of the walls of the silica template.

In conclusion, only the replication of the silica opal is a real replication of the template porosity. The sample has a wide pore size distribution. On the transmission electron micrographs, shown in figure 2.55, we can see the reason for this large distribution: the material contains nanoparticles that compose the walls of its macropores. The interstitial space in between these particles is the origin of the observed mesoporosity.

2.3.2.4 Product properties depending on the surface chemistry of the template

CVD and sucrose replicas of the same silica have similar pore structures but are different in their surface chemistries: the carbon precursor used in the CVD (propylene) gives a hydrophobic carbon surface with only a minimum of functional surface groups. Sucrose on the other hand is decomposed to carbon materials with a more hydrophilic surface that contains oxygenated functional groups on its surface. It can be assumed that the aqueous precursor will wet the sucrose carbon surface more easily than the hydrophobic CVD carbon.

The CVD carbon template and the sucrose replica have been described in section 2.3.1.2 and 2.3.1.2. Figure 2.58 shows the nitrogen physisorption isotherms of the tem-

plates and the HA ceramics for the CVD and the sucrose carbon template. Table 2.17 gathers the corresponding values for the surface area and pore volume. In the case of the sucrose templating, the surface area of the composite is strongly reduced compared to the pure template, more than in the case of the CVD template. This indicates that the pore filling inside the sucrose template is more effective. The isotherm shape becomes flatter, approaching more the type II isotherm of the final HA ceramic. This is another indication of good pore filling. The hysteresis covers a large range, indicating that some pores are incompletely filled, giving rise to smaller pores. The overall pore volume of the composite is very small compared to the template, indicating pore filling or blocking. Comparing the pore size distribution for the sucrose carbon series, we observe that the large pores (over 10 nm) in the template are partially filled, as they disappear in the pore size distribution of the composite. The smallest pores of the template (3.7 nm) are not filled, they remain in the composite and in the ceramic. The smaller pores obtained from incomplete pore filling in the composite add to the small template pores in the case of the composite. The HA obtained after template removal is however not as porous as expected, it has a low surface area and almost no pore volume.

The HA obtained from the CVD template has a higher surface area and a higher pore volume. The comparison of the pore size distributions of the template and the composite shows that larger pores are formed by hydroxyapatite that is deposited outside the porosity of the template: The second peak in the pore size distribution of the composite is larger than in the template and covers pores that are bigger than the pores of the carbon template. The composite isotherm has not changed from the template isotherm as much as in the case of the sucrose template, but the overall product is more porous. This might be due to incomplete filling, adding residual template porosity to the pores of the HA ceramic.

The pore size distributions of the ceramic after template removal are similar; multimodal and with a large distribution. They show a peak centered at around 15 nm that indicates that pores have formed independently from the template as this value exceeds the size of the pores in the two templates. Two other peaks at even higher pore diameters can be attributed to textural porosity.

Figure 2.59 shows the results of thermogravimetric analysis of the HA/carbon composites during oxidation in air. In both cases, we observe four steps of weight loss. The first one (below 100°C) can be attributed to the drying of the compound and the evaporation of water. During this step, the weight loss of the CVD carbon based composite is lower, as the hydrophobic carbon surface adsorbs less humidity than the hydrophilic sucrose carbon surface. The next two steps (they can be differentiated by the change in the slope of the graph) correspond to the decomposition of the two HA precursors, the organic phosphite and the calcium nitrate. The last step is the oxidation of the carbon template. As observed for the pure templates, the sucrose carbon is easier to oxidize and burns at a lower temperature than its CVD counterpart.

The last weight loss step allows an estimation of the carbon mass: 6.9% in the case of the CVD template and 8.5% in the case of the sucrose template. We can also determine the final mass of the ceramic, which is 42% in mass in the case of the CVD carbon template and 27% in the case of the sucrose template. This difference is partly due to

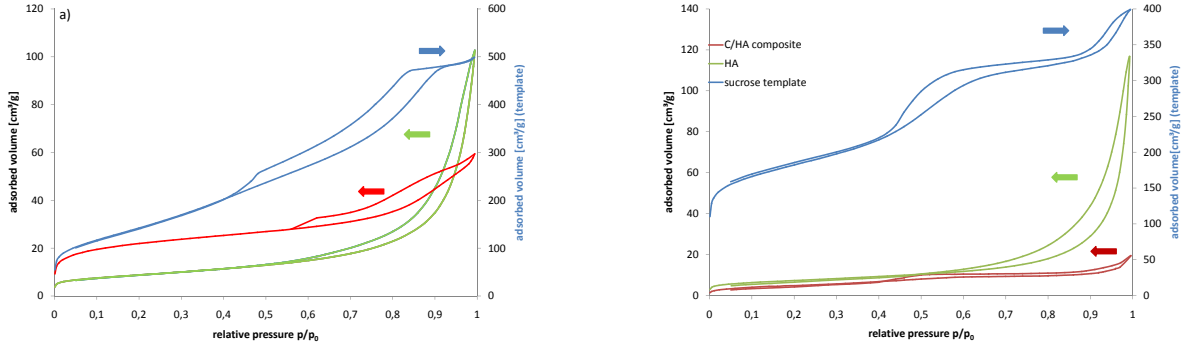


Figure 2.58: Nitrogen physisorption isotherms of the carbon CVD (a) and sucrose (b) template (—), the composites (—) and the final hydroxyapatite ceramic (—). Please note that the secondary ordinate corresponds to the template isotherm.

Sample	S_{BET} [m^2/g]	V_p
CVD template	527.4	0.79
CVD/HA composite	73.9	0.05
HA from CVD template	31.1	0.11
sucrose template	608.4	0.45
sucrose/HA composite	17.8	0.02
HA from sucrose template	25.2	0.01

Table 2.17: Results of nitrogen physisorption of the HA synthesis in sucrose and CVD carbon templates.

the high water content of the sucrose derived composite.

We can conclude that sucrose templates are indeed easier to fill with HA, but that the products obtained from them are less porous than the ones obtained from CVD templates. The higher pore volume of the CVD carbon template allows higher filling ratios with HA despite the unfavorable surface chemistry.

Comparing silica MCF, CVD and sucrose carbon templates, we observe that the chemical composition is affected by the template: The ceramic obtained at 500°C from the CVD carbon template and at 500 and 700°C from the sucrose carbon template show an additional reflex at 29.3° (see red circles in the graphic) that can be attributed to calcite (calcium carbonate, JCPDS file 5-586). This impurity is formed by the reaction of the carbon template with the hydroxyapatite precursors during calcination. If the elimination of the CVD template is carried out at 700°C, the calcite is thermally decomposed, and the reflex disappears from the diffraction pattern. In the case of the sucrose template, the carbonate resists to the heat treatment, and the reflex is still observed at 29.3°. Calcium carbonate decomposes at 825°C [149,150], but the onset of the reaction can occur at lower temperatures. It seems that the carbonate formed inside

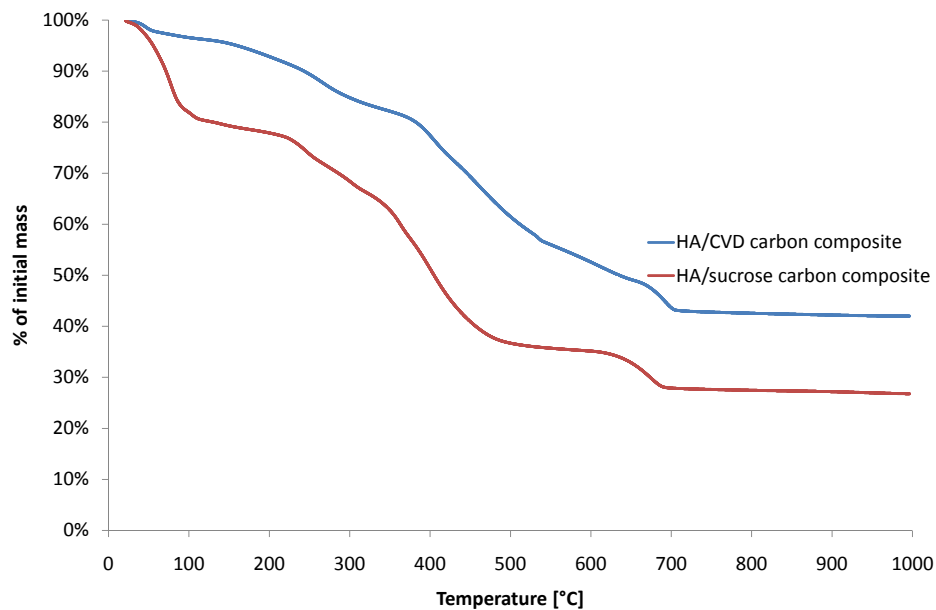


Figure 2.59: Thermogravimetric analysis of the HA/carbon composites in air

the sucrose template is more stable than the one formed from CVD carbon. This might be due to the difference in surface chemistry of the template: it has been shown that favorable interactions between guest (here: the carbonate) and host (the template) can delay evaporation and melting, and protect the guest from decomposition [151]. The hydrophilic sucrose carbon might have more favorable interactions with the carbonate, thus protecting it long enough from decomposition before the template is burned itself.

The choice of the template affects the chemical composition of the ceramic: Carbon templates lead to ceramics that contain calcium carbonate. Calcium carbonate does not affect the biocompatibility of the ceramic as it has been used as an implantation material as well [152–154]. As calcium carbonate is more soluble than hydroxyapatite, it might even be useful to use carbon templates in order to introduce calcium carbonate into the ceramic to tune its solubility.

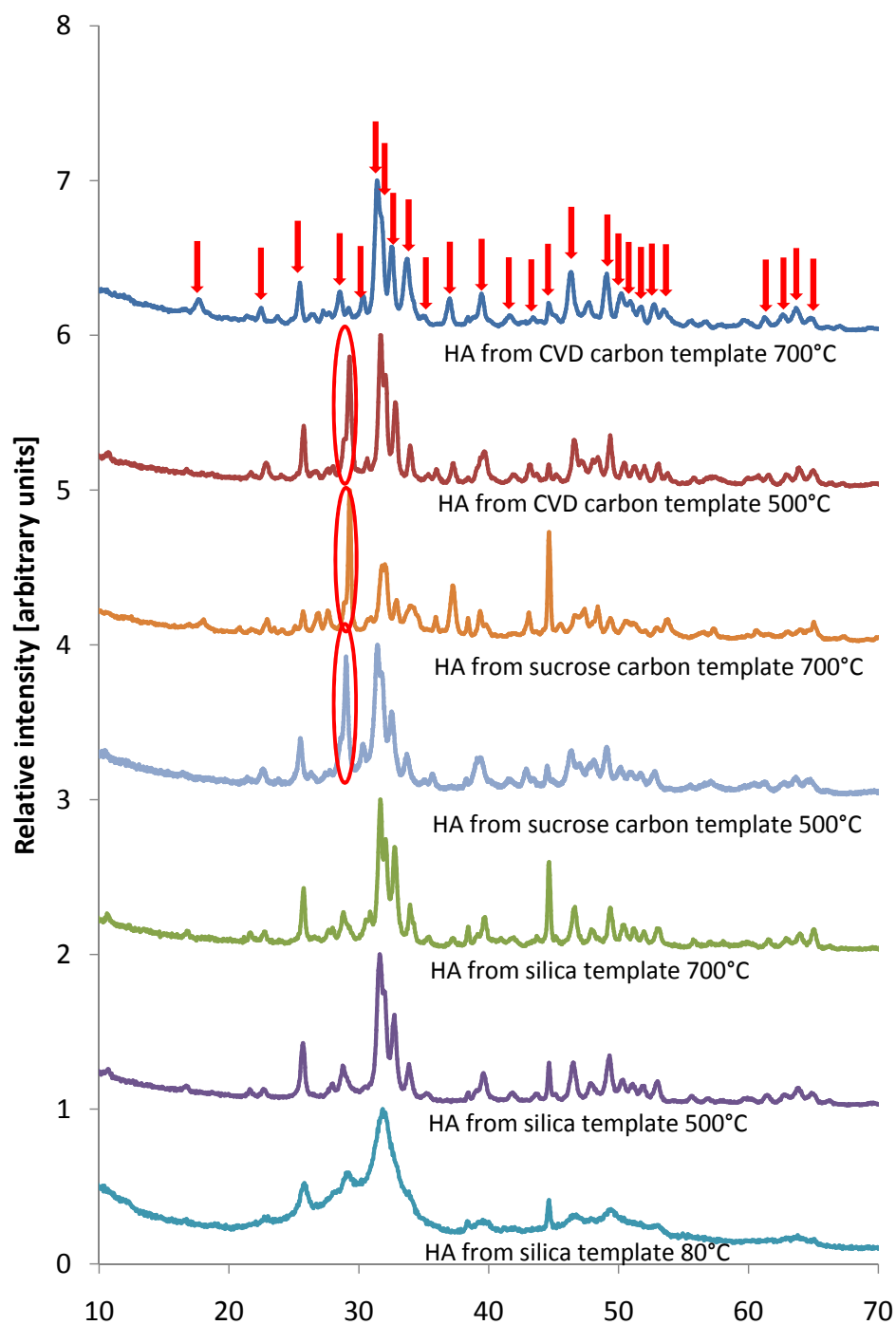
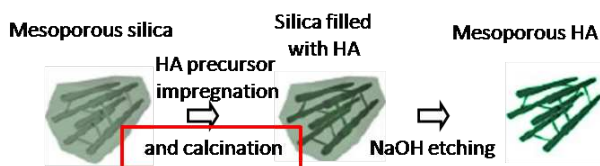


Figure 2.60: Wide angle X-ray diffraction patterns for the ceramics after removal of the templates. Red arrows indicate the reflex positions of hydroxyapatite (JPCDS file 9-432). The peaks marked by a circle correspond to calcium carbonate (5-586).



2.3.3 Products depending on the densification treatment

Calcium nitrate and triethyl phosphite. During the calcination treatment, grain growth – which may destroy porosity – can occur. On the other hand, the calcination stabilizes the ceramic and allows it to crystallize. MCF silica templates filled with HA according to the concentrated solution approach with calcium nitrate and triethyl phosphite have been calcined at 400, 600 and 800°C for 4 h in air. For comparison, one sample was not calcined at all.

Figure 2.62 shows nitrogen physisorption isotherms for the composites and the ceramic samples obtained after template removal. Table 2.19 gathers the corresponding values of the specific surface areas. The comparison of the isotherms for the composites and their pore size distributions shows that the composite is not affected by the heat treatment when the temperature is below 800°C. In the case of the calcination at 800°C, the monomodal pore size distribution observed for the composite before calcination is divided into two peaks. This can be attributed to shrinking effects. The composites that were calcined show higher surface areas due to shrinking of the HA filling inside the template pore during the heat treatment, thus liberating porosity. The isotherms obtained for the ceramics after template removal show significant differences: the samples that have been calcined give higher mesoporous ceramics than the composite that has not been calcined. If the calcination is done at 400°C, the surface area is higher than for the non-calcined sample. However, if the calcination is done at higher temperatures, the surface area decreases. It seems that a compromise has to be found between the shrinking of the HA inside the porosity, which gives high porosity, and the grain growth, which leads to lower surface areas.

Transmission electron micrographs show agglomerated or fused nanoparticles for all products (see figure 2.61 for the silica series). With increased calcination temperatures, the mean particle size increases. Compared to the values obtained by application of the Scherrer formula to X-ray diffraction data (see table 2.18), the particle size increases more than the crystallite size. This indicates that the bigger particles are formed through fusion of smaller particles at high temperatures. This effect can be directly observed when comparing the micrographs for the products obtained after calcination at 500 and at 700°C (subfigures b and c). The crystallographic orientation of the small particles obtained by the sol-gel synthesis is conserved during the calcination giving rise to bigger polycrystalline particles.

The ceramics after template removal have the highest surface area when calcined at low temperatures. The surface area of the sample calcined at 400°C exceeds both the surface area of the non-calcined sample and the one of the sample calcined at higher temperature. It seems that a mild heat treatment is a compromise between stabilization

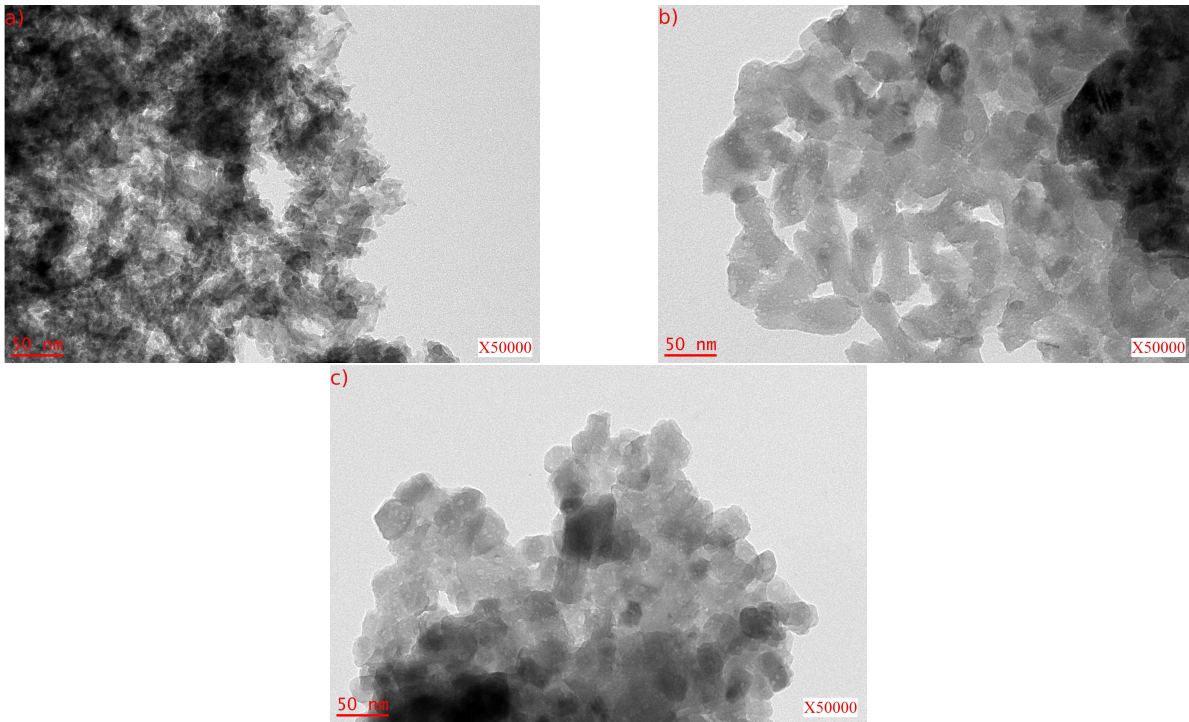


Figure 2.61: Transmission electron micrographs of the hydroxyapatite ceramics obtained from the silica template a) without calcination and after calcination at b) 500°C and at c) 700°C.

Template	Calcination	S_{BET} (m ² /g)	d (nm)
Silica	—	89.6	4.9
Silica	500°C, 12 h	22.1	34
Silica	700°C, 2 h	17.7	42.6
CVD carbon	500°C, 12 h	31.1	42.6
CVD carbon	700°C, 2 h	14.1	56.9
Sucrose carbon	500°C, 12 h	25.2	24.3
Sucrose carbon	700°C, 2 h	16.9	27.6

Table 2.18: Specific surface area S_{BET} and mean crystallite size d for hydroxyapatite samples depending on the template and heat treatment used.

Sample	calcined at	S_{BET} [m ² /g]	V_p [cm ³ /g]
Template		606	1.6
Composites		123	0.3
	400°C	189	0.50
	600°C	192	0.45
	800°C	167	0.43
HA ceramics		74.2	
	400°C	170	
	600°C	47.3	
	800°C	insufficient amount for analysis	

Table 2.19: Specific surface areas obtained by nitrogen physisorption experiments for the silica/HA composites after calcination at different temperatures and for the ceramics after template removal.

of the ceramic and excessive grain growth.

Calcium metaphosphates. Figure 2.63 shows X-ray diffractograms of the raw powder before calcination and of the powders calcined at 200, 400, 600 and 800°C. Before calcination, the product is partially crystalline and contains a hydroxyapatite phase. Side products include calcium silicate, silicon pyrophosphate, sodium calcium silicate and quartz derived from the silica template as well as other calcium phosphates. After calcination at 200°C, the peaks are better defined, indicating improved crystallinity. The product is still a mixture of hydroxyapatite with quartz from the template, calcium silicate and sodium calcium silicate. Calcination at higher temperatures leads to changes in the composition, but side phases can not be eliminated by heat treatment: all the products contain silicates and sodium salts (see figure 2.63 for details).

In conclusion, the polyphosphate precursor reacts with the silica template forming impurities that cannot be eliminated by heat treatment. For the application in templating with porous silicas, this approach is therefore dismissed. It might however be possible to use metaphosphates as precursors in templating with surfactants or inert templates such as carbon.

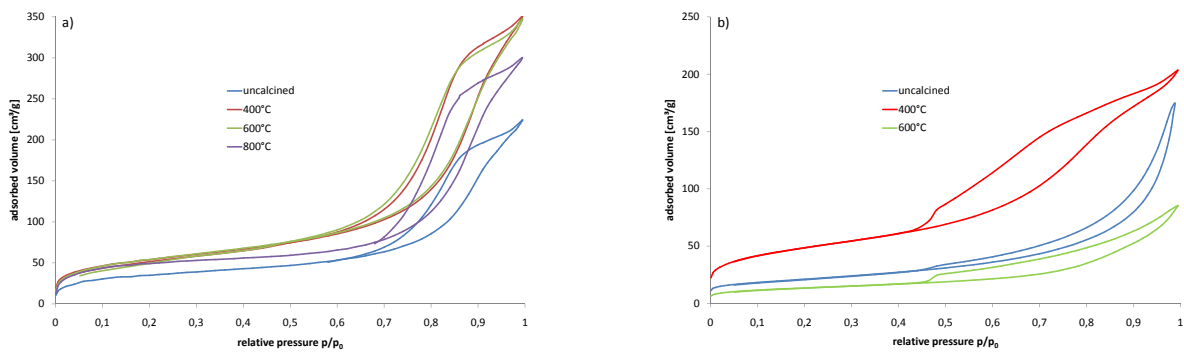


Figure 2.62: Nitrogen physisorption isotherms of the composites after calcination at different temperatures on the left (a) and the ceramics obtained after template removal on the right (b). The amount of HA obtained from the composite calcined at 800°C was not sufficient for analysis.

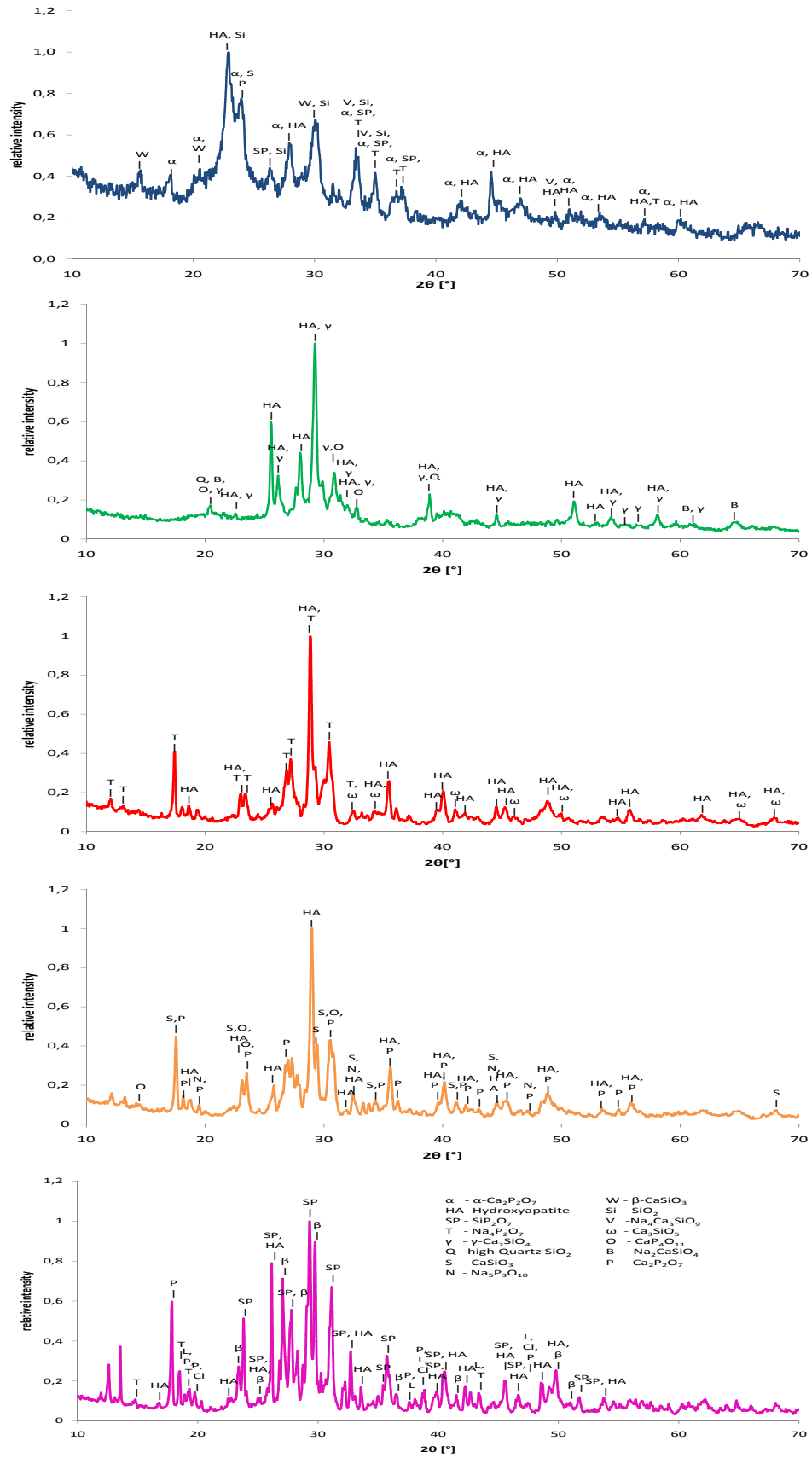


Figure 2.63: Wide angle X-ray diffraction patterns for the calcium metaphosphate materials. Before calcination (—), after calcination at 200 (—), 400 (—), 600 (—) and 800°C(—).

2.4 Discussion

The objective of this work was the synthesis of mesoporous hydroxyapatite by hard templating methods. Starting from mesoporous silica and carbon templates, hydroxyapatite precursors were infiltrated into the porosity. After template removal, mesoporous hydroxyapatite ceramics are obtained. The choice of the hydroxyapatite precursor, of the template as well as the infiltration process and the calcination to which the template/ceramic composite is subjected influence the properties of the final ceramics. In this chapter, we will discuss the influence of each parameter separately before comparing our results to previously published work.

Precursors. Of the tested HA precursors, only the combination of calcium nitrate with triethyl phosphite leads to HA without a high amount of secondary phases. Even in the presence of silica templates, the synthesis leads to HA with little silicate contamination. The synthesis can be carried out from solutions with high concentrations and has high yields. The dead volume effect of the solvent can be minimized when the concentrated solution approach is used.

CAT and $(\text{BuO})_3\text{P}$ did not react inside the carbon template to form HA. The Ca/P ratio measured by EDX is very low. Additionally, the product contains heavy metals from the autoclave wall, which render it unsuitable for implantation. Another reason has however led us to the abandon of this approach: The calcium precursor molecule is big; for a single calcium atom, it introduces more than 80 atoms into the template porosity that do not contribute to the formation of calcium phosphates. A big molecule like this leads to the same dead volume effect as a solvent in diluted solution: the pore volume is filled with atoms that are not needed for the desired product.

The solvent-free syntheses did not lead to calcium phosphate, contrary to what was claimed in the original paper [142]. EDX measurements showed almost no phosphorus in the final product. A synthesis starting from the same precursors $\text{Ca}(\text{EtO})_2$ and $(\text{EtO})_3\text{P}$ has been described by Gross et al. et al. [142]. It seems important to respect the aging period off at least 24 h and to calcine at 800°C in order to obtain pure hydroxyapatite. These conditions have been applied in our experiments (except for the calcination that was carried out at 780°C), but with the addition of only a small amount of ethanol. As the reaction could not be observed even in the absence of the template, it seems reasonable to assume that the template is not the reason why the reaction did not happen. The absolute ethanol used for the synthesis has not been dried prior to its addition to the system. As the precursors are moisture-sensitive, the water traces contained in the solvent might have interfered. The synthesis should be carried out again in complete absence of moisture, in dried glassware and with water-free reagents.

The ethanol-based sol containing calcium nitrate and diammonium hydrogen phosphate is unsuitable for the synthesis in templates as it requires high dilution of the precursors. Although ethanol is more easy to eliminate from the reaction mixture than water due to its higher volatility, this synthesis method requires highly diluted solutions [143]. The presence of a considerable amount of solvent leads to a strong dead volume effect. Alcohol-based systems are interesting for templating approaches as they

can improve the wetting of the template by the precursor [67]. This is most important when hydrophobic templates such as CVD carbon or polymers are used. In the case of hydrophilic silica templates, the wetting with aqueous solutions is not an issue.

Calcium metaphosphates are a very promising system. However, their combination with silica template leads to the formation of silicon-containing secondary products that resist to heat treatments. Contrary to other phosphate species, metaphosphates can react with silanol groups at the surface of silica materials [155]. This reaction has been used for the functionalization of silica with ethyl phosphate groups, and in our case, it leads to a covalent bond between the silica substrate and the calcium phosphate. Upon calcination, silicate containing impurities are formed from these phosphoryl esters. It would be interesting to test this synthesis method in presence of inert templates such as carbon.

The most versatile process is the simple sol-gel synthesis starting from calcium nitrate and triethyl phosphite. It is possible to use high concentrations in order to limit the dead volume effect caused by the solvent, and the product shows only little contamination with silicon-containing phases if silica templates are used. The other methods that have been examined either do not lead to the desired hydroxyapatite phase or give products that contain significant amounts of silicon contamination.

Infiltration process. Starting from the combination of calcium nitrate and triethyl phosphite, the infiltration of a concentrated solution under vacuum leads to a good filling of the template porosity. However, in diluted conditions, the incomplete pore filling gives higher surface areas in the final product. It seems that a choice has to be made: a high surface area products with low yields (in terms of mass of HA that can be synthesized from a given mass of template) or a high yield in terms of quantity with lower surface areas. Melde and Stein [67] have observed similar concentration effects while working on the replication of latex opals. They found improved yields when using concentrated solutions, along with a better replication of the pore structure. Low concentrated precursor solution led to incompletely filled pores and consequently to less accurate pore replication.

Both concentrated and diluted solutions lead to a mesoporous product. However, in both strategies, there is no direct templating effect, as the pore structure of the template is not replicated. In this aspect, our study differs from the one published by Melde and Stein. The authors have worked on systems with a bigger length scale and obtained perfect replicas of the pore structure. Carrying out the infiltration under vacuum instead of in atmospheric pressure improves the filling of the porosity.

Template. Silica foam templates are an improvement compared to SBA-15 type materials: The higher pore volume and the bigger pores allow the preparation of more HA from the same mass of template, and the products are mesoporous.

In the case of carbon templates, the sucrose precursor leads to a surface chemistry that is more suitable for the infiltration, improving the pore filling: the sucrose derived carbon contains a large amount of oxygen-containing surface groups [156, 157] that render the

template surface more hydrophilic. The aqueous HA precursor solution can infiltrate the porosity more easily. Preferential interactions between the precursor and the template greatly improve the filling of the porosity [146].

On the other hand, this improved pore filling does not lead to higher surface area ceramics; on the contrary, the products templated by CVD carbon show higher surface areas and pore volumes. As in the diluted and concentrated solution approaches, incomplete pore filling, as observed in the case of CVD carbon templates, is favorable for high porosity: the residual pore volume of the template adds to the porosity freed by the elimination of the template.

The most suitable template is the mesoporous silica template: As the silica can be dissolved at low temperature, calcination becomes optional and the heat treatment temperature can be chosen in function of the desired crystallinity of the ceramic. It is even possible not to calcine the product at all. In the case of carbon templates, the temperature of calcination must be sufficient to burn the template.

Calcination. It has been shown that calcination at high temperatures causes grain growth and can lead to decreased surface areas. In macroporous systems, calcination above 800°C leads to the collapse of the pore system [67]. At lower temperatures, the reduction in volume of the product inside the template porosity increases the pore volume of the product. This effect is based on the same principle as incomplete pore filling with diluted solutions, which also leads to products with higher porosities. A compromise has to be found between the undesired grain growth of the ceramic and high porosity of the final ceramic. *The ideal calcination temperature seems to be around 400°C.*

Comparison with previously published results. Compared to the literature that has been published on the hard templating of hydroxyapatite, new routes have been explored: Until now, only CMK-3 materials have been used for hard templating approaches. The products described by Zhao and Fan [121,122] are basically non-porous, as can be concluded from their nitrogen physisorption isotherms. Neither of the isotherms shows an early onset of hysteresis, and the surface areas are small (27 and 42 m²/g respectively). Both products have been subjected to heat treatments in order to remove the template. In our experiments, this has been shown to be detrimental for high surface areas. By the use of silica templates and their dissolution at low temperatures by a chemical etching, high temperature treatments can be avoided.

Ceramics with surface areas up to 105.4 m²/g are obtained by silica templating. This value is similar to the highest surface areas achieved by soft templating approaches (140 m²/g [132] by anionic surfactant templating with C₁₂GLU and 263 m²/g [133] by templating with a non-ionic surfactant with solvent extraction of the surfactant). As in the quoted syntheses, real mesoporosity was induced into the ceramic. The paper published by Ng [133] underlines once more the detrimental effects of heat treatment: While solvent extraction of the surfactant gives rise to ceramics with a specific surface area of 263 m²/g, the same sample has a surface area of only 43 m²/g if the surfactant is eliminated by calcination.

In our experiments, the properties of the ceramics obtained by different techniques are similar. Independently of the template or the HA precursor, a direct templating effect – like in the case of CVD on mesoporous silica – has not been observed: the products have porous features that do not correspond to the porosity of the templates.

In order to study protein adsorption, we have obtained several samples of mesoporous hydroxyapatite produced by sol/gel from our partners at the LMI in Clermont-Ferrand. The synthesis methods and the characteristics of these ceramics will be presented in detail in section 3.1.5 on page 131. Briefly, the obtained ceramics feature surface areas in the range of $40 \text{ m}^2/\text{g}$ if calcined and up to $166 \text{ m}^2/\text{g}$ without calcination. The uncalcined sample is almost completely amorphous. It is striking that even with a completely different approach, high surface areas cannot be obtained.

It has been reported before [125] that systems with fast hydrolysis such as transition metal phosphates resist to templating approaches. The system is unstable and condenses before the precursors can penetrate the porosity. It has been proposed that local changes in the pH of the solution due to surface functional groups on the template may trigger the condensation of the precursor system [67]. This is supported by the work of Pereira and her team [158], who have found that silica particles stimulate the precipitation of carbonated HA from salt solutions. We believe that rapid condensation occurs in our systems and in other systems that have been published. This would explain why neither our experiments nor products reported in the literature show templating effects.

2.5 Conclusion

In our experiments, the best products with the highest pore volumes and the highest specific surface areas have been obtained by the combination of silica templates and diluted solutions of calcium nitrate and triethyl phosphite. In these conditions, incomplete pore filling adds to the pores freed by the dissolution of the template and leads to highly porous ceramics. The silica is not only the template with the highest pore volume, but can also be removed at low temperatures. The calcination temperature can therefore be chosen without respecting a minimal temperature like it is necessary for the oxidation of the carbon template.

A choice must be made regarding high surface area and pore volume or high yield synthesis: High surface products are obtained from diluted solutions, but the yield in terms of amount of HA obtained from the same mass of template is low. On the other hand, concentrated solutions lead to high yields but with slightly lower surface area.

It must nevertheless be noted that none of our experiments has shown a real templating effect in which the pores structure of the ceramic is a replication of the pore system of the template. Contrary to the synthesis of macroporous HA, where we obtained imprints of the silica spheres in the ceramic, mesoporous HA replicating the pore structure of the templates has not been obtained – neither by our experiments nor in the literature. We believe that the sol-gel precursor system reacts too fast to allow the penetration of the precursors into the porosity. The condensation of the precursors outside the pores of the template leads to ill-structured ceramics. In order to improve the replication of the

porosity, the reaction kinetics would have to be slowed down.

The second part of this work is the study of the adsorption and release capacities of mesoporous hydroxyapatites. For this, six powders are chosen, among them three powders prepared by the LMI in Clermont-Ferrand and three of our samples. The three powders are representative of the different templates and calcination methods used. All of them were produced from calcium nitrate and triethyl phosphite following the concentrated solution approach in vacuum. The table 2.20 gathers their main characteristics.

Sample	Template	Calcination [°C]	S_{BET} [m ² /g]	$\varnothing_{p,BJH}$ [nm]	V_p cm ³ /g	Crystallinity	Crystallite size [nm]
J	MCF	80	89.6	14	0.36	poor	5
JC	MCF	500	22.1	17	0.09	good	34
K	CVD	500	31.1	13	0.11	good	43

Table 2.20: Three representative hydroxyapatites chosen for protein adsorption experiments.

3 Protein adsorption by porous hydroxyapatite

3.1 Bibliography

3.1.1 Adsorption of proteins on ceramic materials

When a material is immersed into a physiological fluid, salts and proteins are the first to adsorb on the surface. These adsorbed proteins form the basis for the landing of body cells and are crucial for their interaction with the surface [159,160]. An improvement of knowledge about the interaction between bioactive molecules and surfaces should therefore be at the beginning of every study on biomaterials.

Structure, conformation and local order of the proteins on the surface may determine the interaction of the surface with all further incoming species [161].

3.1.1.1 Protein adsorption on calcium phosphate materials

Calcium phosphate materials and especially hydroxyapatite have been used for a long time for the chromatographic separation of proteins [162]. It is known that protein adsorb easily on the surface of hydroxyapatite and that their desorption is less favored [162]. In chromatography, the elution of the adsorbed proteins is forced by solutions with high phosphate concentrations. These ions are able to interrupt the electrostatic interactions between the protein and the hydroxyapatite surface of the column.

The presence of proteins during the formation of hydroxyapatite and other calcium phosphates influences their growth rate, their shape (preferential growth of certain crystal planes) and even their chemical composition [163]. This illustrates that protein adsorption onto hydroxyapatite is preferential on certain crystal planes and therefore strongly depends on crystallinity.

The following section is aimed to explain the interaction of proteins with HA surfaces.

In vacuo, hydroxyapatite is covered with hydroxy groups as evidenced by FTIR [16]. When placed in contact with aqueous media, some of these hydroxy groups will be dissolved. The dissolution is favored by the weak interaction between phosphate ions and hydroxy groups: the phosphate groups form a strongly interacting pattern in which substitutive ions are not included [164]. The formerly negatively charged surface will become positively charged due to the excess of Ca sites on the surface and hydration of the phosphate ions. Ishikawa and Kandori [16] have found that the surface of hydroxyapatite that is presented to the proteins in solution, is composed of positively charged site that are rich in calcium ions or have lost hydroxy groups ("C sites") and negatively

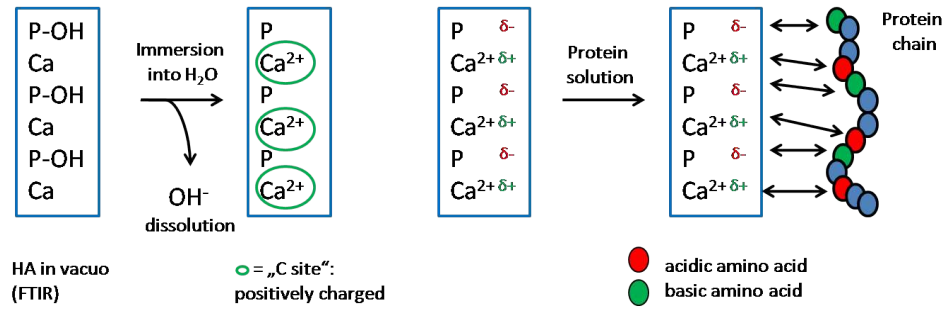


Figure 3.1: Schematic representation of C site formation on the surface of hydroxyapatite during immersion into aqueous media at pH 7. Interaction with the protein chain. Drawn after data from [16].

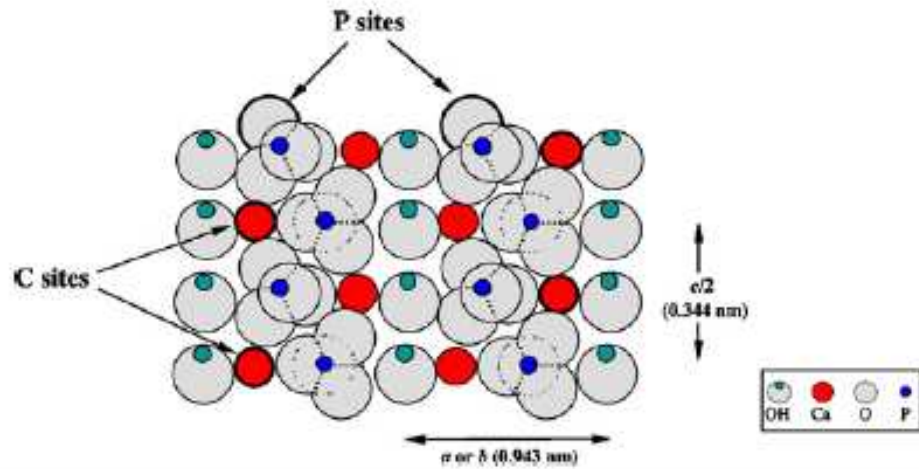


Figure 3.2: Position of C and P sites on hydroxyapatite crystal surface. From [16].

charged phosphate sites ("P sites"). Figure 3.1 schematizes the mechanism of C site formation, figure 3.2 shows the position of C and P sites on the surface of an hydroxyapatite crystal. Both sites contributed too the adsorption of proteins: the C sites interact with acidic amino acid residues, the P sites interact with basic amino acids. The combination of both interactions leads to strong protein adsorption on the hydroxyapatite surface. The adsorption of proteins onto the hydrophilic surface of hydroxyapatite is therefore governed by electrostatic interactions. Both the dissolution of the surface groups and the interaction between the surface and the protein are strongly pH dependent; The charge of the protein chain is a function of the pH of the surrounding media.

Hydroxyapatite crystallizes in the hexagonal crystal system $P6_3/m$. On the ac or bc particle phase, the C sites are arranged in rectangles with distances of 0.943 and 0.344 nm. The C sites on the other hand are hexagonally arranged on the ab phases and distanced by 0.943 nm. It has been suggested that the crystallinity and therefore the order on the particle surface influence the adsorption capacity of a given material [162]. On badly crystalline samples, the interaction sites may be further away from each other,

and thus the interaction with the protein may be less strong.

On the other hand, Cazalbon [165] and coworkers and Ouiza [166] and team who have studied the interaction of poorly crystalline apatites with albumin during maturation have found that a lack of crystallinity can be beneficial for the adsorption of albumin: the authors describe that labile, non-apatitic phosphates decrease during maturation of the apatites and so does the protein adsorption capacity. They suggest that non-apatitic phosphates might be the preferential sites for the adsorption of proteins. In the more recent article [165], the authors describe the adsorption of albumin on sites of high charge density which are the same sites that are used for the precipitation of ions (Ca^{2+} and PO_4^{3-}) during maturation. This explains why the presence of albumin can slow the mineralization of poorly crystallized apatites: the proteins is merely blocking the sites that would be necessary for the precipitation of supplementary ions.

It seems therefore that on poorly crystalline apatite (such as studied by Cazalbon and Ouiza), crystallinity is detrimental for the adsorption of proteins. On highly crystalline samples, however, crystallinity might help the adsorption of proteins. We have to keep in mind that the amount of protein adsorbed by poorly crystalline samples is much bigger than for crystalline samples due to the higher surface area and surface reactivity [166].

On porous materials, interactions between proteins and surface are more complex and less easy to describe. Additionally to structural parameters such as crystallinity, textural parameters such as porosity, pore size and pore interconnection become important.

3.1.1.2 Protein adsorption in (meso)porous materials

As explained in the introduction, mesoporous materials have pores ranging from 2 to 50 nm in diameter. This is typically the size of proteins and other big biomolecules. The adsorption of proteins into pores at their own scale is therefore very interesting for the design of controlled release systems.

Balkus and coworkers were the first to study globular proteins in presence of mesoporous substrates [167]. In this study, cytochrome c, papain, trypsin and horseradish peroxidase were adsorbed on MCM-41, a mesoporous silica material with worm-like pore structure and mesopores between 2 and 10 nm in diameter. A clear dependence from molecular weight was observed: Horseradish peroxidase was not significantly retained by MCM-41, indicating that the molecule was too big to enter the pores. For smaller proteins, a linear decline between the molecular weight and the retained quantity were observed.

Protein adsorption into mesoporous materials was later extensively studied by Vinu and coworkers [168–171]. In [171], this research group even presents a review on mesoporous materials for biological applications and protein adsorption. Although a number of different proteins and materials are explored, the primary results can be summarized as follows:

- Maximum adsorption is achieved near the isoelectric point (zero net charge of the molecule). [169, 170] At this point, the electrostatic repulsion between adjacent proteins on the surface is at its minimum.

Protein	Molecular weight in solution [Da]	Molecular dimensions [Å]	Source
Cytochrome c	11 353	25, 25, 37	[173]
Lysozyme	14 296	45, 30, 30	[173]
Myoglobin	17 183	44, 44, 25	[173]
β -Lactoglobulin	35 000	29, 34, 40	[172]
Ovalbumin	43 000	40, 50, 70	[172]
BSA	66 000	50, 70, 70	[172]
Conalbumin	76 000	50, 56, 95	[172]
Superoxide dimutase	15 534	36, 40, 38	[173]
Ribonuclease	13 673	38, 28, 22	[173]

Table 3.1: Physical properties of some commonly used proteins

- Concentrated protein solutions force more proteins to be adsorbed. [169,170]
- Large pores allow more proteins to be adsorbed. [169,170]
- Powders adsorb more protein than pellets due to higher surface area. [169]

In all cases quoted before, the quantity of absorbed proteins is determined by difference by UV/Vis analysis of the supernatant liquid.

In 2005, M. Hartmann published a review article on the application of mesoporous materials in bioadsorption and -catalysis [12]. First the adsorption of small biomolecules is investigated. In this case, steric hindrance is found to play the crucial role. Consequently, the quantity of absorbed protein depends on the pore size: the larger the pore, the higher the amount of protein adsorbed. If the pores are smaller than the hydrodynamic diameter of the molecule, adsorption does only occur at the surface of the material. The same is true when different proteins are placed in contact with the same material: The larger the protein the smaller the adsorbed quantity in the material. Table 3.1 displays physical properties of some proteins, taken from reference [172]. The molecular dimensions were estimated from crystallographic data. Additionally, figure 3.3 shows some proteins at the same length scale allowing the comparison of the molecular sizes.

A strong dependence on the pH is observed, probably due to increased repulsion between charged adsorbate molecules, the monolayer capacity (density of proteins in monolayer) is highest at the isoelectric point.

In the case of bigger biomolecules, namely proteins, the same tendencies are observed. Additionally, the authors [174] point out that no conformational change, no unfolding, occurs on these mesoporous materials. This is in contrast to the behavior on flat surfaces where proteins tend to spread and unfold. It is concluded that the bioactivity of the products does not change upon adsorption [12]. This hypothesis is supported by cyclic voltametry studies carried out by Balkus et al. [175].

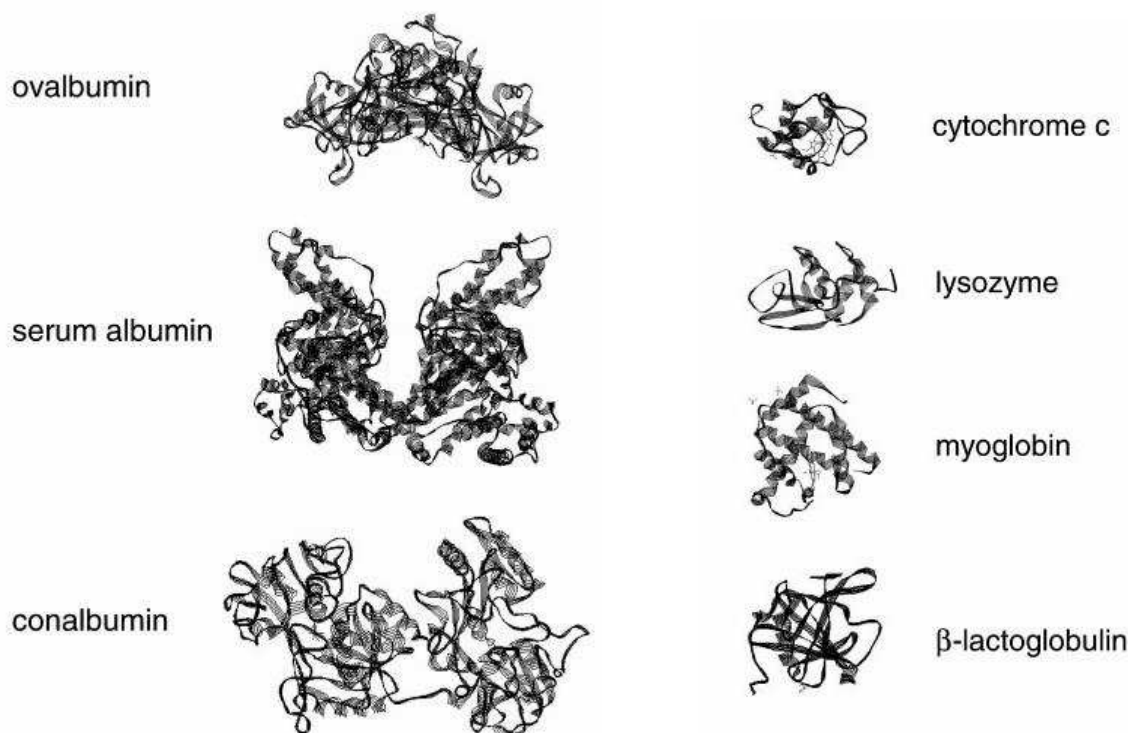


Figure 3.3: Size comparison of some proteins from reference [172]

On the other hand, the mesoporous materials are able to protect proteins from denaturation when they are adsorbed into the porosity [175]. In conditions that would normally denature the protein, it stays stable when immobilized. Ravindra et al. [176] observe the thermal unfolding temperature of RNase (Ribonuclease) to rise by 30 K when adsorbed into MCM-41 materials. Not only a space restriction (excluded volume effect) may cause this behavior, it is although suggested that increased strength is given to the protein on the surface.

Additionally, the evolution of the site of absorption is discussed. Depending on its concentration, a protein may adsorb on the outer surface or inside the pores or not at all. In the article these populations are called "adsorbed", "encapsulated" and "free". Adsorbed proteins are thought to be weakly destabilized, whereas encapsulated species are strengthened. The three populations can be distinguished via DSC experiments as they unfold at different temperatures.

The influence of the surface chemistry is pointed out by Yiu et al. [172]. The analysis of ordinary and thiol functionalized SBA-15 in presence of different proteins showed that the non functionalized silica interacts more tightly with the proteins than the functionalized derivative. The only exception is observed for the case of ovalbumin. The thiol-functionalized SBA-15 material shows strong adsorption of proteins with molecular weights inferior to 44 000 such as bovine serum albumin and conalbumin (ovotransferrin). In the case of smaller proteins, the adsorption is found to be irreversible. The authors conclude that this strong interaction is due to reversible physisorption that is

followed by slower but irreversible chemisorption. Analogous to single file diffusion, Yiu and coworkers suggest that only one protein can be in the mesopore at once when its radius exceeds the pore radius [172].

In summary, for the adsorption of proteins on mesoporous materials, the following parameters play key roles:

- On the material side: pore size and accessibility. The pore size must be adapted to the protein to be adsorbed.
- On the protein side: molecular weight and hydrodynamic radius. The concentration of the protein solution and the interactions between several protein molecules. The net conformation of the protein under the given adsorption parameters.
- For the adsorption conditions: solvent, pH and ionic strength. Those parameters affect the net charge of the protein and influence its adsorption capacity.

3.1.2 Growth factor release systems based on calcium phosphate

Although the adsorption of proteins onto calcium phosphates has been object of several publications (see section 3.1.1.1), few release systems for growth factors have been described that are based on mesoporous scaffolds or on calcium phosphates or both. The most commonly used scaffolds for growth factor release are based on biodegradable polymers with macroporous structure [69,177–182]. The release of the growth factor into the environment of the scaffold is most often achieved by diffusion, the degradation of the polymer plays a secondary role if any [181]. Zisch and coworkers however found a way of triggering the release of VEGF from a polymeric matrix by cell activity: The VEGF is covalently bound to the polymer matrix, and can be released by matrix metalloprotease (MMP) and plasmin (two enzymes that are able to cleave the protein/matrix-bond) secreted by cells cultured on the scaffolds.

VEGF. One example of the association of calcium phosphates with growth factors was described by Lode et al. [183]: The authors impregnated different calcium phosphate cements with VEGF by immersion of the ceramic discs into a protein solution. Weakly adsorbed growth factor was removed from the surface by washing. Release experiments were carried out by placing the loaded samples into culture medium under cell culture conditions (37°C, sterile, 5 % CO₂). The authors were able to show that only a small amount (2.5%) of the growth factor bonded weakly on the surface and could be removed by washing. The burst release within the first 2 h of exposure to the culture medium was limited to 7 %. The release was then observed to decrease to between 20 and 40 ng/mL, depending on the cement, for the first 24 h. The release was sustained for one week, but decreased steadily to almost zero for the 7th day.

This study illustrates the affinity of VEGF to calcium phosphate ceramics by the small amount of protein that attaches only weakly to the surface and by the slow release kinetics. The release of VEGF is however only governed by diffusion, a smart release

system as in the example presented by Zisch et al. is not implemented. A potential biological activity of the calcium phosphate was not monitored.

In order to limit the burst release of protein upon the first contact of the loaded calcium phosphate with the culture medium or the surrounding tissue in the case of implantation, Wernike, Liu and coworkers developed a co-precipitation method that allows the incorporation of proteins into the macroporous calcium phosphate scaffold [184–186]. After the validation of the technique with BSA [184,186], the authors extended the principle to VEGF [185]. In the VEGF paper, they compared the co-precipitated sample to a calcium phosphate that was impregnated with VEGF in a 1 µg/mL solution of VEGF and observed its release kinetics. In addition to these in vitro experiments, in vivo evaluation was carried out by implanting the loaded calcium phosphate into cranial defects of mice. The impregnation of the samples for in vivo evaluation was carried out with an initial protein concentration of 1 µg/mL or 5 µg/mL initial protein concentration. For the in vivo test of two weeks, the authors observed improved vascularisation in the case of 5 µg/mL impregnation for the impregnated samples and for both concentrations for the co-precipitated samples.

This study is one of the rare cases that includes both in vitro and in vivo data on the impregnation with different VEGF concentrations. The protocol of the growth factor adsorption and release experiments in the present work has been adapted from this paper.

TGF. The association of TGF-β1 with tricalcium phosphate for the regeneration of bone defects has been studied for example by Beck and coworkers [187]. The authors used non-porous TCP granules that were wet with TGF-β1 solution and mixed with bone marrow so that the concentration of TGF in the implant was either 0.6 or 3.3 µg per mL of implant. These materials were compared to autogenous bone implants and the untreated defect in the radius of male rabbits. The authors did not observe an effect of the administration of the growth factor on the healing of the bone defects as analyzed by radiography during the recovery period. Histology and mechanical testing indicated similar behavior between the bone marrow associated with TGF and autogenous bone implants.

The authors did not carry out any in vitro testing to prove that the TGF was effectively bonded to the implant. It is possible that the growth factor was washed out within a short time span after implantation which would explain why no effect was observed.

Lind and coworkers used titanium implants coated with tricalcium phosphate in association with TGF-β1 in order to investigate the bone regeneration inside femoral defects of dogs [188]. In this study, the effect of growth factor-loaded and unloaded coatings was compared. Each animal received two implants, one containing 0.3 µg TGF and one without growth factor. Increased bone ingrowth was observed in histology for the impregnated implant. The authors showed in a parallel study with radio-labeled TGF that 90% of the protein contained in the coating were released within 4 h in culture medium. On the other hand, virtually no release was observed when washing with saline solution. This observation illustrates that the presence of serum proteins accelerates the

desorption of TGF from the implant surface.

Link and coworkers performed a similar study using a composite made of gelatin microspheres and macroporous calcium phosphate cement for the regeneration of femoral defects in rabbits [189]. In one case, the gelatin microspheres were loaded with TGF- β 1 prior to the incorporation into the composite. The final amount of TGF was 250 ng per implant based on previous studies and considering the release kinetics of the gelatin microspheres. The gelatin content of the composite was 5% in weight. The cement was injected into the defects via a syringe. The authors observed no higher mechanical strength of the implant/bone interface when TGF was incorporated into the composite. The degradation of the implant however was significantly stronger after 12 weeks post-implantation.

In the study published by Sun et al. the TGF- β 1 was incorporated into collagen/HA/TCP microspheres and implanted in bone defects in the femur of rabbits. The microspheres were composed of HA and TCP and dispersed in a fibrous collagen matrix. The growth factor was injected directly into the defect after filling with the collagen/HA/TCP composite. The authors observed that the defects filled with composite without TGF were filled with fibrous tissue and inflammatory cells after 15 weeks post-implantation. The defects that had been treated with composite and TGF on the other hand showed active bone formation with mature marrow tissue formation after the same time span. In vitro tests to evaluate the retention of the TGF inside the implant or the release from the composite were not carried out. Therefore, the results are qualitative at best; without a precise knowledge of the amount of TGF that remained at the implantation site, no statement on the biologically required concentration can be made.

From these studies, we can conclude that in most cases, in vitro and in vivo experiments were not combined. A number of studies have been carried out with in vivo evaluation only and without precise knowledge of the amount of growth factor available at the implantation site. As it has been shown that VEGF can have severe side effects when not dosed correctly [183], this approach is not suitable for serious examination of the role of the growth factor in the regeneration of the bone defect. Wernike et al. [185] have combined both approaches, carefully quantifying the adsorption capacities of their scaffold and the release kinetics from the ceramic. When changing the concentration for the in vivo experiments however, in vitro results are not presented. Overall, the study seems scientifically sound and will be used as a basis for our own studies.

Even if the combination of calcium phosphates with growth factor for the regeneration of bone defects seems obvious, no study using mesoporous calcium phosphates has been published so far to our knowledge. Macroporous calcium phosphate scaffolds as well as polymer-based compositions have been widely used but mesoporous calcium phosphates have not been available yet.

3.1.3 Techniques for protein quantification

In order to evaluate a biomaterial intended to be implanted into the body, its protein adsorption capacity must be quantified. In many applications a high adsorption is

preferred, but in some cases, it is better to have low adsorption and controlled release. Some proteins can lead to negative effects when released in great quantity. For example, VEGF has been shown to cause undirected vascularisation and ill-formed vessels when released in excess [190].

The traditional techniques used for protein quantification **in solution** are based on colorimetry, fluorometry or direct adsorbance measurements. The most commonly methods are colorimetry after staining.

3.1.3.1 Colorimetry

Colorimetry is the determination of concentration of the colored compound by the measurement of the intensity of its color. The most widespread methods for the colorimetric quantification of proteins are the BCA, the Lowry, the Bradford and the Biuret test. Table 3.2 compares their sensitivity range, accuracy and possible interfering substances [191].

BCA test. In basic solution, the amino groups in proteins and Cu^{2+} ions form a blue complex (Biuret reaction). The Cu^{2+} ions in the complex are reduced and bind to the bicinchoninic acid (BCA) to form a purple complex. The absorbance of this complex is measured at 562 nm.

Lowry test. The Cu^+ ions from the Biuret reaction also form a blue complex with the Folin-Ciocalteu reagent. The intensity of the color of this complex is proportional to the protein concentration. As a number of substances interfere with the chromophore, it is recommended to precipitate the protein from the solution and then to test the precipitate.

Bradford test. The Coomassie brilliant blue G-250 shifts its adsorption maximum from 465 to 595 nm when bound to proteins. The increase of the absorbance at 595 nm is a measure of the protein concentration. The Bradford test is very fast; the color takes only 2 min to develop. On the other hand, some proteins precipitate in the acidic conditions of the test. Strong bases and detergents interfere.

Biuret test. The purple-blue complexes that proteins form with Cu^{2+} in basic solution that is at the origin of the BCA and the Lowry test can be used directly for the determination of the protein concentration. Its absorbance can be measured between 540 and 560 nm. Normally, for the micro-Biuret-test, sodium potassium tartrate and potassium iodide are added to the basic solution. Tartrate prevents the precipitation of copper hydroxide and the iodide the self-reduction of copper. In these conditions, the intensity of color of the purple-blue complex is a direct measure of the proteins concentration. The tests based on the Biuret reaction have the advantage that they are based on the reaction of the peptide bond directly and are therefore independent of side chains and the amino acid composition of the protein.

Assay	Sensitivity	Accuracy	Interference
Biuret	0.5 µg	very high, independent of amino acid composition	organic amines, ammonium salts
Lowry	0-0.01 mg	depends partially on the amino acid composition	acids, chelators, reducing agents
Bradford	0-0.01 mg	depends on amino acid composition	detergents, surfactants
BCA	0-0.05 mg	almost independent of amino acid composition	reducing agents, chelators

Table 3.2: Comparison of the most frequently used method for the colorimetric quantification of proteins

Direct UV absorbance. The peptide bond adsorbs ultraviolet light at 205 nm. This direct absorbance can be used to quantify proteins in a concentration range of 1 to 100 µg/mL. Alternatively, the absorbance can be measured at 280 nm. At this wavelength, the aromatic residues tryptophan, phenylalanine and tyrosine absorb. Contrary to the absorbance at 205 nm, the absorbance at 280 nm depends on the amino acid composition of the protein (number of aromatic residues).

3.1.3.2 Fluorometry

Fluorometry is a related technique to colorimetry and based on the quantification of a fluorophore based on its fluorescence emission. Proteins that contain aromatic residues (tryptophan, phenylalanine or tyrosine) are fluorescent in their pristine state. The measurement of the fluorescence of pure proteins allows the determination of the protein concentration in the range of 5 to 50 µg/mL. For proteins without aromatic residues or in order to improve the fluorescence yield, fluorescent chemicals (fluorochromes) can be used that bind to the protein:

Epicoconone (extracted from the Fungus *epicoccum nigrum*) is a fluorophore that covalently binds to the lysine residue in proteins. The reaction product is fluorescent with a maximum emission at 605 nm. The quantum yield can be improved in the presence of organophilic substances, for example detergents. The advantages of this fluorimetric assay are its large detection range (40 ng/mL to 200 µg/mL) and its tolerance of most surfactants.

O-phthaldialdehyde (OPA) forms fluorescent groups with primary amines in presence of mercaptoethanol. Primary amines are contained in all proteins in the N-terminus and, depending on the amino acid composition, in the lysine residues. The emission of the complex can be stimulated at 360 nm and measured at 460 nm. As the result depends on the amino acid composition of the protein, a standard regression should be carried out with the specific protein.

3.1.3.3 Radio-labeling

Radio-labeling consists of functionalizing the protein with a radioactive tag. This molecule carries a radioactive isotope (^{125}I or ^3H) and covalently binds to the protein, rendering it detectable by scintillation or Geiger counting. The molecular tag is small compared to the size of the protein; it has however been argued that it may interfere with the protein's secondary structure and therefore change its adsorption behavior. As the radiation is able to penetrate solid materials, radio-labeling represents one of the rare methods that allow the detection of proteins trapped inside porous materials.

Methods involving radioactive material require special equipment and authorizations. Therefore, they can only be carried out in specialized laboratories.

3.1.3.4 ELISA

Enzyme linked immunosorbent assays (ELISA) are based on the specific interaction of antibodies with their substrates. Contrary to the before-mentioned methods that quantify the global protein concentration, ELISA can specifically detect a single protein from a protein mixture. The principle of ELISA is the following: the antibody is immobilized on a surface, then the protein solution is applied. The protein binds to the antibody, all the other proteins are rinsed off. The immobilized antibody-protein pair is rendered detectable by adding a second antibody that carries an enzyme. This enzyme transfers a substrate into a colored or fluorescent complex that can be quantified by colorimetry or fluorometry. A more detailed description of the ELISA method is given in section 5.3.

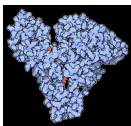
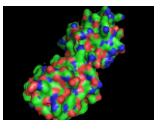
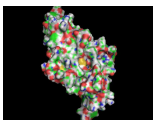
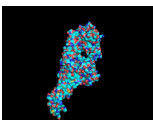
3.1.3.5 Automated methods

In analytical chemistry, automated methods like GC-MS, LC-MS/MS and ICP-MS¹ are used for the determination of the protein concentration. These methods are based on the separation of different proteins by chromatographic methods (GC, LC) or electrophoresis (prior to ICP-MS) and their identification and quantification by mass spectrometry. All of these techniques require specific equipment.

3.1.3.6 Quantification of adsorbed proteins in porous materials

The above described methods allow the quantification of protein in solution, but not the quantification of proteins that are absorbed into porous substrates. A number of techniques have been proposed for the quantification of proteins adsorbed onto surfaces (AFM, SEM, ATR-FTIR, QCM, radio-labeling, etc), but most of them (except for radio-labeling) can not be used in porous substrates. The majority of the studies published in the field therefore use the depletion method: the adsorption is carried out with a solution of known concentration. The concentration in solution is again measured after

¹GC-MS: gas chromatography coupled with mass spectrometry, LC-MS/MS: liquid chromatography with a coupled mass spectrometry detection system, ICP-MS: inductively couple plasma ionization mass spectrometry.

	BSA	Cytochrome C	TGF- β	VEGF
crystal structure				
molecular mass	66 kDa	12.4 kDa [172, 193]	44 kDa	22 kDa
number of amino acids	607	325	390	165 ¹
dimensions [nm]	12 x 3 x 3 [194]	3 x 3 x 3 [172]	7 x 5 x 3	10 x 6 x 3
isoelectric point	4.7	10.0 [193]	9.8	9.27
net charge at pH 7	positive	negative	negative	negative

¹Human VEGF 165 was used for this study. This is the major isoform. Other clones (121, 189 and 206 amino acids) have been found by cDNA analysis [195].

Table 3.3: Important data on the proteins used for adsorption and release experiments

the adsorption. The difference in concentration before and after exposure to the porous substrate is attributed to adsorbed proteins. This method can however not distinguish between surface adsorbed proteins and those who have penetrated the porosity. Errors occur when the protein adsorbs to the glassware used for the experiments and not on the substrate.

Our laboratory has developed a TPD technique allowing the quantification of proteins inside the porosity of mesoporous carbon and ceramic materials [21, 192]. Briefly, this method consists of heating the protein-loaded ceramic in vacuum and of detecting and quantifying the decomposition products of the adsorbed proteins. A more detailed description of the TPD-MS experimental set-up is given in section 5.2.

3.1.4 Proteins used for the study

For the present study, four proteins have been chosen. As explained in section 1, the growth factors TGF- β and VEGF are used because of their biological properties. They are supposed to improve the performance of the materials upon implantation.

On the other hand, these proteins are very expensive as their extraction from human tissues or their recombination by transgenic bacteria is long and costly. For preliminary studies, two model proteins were used. BSA (bovine serum albumin) is extracted from bovine blood and is one of the most frequently used proteins for biological studies. Its advantages are its abundance in bovine serum and its low cost. The dimensions and the molecular mass of BSA are higher than those of the growth factors used, the adsorption into small mesopores might therefore be more difficult.

The second model protein used is Cytochrome C. Cytochrome C is a small heme protein that can be found in the inner membrane of the mitochondrion. It is very soluble and can be handled easily in aqueous solution. As it contains an iron atom in the heme group, it can be analyzed by different physical methods such as XPS, EDX

and PIXE. In our project, analysis will be carried out with PIXE by the LPC team in Clermont. Cytochrome C is smaller than the growth factors and BSA. As the growth factors TGF- β and VEGF, it is a basic protein [73]. Therefore, it should penetrate the porosity of the ceramics in a similar way to the growth factors. For these reasons, Cytochrome C has already been used as a model for TGF [73].

The table 3.3 gathers important physical properties of the four proteins used for the characterization of the protein adsorption and release capacities of the HA materials.

3.1.5 Materials used for the protein adsorption and release experiments

For this part of the study, six powders were chosen for the protein experiments. Three of them were prepared by Olivier Raissle from the LMI in Clermont-Ferrand and three were prepared in our laboratory. They all represent different physical properties:

Sample	Origin	Calcination [°C]	S_{BET} [m ² /g]	$\varnothing_{p,BJH}$ [nm]	V_p cm ³ /g	Crystallinity	Crystallite size [nm]
A	Clermont	650	42.5	8.6	0.06	good	
B	Clermont	650	63.11	15.8	0.18	good	
C	Clermont	300	166		0.50	medium	30
J	Mulhouse	80	89.6	13.9	0.36	poor	4.9
JC	Mulhouse	500	22.1	17.2	0.09	good	34
K	Mulhouse	500	31.1	12.5	0.11	good	42.6

Table 3.4: Physical characteristics of the six HA samples used for protein adsorption experiments.

The powders J, JC and K are obtained by the concentrated solution approach from calcium nitrate and triethyl phosphite. J and JC are replicas of MCF silica. They differ in their heat treatment: J is obtained after drying the composite overnight at 80°C and dissolving the template without further calcination, JC is obtained after calcination of the composite at 500°C for 10 h and dissolution of the template. K is a replica of the carbon foam template obtained by CVD on MCF. The template is removed by selective oxidation at 500°C for 20 h. The heat treatment of the samples JC and K are carried out in similar conditions in order to obtain comparable crystallinities. Figure 3.4 shows the X-ray diffraction patterns of the six ceramics illustrating the different degree of crystallinity of the samples (cf. the width of the diffraction peaks.).

The powders A, B and C are prepared by co-precipitation methods in different conditions:

- Sample A. The synthesis is based on the co-precipitation of calcium hydroxide and ammonium dihydrogen phosphate. $\text{Ca}(\text{OH})_2$ and $\text{NH}_4\text{H}_2\text{PO}_4$ are dissolved separately in a mixture of water and ethanol. The phosphate solution is added

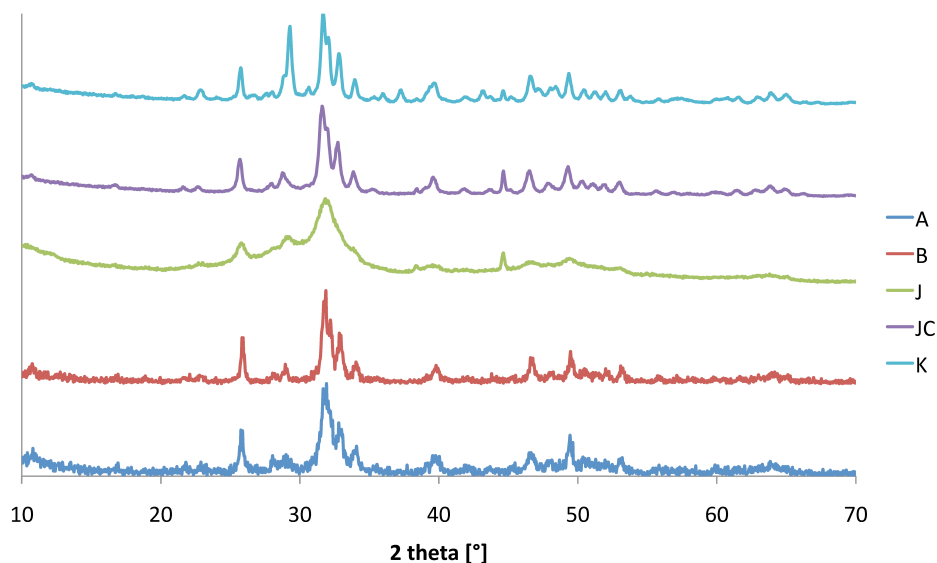


Figure 3.4: X-ray diffraction patterns of five of the six ceramic samples that have been used in the study of protein adsorption. Sample C was delivered later and was not available for characterization.

dropwise to the calcium solution while keeping the pH at 9. The solution is stirred for 24 h, freeze dried and calcined at 650°C.

- Sample B. Same method as for sample A, but instead of freeze-drying, the powder is dried at 100°C for 24 h before calcination.
- Sample C². The synthesis is based on the co-precipitation of calcium pantothenate and dipotassium hydrogenphosphate in presence of the non-ionic surfactant pluronic® F127. Figure 3.5 shows the formula of the surfactant and of the pantothenate ion. F127 is mixed into the solution of $\text{Ca}(\text{C}_9\text{H}_{16}\text{NO}_5)_2$. The K_2HPO_4 solution is added dropwise to this solution at pH 12. The mix is stirred for 24 h, then filtered and the powder is washed five times with ethanol in order to eliminate the surfactant. The powder is dried at 100°C for 12 h, then calcined at 300°C.

²C* in the nomenclature of Olivier Raissle. In the present thesis, this powder will always be referred to as C.

3.2 Experimental

3.2.1 Characterization of the ceramics in view of the protein experiments

3.2.1.1 ζ -Potential

When ceramic particles are dispersed in a liquid, ions on their surface dissolve into the solution, leaving a electrically charged surface. The dissolution process depends on the nature of the ceramic surface, the pH and the ionic strength of the solution. The charged ceramic particles repulse each other at long distances due to electrostatics. A stable colloidal solution is obtained when the repulsive forces are sufficiently strong to prevent the particles from diffusing near each other; At short distances attractive Van-der-Waals forces dominate over the repulsion and lead to aggregation and precipitation.

The repulsion of two particles in dispersion depends on the particle size, the concentration of mobile ions and the surface charge (in which we are interested here). The attraction depends on the strength of the van-der Waals forces which are described by the Hamaker coefficient. The estimation of attraction and repulsion of charged particles in dispersion can be described by the DLVO theory. In solution, the charged particles are surrounded by ions of the opposite charge. These ions create a shielding effect causing the electrical field of the particle to reduce with increasing distance from the surface. The diminution of the electric field is more abrupt when the salt concentration of the solution is high. The particle surface and the surrounding ions form the so called *electric double layer*. The thickness of the electric double layer is commonly referred to as the Debye-Hückel screening length κ^{-1} . The zeta-potential, ζ is defined as the electrical potential at the "shear plane" of the particle. In stable colloidal solutions this shear plane is close to the surface of the particle and the value of ζ is therefore a good approximation of the surface charge of the particle. The ζ -potential can be calculated from the electrophoretic mobility of the particles in dispersion (Smulochowski equation):

$$\zeta = \frac{4\pi\eta}{\epsilon} \cdot U \quad (3.1)$$

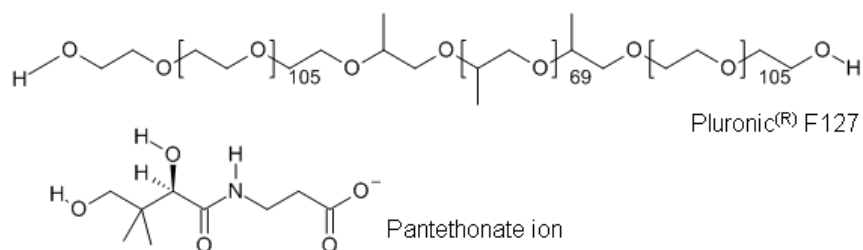


Figure 3.5: Chemical formula of Pluronic ® F127 and the pantethonate ion.

$$U = \frac{\nu \cdot L}{V} \quad (3.2)$$

where

ζ the ζ -potential,

η the viscosity of the solution,

ϵ the dielectric constant of the solution

U the electrophoretic mobility of the particle

ν the speed of the particle

V the voltage and

L the distance of the electrodes.

5 mg of hydroxyapatite are treated with ultrasonics for 5 min in 10 mL distilled water, PBS or culture medium (DMEM). The ζ -potential of the supernatant dispersion is immediately measured on a Malvern Instruments Nano ZS at 25°C. The sample is allowed to stabilize for 1 min and then measured with an initial voltage of 1.2 mV. In the case of sample C, the signal-to-noise ratio was very low, and the measurement was repeated with increased concentration. The ζ -potential is calculated by the build-in software of the instrument using the Smoluchowski formula (see equation 3.1 on page 133). The following parameters are assumed for the dispersants:

Dispersant	refractive index	dielectric constant	viscosity [cPo]
Water	1.333	80.1	1 ¹
PBS	1.399	80	1.05 [196]
DMEM	1.3395	80	0.9009 [197]

¹ build-in model of the ZetaSizer software

3.2.1.2 Dissolution kinetics of the ceramics

During the protein adsorption and release experiments, the ceramics are exposed to saline solutions. A series of preliminary tests is carried out in order to observe their dissolution behavior in presence of water, PBS and culture medium (DMEM). 10 mg of HA are filled into an Eppendorf tube and 1000 μ L of liquid are added. The samples are agitated at room temperature on a stumbling shaker for 1, 8 or 30 h. The tube is centrifuged and the liquid retrieved using a micropipette. The Ca^{2+} concentration of the supernatant is determined using the DiaSys Calcium As FS* kit. This kit is based on the formation of a blue complex between Arsenazo III and calcium ions in neutral solution. The concentration is determined by absorbance measurements at 650 nm. The reference solution was prepared with pure distilled water and the reagent. Calcium concentrations were calculated from a 8 point regression curve between 0.1 and 1 mg/mL.

For comparison, the concentration of calcium in water, PBS and DMEM was determined by the same method.

3.2.2 Model proteins: BSA and Cytochrome C

Proteins and PBS tablets were obtained from Sigma-Aldrich and were used as received. Protein solutions were kept at 2°C and used within two weeks. Experiments with model proteins were carried out on samples A, B, J, JC and K.

For the adsorption of BSA, powder samples with a weight between 9 and 11 mg were weighted into 1.5 mL eppendorf tubes. A stock solution of 10.15 $\mu\text{mol/L}$ of BSA in PBS were prepared and stored at 2°C. 400 μL of this solution were added to the eppendorff tubes and stirred using a rotative table at 100 rpm at room temperature (the room was not air conditioned). After given time periods, the tubes were centrifuged at 1200 rpm for 5 minutes, and the supernatant was retrieved carefully using a micropipette. For every time point, two samples were used.

50 μL of the protein solution were mixed with 1.5 mL Bradford solution³ and allowed to react for 10 minutes at room temperature. The solutions were transferred into single use polystyrene cuvettes that were 10 mm large. The adsorbance was measured at 595 nm against a sample of Bradford solution mixed with 50 μL of PBS. Every sample of supernatant was assayed twice.

The concentration of the solution was calculated from the adsorbance using a ten point regression curve for concentrations between 0.2 and 10 $\mu\text{mol/L}$. A normalization was carried out to compensate the mass difference: the concentration calculated for the sample was divided by the exact mass of the powder sample to make sure that mass differences did not interfere with the results.

For the adsorption of Cytochrome C, powder samples with a weight between 9 and 11 mg were weighted into 1.5 mL eppendorf tubes. A stock solution of 40 $\mu\text{mol/L}$ of Cytochrome C in water was prepared. The pH of the water was adjusted to 8.5 with NaOH and HCl and controlled after the dissolution of the protein. Adjusting was carried out if necessary. 500 μL of this solution were added to each tube containing the powder and shaken at room temperature at 100 rpm for a given period. The tubes were centrifuged at 1200 rpm for 5 minutes, and the supernatant was carefully retrieved using a micropipette. For every time point, two samples were used.

The supernatant was transferred to a single use polystyrene cuvette that was 10 mm large. The adsorbance was measured directly at 409 nm against water adjusted to pH 8.5. Only one measurement was carried out per sample.

The concentration of the protein solution was calculated from a six point regression curve for concentrations between 5 and 40 $\mu\text{mol/L}$. The concentration was normalized as described for the BSA adsorption.

For the BSA release experiments, adsorption was carried out for 24 h as described. The samples were centrifuged and the supernatant was retrieved. Every sample was

³Coomassie Plus - the better Bradford Assay TM Reagent, Thermo Scientific Product Number 23238

washed rapidly with 400 μ L DMEM and centrifuged again. The supernatant was retrieved and assayed as described previously. It will be referred to as *washout* in the following. 400 μ L DMEM were then added to the sample and the tube was agitated at room temperature for 1, 2 or 3 days. All samples were run in duplicates. The tube was centrifuged and the supernatant assayed twice.

For the Cytochrome C release experiments, adsorption was carried out for 24 h as described above. The samples were centrifuged and the supernatant was retrieved. Every samples was washed rapidly with 500 μ L DMEM and centrifuged again. The supernatant was retrieved and assayed as described previously. It will be referred to as *washout* in the following. 500 μ L DMEM were then added to the sample and the tube was agitated at room temperature for 1, 2 or 3 days. All samples were run in duplicates. The tube was centrifuged and the supernatant assayed.

3.2.3 Growth factors TGF-beta and VEGF

Proteins were purchased from Peprotech and used as received. TGF- β was reconstituted in 10 mM solution of citric acid and VEGF₁₆₅ in distilled water. Aliquots were stored at -20°C. Prior to use, proteins were thawed at room temperature and diluted to a working concentration of 1 μ g/mL. Diluted protein solutions were used the same day. Reconstitution and dilution were carried out under sterile conditions.

The determination of the protein concentration was carried out by sandwich ELISA kits obtained from R & D systems⁴ following the instructions provided by the manufacturer. A description of the principle of ELISA protein quantification can be found in section 5.3 on page 175.

For the adsorption of growth factors, powder samples with a weight between 9 and 11 mg were weighted into 1.5 mL Eppendorf tubes. 300 μ L of protein solution were added to each sample. The tubes were agitated at room temperature at 90 rpm using a tumbling shaker. After the desired time period, the tubes were centrifuged and the supernatant carefully retrieved using a micropipette. For every time point, two samples were used. The supernatant was either frozen and thawed before analysis or analyzed the same day.

The determination of the protein concentration was carried out by sandwich ELISA assays and run in duplicates.

For the growth factor desorption experiments, powder samples weighing between 9 and 11 mg were sterilized at 180°C in dry heat for at least one hour. They were then cooled down to room temperature and transferred to autoclaved 2 mL eppendorff tubes in sterile conditions. Protein solutions were prepared under sterile conditions. 300 μ L of protein solution were added to each sample. Adsorption was carried out for 24 h in

⁴TGF- β : Human TGF-beta 1 DuoSet, Reference DY240; VEGF: Human VEGF DuoSet, Reference DY293B

an air conditioned room at 24°C. The tubes were centrifuged at 1200 rpm for 5 min. The supernatant was retrieved using a micropipette and frozen for ELISA assay. The powders were washed with 300 μ L DMEM and centrifuged again. The supernatant was retrieved and frozen for ELISA. It will be referred to as *washout* in the following. 300 μ L fresh DMEM were added to each sample. The tubes were agitated for 1, 2, 3 or 4 days on a tumbling shaker at 90 rpm at 24°C. The tubes were then centrifuged and the supernatant was retrieved and stored at -20°C until analysis by ELISA. Every sample was assayed twice.

3.2.4 Thermo-programmed desorption

The principle of TPD experiments is briefly described in section 5.2 on page 174.

All TPD experiments were carried out in a custom-build TPD apparatus equipped with a quadrupole mass spectrometer (Inficon Transpector II). The apparatus was specifically adapted to small gas volumes by reducing the volume of its ramps and conducts to the strict minimum. The high vacuum was achieved using a turbomolecular pump. The overall gas pressure was measured with a ionization pressure gauge. The sample was introduced into a horizontal quartz tube in a fused silica vessel. In the case of liquid samples (protein solutions), the sample was kept under primary vacuum for several hours until the pressure had diminished under 10^{-7} Torr. In this case, the sample was first heated to 150°C and kept for at least 1 h in order to desorb a maximum amount of water.

The measurements were carried out using a 2 K/min heating rate and a maximum temperature of 600°C. Mass spectra were recorded all 30 s in a mass range of 1-100 mass units. The sensibility of the spectrometer was tested before each experiment by the injection of pure nitrogen. In order to allow the precise quantification of the decomposition gases, the spectrometer was calibrated with known quantities of hydrogen, nitrogen, carbon dioxide, carbon monoxide, hydrogen sulfide and ammonia. For the analysis of H_2S , the signals at $m/z=33$ and $m/z=34$, corresponding to HS^+ and H_2S^+ respectively, were used. The total amount of a gas desorbed during the experiment can be calculated by the integration of its desorption curve.

Ceramic	ζ -potential [mV]		
	in water	in PBS	in DMEM
A	-13.6	-16.2	-4.1
B	-5.5	-14.0	-1.8
C	-8.6	-7.9	¹
J	-15.3	-16.9	-6.15
JC	-23.3	-18.6	-6.7
K	-14.0	-18.5	-10.7

¹ Here, the ζ -potential was close to zero, causing the particles to precipitate.

Table 3.5: ζ -Potential of the ceramic samples in different media at 25°C.

3.3 Results

3.3.1 Characterization of the ceramics in view of the protein experiments

3.3.1.1 ζ -Potential

The adsorption of proteins onto ceramics depends on the charge both of the bioorganic molecule and the surface charge of the ceramic particles. The surface charge of the ceramic can be evaluated by measuring its ζ -potential.

Table 3.5 summarizes the results of ζ -potential measurement of the six ceramics in water, PBS and DMEM. In all cases, the ζ -potential of the ceramics is negative, indicating that the surface of the ceramics carries a negative net charge. Except for JC, the ζ -potential in PBS is more negative than in water. This can be attributed to a shielding effect of positive ions contained in the solution: the negatively charge ceramic surface favors the approach of cations which will favour the approach of anions, so that the overall charge of the particle is more negative than in water. Besides ions, DMEM additionally contains amino acids, sugars and vitamins. Compared to PBS the ionic strength is higher. The high ionic strength causes the electric double layer to shrink and to become more dense. This reduction of the layer thickness results in a decrease of the absolute value of the ζ -potential.

3.3.1.2 Dissolution kinetics of the ceramics

Table 3.6 gathers the results of the dissolution tests for the different ceramic samples.

For comparison, the initial calcium concentration in the three media was measured. Whereas water and PBS contain no calcium, the initial calcium concentration in DMEM is 0.44 mg/mL.

solution	A			B			C		
	1 h	8 h	30 h	1 h	8 h	30 h	1 h	8 h	30 h
H ₂ O	0.13	0.20	0.14	Ø	Ø	Ø	Ø	Ø	Ø
PBS	Ø	Ø	0.24	Ø	Ø	Ø	Ø	Ø	Ø
DMEM	Ø	0.18	0.13	0.28	0.24	0.20	Ø	Ø	0.16

solution	J			JC			K		
	1 h	8 h	30 h	1 h	8 h	30 h	1 h	8 h	30 h
H ₂ O	0.3	0.24	0.35	Ø	0.38	1.35	0.24	0.15	0.13
PBS	Ø	Ø	Ø	Ø	Ø	Ø	0.16	Ø	Ø
DMEM	1.46	1.55	1.55	0.62	0.50	0.82	0.56	0.62	0.59

Concentrations in mg/mL.
Ø stands for non-quantifiable (concentration inferior to 0.1 mg/mL).
The calcium concentration in water and PBS is zero and in DMEM 0.44 mg/mL.

Table 3.6: Calcium concentration in water, PBS and DMEM after exposure to the different ceramic samples.

Sample A shows light dissolution in water at all time points and in PBS, after 30 h. In DMEM, re-precipitation is observed: the concentration of the supernatant is lower than in the DMEM that was not in contact with the ceramic. After the first hour the concentration in the supernatant DMEM is that low that it can not be quantified. After prolonged exposure, the concentration rises again, but does not attain the initial concentration of pure DMEM.

Sample B and C do not dissolve in water or PBS. In DMEM, the initial calcium concentration is lowered, evidencing precipitation of calcium species from the solution. The precipitation is stronger on sample C than on sample B. In the case of sample C, the calcium contained in the culture medium is precipitated completely at short exposition times. For longer exposition, a light re-dissolution is observed.

Sample J dissolves in water and DMEM, but not in PBS. It is the sample with the most important dissolution in culture medium of all tested ceramics.

Sample JC dissolves in water and DMEM. Compared to the sample J, the dissolution in water onsets later, but is more important at longer exposition times. In DMEM the dissolution is weaker than for J.

Sample K shows light dissolution in water at all time points and at short exposition times in PBS. After the first hour the calcium species that have dissolved into the solution, are re-precipitated and the concentration in solution decreases again. The concentration release into water is higher than in PBS. Light dissolution is observed in DMEM as well, but no re-precipitation.

Figures 3.6 and 3.7 show Scanning Electron Micrographs for the ceramic samples before and after exposure to 300 µL VEGF solution for 24 h, followed by exposure to

	A		B		C		J		JC		K	
	before	after	before	after	before	after	before	after	before	after	before	after
Ca/P	1.26	1.64	1.31	1.55	1.4	1.28	1.69	1.73	1.67	1.57	1.71	1.55
Ca	5.54	16.31	8.37	18.63	6.75	13.09	9.86	15.25	13.94	17.33	10.82	15.2
P	4.40	9.92	6.39	12.04	4.81	10.24	5.84	8.80	8.35	11.05	6.34	9.81
C	47.58	12.26	34.77	–	48.00	–	27.62	–	20.20	5.02	32.38	8.05
O	42.33	32.98	50.32	65.92	40.09	69.85	51.07	61.82	54.94	63.09	50.47	64.19
Si	–	–	–	–	–	–	3.97	4.51	1.43	1.04	–	–
Na	–	0.93	–	1.66	0.26	3.39	1.65	2.85	1.16	0.86	–	1.31
Cl	–	0.87	–	1.72	0.10	2.29	–	5.41	–	1.62	–	1.43

Table 3.7: EDX results for ceramic samples before and after exposure to 1 mL VEGF solution and DMEM for 24 h each. All values are in atomic percent.

DMEM for 24 h (first two stages of desorption experiments). The EDX results of the same samples are summarized in table 3.7. It has to be noted that EDX is not a method of choice for the quantification of elements within a ceramic sample: the analysis only reaches a certain surface layer of the sample and is at best semi-quantitative. Nevertheless, EDX can be used to compare differences of the same sample before and after exposure of the ceramic to the protein solution.

First of all, we notice that the Ca/P ration of the powders A, B and C is lower than the expected value of HA (1.67). We could therefore assume that this samples are not composed of pure HA, and contain other calcium phosphates. However, the X-ray diffraction patterns (see figure 3.4 on page 132) confirm that the bulk is composed of hydroxyapatite. It must be kept in mind that EDX only analyzes the surface of the particle whose chemical composition can be different from the bulk. ICP-AAS analyses that have been realized at the LMI in Clermont confirm that the samples are mainly hydroxyapatite (internat communication).

All samples contain sodium and chlorine after their exposure to culture medium. These ions are contained in the medium and appear on the samples in EDX. Before EDX, the samples were not washed and dried directly.

Sample A shows an increase of the Ca/P ratio after exposure to protein solution and culture medium. The initial ratio of 1.26 rises to 1.64 and thus approaches the theoretical ratio of pure hydroxyapatite. The calcium and the phosphorus content rise, too, whereas the carbon and oxygen content are observed to decrease. From these observations we can conclude that the powder initially contained carbonates and calcium deficient HA. After the treatment, the carbonate was dissolved and a Ca richer, but still deficient HA remained. The raster electron micrographs show a smooth surface for the initial compound and a rough surface after the exposure. Small grains are precipitated on the surface and holes have appeared due to dissolution. This is consistent with the Ca concentration in DMEM, which decreases by exposure to the ceramic, evidencing some precipitation.

Sample B did not show dissolution in water or PBS, but slight precipitation in DMEM.

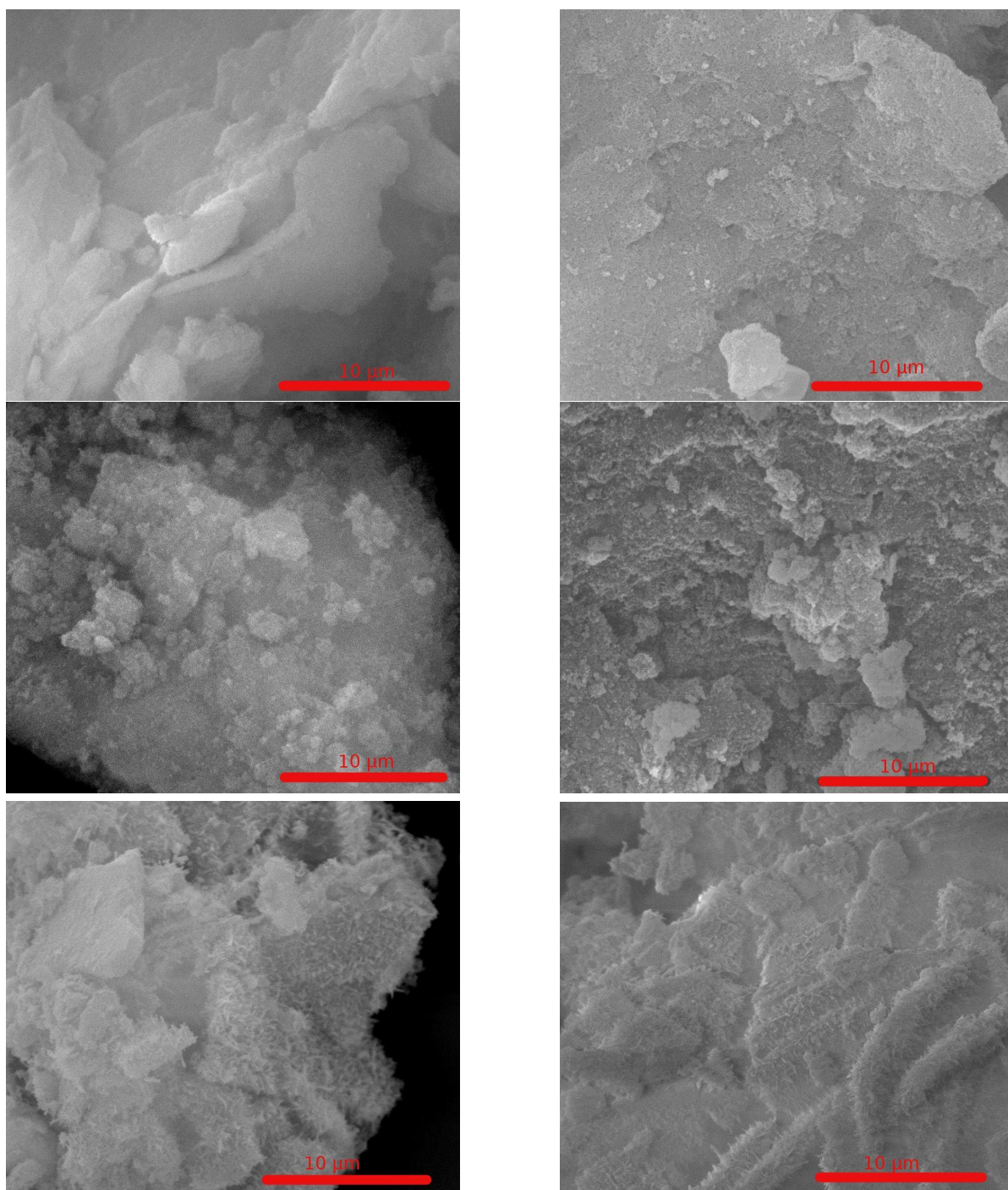


Figure 3.6: Scanning electron micrographs of the samples A, B and C (from top to bottom) before (left) and after (right) exposure to protein solution and DMEM.

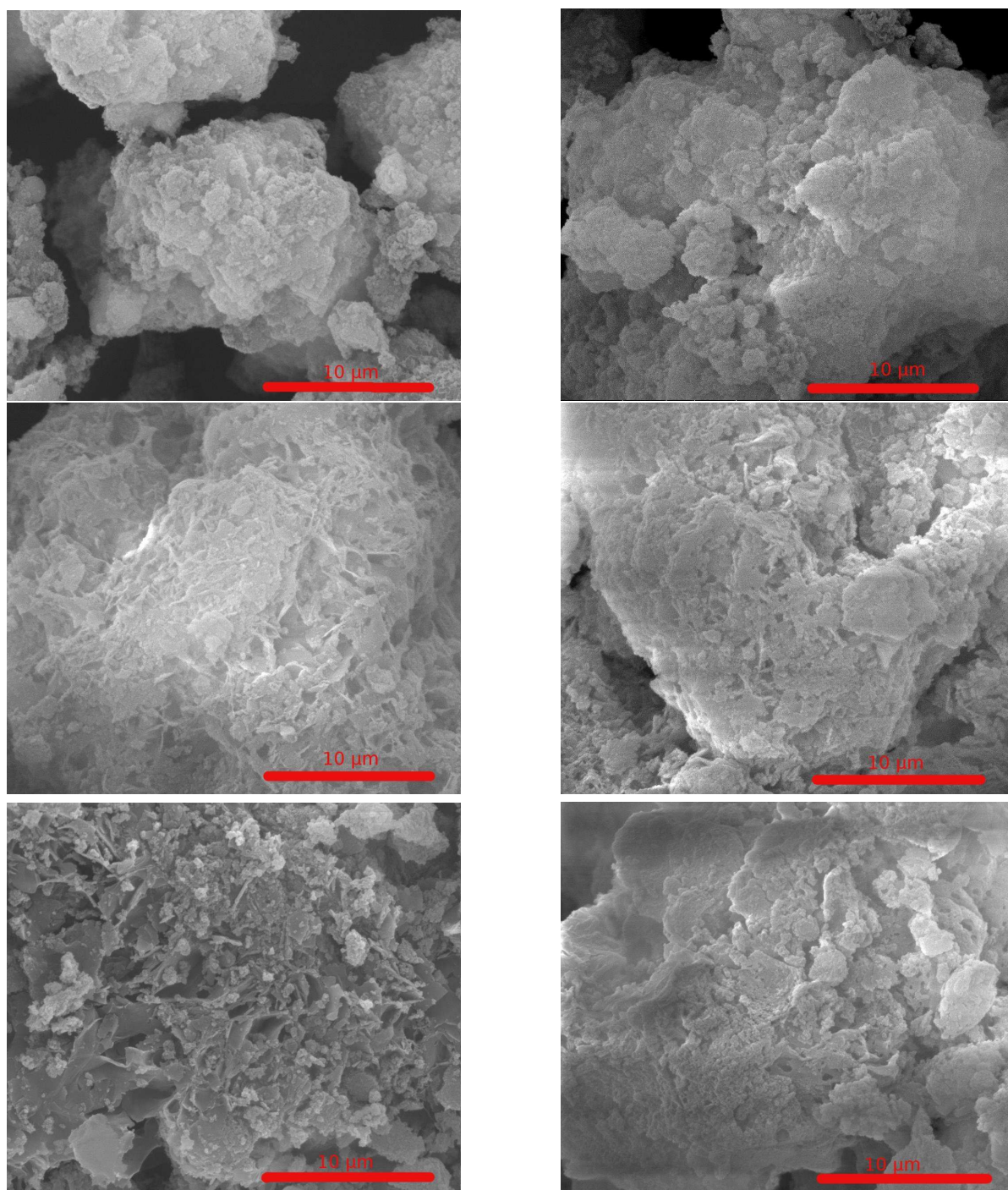


Figure 3.7: Scanning electron micrographs of the samples J, JC and K (from top to bottom) before (left) and after (right) exposure to protein solution and DMEM.

The initial Ca/P ratio is low (1.33) and rises with exposure to 1.55. Even so, the product is still calcium deficient. The smoother surface as shown in the SEM images (figure 3.6) of the initial powder compared to the treated one and the rising Ca concentration in DMEM evidence precipitation in culture medium. We can conclude from these observations that the initial powder contained soluble low-calcium impurities.

Sample C showed precipitation in DMEM, but the Ca/P ratio decreases from 1.4 to 1.28 during exposure. It seems that the initial powder contained soluble calcium species that are eliminated during DMEM exposure. C is the only sample that contained sodium and chlorine before exposure to culture medium. It is possible that the sample contained a soluble calcium phosphate, for example TCP⁵. This would explain the decrease in calcium content and the increase of the atomic percentage of oxygen in the sample after exposure. The SEM images seem unchanged before and after exposure. Both images show a characteristic surface structure composed of vertical platelets that are agglomerated on bulk surfaces. It is possible that precipitated particles are inserted between the platelets and are not apparent on the images.

Sample J dissolves to a large extent. In consequence, the surface of the grains are smoother after exposure to culture medium (see figure 3.7 as sharp edges dissolve first due to higher surface energy). The Ca/P ratio increases from 1.69 to 1.73, indicating the dissolution of a carbon-rich phosphorus species. This could be unreacted (EtO)₃PO because the sample was not calcined. The sample contains silica and sodium before exposure. The silica is certainly residual template that has not been eliminated completely. The sodium may derive from the NaOH template removal treatment. SEM images show relatively smooth surfaces both before and after exposure. After exposure, the roughness is even reduced compared to the pristine sample.

Sample JC dissolves slightly in DMEM and its Ca/P ratio is reduced after exposure. It contains silica and sodium just as sample J from which it is derived. The initial Ca/P ratio was the one of pure HA (1.67), but decreases a bit during exposure to reach 1.57. We can conclude that the sample contained soluble calcium species. Interestingly, the sample is subject of important chlorine deposition in culture medium. The SEM images show no evident change, but the surface seems slightly smoothed due to the deposition of precipitates from the culture medium.

Sample K shows a very rough surface in the SEM images. Platelets and spherical particles coexists on the bulky grains. After exposure, the surface is considerably smoothed and appear homogeneous, now. Despite the calcination, the sample dissolves partially. After protein desorption experiments, white grains are visible on the gray powder, evidencing re-precipitation. In EDX, the Ca/P ratio decreases from 1.71 to 1.55 during exposure. Oxygen content increases whereas carbon content decreases. We can conclude that calcium-rich species dissolve and that these species probably contain carbon as well. the extent of the dissolution is considerable as show the high calcium concentrations in the supernatant and the SEM images.

⁵Such a phase has not been detected by X-ray diffraction. It is possible that the TCP is amorphous and does not diffract the X-ray beam. Another possibility is that the calcium content decreases only locally at the surface of the grain). EDX is not able to determine the elemental composition of the bulk material.

Sample	BSA [$\mu\text{mol/g}$]	Cytochrome C [$\mu\text{mol/g}$]
A	0.23	0.73
B	0.17	0.89
J	0.056	1.03
JC	0.038	1.74
K	0.044	1.28

Table 3.8: Amount of protein adsorbed after 24 h of exposition to the protein solution. Normalized per g.

3.3.2 Model proteins

Figure 3.8 shows the results of the adsorption experiments of BSA on five different ceramic samples. The kinetics seem to be comparable and fast: The maximum amount of BSA is adsorbed after the first hour of exposition to the protein solution and does not evolve with time. The amount that can be adsorbed varies with the ceramic: The powders A and B adsorb about $0.2\mu\text{mol/g}$ respectively. This corresponds to 120 mg/g . The powders J, JC and K only adsorb less than half that amount. The exact values can be found in table 3.8.

Results of release experiments are shown in figure 3.9. The first two points correspond to the initial loading of the ceramic after 24 h of adsorption and the loading remaining after wash out respectively. In the case of the samples A, B, and J, the initial loading rate is higher than for the ceramics JC and K, but most of the protein is eliminated during washout. The powders JC and K on the other hand, retain less protein but the protein adsorbed on these samples withstands washing and is released over one day.

The adsorption profiles for Cytochrome C are shown in figure 3.10. The adsorption is fast for all powders and reaches its maximum after the first hour (except on J, where the adsorption takes two hours). The amount of protein on the other hand varies greatly from one ceramic to the others. The variation are however not as pronounced as for BSA: A and B adsorb 0.73 and $0.89\mu\text{mol/g}$ respectively, J, JC and K adsorb 1.03 , 1.74 and $1.28\mu\text{mol/g}$. The amount of protein retained follows an opposed trend compared to BSA: A and B that adsorb the highest amounts of BSA adsorb less Cytochrome C than the other samples. Table 3.8 compares the amounts of BSA and Cytochrome C adsorbed after 24 h.

Figure 3.11 shows the kinetics of desorption for Cytochrome C. Contrary to BSA, Cytochrome C is only partially washed out, and the remaining protein can be release progressively over at least two days.

3.3.3 Growth factors

Figure 3.12 shows the adsorption kinetics of TGF on the different ceramic samples. Unlike the model proteins, the TGF adsorbs more slowly in the ceramics. The adsorption

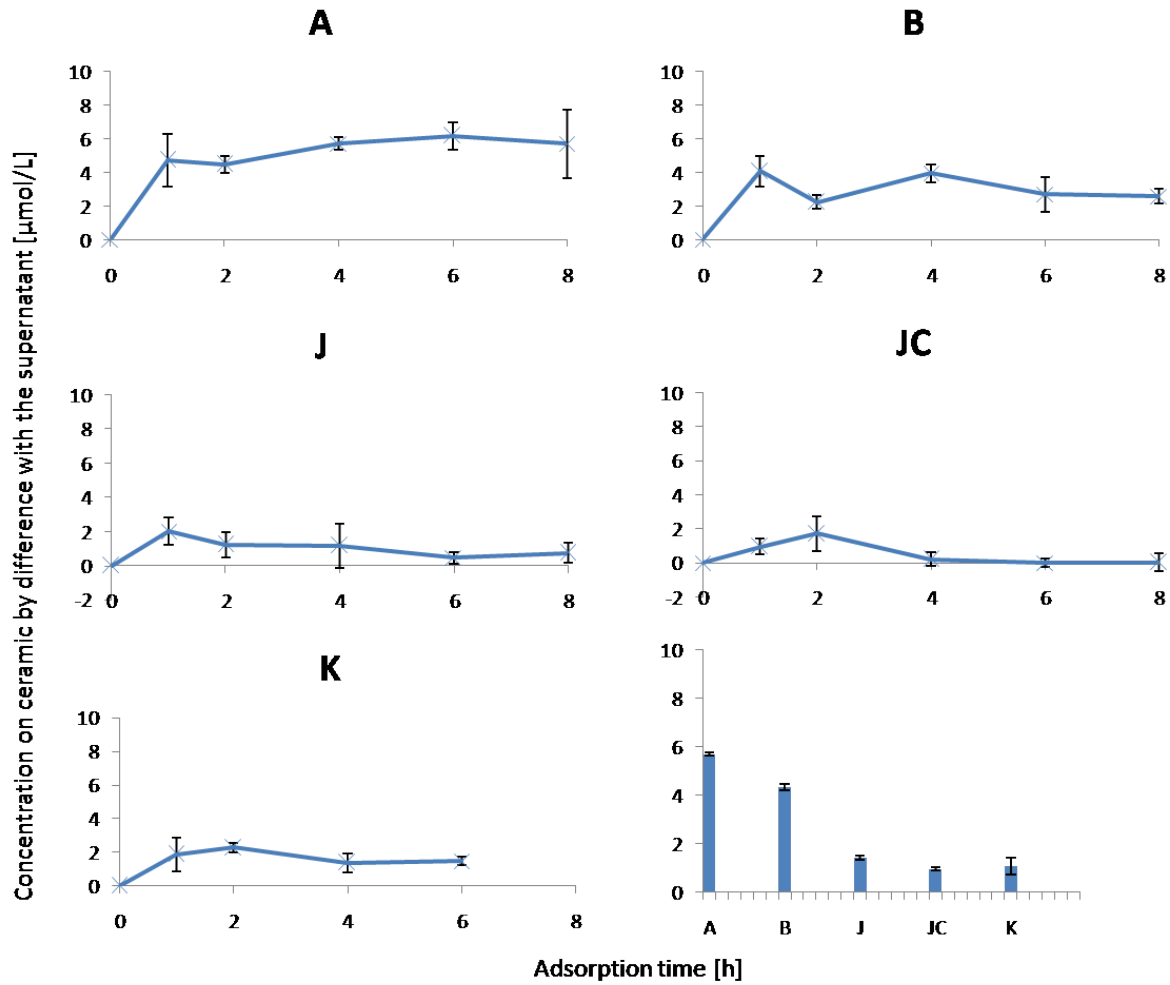


Figure 3.8: Adsorption kinetics of BSA on different ceramic samples. Initial concentration was $10.15 \mu\text{mol/L}$. The graphic down right shows the quantity of protein adsorbed after 24h. Error bars were obtained for two samples at each time point and two measurements of each concentration.

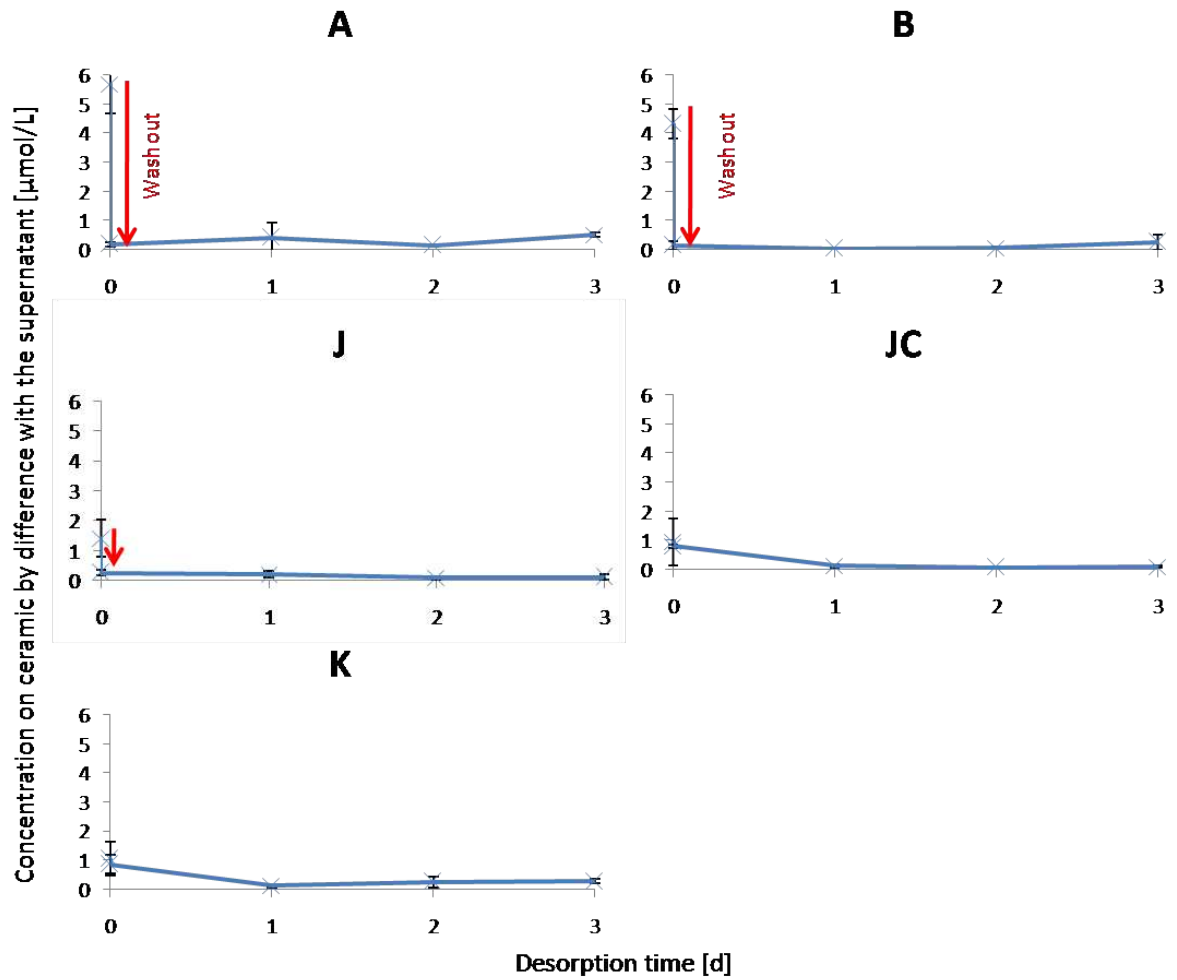


Figure 3.9: Release experiments of BSA impregnated samples. The first two values correspond to the original loading of the ceramic after adsorption of 24 h, and the protein loading after wash out. Error bars were obtained for two samples at each time point and two measurements of each concentration.

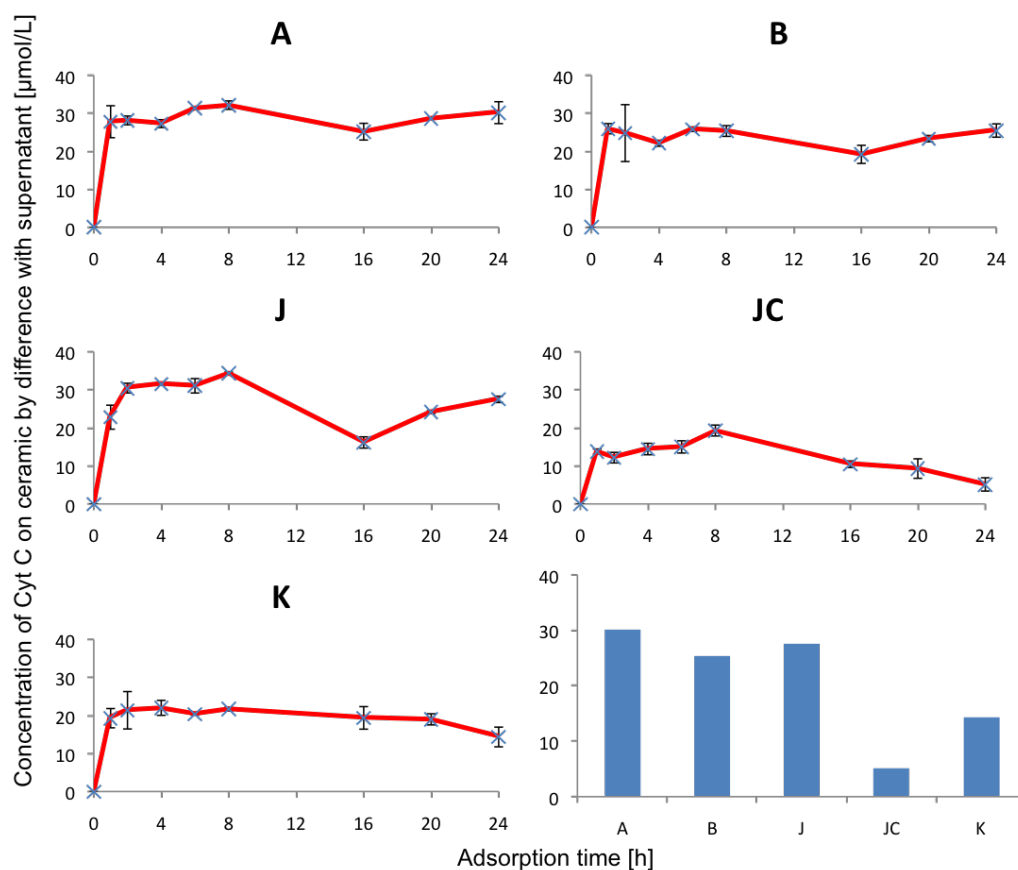


Figure 3.10: Adsorption kinetics of Cytochrome C on different ceramic samples. The 12 h data point was omitted due to temperature induced fluctuations. Initial concentration was $40 \mu\text{mol/L}$. Error bars were obtained for two samples at each time point. The last graphic shows the amount of Cytochrome C adsorbed after 24 h on the different ceramics.

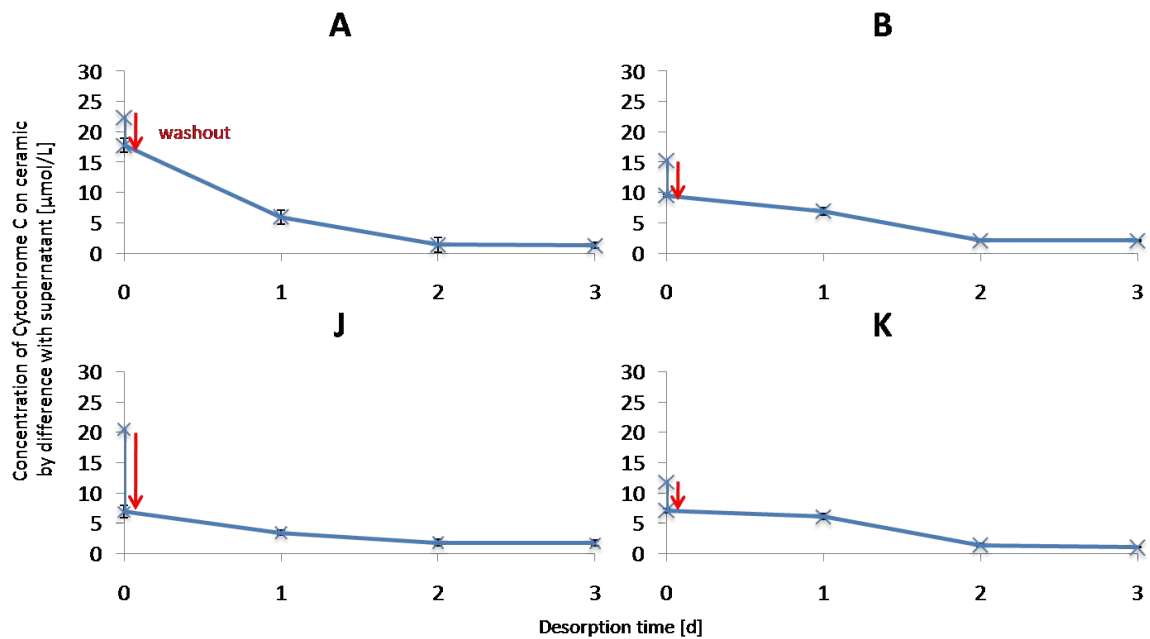


Figure 3.11: Desorption kinetics for Cytochrome C. Errors bars obtained from two samples per time point.

capacities of the different ceramics are quite close: after 8 h of exposition, the ceramics adsorbed between 23 and 28 μg par gram of powder. The exact values can be found in table 3.9. The only sample that shows less adsorption is the ceramic JC which adsorbs the least amount of protein.

Desorption kinetics for the release of TGF from the ceramic samples are shown in figure 3.13. During wash-out, no protein is released into the solution, the totality of the protein remains on the ceramic sample. All samples except sample K show desorption into the culture medium in the first 24 h. For sample A, further desorption is observed between the second and the third day, whereas the other samples (except JC) remain

Sample	TGF- β [μg/g]	VEGF [μg/g]
A	25.2	27.6
B	23.7	25.8
C	27.6	27.3
J	23.4	28.2
JC	19.2	27.0
K	23.1	33.0

Table 3.9: Growth factor adsorption on the different ceramics after 8 h of exposition. Initial concentration was 1 μg/mL.

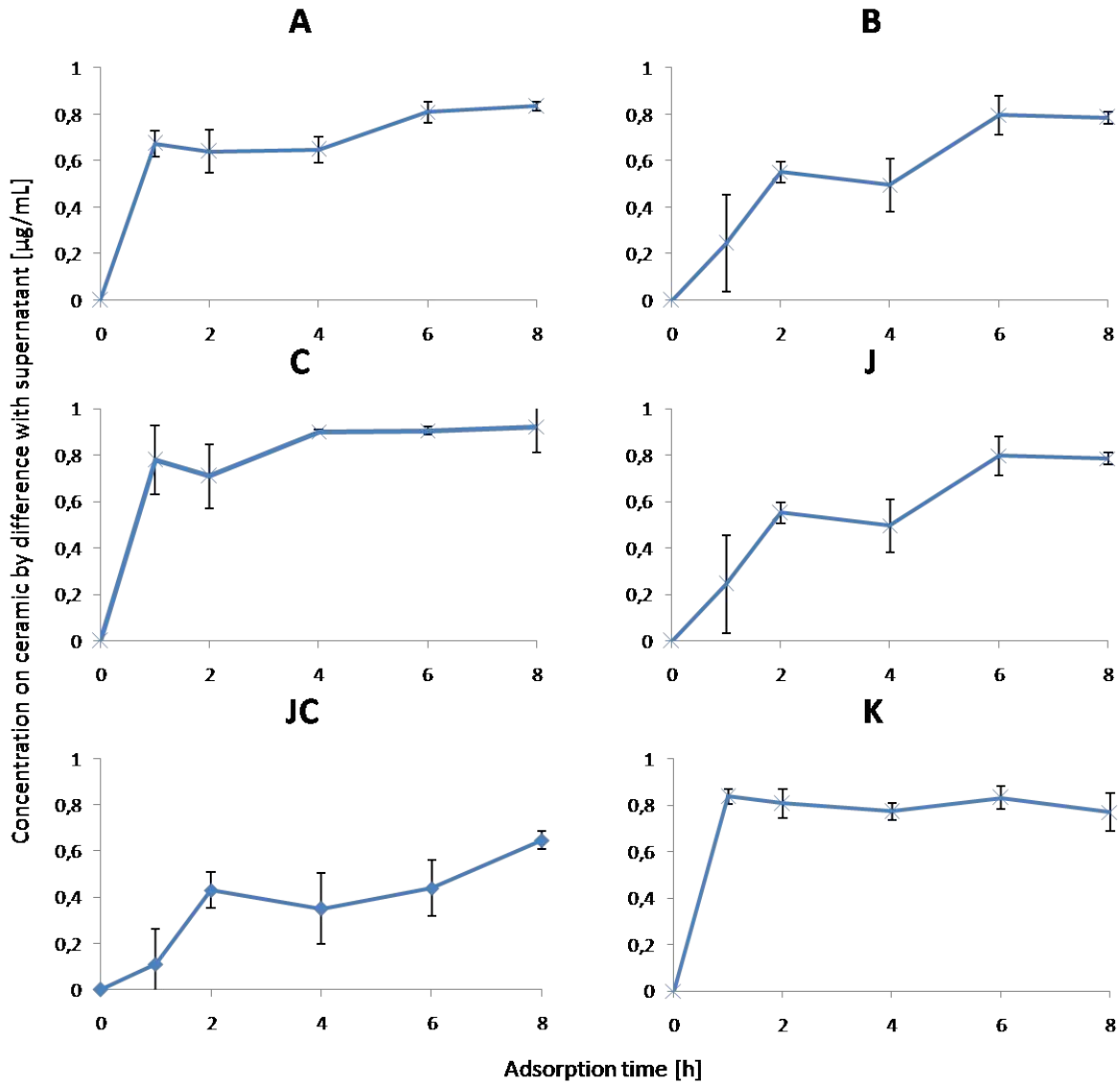


Figure 3.12: Adsorption kinetics of TGF- β on different ceramic samples. Error bars were obtained for two samples at each time point and two measurements per sample. The initial concentration of the protein solution was $1\mu\text{g/mL}$.

stable after the initial desorption. Considering the large error bar for the value after the first day in the case of sample C, we can conclude that the protein concentration in the supernatant is stable after the first day of desorption. In all cases, only a small part of the initial protein load is released into the culture medium, the majority (between 9.6 for sample JC and 22.6 μg for sample C) remain on the ceramic. As during adsorption, the behavior of the sample JC is different from the others. JC continues to release protein after the first day, and might continue to do so if exposed longer. During the experiments, the release seems to slow down after the third day of exposure, but an extrapolation of future behavior is difficult. Sample K does not show any desorption at all over the whole analysis period (3 days).

Figure 3.14 shows the results of the adsorption experiments with VEGF. Results from desorption experiments are shown in figure 3.15. The adsorption of VEGF on the different samples is fast and complete. Within one hour, all samples adsorb ninety percent of the protein present in solution. The differences between different ceramics are neglectable. Considering the standard deviation of the measurement, the desorption behavior of all samples has to be considered equivalent for all samples: During washing, no protein is released into the solution. During the exposition to the culture medium, all samples release about a third of their initial protein loading within the first day of exposition. After that, the remaining protein is maintained in the ceramic.

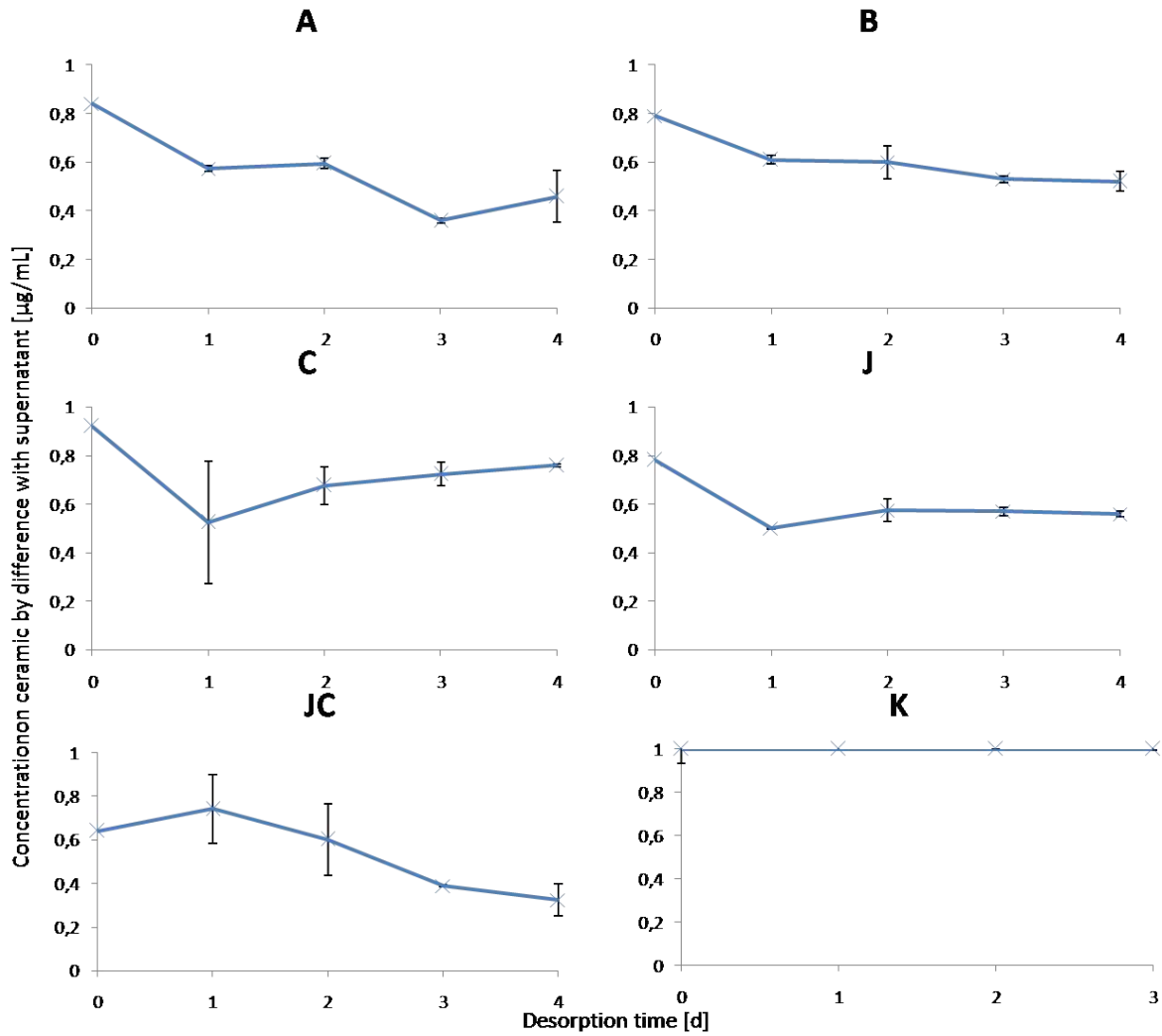


Figure 3.13: Desorption kinetics of TGF- β into DMEM from different ceramic samples. Error bars were obtained for two samples at each time point and two measurements per sample.

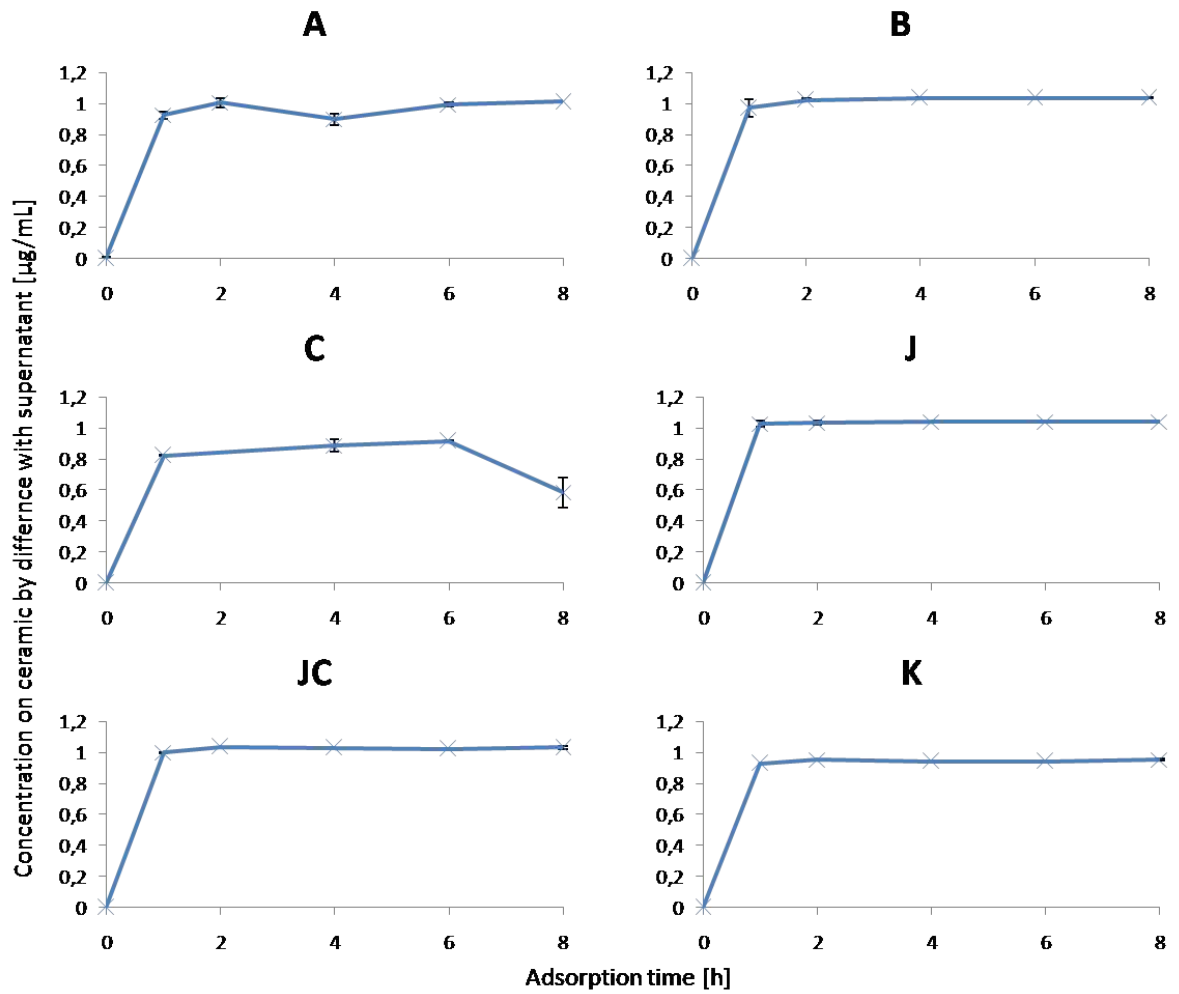


Figure 3.14: Adsorption kinetics of VEGF on different ceramic samples. Error bars were obtained for two samples at each time point and two measurements per sample. The initial concentration of the protein solution was $1\mu\text{g/mL}$.

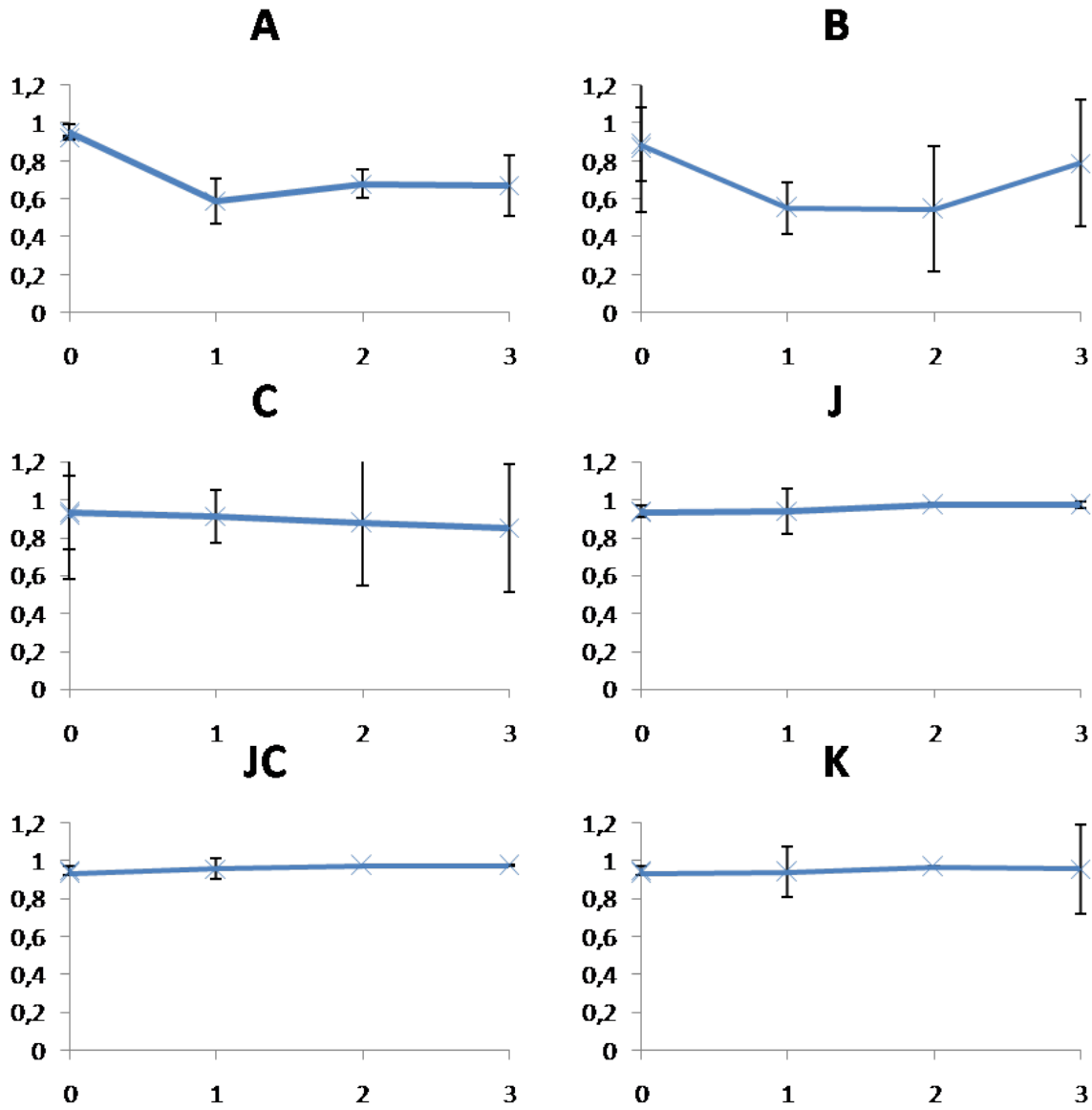


Figure 3.15: Desorption kinetics of VEGF from different ceramic samples. Error bars were obtained for two samples at each time point and two measurements per sample.

3.3.4 Protein quantification by TPD

Thermo-programmed desorption coupled with mass spectrometry consists of heating a sample in vacuum and detecting the gases that evolve by mass spectroscopy. The mass spectroscopy allows the identification and quantification of these gases. A more detailed description of the principle of protein quantification by TPD-MS is given in section 5.2 on page 174.

3.3.4.1 TPD of the ceramics

In order to analyze the stability of the ceramics during TPD experiments which involve heating of the sample up to 600°C, the ceramics were first passed through the TPD alone. Figure 3.16 shows the resulting thermograms. As can be seen from these graphics, the ceramics are not stable during the heat treatment under vacuum, but release water, carbon oxides and hydrogen. Table 3.10 shows the amounts of gas detected during the heat treatment for the different ceramics. Especially the ceramic J that has not been calcined during synthesis releases high amounts of water and carbon dioxide when heated. In the attempt to quantify the small amounts of H₂S that are generated by the decomposition of proteins on the ceramics, the high total pressure caused by the gases desorbing from the ceramic is unfavorable. In order to stabilize the ceramics it would be useful to calcine them at 600°, but this would reduce their specific surface area and pore volume as shown in section 2.3.3. Without stabilization of the ceramics, the protein detection on these samples by TPD is very difficult.

3.3.4.2 Quantification of protein traces by TPD

TPD has proven effective for the protein quantification on carbon and hydroxyapatite in the case of BSA [20, 21] and serum proteins [192] in concentrations in the range of milligrams. For the present study it is necessary to quantify smaller amounts, in the microgram range. In order to see if the TPD set-up is able to detect such small quantities, a regression study is done with different known quantities of VEGF that are directly introduced into the vessel of the TPD. The amount of protein calculated from the H₂S desorption during TPD is then compared to the real amount. Figure 3.17 shows the resulting “correlation”. As the quantification is obviously not good, we intended to investigate if the quantification of such small amounts was possible with BSA, a protein which has been used extensively in our laboratory for TPD studies.

Figure 3.18a shows the thermograms of the H₂S peak obtained for BSA at different concentrations. Additionally, the peak caused by the PBS solution alone is reported, evidencing that the buffer alone creates a signal even if it does not contain any sulfur. This signal is probably caused by phosphine PH₃ that gives rise to a similar mass spectrum as H₂S (see figure 3.19). This molecule might arise from the decomposition of phosphate that is contained in the buffer. Comparing the different signals we notice that the signal shift and the peaks change their shape. Both observations hint towards difficulties in the quantification of small amounts of protein. In the presence of a buffer that gives rise to a signal as well, the protein quantification by TPD is not reliable: Figure 3.18b

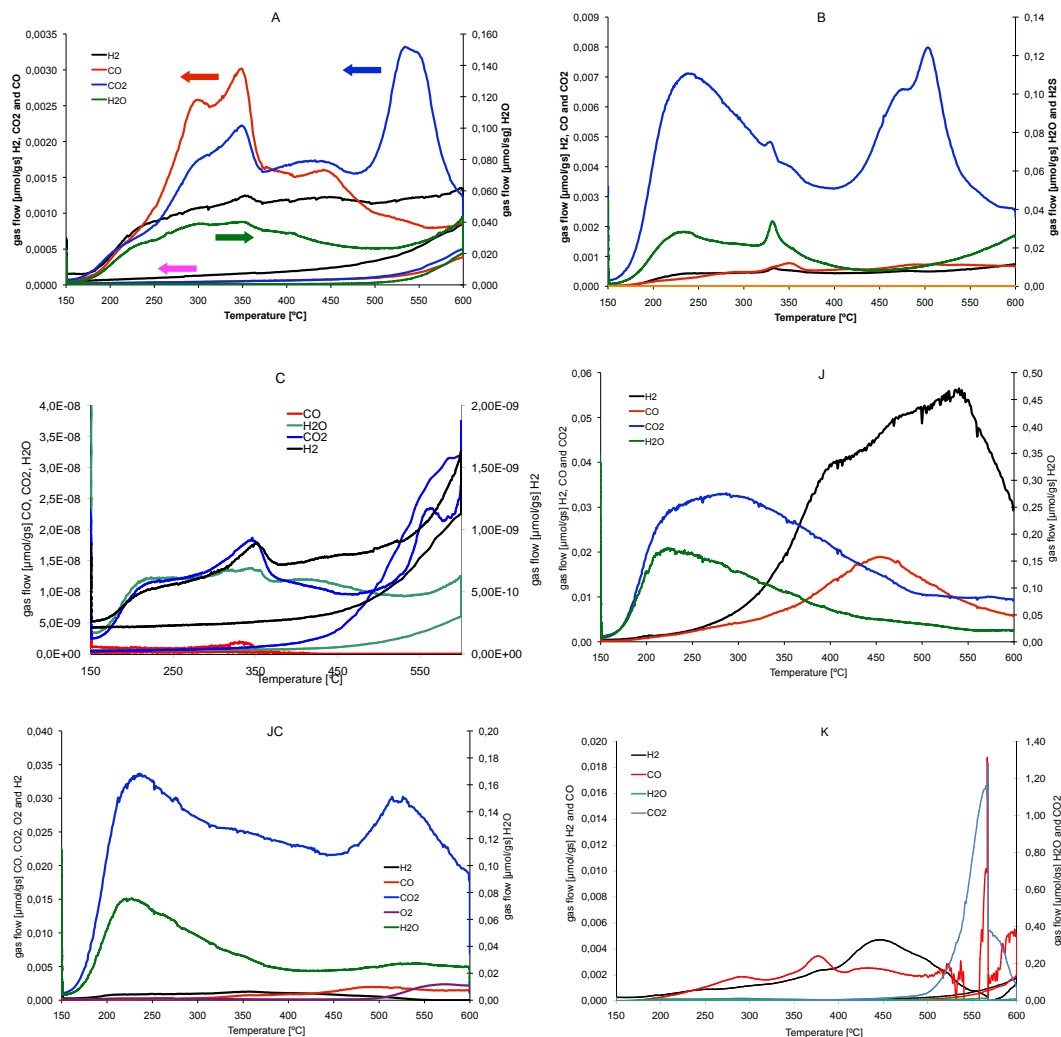


Figure 3.16: Thermo-programmed desorption for the ceramics alone. The ceramics were heated to 600°C with 2 K/min and hold for 30 minutes before being allowed to cool down to room temperature in the oven. The ceramic mass was 0.05 g approximately. In the case of sample C, the ceramic was maintained at 150°C for 1 h in order to dry it.

Temperature range	H ₂	H ₂ O	CO	CO ₂
A				
25 – 600°C	12	644	10	76
150 – 600°C	8	257	8	65
B				
25 – 600°C	23	604	23	26
150 – 600°C	17	430	19	23
J				
25 – 600°C	387	3376	123	352
150 – 600°C	380	1065	114	269
JC				
25 – 600°C	18	1062	17	405
150 – 600°C	10	494	14	359
K				
25 – 600°C	15	537	37	64
150 – 600°C	11	330	35	60

Table 3.10: Total of gases desorbed during TPD experiments on the pure ceramics. All amounts in $\mu\text{mol/g}$.

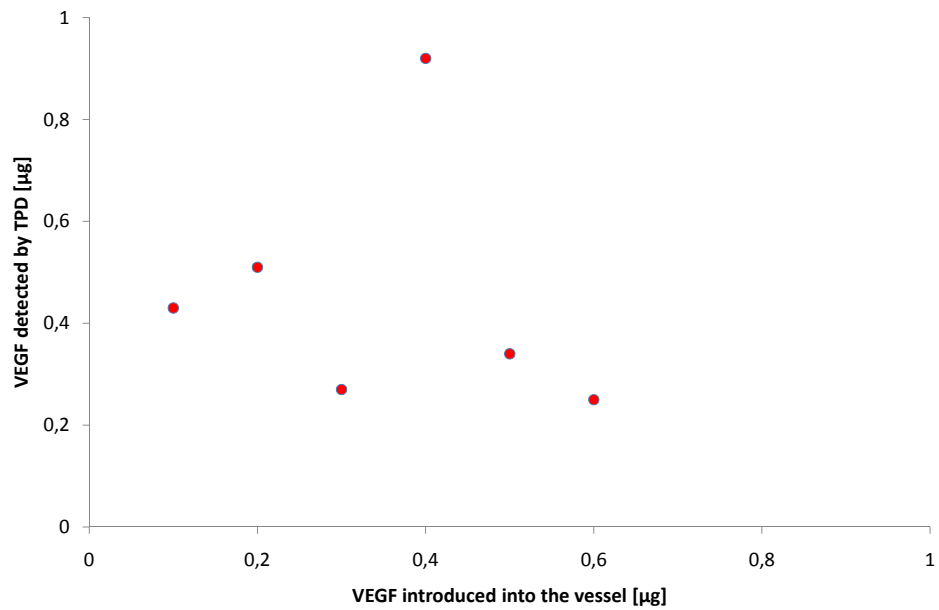


Figure 3.17: Comparison between real and detected amounts of VEGF in TPD without ceramic support

shows a scatter plot of the H_2S quantifications in function of amount of BSA initially introduced in the TPD vessel. For the mass of $5\text{ }\mu\text{g}$, two points have been obtained with different dilutions of the BSA in PBS. The quantifications of these two experiments are further away than quantifications of different masses.

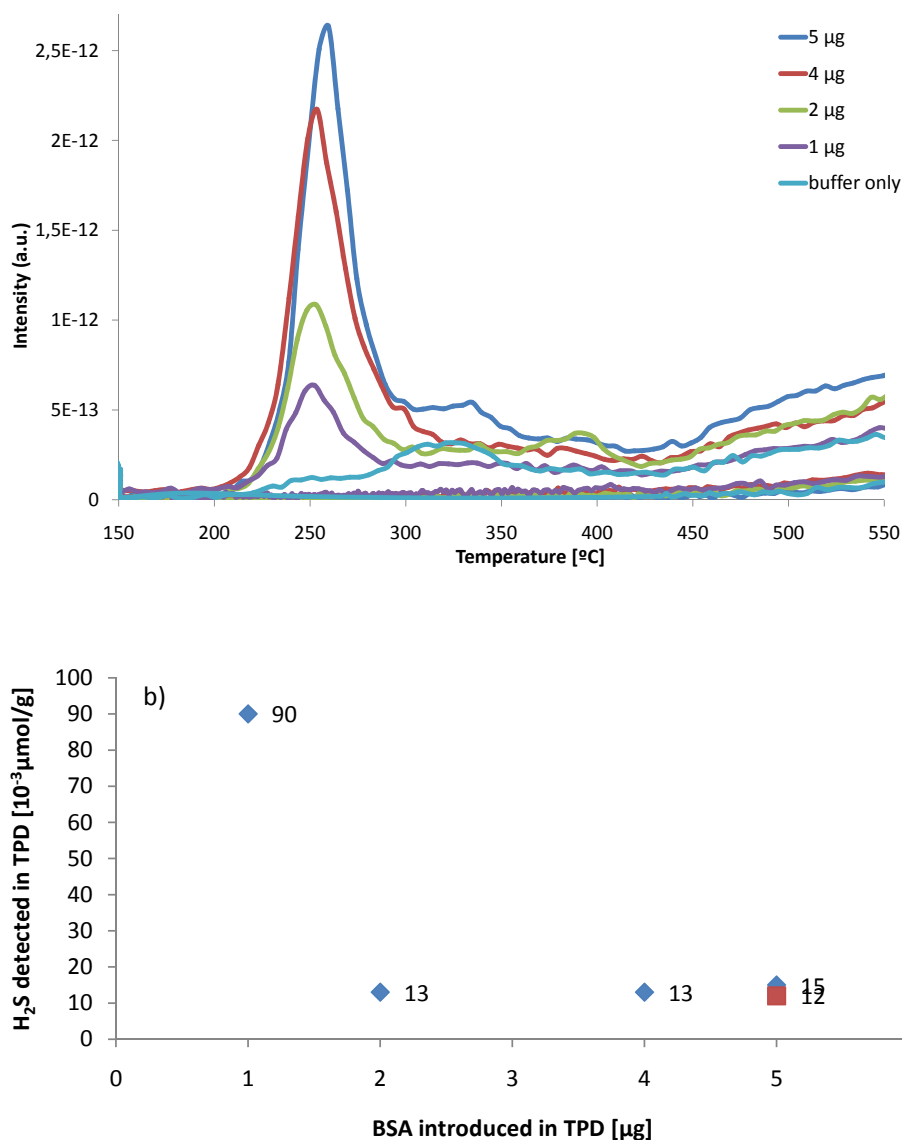


Figure 3.18: a) Thermo-programed desorption for BSA dilutions. Only the peak at 34 m/z is reported, as this is the peak that will be used for the quantification of H₂S. b) Scatter plot of the H₂S quantifications by TPD in function of the BSA introduced in the TPD vessel. The two points for 5 µg are obtained with different dilutions. The number next to the points indicate the ordinates of the data point.

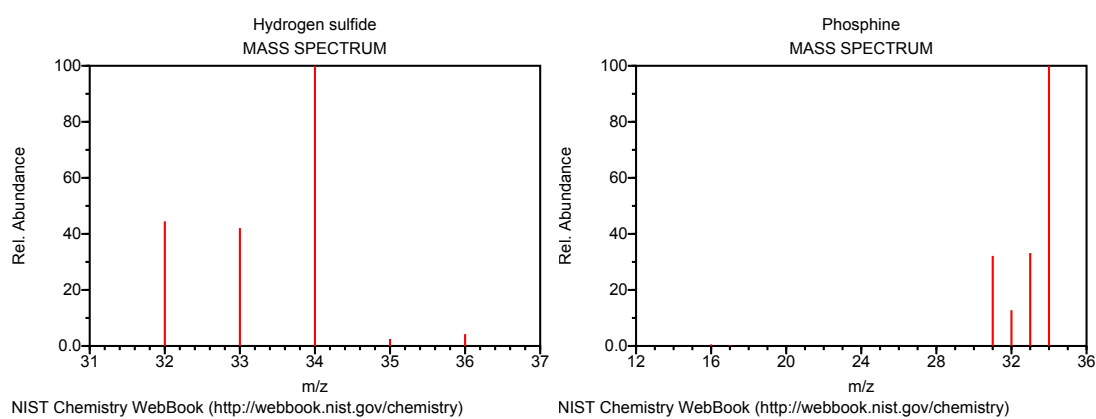


Figure 3.19: Theoretical mass spectra of H_2S and PH_3 . From the NIST Chemistry Web-Book

3.4 Discussion

Table 3.11 summarizes the most important characteristics of the ceramic samples and the results of the protein adsorption and release experiments. In the following section, we will discuss these results within the bibliographic context and analyze the implications for the application of the growth factor-loaded hydroxyapatites in bone regeneration.

While discussing the adsorption of proteins on the surface or inside the porosity of ceramics, two concepts have to be distinguished:

- amount of protein adsorbed: this only refers to how much protein is adsorbed on the surface
- strength of adsorption: qualifies the forces between the protein and the surface

If we speak about “strong adsorption”, we do not make any statement on the amount of protein adsorbed. On the other hand, when speaking about “high adsorption”, we only assess the amount of protein adsorbed and do not differentiate between weakly and strongly bonded proteins.

	S_{BET}	ζ_{PBS} pH 7	ζ_{DMEM}	BSA ads	BSA rel	Cyt C ads	Cyt C rel	TGF ads	TGF rel	VEGF ads	VEGF rel
A	42.5	−16.2	−4.2	++	−	0	++	0	+	++	++
B	63.1	−14.0	−1.8	+	−	0	+	0	++	++	++
C	166	−7.9	0	n.d.	n.d.	n.d.	n.d.	++	+	++	++
J	89.6	−16.9	−6.2	0	−	+	0	0	+	++	++
JC	22.1	−18.6	−6.7	0	0	++	n.d.	0	0	++	++
K	31.1	−18.5	−10.7	0	0	+	+	+	++	++	++

Table 3.11: Summary of the most important characteristics of the ceramics and their results in the protein experiments. ads = adsorption experiment, rel = release experiment. The performance is judged using the following scale: ++ very good, + good, 0 mean, and − poor. In the case of adsorption experiments, high adsorption was considered good, whereas in release experiments, high retention was considered good. n.d. stands for no data: Sample C had not yet been synthesized when the experiments with the model proteins were done.

3.4.1 Model proteins

BSA is the biggest molecule used for our adsorption studies. Its dimensions ($13 \times 3 \times 3$ nm) are close to or even slightly higher than the pore size of the tested ceramics (9–17 nm). It is therefore reasonable to assume that the adsorption of the protein is restricted to the surface [12]. It has been found before that the adsorption of proteins into mesoporous silica matrices is size-selective and that albumins are too big to penetrate

into mesopores of the ceramic particles [172]. Our observations are therefore in good agreement with this study on mesoporous silica samples.

The superficial adsorption explains why the molecule can be washed out easily. Only in the case of the sample JC and K is the protein fixed more tightly to the ceramic: These two samples retain the protein load during washing and allow the release over 24 h. JC and K have in common that they are prepared from the same precursors and, contrary to sample J, have been calcined at 500°C. It seems that the more crystalline surface is favorable for the retention of BSA. On the other hand, the equally calcined samples A and B do not show retention. The adsorption amount is high due to the high surface area, but adsorption is weak as the protein can be washed out completely.

It is interesting to note that the sample with the highest surface area, J, does not adsorb more protein than the other ceramics. This sample was prepared from the same precursors as JC and K but was not calcined. The calcination improves the crystallinity of the sample and therefore the distribution of C and P sites on the crystal surface. This improves the adsorption strength of the protein on the surface [16]. Samples A and B have been calcined at 650°C, and X-ray diffraction shows that they are well crystallized. These two samples show the highest BSA adsorption capacities of all studied powders. Crystallinity has been shown to be favorable for protein adsorption [198], but some authors have observed no effect of increased crystallinity [199] on the attachment of BSA. On the contrary, our study supports the findings of Marina Gorbunoff [198] and of the team of Kandori [16], underlining the importance of an ordered pattern of calcium and phosphate ions on the surface of hydroxyapatite in order to adsorb proteins efficiently. The study of Yang and coworkers [199] may lead to different results (no effect of increased crystallinity) because their samples are obtained by mixing crystalline hydroxyapatite with amorphous calcium phosphate: The amorphous phase is not specified nor further characterized. It is possible that this phase represents a calcium phosphate of different chemical composition that behaves differently from HA in contact with proteins.

To conclude, the crystallinity of the surface seems to be crucial for the adsorption of BSA. A high specific surface area is less decisive. From the desorption experiments we have seen that the BSA is adsorbed onto the surface of the grains only, and that the porosity is not penetrated by the protein. This is the reason why porosity is less important for the adsorption of BSA: the protein is too big to access the internal surface.

Cytochrome C. Regarding the amount of Cytochrome C adsorbed by the different ceramics, the tendency is inverse compared to BSA: JC and K, the two samples that adsorbed the lowest amounts of BSA, adsorb the most Cytochrome C. Contrary to BSA, Cytochrome C is smaller than the growth factors and should therefore be able to penetrate the mesoporosity of the ceramic samples. The specific surface area of the ceramic is therefore an important parameter that improve Cytochrome C adsorption. However, the fact that JC and K adsorb more Cytochrome C than the sample J, which has a higher pore volume, underlines once more the importance of crystallinity. The more crystalline samples adsorb more Cytochrome C than the amorphous sample, even if the latter has a higher surface area.

Contrary to the BSA adsorption, the surface chemistry of the samples prepared at the IS2M (J, JC and K) is more favorable for high Cytochrome C adsorption. This difference can be explained by the isoelectric points of the two molecules: BSA is an acidic protein, its net charge at pH 7 is negative; Cytochrome C is basic, and its net charge at pH 7 is positive. The growth factors used in this study are basic proteins as well. The ζ potential of the ceramics B and C is less negative than for the other samples, in DMEM the surface charge of sample C is even close to zero. The positively charged Cytochrome C will therefore adsorb more strongly on more negatively charged ceramics. The effect of protein charge on the adsorption on hydroxyapatite surfaces has been studied by Gorbunoff [162]. She has shown that acidic proteins eluted easier from HA chromatography columns than basic proteins, evidencing that acidic proteins adsorb less strongly. Our findings agree with the observations in chromatography: the basic proteins Cytochrome C, VEGF and TGF adsorb more strongly on the hydroxyapatite surface than does the acidic protein BSA.

Contrary to BSA, Cytochrome C is a small molecule and can penetrate the mesoporosity of the ceramics. As a consequence, the specific surface area is an important parameter for the amount of adsorption. The strength of adsorption depends on the surface charge of the ceramic: Cytochrome C adsorbs stronger on hydroxyapatite samples with high negative surface charge at neutral pH.

3.4.2 Growth factors

TGF- β . While adsorbing TGF, the ceramic C retained most of the protein. Sample C was not included in the experiments with the model proteins as this sample was prepared only after completion of these tests. We therefore cannot compare the results of Cytochrome C adsorption to the results of TGF adsorption for this sample. TGF, being a small protein, is able to penetrate into the mesopores of the ceramics. Contrary to the experiments with BSA, the specific surface area is therefore crucial for the adsorption of TGF. It is however not the single relevant parameter, as shown by the fact that the sample J adsorbs a lower amount of TGF than the sample A even though it has a higher specific surface area. As the ζ potentials of both samples are similar, the surface charge is not the origin of this difference either. We assume that different surface chemistries may influence the adsorption of TGF, as EDX analyses have shown slightly different Ca/P ratios on the ceramic surface for samples A and J. In contrast to the model protein, the crystallinity does not seem to influence the adsorption of TGF: the calcined and well crystallized sample A shows a similar release profiles as does sample J which is amorphous.

The association of TGF with calcium phosphates has been studied mainly by in vivo experiments that have proven its efficiency in the regeneration of bone defects [187–189]. However, the adsorption and release kinetics of TGF on hydroxyapatite ceramics have not yet been studied systematically. The study presented by Lind et al. [188] presents some interesting results on the release of TGF from macroporous tricalcium phosphate coating, showing that the majority of the protein is released within the first 4 h. This is different from our findings, as we have observed that TGF is released slowly into the

culture medium from our samples. The release was sustained over several days and not completed after 4 days. This difference is probably due to the presence of mesopores in our ceramics, in which the growth factors have adsorbed.

VEGF. In the experiments on the adsorption and release of VEGF, all ceramics perform equivalently. The adsorption is fast and complete, showing that the ceramics are not saturated with protein. In order to discriminate between them, it would be necessary to adsorb higher quantities. However, the adsorption of higher quantities of VEGF is not reasonable as the concentration in the ceramic is already sufficient for the application and because higher concentrations have been shown to have harmful effects [190]. The desorption experiments are not more discriminating, since here too, all the ceramics perform equally well.

The results of the adsorption of VEGF are in good agreement with the study published by Lode et al. [183]. Lode and coworkers observed that VEGF bonds tightly to the surface of the calcium phosphate material and that only a small amount can be removed by washing. In our experiments, VEGF adsorbed strongly on the HA samples and can neither be washed out nor released into the culture medium. On the contrary, Lode and his team observed release into the solution when they exposed their samples to culture medium. The strong adsorption of the growth factor on ceramic is very important for the application in implantation: it ensures that the protein is not released in burst in the first hours after implantation, which would cause severe side effects.

Wernike and coworkers [185] observed passive release of VEGF into culture medium as well. The desorption was up to 80 % for the sample where VEGF was adsorbed on the surface of calcium phosphate cements. The ceramics that they used for their experiments are composed of a mixture of HA (80%) and TCP, whereas our samples are pure HA. The composition of the samples used by Lode and coworkers is more complex, they contain mainly α -TCP and calcium hydrogen phosphate (CaHPO_4). In some samples, collagen was added to the preparation. The difference in the release kinetics may be related to the different chemical composition, but also to the mesoporosity that allows the penetration of the growth factor into the ceramic, protecting it from the culture medium.

The small growth factors penetrate the mesoporosity of the ceramics. Due to the confinement inside the mesopores and their strong interaction with the HA surface, the adsorption is partially irreversible. The strong adsorption insures that no burst release occurs upon implantation. This is important for the application as high local doses of growth factors can have detrimental side effects.

3.5 Conclusion

3.5.1 Model proteins

The behavior of the model proteins and of the growth factors has been significantly different during our adsorption and release experiments. It seems that BSA is too big to use the mesoporosity for adsorption and therefore cannot differentiate between ceramics with different specific surface areas. Additionally, BSA is an acidic protein and is therefore negatively charged in aqueous solutions at physiological pH. The negatively charged protein does not well adsorb on the negatively charged ceramics.

Cytochrome C is a better model for the growth factors as it is closer in size to them and basic. Like the growth factors, it can penetrate the mesoporosity and use the inner surface area for adsorption.

However, the question remains whether it is reasonable to model the adsorption of growth factors whose biologically active concentration is in the range of $\mu\text{g/mL}$ by the “model proteins” with concentrations in the mg/mL range. The adsorption mechanisms in concentrated solution must differ from those in high dilution: It has been shown that adsorbed molecules on surfaces undergo conformational changes and can “remodel” in order to make space for additional proteins if the concentration of the protein solution is increased [200]. In diluted solution, proteins can attach to the surface without being disturbed by adjacent molecules. It is furthermore probable that in diluted solution, only the surface spots with the highest surface energies are occupied whereas in concentrated solution spots with weaker adsorption potential are used as well.

3.5.2 Growth factors

To our knowledge, this work is the first comprehensive study of the adsorption kinetics of both model proteins and growth factors on mesoporous hydroxyapatite. Previous studies have been carried out either with macroporous calcium phosphate scaffolds or with co-precipitated systems. Also, a comparative study involving different hydroxyapatite and calcium deficient apatite materials obtained by different synthesis ways and presenting different properties has not been published yet.

As the growth factors are strongly adsorbed onto the ceramics, no burst release is expected to occur when the powders will be implanted. The desorption can not be triggered by diffusion alone, the decomposition of the ceramic scaffold is necessary to release the protein. The powders are designed to be injected into bone cavities. For this application, it would have been preferable to have a certain amount of VEGF release immediately in order to promote vascularisation of the implant right from the start, but this can be achieved by adding free VEGF to the injectable preparation. The powder will act as reservoir for the sustained release at longer time periods.

4 General conclusion and perspectives

4.1 Conclusion

This thesis describes the hard templating synthesis of mesoporous hydroxyapatite by silica templates for the first time. In contrast to the synthesis starting from tubular carbon templates, these templates have higher pore volumes and a pore shape that is more suitable for the infiltration with precursor solution. The products that result from this synthesis method are composed of agglomerated nanoparticles and possess mesoporosity. The surface area and the pore volume depend on the calcination treatment to which the template/HA composite is subjected.

The most versatile process for the hard templating synthesis of hydroxyapatite is the simple sol-gel synthesis starting from calcium nitrate and triethyl phosphite. It is possible to use high concentrations in order to limit the dead volume effect caused by the solvent, and the product shows only little contamination with silicon-containing phases if silica templates are used. The other methods that have been studied either do not lead to the desired hydroxyapatite phase or contain significant amounts of silicon contamination.

Like the products reported in the literature, our experiments do not show a real templating effect for the hydroxyapatite; even though our products are mesoporous, they do not replicate the pore shape of the template. On the contrary, the products obtained from different templates with distinctive pore structures are quite similar in surface area, pore size and texture. It has been shown that the template porosity has little effect on the porosity of the final ceramic. We believe that this is because the HA precursors condensate before they penetrate the porosity of the template, similar to what has been shown for transition metal phosphates [125]. We believe that this limitation is intrinsic to mesoporous hydroxyapatite from sol-gel systems. This hypothesis is supported by the hydroxyapatites obtained by sol/gel methods and soft templating by our partners at the LMI: these materials have equally low surface areas. The only exception are uncalcined powders which feature surface areas in the range of 100 to 200 m²/g. These powders are however poorly crystalline. As the crystallinity influences the dissolution of the ceramic upon implantation, higher crystallinity might be required for the application as bone filling material.

However, in the case of silica opal templates, a templating effect is observed. The resulting ceramic is composed of agglomerated nanograins that have filled the voids between the silica spheres. The ceramic combines meso- and macroporosity and is especially interesting for implantation applications: the mesoporosity can act as a reservoir for growth factors, and the macroporosity allows the circulation of body fluids.

These ceramic materials as well as hydroxyapatites obtained by soft templating and sol-gel syntheses (provided by the LMI team in Clermont) are suitable for the adsorption of proteins, especially the growth factors TGF and VEGF. Our experiments have shown a significant difference between the behavior of model proteins and the growth factors, partly due to different concentration ranges: the solutions used for the experiments with the model proteins are in the mg/mL range whereas the growth factor concentrations were in the $\mu\text{g/mL}$ range. We must assume that the adsorption mechanisms at such different concentrations cannot be the same: In concentrated solutions, even adsorption sites with less favorable interactions are used, whereas in diluted solution only the most favorable adsorption sites are occupied.

Using BSA as a model protein has additional drawbacks: this protein is bigger than the growth factors and cannot penetrate the mesoporosity of the ceramics. Therefore, its adsorption is governed by the crystallinity of the HA surface. For the other proteins, the surface crystallinity is less important than the specific surface area. Unlike the growth factors and Cytochrome C, BSA is an acidic protein that is negatively charged at physiological pH. Its interaction with negatively charged hydroxyapatite surfaces is less favorable.

It must therefore be deduced that experiments carried out with BSA and Cytochrome C do not allow any conclusions on the behavior of growth factors.

The adsorption of growth factors on the ceramics is strong and at least partially irreversible. The release of the growth factors (especially VEGF) therefore depends on the dissolution of the ceramic matrix within the biological system. Thus, the ceramic represents a reservoir system that releases growth factors over a prolonged period. This is very important for the application in implantation because it was shown that high local doses of VEGF have severe side-effects. It is therefore crucial to avoid a burst release during the first hours after implantation.

In order to trigger the vascularisation process, it would have been preferable to have a certain amount of VEGF released immediately after the implantation, but this can be achieved by adding free VEGF to the injectable preparation. The powder will then act as a reservoir for the sustained release at longer time periods.

4.2 Perspectives

4.2.1 Biological evaluation

The ceramics are subject to different in vitro and in vivo tests: the IBTH team in Reims is testing the powders J, A, B and a calcined sample of C for their inflammatory potential. For this, human monocytes are cultured in the presence of the powders. The expression of vesicular mediators is analyzed in the cell culture supernatants by protein quantification. The production of messenger RNA was analyzed by real-time PCR in the cell lysates. The first series of these tests have shown that the powders A, B and C are equivalent in their inflammatory potential whereas the powder J provokes a strong inflammatory response. Of all four samples, only the powder A has caused

the concentration of IL-10¹ to rise, indicating that it might have anti-inflammatory effects upon implantation. From the tested powders, this might be the most suitable for implantation.

In parallel, the teams in Bordeaux did *in vitro* cell culture tests with human bone cells that showed no detrimental effect for extracts of the powders A, B and C. Discs fabricated by pressing powder J have been used as support for the culture of human osteoprogenitor cells. The live/dead test does not show any significant difference between the hydroxyapatite disc and the bottom of the culture well that was used as control. The cells proliferate less on the HA disc than on the control, but the material does not completely prevent them from proliferating. The tested powders are not cytotoxic in the conditions of the test.

At the moment, *in vivo* tests are underway in Bordeaux: powdered samples of JC and C are mixed with NaCl-solution to form a paste and implanted into cranial defects in mice. In addition, discs made of the same powders are implanted subcutaneously in the back of mice in order to evaluate if the ceramics can induce bone formation outside of bone sites and if vascularisation occurs. When implanted subcutaneously in the back of mice, both samples are surrounded by fibrous tissue. The inflammatory reaction is weak and after 15 days, the samples are already partially resorbed. When implanted into bone sites, sample C shows a strong inflammatory response whereas the reaction to sample JC is weak. In this first experiments, it seems that JC is more suitable for the implantation than C. In order to complete this study, additional tests will be carried out comparing all six powders.

All these tests are conducted in order to choose the most appropriate powders for the impregnation with growth factors. The impregnated ceramics will then be implanted into intramuscular pouches and femoral defects in mice in order to validate the association of the two growth factors with the ceramic.

4.2.2 Possible further improvements of the synthesis of mesoporous hydroxyapatite

We assume from our observations that the kinetics of the sol-gel system are too fast to allow templating. In order to improve the replication of the template porosity, the system has to be slowed down. In the synthesis of zeolites, fluoride ions can be added to the solutions in order to slow down the reactions [125]. Due to the high affinity between calcium and fluorine, this method would lead to calcium fluoride in our case, but another substance that slows the reaction between the calcium and the phosphate can certainly be found.

Working in higher dilutions can have a similar effect. However, we have shown that the yield of the reactions (in terms of the amount of hydroxyapatite that can be obtained from the same amount of template) is considerably lower when working in diluted systems. It would be interesting to do a systematic dilution study in order to find the

¹IL-10 (Interleukin 10), also known as the human cytokine synthesis inhibitory factor, is a cytokine with anti-inflammatory effect.

perfect balance between slowed reaction kinetics and reasonable yields of the synthesis. This approach would certainly have to be combined with multiple infiltrations in order to compensate for the reduced yield.

Another possibility of reducing the reaction velocity is the use of different precursors. One step in this direction has been the “solvent free” synthesis starting from calcium ethoxide and different phosphites. Although this route has not been successful in this work, it is worth exploring as the reaction kinetics are considerably slower than for the water based system.

The synthesis of hydroxyapatite from calcium metaphosphates is incompatible with silica templates, but very promising. It would be interesting to use calcium metaphosphates in combination with inert templates, for example with carbon. The kinetics of the metaphosphate system are different from the tested sol-gel systems and might be more favorable for the application in templating.

The surface chemistry of the carbon templates is a key parameter for the wetting with and the infiltration of the hydroxyapatite precursors. In this work, we have only used two different carbon samples, derived from CVD with propylene and from sucrose infiltration. Other methods exist to modify the carbon surface chemistry and texture: Instead of treating the CVD carbon with hypochlorite, which, as we have shown, destroys some of the mesoporosity, carbon can also be treated with molten potassium hydroxide in order to introduce additional microporosity. Boiling the carbon in diluted nitric acid introduces carboxylic acids on the surface. These functional groups improve the infiltration with hydroxyapatite precursor solutions. By changing the surface chemistry of the carbon template, it might be possible to speed up the infiltration sufficiently to allow the penetration of the porosity before the precursor system condenses.

In the project proposal, we had proposed to combine both hard and soft templating approaches in order to obtain hierarchical pore systems combining pores of different sizes. The most suitable hard template for this approach would be the silica opal, as it is the only one that really acts as a template. The silica opal would have to be infiltrated with a sol containing a surfactant. After the condensation of this system, the surfactant should be removed by solvent extraction instead of being burned. This has been shown to increase the specific surface area of the ceramic [133].

5 Appendix

5.1 Fundamentals of physisorption

The adsorption of nitrogen near its boiling point at 77K is the most common method to characterize a material's surface area and porosity. The *adsorption isotherm* plots the amount of gas adsorbed (V_{ads}) in function of the relative pressure p/p_0 (where p_0 is the saturation pressure at the 77 K). The shape of the isotherm and its *hysteresis* (difference between the adsorption and the desorption branch) allow interpretations of the sample's porosity. The calculation of the *specific surface area* from nitrogen physisorption data was first introduced by Brunauer, Emmet and Teller in 1934 [201] and is therefore called *BET* theory. The BET theory is based on the assumption that condensation forces are responsible for the formation of multilayers, and that therefore the heat of adsorption for the second and all following layers equals the heat of liquefaction of the gas. From these considerations, the isotherm can be described by the following equation:

$$V_{ads} = \frac{V_m c p}{(p - p_0) \{1 + (c - 1)(\frac{p}{p_0})\}} \quad (5.1)$$

This equation can be linearized as:

$$\frac{p}{V_{ads}(p - p_0)} = \frac{1}{V_m c} + \frac{c - 1}{V_m c} \frac{p}{p_0}. \quad (5.2)$$

The volume of gas necessary for the formation of a monolayer V_m and the constant c can be calculated from plotting $p/V_{ads}(p - p_0)$ against p/p_0 . V_m being the slope and c the intercept of the ordinate. V_m is used to calculate the specific surface area S_{BET} . The constant c is

$$c \approx \exp\left(\frac{E_1 - E_L}{RT}\right) \quad (5.3)$$

where E_1 is the heat of adsorption for the first layer and E_L is the heat of liquefaction of the gas.

If the thickness of the adsorbed layers cannot be greater than a finite number n (for example inside a pore of finite diameter), the isotherm can be described by the equation:

$$V_{ads} = \frac{V_m c x}{1 - x} \left\{ \frac{1 - (n + 1)x^n + nx^{n+1}}{1 + (c - 1)x - cx^{n+1}} \right\} \quad (5.4)$$

where $x = \frac{p}{p_0}$. This equation reduces to 5.1 for $n = \infty$.

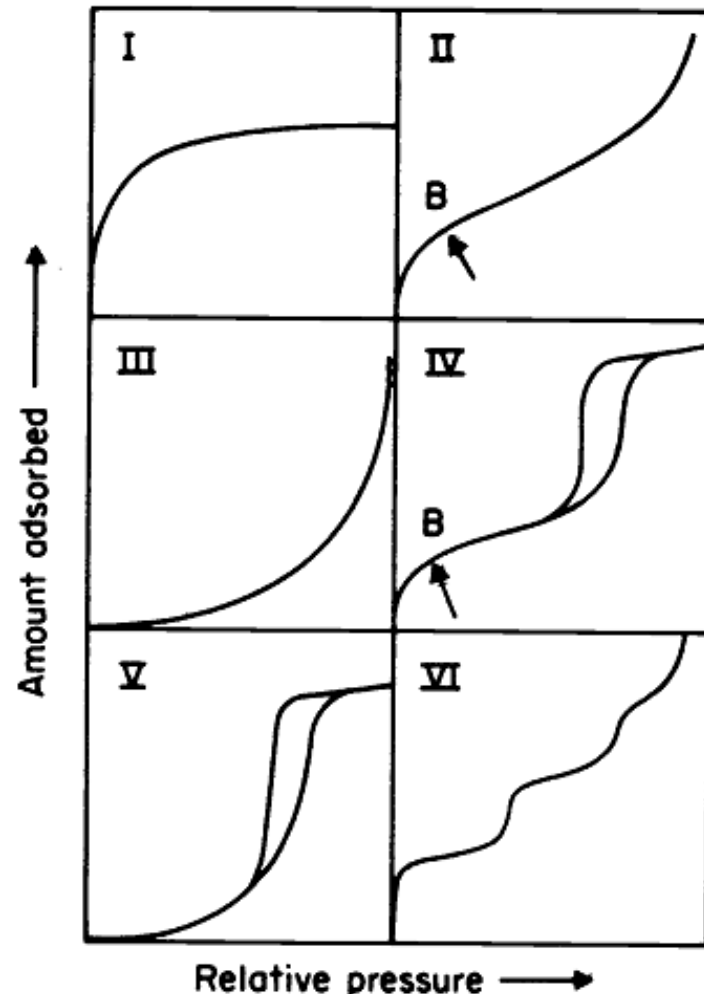


Figure 5.1: The six standard isotherm shapes. From [104]

Five standard isotherms have been defined by Brunauer, Deming, Deming and Teller [202]. A sixth one has been added by the IUPAC as type IV [203]. Their typical form is shown in 5.1.

From the shape of the isotherm the solid can be described [204]:

- A type I isotherm is obtained when only a monolayer can be adsorbed on the material surface for example in microporous samples. This corresponds to $n=1$ in equation 5.4.
- The S-shaped isotherm of type II is characteristic for multilayer adsorption on non-porous samples or on samples with textural porosity (porosity between the particles). This isotherm is obtained when the adsorption on the surface is preferred over adsorption in multilayers, that is $c \gg 1$.
- If $c < 1$ in equation 5.1, i.e. $E_1 < E_L$, a type III isotherm is obtained. The liquefaction of the adsorbent is preferred over adsorption on the surface. This unfavorable adsorbent-adsorbent interaction is not observed for nitrogen physisorption, Brunauer and coworkers give the example of bromine adsorbed on silica for this type of isotherm.
- A type IV isotherm results from the capillary condensation in mesoporous solids. The desorption branch shows hysteresis to the adsorption branch. This behavior is described by equation 5.4 for a finite number of n .
- As type III and IV isotherms, type V isotherms occur for a finite number n of layers with $n > 1$ (i.e. limited pore sizes with capillary condensation) and $c < 1$ (weak adsorbent/adsorbate interactions). An example for type V isotherms is the adsorption of water vapor on charcoal at 100°C.
- The type VI isotherm is seldom observed in practice. It can be obtained for a completely homogeneous non-porous surface on which each adsorption layer is completed before the next one begins. One example is the adsorption of methane or krypton on carbon nanotube bundles [205].

In analogy to the isotherm shapes, the shapes of the hysteresis loops can be classified as well. Figure 5.2 shows examples for the four types encountered in nitrogen physisorption.

Table 5.1 opposes a description of the shape of the hysteresis with the usual interpretation that can be drawn from it.

In general, it can be said that more the hysteresis is shifted to higher relative pressures, the bigger the mesopores are. From hysteresis on very high relative pressures, textural porosity can be concluded. Textural porosity is created by interstitial space between (nano)particles.

There appears to be a relative pressure below with the hysteresis does not occur and the desorption branch joins the adsorption branch. This pressure has been determined

Type	Characteristics	Usual interpretation
H1	Nearly vertical and parallel adsorption and desorption branches	Regular even pores without inter-connecting channels
H2	Sloping adsorption branch and nearly vertical desorption branch	Pores with narrower and wider sections, possibility of interconnecting channels
H3	Sloping adsorption and desorption branches covering a large range of relative pressures. Underlying isotherm is type II.	Slit-like pores on adsorbent/adsorbate pair that would lead to a type II isotherm without pores
H4	Large range for the hysteresis loop on underlying type I adsorbent/adsorbate pair	Slit-like pores for type I adsorbent/adsorbate pair

Table 5.1: Description and interpretation of the hysteresis loops. From [206]

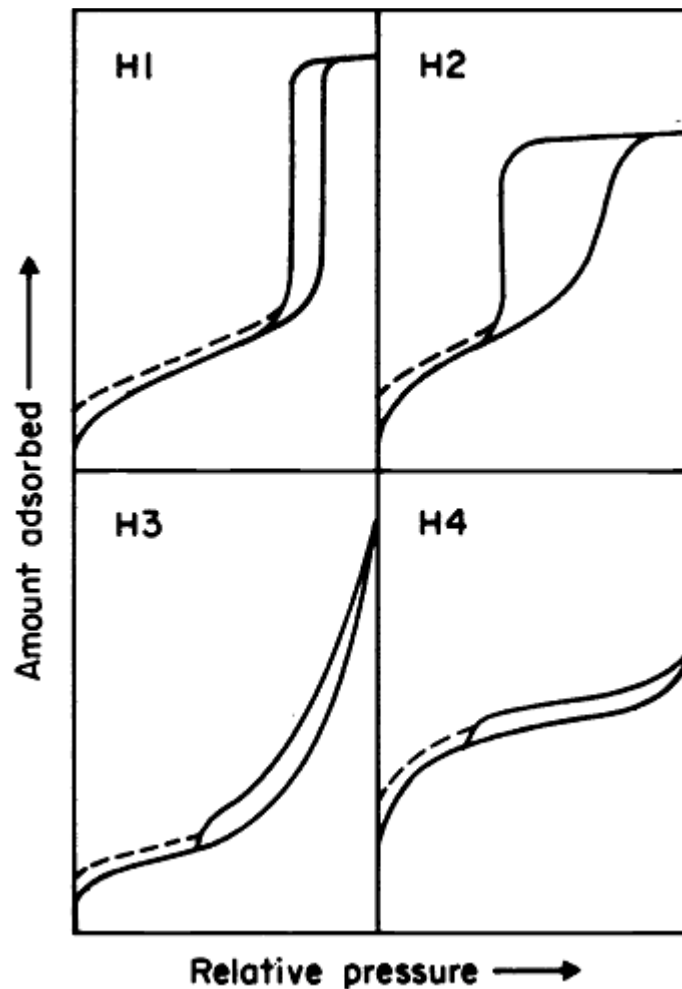


Figure 5.2: The four types of hysteresis loops. From [104]

to 0.42 for nitrogen physisorption [206]. This intersection of the adsorption and desorption branch at low pressure has been related to the thermodynamic properties of the adsorbent. Especially, it seems that the Clausius-Clapeyron equation is respected. This indicates that the reversible pore filling is a first-order gas-liquid transition. The enthalpy of this transition exceeds the gas-liquid transition in the bulk as the interaction of the solid supplies extra energy.

If in the experiment the desorption and adsorption branches do not join at low pressures, the pressures recorded are not equilibrium values. This is often observed if the pores are small and obstructed and the desorption is sterically hindered. In order to obtain correct data from these samples, the equilibrium time must be extended.

5.1.1 Determination of pore size distribution

The most commonly used method for the determination of the pore size distribution has been proposed by Barrett, Joyner and Halenda in 1951 [207]. This method is based on the assumption that the sample contains cylindrical pores that are open-ended and not interconnected. The BJH method involves the area of the pore walls, and uses the Kelvin equation to correlate the relative pressure to the size of the pores in which capillary condensation occurs.

The progressive filling of the mesopores of the sample is governed by capillary condensation. Successive layers of adsorbent are deposited on the surface until all macro- and mesopores are filled with liquefied gas. The process is completed near relative pressures $p/p_0 = 1$. In order to obtain the desorption branch of the isotherm, the pressure is progressively reduced and gas is allowed to desorb from the sample. As it is assumed that the pores are filled with liquid rather than gas, the desorbed volume is converted into equivalent liquid volumes.

The core radius of the liquid in the capillary can be calculated from the Kelvin equation:

$$RT \ln \frac{p}{p_0} = -2\gamma \frac{V_M}{R_K} \quad (5.5)$$

where

γ the surface tension of the adsorbent at T,

R the universal gas constant,

T the measurement temperature,

V_M the molar volume of the adsorbent,

R_K the Kelvin radius.

By substituting the constants and the values known for the case of nitrogen, the equation solves to:

$$R_K[\text{\AA}] = 4.14 \log \frac{p}{p_0}. \quad (5.6)$$

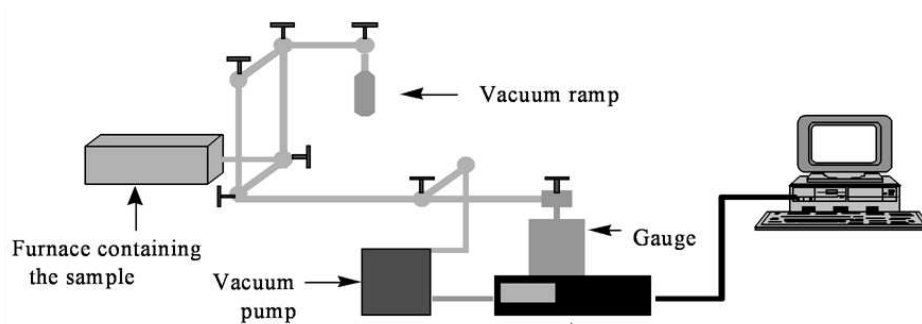


Figure 5.3: Schematic drawing of the TPD-MS setup used for the quantification of proteins in porous materials

5.2 Mass Spectrometer coupled Thermoprogrammed Desorption (TPD-MS)

Figure 5.3 shows the set-up of a typical thermoprogrammed desorption apparatus as used in our experiments. The principle of thermoprogrammed desorption coupled with mass spectroscopy is simple: A sample is heated under vacuum and the desorbing gases are identified by mass spectroscopy. The calibration of the spectrometer with known quantities of the different gases allows their quantification. In the case of proteins entrapped inside the porosity of mesoporous materials, the biomolecules are decomposed due to the heat treatment so that the term "desorption" is inadequate. The decomposition products are detected, identified and quantified by MS.

Proteins are poly(amino acids) and are essentially composed of organic carbon, nitrogen, oxygen, and hydrogen. The products of thermal decomposition are therefore CO, CO₂, H₂O, H₂, NH₃, nitrogen oxides and alkanes. Cysteine and methionine additionally contain a sulfur atoms. The free thiol group in cystein can form disulfur bridges between two cystein groups. Together with hydrogen bonds, hydrophobic interactions, Van der Waals interactions and electrostatic attractions, these bridges contribute to the tertiary structure of the protein chain.

During TPD experiments, disulfur bridges decompose before the organic backbone of the protein is damaged. Previous studies in our laboratory have shown that the decomposition of disulfur bridges in BSA takes place between 180 and 290°C. This decomposition is evidenced by the appearance of peaks at 34 and 33 m/z in the mass spectrogram corresponding to H₂S and HS-ions respectively. The decomposition of the organic backbone, accompanied by the evolution of ammonia and carbon dioxide, takes place at higher temperatures [21].

5.3 ELISA

Enzyme-linked immunosorbent assay (ELISA) is a biotechnical technique allowing the detection and quantification of an antibody in solution. ELISAs are used in diagnostic medicine, in plant pathology and as a tool for quality control in various industries. In the simplest case, the principle is the following: the solution containing the protein is placed in contact with the adsorptive surface (normally the well of a microtiter plate) and the protein adsorbs on the surface. The solution is decanted and a specific antibody is applied. This specific antibody binds only to the protein which is immobilized on the surface. The interaction of the antibody and the protein is specific, thus, other proteins are not bound by the antibody. The detection antibody is linked to an enzyme, and as a final step, a substrate is added. The substrate is converted by the enzyme into a detectable signal, often in form of a colored or fluorescent reaction product. In between the different steps, the surface is washed with a mild detergent that remove unspecifically bound substances.

In our case, the quantification of the growth factors is carried out by sandwich ELISA. Sandwich ELISAs involve more steps than simple ELISA, but a very specific and sensitive. The sandwich ELISA for TGF and VEGF involves the following steps (see figure 5.4 for a schematic illustration):

- Coat the well surface with the capture antibody and allow to bind overnight.
- Wash the plate to remove unbound capture antibody.
- Block the plate with BSA or bovine serum to avoid unspecific bounding.
- Wash the plate to remove residual blocking agents.
- Apply the sample and standards and allow to bind for two hours. The growth factors bind specifically to the capture antibody on the well surface. Direct binding of the protein to the well surface is prevented by the previous blocking step.
- Wash the plate to remove unbound protein.
- Apply a second antibody (detection antibody) that binds to the adsorbed growth factors.
- Wash to remove unbound antibody.
- React the detection antibody with streptavidin-HRP. The streptavidin part of this molecule bind tightly to the detection antibody. The HRP (horse radish peroxidase) is the enzyme that converts the substrate (tetramethylbenzidine) into the blue product.
- Wash the plate to remove unbound enzyme.
- Add the substrate solution (tetramethylbenzidine and hydrogen peroxide) and allow to react in the dark (HRP is photosensitive).

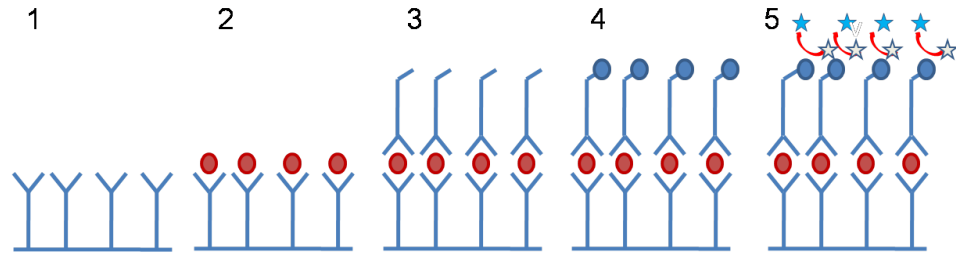


Figure 5.4: Principle steps of sandwich ELISA, used for the quantification of the growth factors in solution: 1) The capture antibody is fixed on the plate. 2) The sample is added and the protein binds to the antibody. 3) The second antibody is added and attaches to the protein. 4) The enzyme is added and attaches to the second antibody via its streptavidin chain. 5) The enzyme converts the colorless substrate into the blue detectable product.

- Stop the reaction with sulphuric acid. The initial blue color is converted into yellow.
- Detect the intensity of the color by colorimetry at 450 nm.

5.4 List of samples prepared

Name	template	calcium precursor	phosphate precursor	Infiltration			calcination
				solution	pressure	conditions	
SiHA1	MCF	nitrate	TEP	diluted	atmospheric		none
SiHA2	MCF	nitrate	TEP	diluted	atmospheric		none
HA00201	CF	CAT	TEP	diluted	vacuum	steel autoclave synthesis	500°C, 4h
HA00301	none	nitrate	P ₂ O ₅	ethanol solution	atmospheric		900°C, 12h
HA00302	none	nitrate	P ₂ O ₅	ethanol solution, diluted	atmospheric		900°C, 12h
HA00401	MCF	nitrate	TEP	diluted	vacuum		600°C, 4h
HA00501	MCF	nitrate	DAHP	diluted	vacuum	double infiltration, incipient wetness volume x3	none
HA00601	MCF	nitrate	TEP	diluted	vacuum	0.5g template + 6 mL sol, simple infiltration	500°C, 4h
HA00602	MCF	nitrate	TEP	diluted	vacuum	as HA00601, double infiltration	500°C, 4h
HA00603	MCF	nitrate	TEP	diluted	vacuum	as HA00601, triple infiltration	500°C, 4h
HA00701	CF	nitrate	TEP	diluted	vacuum	0.5g template + 6 mL sol, simple infiltration	500°C, 4h, argon
HA00702	CF	nitrate	TEP	diluted	vacuum	as HA00701, double infiltration	500°C, 4h, argon
HA00703	CF	nitrate	TEP	diluted	vacuum	as HA00701, triple infiltration	500°C, 4h, argon
HA0061X	MCF					HA0060X after calcination, before template removal	
HA0071X	CF					HA0070X after calcination, before template removal	750°C, 2h

Name	template	calcium precursor	phosphate precursor	Infiltration			calcination
				solution	pressure	conditions	
HA00801	MCF	nitrate	TEP	diluted	atmospheric		400°C, 4h
HA00901	none	Ca(OH) ₂	NH ₄ H ₂ PO ₄	diluted	atmospheric	upscale HA00901	800°C, 6h
HA01001	none	Ca(OH) ₂	NH ₄ H ₂ PO ₄			as HA00801, upscale	none
HA01101	none	nitrate	TEP			upscale, reference sample	TG
HA01201	none	nitrate	TEP			different calcination treatments of HA01201	900°C, 0.5h
HA01211	none	nitrate	TEP			upscale HA00901	200, 400, 600, 800°C, 1h
HA01301	none	Ca(OH) ₂	NH ₄ H ₂ PO ₄				900°C, 0.5h
HA02001	MCF	nitrate	TEP	concentrated	vacuum	solvent is evaporated regularly, sol is reapplied until used up, four infiltration cycles	900°C, 0.5h
HA02002	MCF	nitrate	TEP	concentrated	vacuum		600°C, 1h
HA02101	MCF	nitrate	TEP	concentrated	vacuum		none
HA02201	SBA	nitrate	TEP	concentrated	vacuum		none
HA02301	MCF	nitrate	TEP	concentrated	vacuum		none
HA02401	CF	nitrate	TEP	concentrated	vacuum	sol preparation in presence of the template	none
HA02601	none	nitrate	TBP	ethanol solution			none
HA02701	MCF	nitrate	TEP	concentrated	vacuum	upscale HA02301, for pellets for in vitro tests Bordeaux	none
HA02801	MCF	nitrate	TEP	concentrated	vacuum	composite of sample J, same as HA02701	none

Name	template	calcium precursor	phosphate precursor	Infiltration			calcination
				solution	pressure	conditions	
HA04011	MCF	nitrate	TEP	concentrated	vacuum	calcination of HA02701	500°C, 12h
HA04111	MCF	nitrate	TEP	concentrated	vacuum	calcination of HA02701	700°C, 1h
HA04201	CS	nitrate	TEP	concentrated	vacuum	sol preparation in presence of template	700°C, 1h, argon
HA04301	SS	nitrate	TEP	concentrated	vacuum	sol preparation in presence of template, carbon monolith template (Sébastien Schlienger)	
HA04401	SO	nitrate	TEP	concentrated	vacuum	sol preparation in presence of opal template	600°C, 4h
HA04501	none	Ca(OEt) ₂	TEP			solvent free synthesis	780°C, 4h
HA04601	CF	nitrate	TEP	concentrated	vacuum	sample CVD-HA for SPS, double infiltration	
HA04701	CS	nitrate	TEP	concentrated	vacuum	sample CS-HA for SPS, double infiltration	
HA04801	MCF	nitrate	TEP	concentrated	vacuum	sample Si-HA for SPS, double infiltration	
HA04901	MCF	nitrate	TEP	concentrated	vacuum	composite of sample JC, sol preparation in presence of template	500°C, 10h
HA05001	CF	nitrate	TEP	concentrated	vacuum	composite of sample K, sol preparation in presence of template	500°C, 20h
HA05101	none	Ca(EtO) ₂	TEP			solvent free synthesis, no template	780°C, 4h
CM00101	none	nitrate	SMP			no template, first test	drying at 80°C
CM00102	none	nitrate	SMP			as CM00101, drying at room temperature	

Name	template	calcium precursor	phosphate precursor	Infiltration			calcination
				solution	pressure	conditions	
CM00103	none	nitrate	SMP			as CM00102, upscale x5	
CM00201	MCF	nitrate	SMP		vacuum	add polyphosphate first, dry, add calcium solution, react, filter, dry	
CM00202	MCF	nitrate	SMP		vacuum	as CM00201, double infiltration	
CM00203	none	nitrate	SMP		vacuum	upscale CM00102	
CM00204	none	nitrate	SMP		vacuum	heat treatments at different temperatures	200, 400, 600, 800 °C, 1h
HA02501	MCF	nitrate	SMP		vacuum		none

Abbreviations: MCF - mesoporous silica foam template, CF - carbon foam (MCF replica by CVD), SBA - SBA-15 silica template, CS - carbon from sucrose (MCF replica by sucrose infiltration), SS - Monolithic carbon template provided by S. Schlienger, SO - silica opal template provided by J-L. Rehspringer. TEP - triethyl phosphite, TBPa - tributyl phosphate, DAHP - diammonium hydrogen phosphate, SMP - sodium metaphosphate.

Bibliography

- [1] D. F. Williams, On the nature of biomaterials, *Biomaterials* **30** (30) 5897 – 5909 (2009).
- [2] L. Hench, Bioceramics: from concept to clinic, *J. Am. Chem. Soc.* **74** 1487–510 (1991).
- [3] M. Long, H. J. Rack, Titanium alloys in total joint replacement—a materials science perspective, *Biomaterials* **19** (18) 1621 – 1639 (1998).
- [4] J. Jones, L. Hench, Regeneration of trabecular bone using porous ceramics, *Curr. Op. Solid State Mater. Sci.* **7** 301–07 (2003).
- [5] J. Heller, R. Baker, R. Gale, J. Rodin, Controlled drug release by polymer dissolution: I. partial esters of maleic anhydride copolymers-properties and theory, *J. Appl. Polymer Sci.* **22** (7) 1991–2009 (2003).
- [6] R. Langer, J. Vacanti, Tissue engineering, *Science* **260** 920–26 (1993).
- [7] P. N. Baker, J. H. van der Meulen, J. Lewsey, P. J. Gregg, The role of pain and function in determining patient satisfaction after total knee replacement: Data from the national joint registry for england and wales, *J Bone Joint Surg Br* **89-B** (7) 893–900 (2007).
- [8] Y. Kadono, H. Yasunaga, H. Horiguchi, H. Hashimoto, S. Matsuda, S. Tanaka, K. Nakamura, Statistics for orthopedic surgery 2006-2007: data from japanese diagnosis procedure combination database, *J. Othop. Sci.* **15** 162–70 (2010).
- [9] Y. Okazaki, E. Gotoh, Comparison of metal release from various metallic biomaterials in vitro, *Biomaterials* **26** (1) 11 – 21 (2005).
- [10] S. Dorozhkin, Calcium orthophosphates, *J. Mater. Sci.* **42** 1061 (2007).
- [11] R. Geesink, K. de Groot, C. Klein, Bonding of bone to apatite coated implants, *J. Bone Joint Surg.* **70B** (1) 17–22 (1988).
- [12] M. Hartmann, Ordered mesoporous materials for bioadsorption and biocatalysis, *Chem. Mater.* **17** 4577–93 (2004).
- [13] S. Best, A. Porter, E. Thain, J. Huang, Bioceramics: past, present and future, *J. Eur. Ceram. Soc.* **28** (7) 1319–27 (2008).

- [14] S. Dorozhkin, Nanodimensional and nanocrystalline apatites and other calcium orthophosphates in biomedical engineering, biology and medicine, *Materials* **2** 1975–2045 (2009).
- [15] S. Dorozhkin, Calcium orthophosphates in nature, biology and medicine, *Materials* **2** 399–498 (2009).
- [16] K. Kandori, S. Tsuyama, H. Tanaka, T. Ishikawa, Protein adsorption characteristics of calcium hydroxyapatites modified with pyrophosphoric acids, *Colloids Surf. B* **58** (2) 98 – 104 (2007).
- [17] N. H. Leeuw, Density functional theory calculations of local ordering of hydroxy groups and fluoride ions in hydroxyapatite, *Phys. Chem. Chem. Phys.* **4** 3865–71 (2002).
- [18] V. Orlovskii, V. Komlev, S. Barinov, Hydroxyapatite and hydroxyapatite-based ceramics, *Inorg. Mater.* **973-84** 1159–72 (2002).
- [19] M. Hammadouche, L. Sedel, Ceramics in orthopaedics, *J. Bone Joint Surg. [Br]* **82B** 1095–99 (2000).
- [20] M. Vijayaraj, R. Gadiou, K. Anselme, C. Ghimbeu, C. Vix-Guterl, H. Orikasa, T. Kyotani, S. Ittsanronnachai, The influence of surface chemistry and pore size on the adsorption of proteins on nanostructured carbon materials, *Adv. func. Mater.* **20** (15) 2489–99 (2010).
- [21] R. Gadiou, E. dos Santos, M. Vijayaraj, K. Anselme, J. Dentzer, G. Soares, C. Vix-Guterl, Temperature-programmed desorption as a tool for quantification of protein adsorption capacity in micro- and nanoporous materials, *Colloids Surf. B* **73** (2) 168 – 174 (2009).
- [22] P. Weiss, O. Gauthier, J. Bouler, G. Grimandi, G. Daculsi, Injectable bone substitute using a hydrophilic polymer, *Bone* **25** 67S–70S (1999).
- [23] M. Böhner, G. Baroud, Injectability of calcium phosphate pastes, *Biomaterials* **26** (13) 1553 – 1563 (2005).
- [24] K. Anselme, B. Noel, B. Flautre, M.-C. Blary, C. Delecourt, M. Descamps, P. Hardouin, Association of porous hydroxyapatite and bone marrow cells for bone regeneration, *Bone* **25** (2 Supplement) 51S–54S (1999).
- [25] B. Flautre, K. Anselme, C. Delecourt, J. Lu, P. Hardouin, M. Descamps, Histological aspects in bone regeneration of an association with porous hydroxyapatite and bone marrow cells, *J. Mater. Sci: Mater. Med.* **10** 811–14 (1999).
- [26] R. Bareille, M. Lafage-Proust, C. Fauchoux, N. Laroche, R. Wenz, M. Dard, J. Amedee, Various evaluation techniques of newly formed bone in extraosseous site, *Biomaterials* **21** 1345–52 (2000).

- [27] L. Pothuaud, J. Fricain, S. Pallu, R. Bareille, M. Renard, M. Durrieu, M. Dard, J. Amedee, Mathematical modelling of the distribution of newly formed bone in bone tissue engineering, *Biomaterials* **26** 6788–97 (2005).
- [28] S. Nicoll, S. Radin, E. Santos, R. Tuan, P. Ducheyne, In vitro release kinetics of biologically active transforming growth factor-b1 from a novel porous glass carrier, *Biomaterials* **18** 853–59 (1997).
- [29] V. Midy, E. Hollande, C. Rey, M. Dard, J. Plouet, Adsorption of vascular endothelial growth factor to two different apatitic materials and its release, *J. Mater. Sci: Mater Med.* **12** 293–98 (2001).
- [30] P. Ruhe, H. K.-D. J. Wolke, P. Spauwen, J. Jansen, Bone inductive properties of rhbmp-2 loaded porous calcium phosphate cement implants in cranial defects in rabbits, *Biomaterials* **25** 2933–40 (2004).
- [31] M. Bohner, Calcium orthophosphates in medicine: from ceramics to calcium phosphate cements, *Injury* **31** S–D37–S–D47 (2000).
- [32] G. Daculsi, Biphasic calcium phosphate concept applied to artificial bone, implant coating and injectable bone substitute, *Biomaterials* **19** 1473–1478 (1998).
- [33] W. Paul, C. Sharma, Ceramic drug delivery: a perspective, *J. Biomed. Appl.* **17** 253–64 (2003).
- [34] D. Malik, G. Warwick, M. Venturi, M. Streat, K. Hellgardt, N. Hoenich, J. Dale, Preparation of novel mesoporous carbons for the adsorption of an inflammatory cytokine (il-1beta), *Biomaterials* **25** 2933–40 (2004).
- [35] A. Chong, X. Zhao, Functionalized nanoporous silicas for the immobilization of penicillin acylase, *Appl. Surf. Sci.* **237** 398–404 (2004).
- [36] A. Katiyar, L. Ji, P. Smirniotis, N. Pinto, Adsorption of bovine serum albumin and lysozym on siliceous MCM-41., *Micro. Meso.* **80** 311–20 (2005).
- [37] M. Choi, F. Kleitz, D. Liu, H. Lee, W. Ahn, R. Ryoo, Controlled polymerization in mesoporous silica towards the design of organic-inorganic composite nanoporous materials, *J. Am. Chem. Soc.* **127** 1924–32 (2005).
- [38] R. Gadiou, C. Vix-Guterl, Properties of carbon materials synthesized inside a confined medium, *Ann. Chim. - Sci. Mater.* **30** 425–30 (2005).
- [39] C. Vix-Guterl, S. Boulard, J. Parmentier, J. Werckmann, J. Patarin, Synthesis of ordered carbon material by cvl starting from a silica template, *Chem. Lett.* **10** 1065 (2002).
- [40] C. Vix-Guterl, I. Alix, P. Ehrburger, Synthesis of tubular silicon carbide (SiC) from a carbon-silica material by using a reactive replica technique: mechanism of formation of SiC, *Acta Mater.* **52** 1639–51 (2004).

- [41] C. Vix-Guterl, S. Saadallah, L. Vidal, M. Reda, J. Parmentier, J. Patarin, Template synthesis of a new type of mesoporous carbon structure from pitch, *J. Mater. Chem.* **13** 2535–39 (2003).
- [42] E. Jallot, J. Nedelec, A. Grimaud, E. Chassot, A. Grandjean-Laquerriere, P. Laquerriere, D. Laurent-Maquin, STEM and EDXS characterisation of physico-chemical reactions at the periphery of sol/gel derived Zn-substituted hydroxyapatites during interactions with biological fluids, *Colloids Surf. B* **42** 205–10 (2005).
- [43] C. Kinowski, B. Capoen, L. Hench, J. nedelec, R. Bechara, S. Turrell, M. Bouazoui, Structural and textural study of the effects of metals on the densification kinetics of nanoporous silica xerogels, *J. Non-Cryst. Solids* **345-46** 570–74 (2004).
- [44] A. Grandjean-Laquerriere, P. Laquerriere, E. Jallot, J. Nedelec, D. Laurent-Maquin, T. Philips, Influence of the zinc concentration of sol/gel derived zinc substituted hydroxyapatite on cytokine production by human monocytes in vitro, *Biomaterials* **27** (17) 3195–200 (2006).
- [45] F. Villars, B. Guillotin, T. Amedee, S. Dutoya, L. Bordenave, R. Bareille, J. Amedee, Effect of huvec on human osteoprogenitor cell differentiation needs heterotypic gap junction communication, *Am. J. Physiol. Cell Physiol.* **282** C775–85 (2002).
- [46] L. Bordenave, B. Chaudet, R. Bareille, P. Feranndez, J. Amedee, In vitro assessment of endothelial cell adhesion mechanism on vascular patches, *J. Mater. Sci: Mater. Med.* **10** 807–10 (1999).
- [47] P. Laquerriere, A. Grandjean-Laquerriere, E. Jallot, G. Balossier, M. Guenounou, Importance of hydroxyaptite particles characteristics on cytokine production by human monocytes in vitro, *Biomaterials* **24** 2739–47 (2003).
- [48] P. Laquerriere, A. Grandjean-Laquerriere, L. killian, A. Beorchia, M. Guenounou, E. Jallot, P. Frayssinet, G. Balossier, Influence of the hydroxyapatite particle characteristics on the [K]/[Na] ratio: a human monocytes in vitro study, *Colloids Surf. B* **33** 49–55 (2004).
- [49] K. Anselme, P. Sharrock, P. Hardouin, M. Dard, In vitro growth of human adult bone-derived cells on hydroxyapatite plasma-sprayed coatings, *J. Biomed. Mater. Res.* 247–59 (1997).
- [50] B. Flautre, G. Pasquier, M. Blary, K. Anselme, P. Hardouin, Evaluation of hydroxyapatite powder coated with collagen as an injectable bone substitute: microscopic study in rabbit, *J. Mater. Sci: Mater. Med.* **7** 63–67 (1996).
- [51] J. Lu, A. Gallur, B. Flautre, K. Anselme, M. Descamps, B. Thierry, P. Hardouin, Comparative study of tissue reactions to calcium phosphate ceramics among cancellous, cortical, and medullar bone sites in rabbits, *J. Biomed. Mater. Res.* **42** 357–67 (1998).

- [52] E. Jallot, J. Irigaray, G. Weber, P. Frayssinet, In vivo characterization of the interface between cortical bone and biphasic calcium phosphate by the PIXE method, *Surf. Interf. Anal.* **27** 648–52 (1999).
- [53] E. Jallot, J. Irigaray, H. Oudadesse, V. Brun, G. Weber, P. Frayssinet, Resorption kinetics of four hydroxyapatite-based ceramics by particle induced x-ray emission and neutron activation analysis, *Europ. Phys. J: Appl. Phys.* **6** 205–15 (1999).
- [54] P. Laquerriere, L. Killian, A. Bouchot, E. Jallot, M. Grandjean, M. Guenounou, G. Balossier, P. Frayssinet, p. Bonhomme, effect of hydroxyapatite sintering temperature on intracellular ionic concentrations of monocytes: a tem-cryo-x-ray microanalysis study, *J. Biomed. Mater. Res.* **58** 238–46 (2001).
- [55] F. Schüth, Non-siliceous mesostructured and mesoporous materials, *Chem. Mater.* **13** 3184–95 (2001).
- [56] M. Kruk, M. Jaroniec, Characterization of the porous structure of SBA-15, *Chem. Mater.* **12** 1961–68 (2000).
- [57] P. Schmidt-Winkel, C. Glinka, G. Stucky, Microemulsion templates for mesoporous silica, *Langmuir* **16** 356–61 (2000).
- [58] U. Ciesla, D. Demuth, R. Leon, P. Petroff, G. Stucky, K. Unger, F. Schüth, Surfactant controlled preparation of mesopstructured transition-metal oxide compounds, *J. Chem. Soc. Chem. Comm.* **11** 1387–88 (1994).
- [59] J. Yao, W. Tjandra, Y. Chen, K. Tam, J. Ma, B. Soh, Hydroxyapatite nanostructured material derived using cationic surfactant as a template, *J. Mater. Chem.* **13** 3053–57 (2003).
- [60] G. Bezzi, G. Celotti, E. Landi, T. M. G. L. Torretta, I. Sopyan, A. Tampieri, A novel sol-gel technique for hydroxyapatite preparation, *Mater. Chem. Phys.* **78** (3) 816 – 824 (2003).
- [61] W.Weng, S. Zhang, K. Cheng, H. Qu, P.Du, G. Shen, J. Yuan, G. Han, Sol-gel preparation of bioactive apatite films, *Surf. Coat. Tech.* **167** 292–96 (2003).
- [62] K. Cheng, G. Shen, W. Weng, G. Han, J. M. F. Ferreira, J. Yang, Synthesis of hydroxyapatite/fluoroapatite solid solution by a sol-gel method, *Mater. Lett.* **51** (1) 37 – 41 (2001).
- [63] C. Klein, A. Driessens, K. de Groot, A. V. der Hoff, Biodegradation behaviour of of various calcium phosphate materials in bone tissue, *J. Biomed. Mater. Res.* **17** 769–84 (1983).
- [64] G. Daculsi, R. L. Geros, D. Mitre, Crystal dissolution of biological and ceramic apatites, *Calcif. Tissue Int.* **45** 95–103 (1989).

- [65] E. I. Suvorova, F. Christensson, H. E. L. Madsen, A. A. Chernov, Terrestrial and space-grown HAP and OCP crystals: effect of growth conditions on perfection and morphology, *J. Cryst. Growth* **186** (1-2) 262 – 274 (1998).
- [66] A. Stein, Sphere templating methods for periodic porous solids, *Micro. Meso.* **44-45** 227–39 (2001).
- [67] B. Melde, A. Stein, Periodic macroporous hydroxyapatite-containing calcium phosphates, *Chem. Mater.* **14** 3326–31 (2002).
- [68] A. Stein, R. Schrodén, Colloidal crystal templating of three-dimensionally ordered macroporous solids: materials for photonics and beyond, *Curr. Op. Solid State Mater. Sci.* **5** 553–64 (2001).
- [69] P. B. Malafaya, G. A. Silva, E. T. Baran, R. L. Reis, Drug delivery therapies ii.: Strategies for delivering bone regenerating factors, *Curr. Op. Solid State Mater. Sci.* **6** (4) 297 – 312 (2002).
- [70] K. Janssens, P. T. Dijke, S. Janssens, W. V. Hul, TGF- β 1 to the bone, *Endocrine Rev.* **26** 743–74 (2005).
- [71] J. K. Leach, D. Kaigler, Z. Wang, P. H. Krebsbach, D. J. Mooney, Coating of VEGF-releasing scaffolds with bioactive glass for angiogenesis and bone regeneration, *Biomaterials* **27** (17) 3249 – 3255 (2006).
- [72] T. Boonthekul, D. J. Mooney, Protein-based signaling systems in tissue engineering, *Curr. Opin. Biotechnol.* **14** (5) 559 – 565 (2003).
- [73] T. Matsumoto, M. Okazaki, M. Inoue, S. Yamaguchi, T. Kusunose, T. Toyonaga, Y. Hamada, J. Takahashi, Hydroxyapatite particles as a controlled release carrier of protein, *Biomaterials* **25** 3807–12 (2004).
- [74] J. V. nd T. Bohling, H. Goransson, P. Pouolakkaien, Transforming growth factor beta released from natural coral implants enhances bone growth at calvarium of mature rat., *J. Biomed. Mater. Res.* **59** 152–59 (2002).
- [75] M. Lind, Growth factor stimulation of bone healing. Effects on osteoblasts, osteomies, and implant fixations, *Acta Orthop. Scand. Suppl.* **283** 2–37 (1998).
- [76] E. Arnaud, C. Morieux, M. Wybier, M. Vernejoul, Potentiation of transforming growth factor beta (tgf β 1) by natural coral and fibrin in a rabbit cranioplastiy model, *Calcif. Tissue Int.* **54** 493–98 (1994).
- [77] H. Baur, S. Kasperek, E. Pfaff, Criteria of viablity of isolated liver cells, *Hopp-Seyler's Z. Physiol. Chem.* **356** 827–38 (1975).
- [78] Y. Wang, J. Chen, K. Wei, S. Zhang, X. Wang, Surfactant-assited synthesis of hydroxyapaptite particles, *Mater. Lett.* **60** 3227–31 (2006).

- [79] E. Tkalcec, M. Sauer, R. Nonninger, H. Schmidt, Sol-gel-derived hydroxyapatite powders and coatings, *J. Mater. Sci.* **36** 5253–63 (2001).
- [80] S. Meejoo, W. Maneeprakorn, P. Winotai, Phase and thermal stability of nanocrystalline hydroxyapatite prepared via microwave heating, *Thermochim. Acta* **447** 115–20 (2006).
- [81] V. Rudin, V. Bozhevolnov, V. Zuev, V. Komarow, I. Melikhov, V. Minaev, A. Orlov, Method for producing a suspension of hydroxylapatite, Patent US 6254855 (2001).
- [82] L. Hammari, A. Laghzizil, P. Barboux, A. Saoiabi, K. Lahlil, Crystallinity and fluorine substitution effects on the photon conductivity of porous hydroxyapatite, *J. Solid State Chem.* **177** 134 (2004).
- [83] L. Hammari, H. Merroun, T. Coradin, S. Cassaignon, A. Laghzizil, A. Saoiabi, Mesoporous hydroxyapatite prepared in ethanol-water media/ structure and surface properties, *Mat. Chem. Phys.* **104** 448–53 (2007).
- [84] E. Fujii, M. Ohkubo, K. Tsuru, S. Hayakawa, A. Osaka, K. Kawabata, C. Bonhomme, F. Babonneau, Selective protein adsorption property and characterization of nano-crystalline zinc-containing hydroxyapatite, *Acta Biomater.* **2** 69–74 (2006).
- [85] T. Thamaraiselvi, K. Prabakaran, S. Rajeswari, Synthesis of hydroxyapatite that mimic bone mineralogy, *Trends Biomater. Artif. Organs* **19** (2) 81–83 (2006).
- [86] L. Gan, R. Pilliar, Calcium phosphate sol-gel-derived thin films on porous-surfaced implants for enhanced osteoconductivity. Part I: Synthesis and characterisation, *Biomaterials* **25** 5303–12 (2004).
- [87] T. Brendel, A. Engel, C. Ruessel, Hydroxyapatite coatings by a polymeric route, *J. Mater. Sci.-Mater. Med.* **3** 175–79 (1992).
- [88] A. Chaudhry, S. Haque, S. Kellici, P. Boldrin, I. Rehman, F. Khalid, J. Darr, Instant nano-hydroxyapatite: a continuous and rapid hydrothermal synthesis, *Chem. Commun.* 2286–88 (2006).
- [89] M. Saeri, A. Afshar, M. Ghorbani, N. Ehsani, C. Sorrell, The wet precipitation process of hydroxyapatite, *Mater. Lett.* **57** 4064–69 (2003).
- [90] J. Cihlar, K. Castkova, Synthesis of calcium phosphates from alkyl phosphates by the sol-gel method, *Ceramics-Silikaty* **42** (4) 164–67 (1998).
- [91] C. Li, F. Meng, Nano-crystalline hydroxyapatite synthesized by neutralization with the assist of citric acid, *Mater. Lett.* **62** 932–34 (2008).

- [92] K. Cheng, W. Weng, H. Wang, S. Zhang, In vitro behavior of osteoblast-like cells on fluoridated hydroxyapatite coatings, *Biomaterials* **26** 6288–95 (2005).
- [93] G. Spoto, E. Ciliberto, G. Allen, A new synthetic route to hydroxyapatite coatings, *J. Mater. Chem.* **4** (2) 1849–50 (1994).
- [94] R. Terpstra, Y. Roman, K. Timmer, H. Meinema, Method for manufacture a fiber-reinforced bioactive ceramic implant, Patent US 6248392 (2001).
- [95] J. Darr, Z. Guo, V. Raman, M. Bououdina, I. Rehman, Metal organic chemical vapour deposition (MOCVD) of bone mineral like carbonated hydroxyapatite coatings, *Chem. Commun.* 696–97 (2004).
- [96] R. R. Rao, H. Roopa, T. Kannan, Solid state synthesis and thermal stability of HAP and HAP- β -TCP composite ceramic powders, *J. Mater. Sci: Mater. Med.* **8** 511–18 (1997).
- [97] K. Yeong, J. Wang, S. Ng, Mechanochemical synthesis of naocrystalline hydroxyapatite from Ca and CaHPO_4 , *Biomaterials* **22** 2705–12 (2001).
- [98] B. Chang, C. Lee, K. Hong, H. Youn, H. Ryu, S. Chung, K. Park, Osteoconduction at porous hydroxyapatite with various pore configurations, *Biomaterials* **21** 1291–1298 (2000).
- [99] H. Y. Juang, M. H. Hon, Effect of calcination on sintering of hydroxyapatite, *Biomaterials* **17** (21) 2059 – 2064 (1996).
- [100] L. Hench, J. Polak, Third-generation biomedical materials, *Science* **295** (5557) 1014–17 (2002).
- [101] M. Okada, T. Furuzono, Fabrication of high-dispersibility nanocrystals of calcined hydroxyapatite, *J. Mater. Sci.* **41** 6134–37 (2006).
- [102] H. Liu, T. Chin, L. Lai, S. Chiu, K. Chung, C. Chang, M. Lui, Hydroxyapatite synthesized by a simplified hydrothermal method, *Ceram. Int.* **23** 19–25 (1997).
- [103] P. Dibandjo, L. Bois, C. Estournes, B. Durand, P. Miele, Silica, carbon and boron nitride monoliths with hierarchical porosity prepared by spark plasma sintering process, *Micro. Meso.* **111** (1-3) 643 – 648 (2008).
- [104] K. Sing, D. Everett, R. Haul, L. Moscou, J. Pierrotti, J. Roquerol, T. Siemieniowska, Reporting physisorption data for gas/solid systems with special reference to the determination of surface area and porosity, *Pure Appl. Chem.* **57** 603 (1985).
- [105] Y. Wan, H. Yang, D. Zhao, "Host-guest" chemistry in the synthesis of ordered non-siliceous mesoporous materials, *Acc. Chem. Res.* **39** (7) 423–432 (2006).
- [106] F. Schüth, Non-siliceous mesostructured and mesoporous materials, *Chem. Mater.* **13** 3184–95 (2001).

- [107] S. Inagaki, A. Koiwai, N. Suzuki, Y. Fukushima, K. Kuroda, Synthesis of highly ordered mesoporous materials, FSM-16, derived from kameinite, *Bull. Chem. Soc. Jpn.* **69** (5) 1449–57 (1996).
- [108] J. Ying, C. Mehnert, M. Wong, Synthesis and applications of supramolecular-templated mesoporous materials, *Angew. Chem. Int. Ed.* **38** 56–77 (1999).
- [109] J. H. Knox, B. Kaur, G. Millward, Structure and performance of porous graphitic carbon in liquid chromatography, *J. Chromatogr. A* **352** 3 – 25 (1986).
- [110] R. Ryoo, S. Joo, M. Kruk, M. Jaroniec, Ordered mesoporous carbons, *Adv. Mater.* **13** (9) 677–81 (2001).
- [111] J. Parmentier, S. Saadallah, M. Reda, P. Gibot, M. Roux, L. Vidal, C. Vix-Guterl, J. Patarin, New carbons with controlled nanoporosity obtained by nanocasting using a SBA-15 mesoporous silica host matrix and different preparation routes, *J. Phys. Chem. Solids* **65** (2-3) 139–146 (2004).
- [112] F. Schüth, Endo- and exotemplating to create high-surface-area inorganic materials, *Angew. Chem. Int. Ed.* **42** 3604–22 (2003).
- [113] I. Sopyan, M. Mel, S. Ramesh, K. Khalid, Porous hydroxyapatite for artificial bone applications, *Sci. Technol. Adv. Mater.* **8** (1-2) 116 (2007).
- [114] M. Potoczek, Hydroxyapatite foams produced by gelcasting using agarose, *Chem. Mater.* **62** 1055–57 (2008).
- [115] J. Tulliani, V. Naglieri, M. Lombardi, L. Montanaro, Gel casting of porous alumina and zirconia bodies, *Adv. Technol. Mater. Mater. Proc.* **11** (1).
- [116] Y. Tang, Y. Tang, C. Lv, Z. Zhao, Preparation of uniform porous hydroxyapatite biomaterials by a new method, *Appl. Surf. Sci.* **254** (17) 5359–62 (2008).
- [117] D. Liu, Influence of porosity and pore size on the compressive strength of porous hydroxyapatite ceramics, *Ceram. Int.* **23** 135–39 (1997).
- [118] M. Fujishima, Y. Okawa, K. Uchida, Hierarchical trimodal porous hydroxyapatite fabricated by colloidal crystal templating using single-size latex particles, *J. Am. Chem. Soc.* **91** 3749–52 (2008).
- [119] M. Descamps, O. Richart, P. Hardouin, J. Hornez, A. Leriche, Synthesis of macroporous beta-calcium phosphate with controlled porous architectural, *Ceram. Int.* **34** 11331–37 (2008).
- [120] D. Wang, X. Duan, J. Zhang, A. Yao, L. Zhou, W. Huang, Fabrication of superparamagnetic hydroxyapatite with highly ordered three-dimensional pores, *J. Mater. Sci.* **44** 4020–25 (2009).

- [121] J. Fan, J. Lei, C. Yu, B. Tu, D. Zhao, Hard-templating synthesis of a novel rod-like nanoporous calcium phosphate bioceramics and their capacity as antibiotic carriers, *Mater. Chem. Phys.* **103** 489–93 (2007).
- [122] Z. Xia, L. Liao, S. Zhao, Synthesis of mesoporous hydroxyapatite using a modified hard-templating route, *Mater. Res. Bull.* **44** 1626–29 (2009).
- [123] W. He, Z. Li, Y. Wang, X. Cheng, X. Zhang, H. Zhao, S. Yan, W. Zhou, Synthesis of mesoporous structured hydroxyapatite particles using yeast cells as template, *J. Mater. Sci.: Mater. Med.* **21** 155–59 (2010).
- [124] S. Mann, G. Ozin, Synthesis of inorganic materials with complex form, *Nature* **382** 313–18 (1996).
- [125] G. J. d. A. A. Soler-Illia, C. Sanchez, B. Lebeau, J. Patarin, Chemical strategies to design textured materials: from microporous and mesoporous oxides to nanonetworks and hierarchical structures, *Chem. Rev.* **102** (11) 4093–4138 (2002).
- [126] S. Bailliez, A. Nzihou, The kinetics of surface area reduction during isothermal sintering of hydroxyapatite adsorbent, *Chem. Eng. J.* **98** 141–52 (2004).
- [127] P. Yang, T. Deng, D. Zhao, P. Feng, D. Pine, B. Chmelka, G. Whitesides, G. Stucky, Hierarchically ordered oxides, *Science* **282** 2244–46 (1998).
- [128] S. Schmidt, J. McDonald, E. Pinada, A. Verwilt, Y. Chen, R. Josephs, A. Ostafin, Surfactant based assembly of mesoporous patterned calcium phosphate micron-sized rods, *Micro. Meso.* **94** 330–38 (2006).
- [129] B. Prelot, T. Zemb, Calcium phosphate precipitation in cationic templates, *Mater. Sci. Eng. C* **25** 553–59 (2005).
- [130] W. Zhang, L. Zhang, J. Xiu, Z. Shen, Y. Li, P. Ying, C. Li, Pore size design of ordered mesoporous silicas by controlling micellar properties of triblock copolymer EO20PO70EO20, *Micro. Meso.* **89** 179–85 (2006).
- [131] X. Xiao, R. Liu, F. Liu, X. Zheng, D. Zhu, Effect of poly(sodium 4-styrenesulfonate) on the crystal growth of hydroxyapatite prepared by hydrothermal method, *Mater. Chem. Phys.* **120** (2-3) 603–07 (2010).
- [132] N. Ikawa, H. Hori, T. Kimura, Y. Oumi, T. Sano, Unique surface property of surfactant-assisted mesoporous calcium phosphate, *Micro. Meso.* **in press**.
- [133] S. Ng, J. Guo, J. Ma, S. C. J. Loo, Synthesis of high surface area mesostructured calcium phosphate particles, *Acta Biomater.* **6** 3772–3781 (2010).
- [134] Y. Zhao, J. Ma, triblock co-polymer templating synthesis of mesostructured hydroxyapatite, *Micro. Meso.* **87** 110–17 (2005).

- [135] G. de A.A. Soler-Illia, E. Crepaldi, D. Grosso, C. Sanchez, Block copolymer-templated mesoporous oxides, *Curr. Op. Coll. Interf. Sci.* **8** 109–26 (2003).
- [136] H. Wang, L. Zhai, Y. Li, T. Shi, Preparation of irregular mesoporous hydroxyapatite, *Mater. Res. Bull.* **43** 1607–14 (2008).
- [137] A.-H. Lu, W.-C. Li, W. Schmidt, F. Schüth, Template synthesis of large pore ordered mesoporous carbon, *Micro. Meso.* **80** (1-3) 117 – 128 (2005).
- [138] P. Schmidt-Winkel, W. L. Jr, D. Zhang, P. Yang, B. Chmelka, G. Stucky, Mesocellular siliceous foams with uniform sized cells and windows, *J. Am. Chem. Soc.* **121** 254–55 (1999).
- [139] P. Schmidt-Winkel, W. L. Jr, P. Yang, D. Margolese, J. Lettow, J. Ying, G. Stucky, Microemulsion templating of siliceous mesostructured cellular foams with well-defined ultralarge mesopores, *Chem. Mater.* **12** 686–96 (2000).
- [140] R. Ryoo, S. H. Joo, S. Jun, Synthesis of highly ordered carbon molecular sieves via template-mediated structural transformation, *J. Phys. Chem. B* **103** (37) 7743–7746 (1999).
- [141] P. Vinke, M. Van der Eijk, M. Verbree, A. Voskamp, H. Van Bekkum, Modification of the surfaces of a gasactivated carbon and a chemically activated carbon with nitric acid, hypochlorite, and ammonia, *Carbon* **32** (4) 675–686 (1994).
- [142] A. Jillavenkatesa, R. C. Sr, Sol-gel processing of hydroxyapatite, *J. Mater. Sci.* **33** 4111–4119 (1998).
- [143] T. Kuriakose, S. Kalkura, M. Palanichamy, D. Arivuoli, K. Dierks, G. Bocelli, C. Betzel, Synthesis of stoichiometric nano crystalline hydroxyapatite by ethanol-based sol-gel technique at low temperature, *J. Crystal Growth* **263** 517–23 (2004).
- [144] L. Cao, H. Dong, L. Huang, K. Matyjaszewski, M. Kruk, Synthesis of large-pore SBA-15 silica using poly(ethylene oxide)-poly(methyl acrylate) diblock copolymers, *Adsorption* **15** 156–66 (2009).
- [145] C. Liang, Z. Li, S. Dai, Mesoporous carbon materials: synthesis and modification, *Angew. Chem. Int. Ed.* **47** 3696–717 (2008).
- [146] Y. Wan, H. Yang, D. Zhao, “Host- Guest” Chemistry in the Synthesis of Ordered Nonsiliceous Mesoporous Materials, *Acc. Chem. Res* **39** (7) 423–432 (2006).
- [147] D. Liu, T. Troczynski, W. Tseng, Water-based sol-gel synthesis of hydroxyapatite: process development, *Biomaterials* **22** 1721–30 (2001).
- [148] V. Sinyaev, E. Shutstikova, L. Levchenko, A. Sedunov, Synthesis and hydration of amorphous calcium phosphate, *Inorg. Mater.* **37** 735–38 (2001).

- [149] G. Narsimhan, Thermal decomposition of calcium carbonate, *Chem. Eng. Sci.* **16** (1-2) 7–20 (1961).
- [150] C. Satterfield, F. Feakes, Kinetics of the thermal decomposition of calcium carbonate, *AIChE Journal* **5** (1) 115–122 (1959).
- [151] C. Alba-Simionesco, B. Coasne, G. Dosseh, G. Dudziak, K. Gubbins, R. Radhakrishnan, M. Sliwinska-Bartkowiak, Effects of confinement on freezing and melting, *J. Phys: Condens. Mater.* **18** R15–R68 (2006).
- [152] C. Combes, B. Miao, R. Bareille, C. Rey, Preparation, physical-chemical characterisation and cytocompatibility of calcium carbonate cements, *Biomaterials* **27** (9) 1945–1954 (2006).
- [153] E. Shors, E. White, G. Kopchok, Biocompatibility, osteoconduction and biodegradation of porous hydroxyapatite, tricalcium phosphate, sintered hydroxyapatite and calcium carbonate in rabbit bone defects, in: *Biomedical Materials and Devices*, MRS, Materials Research Society, 9800 McKnight Rd, Suite 327, Pittsburgh, Pennsylvania 15237, USA, Boston, Massachusetts; USA, 1987, pp. 211–217.
- [154] H. Ohgushi, M. Okumura, T. Yoshikawa, K. Inboue, N. Senpuku, S. Tamai, E. Shors, Bone formation process in porous calcium carbonate and hydroxyapatite, *J. Biomed. Mater. Res.* **26** (7) 885–895 (1992).
- [155] L. Quin, Practical aspects of the chemistry of metaphosphates and other transient dioxophosphates, *Coord. Chem. Rev.* **137** 525–59 (1994).
- [156] J. Parmentier, S. Saadhallah, M. Reda, P. Gibot, M. Roux, L. Vidal, C. Vix-Guterl, J. Patarin, New carbons with controlled nanoporosity obtained by nanocasting using a sba-15 mesoporous silica host matrix and different preparation routes, *J. Phys. Chem. Solids* **65** (2-3) 139 – 146 (2004).
- [157] M. Inagaki, H. Konno, O. Tanaike, Carbon materials for electrochemical capacitors, *J. Power Sources* **195** (24) 7880 – 7903 (2010).
- [158] M. Pereira, L. Hench, Mechanisms of hydroxyapatite formation on porous gel-silica substrates, *J. Sol-gel Sci. Techn.* **7** 59–68 (1996).
- [159] C. Wilson, R. Clegg, D. Leavesley, M. Percy, Mediation of biomaterial-cell interactions by adsorbed proteins: a review, *Tissue Eng.* **11** (1/2) 1–17 (2005).
- [160] C. Combes, C. Rey, Adsorption of proteins and calcium phosphate materials bioactivity, *Biomaterials* **23** (13) 2817–2823 (2002).
- [161] S. Barlow, K. Kitching, S. Haq, N. Richardson, A study of glycine adsorption on Cu(110) surface using reflection adsorption infrared spectroscopy, *Surf. Sci.* **401** 322–335 (1998).

- [162] M. Gorbunoff, The interaction of proteins with hydroxyapatite: I. Role of protein charge and structure, *Anal. Biochem.* **136** 425–32 (1984).
- [163] C. Combes, C. Rey, M. Freche, In vitro crystallization of octacalcium phosphate on type I collagen: influence of serum albumin, *J. Mater. Sci.: Mater. Med.* **10** (3) 153–160 (1999).
- [164] G. Penel, G. Leroy, C. Rey, B. Sombret, J. Huvenne, E. Bres, Infrared and raman microspectroscopy study of fluor-fluor-hydroxy and hydroxy-apatite powders, *J. Mater. Sci.: Mater. Med.* **8** 271–76 (1997).
- [165] C. Cazalbou, C. Combes, D. Eichert, C. Rey, M. Glimcher, Poorly crystalline apatites: evolution and maturation in vitro and in vivo, *J. Bone Miner. Metab.* **22** 310–317 (2004).
- [166] S. Ouizat, A. Barroug, A. Legrouri, C. Rey, Adsorption of bovine serum albumin on poorly crystalline apatite: influence of maturation, *Mater. Res. Bull.* **34** (14/15) 2279–89 (1999).
- [167] J. Diaz, K. B. Jr, Enzyme immobilization in MCM-41 molecular sieve, *J. Mol. Cat. B: Enzymatic* **2** 115–126 (1996).
- [168] A. Vinu, V. Murugesan, M. Hartmann, Adsorption of lysozyme over mesoporous molecular sieves MCM-41 and SBA-15: influence of pH and aluminium incorporation, *J. Phys. Chem. B* **108** 7323–30 (2004).
- [169] A. Vinu, V. Murugesan, O. Tangermann, M. Hartmann, Adsorption of cytochrome c on mesoporous molecular sieves: Influence of pH, pore diameter, and aluminium incorporation, *Chem. Mater.* **16** 3056–65 (2004).
- [170] A. Vinu, M. Miyahara, K. Agira, Biomaterial immobilization in nanoporous carbon molecular sieves: Influence of solution pH, pore volume, and pore diameter, *J. Phys. Chem. B* **109** 6436–41 (2005).
- [171] A. Vinu, T. Mori, K. Ariga, New families of mesoporous materials, *Sci. Technol. Adv. Mat.* **7** 753–771 (2006).
- [172] H. Yiu, C. Botting, N. Botting, P. Wright, Size selective protein adsorption on thiol-functionalized SBA-15 mesoporous molecular sieves, *Phys. Chem. Chem. Phys.* **3** 2983–85 (2001).
- [173] J. Andrade, V. Hlady, A. Wei, C. Ho, A. Lea, S. Jeon, Y. Lin, Proteins at interfaces: Principles, multivariate aspects, protein resistant surfaces, and direct imaging and manipulation of adsorbed proteins, *Clin. Mater.* **11**.
- [174] A. Vinu, G. Chandrasekar, M. Hartmann, Adsorption of vitamin E on mesoporous carbon molecular sieves, *Chem. Mater.* **17** 829–833 (2005).

- [175] L. Washmon-Kriel, V. Jimenez, K. B. Jr, Cytochrome c immobilization into mesoporous molecular sieves, *J. Surf. Sci. Catal. B* **10** 453–69 (2000).
- [176] R. Ravindra, S. Zhao, H. Gies, R. Winter, Protein encapsulation in mesoporous silicate: the effect of confinement on protein stability, hydration and volumetric properties, *J. Am. Chem. Soc.* **126** 12224–25 (2004).
- [177] A. H. Zisch, M. Lutolf, M. Ehrbar, G. Raeber, S. Rizzi, N. Davies, H. Schmökel, D. Bezuidenhout, V. Djonov, P. Zilla, J. Hubbell, Cell-demanded release of VEGF from synthetic cell-ingrowth matrices for vascularized tissue growth, *FASEB Journal* **in press**.
- [178] Y. Tabata, The importance of drug delivery systems in tissue engineering, *Pharm. Sci. Technol. Today* **3** (3) 80–88 (2000).
- [179] J. Tessmar, A. Göpferich, Matrices and scaffolds for protein delivery in tissue engineering, *Adv. Drug Deliv. Rev.* **59** 274–91 (2007).
- [180] M. H. Sheridan, L. D. Shea, M. C. Peters, D. J. Mooney, Bioabsorbable polymer scaffolds for tissue engineering capable of sustained growth factor delivery, *J. Controlled Release* **64** (1-3) 91 – 102 (2000).
- [181] W. L. Murphy, M. C. Peters, D. H. Kohn, D. J. Mooney, Sustained release of vascular endothelial growth factor from mineralized poly(lactide-co-glycolide) scaffolds for tissue engineering, *Biomaterials* **21** (24) 2521 – 2527 (2000).
- [182] J. W. M. Vehof, J. P. Fisher, D. Dean, J.-P. C. M. van der Waerden, P. H. M. Spauwen, A. G. Mikos, J. A. Jansen, Bone formation in transforming growth factor beta-1-coated porous poly(propylene fumarate) scaffolds, *J. Biomed. Mater. Res.* **60** (2) 241–251 (2002).
- [183] A. Lode, C. Wolf-Brandstetter, A. Reinstorf, A. Bernhardt, U. König, W. Pompe, M. Gelinsky, Calcium phosphate bone cements, functionalized with VEGF: release kinetics and biological activity, *J. Biomed. Mater. Res.* **81A** 474–83 (2007).
- [184] E. Wernike, W. Hofstetter, Y. Liu, G. Wu, H.-J. Sebald, D. Wismeijer, E. B. Hunziker, K.-A. Siebenrock, F. M. Klenke, Long-term cell-mediated protein release from calcium phosphate ceramics, *J. Biomed. Mater. Res.* **92A** (2) 463–474 (2010).
- [185] E. wernike, M.-O. Montjovent, Y. Liu, D. Wismeijer, E. Hunziker, K.-A. Siebenrock, W. Hofstetter, F. Klenke, VEGF incorporation into calcium phosphate ceramics promotes vascularisation and bone formation in vivo, *Eur. Cells Mater.* **19** 30–40 (2010).
- [186] Y. Liu, P. Layrolle, J. de Bruijn, C. van Blitterswijk, K. de Groot, Biomimetic coprecipitation of calcium phosphate and bovine serum albumin on titanium alloy, *J. Biomed. Mater. Res.* **57** (3) 327–335 (2001).

- [187] L. Beck, R. Wong, L. DeGuzman, W. Lee, B. Ongpipattanakul, T. Nguyen, Combination of bone marrow and $\text{tgf-}\beta 1$ augemnt the healing of critical-sized bone defects, *J. Pharmaceut. Sci.* **87** 1379–86 (1998).
- [188] M. Lind, S. Overgaard, B. Ongpipattanakul, T. Nguyen, C. Bunger, K. Soballe, Transfroming growth factor- $\beta 1$ stimulates bone ongrowth to weight-loaded tricalcium phosphate coated implants, *J. Bone Joint Surg.* **78B** 377–82 (1996).
- [189] D. Link, J. van der Dolder, J. van dern Beucken, J. Wolke, A. Mikos, J. Jansen, Bone reponse and mechanical strength of rabbit femoral defects filled with injectable cap cements containing $\text{tgf-}\beta 1$ loaded gelatine micorparticles, *Biomaterials* **29** 675–82 (2008).
- [190] M. Detmar, L. F. Brown, M. P. Schon, B. M. Elicker, P. Velasco, L. Richard, D. Fukumura, W. Monsky, K. P. Claffey, R. K. Jain, Increased microvascular density and enhanced leukocyte rolling and adhesion in the skin of VEGF transgenic mice, *J. Invest. Dermatol.* **111** (1) 1–6 (1998).
- [191] H. Rehm, Der Experimentator Proteinbiochemie/Proteomics, 5, Spektrum Akademischer Verlag, Elsevier GmbH, Munchen, 2006.
- [192] M. Rouahi, E. Champion, O. Gallet, A. Jada, K. Anselme, Physico-chemical characteristics and protein adsorption potential of hydroxyapatite particles: Influence on in vitro biocompatibility of ceramics after sintering, *Coll. Surf. B* **47** 10–19 (2006).
- [193] J. Deere, E. Magner, J. Wall, B. Hodnett, Adsorption and activity of cytochrome c on messoporous silicates, *Chem. Comm.* 465–66 (2001).
- [194] D. H. Wassell, R. Hall, G. Embery, Adsorption of bovine serum albumin onto hydroxyapatite, *Biomaterials* **16** 697–702 (1995).
- [195] N. Ferrara, T. Davis-Smyth, The biology of vascular endothelial growth factor, *Endocrine Rev.* **18** 4–24 (1997).
- [196] Fluxion, Viscosity-understanding effects of viscosity in the bioflux system, Tech. rep., Fluxion Biosciences (2008).
- [197] K. Turan, K. Nagata, Chitosan-DNA nanoparticles: the effect of cell type and hydrolysis of chitosan on in vitro dna transfection, *Pharm. Dev. Technol.* **11** 503–12 (2006).
- [198] M. Gorbunoff, The interaction of proteins with hydroxyapatite: Ii. Role of acidic and basic groups, *Anal. Biochem.* **136** 433–39 (1984).
- [199] Y. Yang, D. Dennison, J. Ong, Protein adsorption and osteoblast precursor cell attachment to hydroxyapatite of different cristallinities, *Int. J. Oral Maxillofacial Implants* **20** 187–92 (2005).

- [200] B. D. Fair, A. M. Jamieson, Studies of protein adsorption on polystyrene latex surfaces, *J. Coll. Interf. Sci.* **77** (2) 525 – 534 (1980).
- [201] S. Brunauer, P. H. Emmett, E. Teller, Adsorption of gases in multimolecular layers, *J. Am. Chem. Soc.* **60** 309–319 (1938).
- [202] S. Brunauer, L. S. Deming, W. E. Deming, E. Teller, On a theory of the van der Waals adsorption of gases, *J. Am. Chem. Soc.* **62** (7) 1723–1732 (1940).
- [203] S. J. Gregg, K. S. W. Sing, Adsorption, Surface Area and Porosity, 2nd Edition, Academic Press, London, 1982.
- [204] B. Siegert, Filling carbon nanotubes for nanoenergetic formulations, Ph.D. thesis, Universite de Strasbourg (2010).
- [205] M. Muris, N. Dufau, M. Bienfait, N. Dupont-Pavlovsky, Y. Grillet, J. Palmari, Methane and krypton adsorption on single-walled carbon natubes, *Langmuir* **16** 7019–22 (2000).
- [206] J. B. Condon, Surface area and porosity determination by physisorption - measurements and theory, Elsevier Limited, Amsterdam, 2006.
- [207] E. Barrett, L. Joyner, P. Halenda, The determination of pore volume and area distributions in prous substances. I. Computations from nitrogen isotherms, *J. Am. Chem. Soc.* **73** 373–80 (1951).

Résumé étendu en français

Introduction et contexte

Les biomatériaux et l'ingénierie tissulaire

Une définition générale du terme « biomatériau » n'est pas facile à trouver puisque le domaine des biomatériaux est très interdisciplinaire. La définition suivante, proposée en 1990 par D.F. Williams, est toujours largement acceptée par les chercheurs dans le domaine : *Un biomatériau est un matériau non-vivant qui est destiné à être à l'interface avec les systèmes biologiques pour évaluer, traiter, augmenter ou remplacer un tissu, un organe ou une fonction dans le corps* [1]. Il est important de noter que le biomatériau se définit par son interface avec le système biologique, un stimulateur cardiaque hermétiquement fermé ne peut donc pas être considéré comme un biomatériau. Williams élargit sa définition pour donner plus de possibilités vis-à-vis de développements futurs : *Un biomatériau est une substance qui a été créée dans une forme qui, seule ou dans un système complexe est utilisée pour diriger, par contrôle des interactions avec les composantes des systèmes vivants, le déroulement d'un procédé thérapeutique ou diagnostique dans la médecine humaine ou vétérinaire.*

L'ingénierie tissulaire est la combinaison de matériaux artificiels avec des composantes biologiques. Elle comprend :

- des cellules isolées
- des substances qui induisent la formation de tissu
- des cellules sur des matrices.

Notre projet s'inscrit dans le cadre des substances qui induisent la formation de tissu.

Les phosphates de calcium sont couramment utilisés pour l'ingénierie tissulaire osseuse parce que leur composition chimique se rapproche de la phase minérale de l'os. Ils sont biocompatibles et forment une liaison étroite avec le tissu osseux qui les entoure. Dans notre projet, nous utilisons de l'hydroxyapatite $\text{Ca}_{10}(\text{PO}_4)_6(\text{OH})_2$. L'hydroxyapatite est peu soluble dans l'eau et se résorbe lentement après implantation. Elle forme une liaison avec l'os par les étapes suivantes : dans un premier temps, des cellules ostéocompétentes adhèrent à la surface du matériau. L'hydroxyapatite induit une différenciation de ces cellules. Progressivement, une matrice osseuse se forme à l'interface. Cette interface est majoritairement amorphe, mais contient déjà des cristaux d'apatite. A la fin, l'hydroxyapatite est liée à l'os par une fine couche épitaxiale.

Le projet ANR

Les travaux de cette thèse s'inscrivent dans le cadre du projet ANR PNano NANO-BONEFILLER qui a été déposé en 2006 par six laboratoires français. Ce projet a pour but de développer un nouveau système de comblement osseux à base de phosphates de calcium mésoporeux associés à des facteurs de croissance. Le projet associe des chimistes spécialistes dans le domaine des matériaux poreux et des synthèses de phosphates de calcium, des médecins pour la caractérisation approfondie des céramiques et de l'interface implant/tissu et des biologistes pour l'évaluation des matériaux *in vitro* et *in vivo*. Le déroulement du projet peut être divisé en cinq phases :

1. Synthèse de phosphates de calcium à porosité contrôlée
2. Validation de la capacité de rétention de protéines des céramiques poreuses
3. Analyse du potentiel inflammatoire des céramiques
4. Validation du potentiel ostéogénique des céramiques chargées en facteurs de croissance *in vitro* et *in vivo*
5. Caractérisation de l'interface entre l'implant et le tissu osseux par cartographie chimique

Les travaux présentés dans cette thèse font partie des deux premières phases de ce projet : Dans un premier temps, des techniques de réplique sont développées pour la synthèse des phosphates de calcium mésoporeux : des mousses de silice mésoporeuses sont obtenues par condensation des tétraéthyle orthosilicate (TEOS) en présence de micelles de surfactant. Des répliques carbonées de ces silices sont réalisées par infiltration en phase vapeur de propylène ou par infiltration liquide de saccharose en solution acide. La dissolution de la silice par un traitement d'acide fluorhydrique libère la porosité de la matrice carbonée. L'hydroxyapatite est ensuite synthétisée dans la porosité des templates siliciques ou carbonés par infiltration de précurseurs en solution aqueuse. L'élimination de la matrice s'effectue par dissolution chimique par de la soude dans le cas du template silicique et par oxydation sélective sous air dans le cas du template carboné.

Dans un deuxième temps, les cinétiques d'adsorption et de relargage de protéines sont analysées sur un certain nombre de céramiques représentatives. Parmi ces céramiques, la moitié des échantillons provient du laboratoire LMI à Clermont, qui synthétise des phosphates de calcium mésoporeux par une approche sol-gel impliquant des surfactants. Après la validation d'un protocole d'adsorption de protéine avec les protéines modèles BSA (albumine du sérum bovin) et Cytochrome C, des essais avec les facteurs de croissance TGF- β et VEGF sont effectués. La concentration des protéines sur la céramique est déterminée par une méthode de déplétion : la concentration de protéine est mesurée dans le surnageant par absorbance UV/Vis pour les protéines modèles et par ELISA pour les facteurs de croissance.

Synthèse d'hydroxyapatite par réplique

Dans ce chapitre, les méthodes de synthèse d'hydroxyapatite mésoporeuse sont décrites. Après une partie bibliographique plus générale qui introduit les synthèses d'hydroxy-

apatite et les approches de réplique, les synthèses d'hydroxyapatite mésoporeuse dans la littérature sont discutées. La partie expérimentale décrit les synthèses effectuées au cours de ce travail de thèse. Les résultats de différentes techniques de caractérisation sont présentés dans la partie suivante. Dans la discussion, les résultats sont discutés par rapport au contexte bibliographique. Une conclusion résume les résultats les plus importants.

Bibliographie

Dans un premier temps, nous donnons un aperçu des techniques de synthèse d'hydroxyapatite en présentant les précurseurs et les techniques de synthèse habituellement utilisés sous forme d'une revue bibliographique. Ensuite, les techniques de réplique sont introduites : les termes les plus importants (réplique, endo-réplique, exo-réplique etc.) sont définis. Dans la partie bibliographie de ce chapitre nous discutons les synthèses d'hydroxyapatite mésoporeux qui ont été publiés jusqu'à ce jour.

Il faut noter que seulement deux synthèses d'hydroxyapatite mésoporeux par nanoréplique ont été publiées. Les nanorépliques s'appliquent en général uniquement à des céramiques macroporeuses, les céramiques mésoporeuses sont obtenues avec des surfactants (autoassemblage). Les deux synthèses de nanoréplique utilisent des matériaux carbonés de type CMK-3 comme matériau hôte. L'équipe de Fan et Zhao [121] obtient des céramiques avec des surface spécifiques de l'ordre de $30 \text{ m}^2/\text{g}$ sous forme de nano-aiguilles. Néanmoins, l'isotherme d'adsorption d'azote montre que la porosité est texturale (porosité entre les grains). Il ne s'agit donc pas d'une vraie mésoporosité. Les résultats obtenus par Xia et son équipe [122] sont similaires. Même si la surface spécifique est un peu plus élevée ($40 \text{ m}^2/\text{g}$), la porosité est texturale. Dans les deux cas, les auteurs n'observent pas d'effet de réplique, c'est-à-dire la porosité de la céramique ne correspond pas à la structure de l'hôte.

Partie expérimentale et résultats

Dans la partie expérimentale, les méthodes utilisées dans cette thèse sont présentées. Les résultats de ces expériences sont décrits dans la partie suivante « résultats ». Contrairement aux méthodes décrites dans la partie bibliographie, différents matériaux hôtes sont utilisés : les silices de type mousse possèdent une porosité plus grande (en terme de volume poreux et de taille de pores), plus favorable à l'imprégnation avec un précurseur d'hydroxyapatite. Les répliques carbonées de ces silices possèdent une grande surface spécifique et une porosité ouverte. Les silices et les répliques carbonées servent d'hôte pour la synthèse d'hydroxyapatite.

Cinq combinaisons de précurseurs sont utilisées pour les synthèses :

- un sol/gel aqueux élaboré à partir de $\text{Ca}(\text{NO}_3)_2$ et de $(\text{EtO})_3\text{P}$,
- une méthode « sans solvant » à partir de $\text{Ca}(\text{EtO})_2$ et de $(\text{RO})_3\text{PO}$,
- une infiltration de sel fondu avec du CAT¹ et du $(\text{BuO})_3\text{P}$,

¹Calcium di(hexafluoro-2,4-pentadione)(tetraglyme), pour la formule chimique voir la figure 2.1, page

- un sol en solution d'éthanol de $\text{Ca}(\text{NO}_3)_2$ et de $(\text{NH}_4)_2\text{HPO}_4$
- et finalement une approche basée sur les métaphosphates partant de $\text{Ca}(\text{NO}_3)_2$ et de $(\text{NaPO}_3)_n$.

Les techniques d'infiltration, la concentration du précurseur, l'infiltration sous vide ou en pression atmosphérique, la calcination et les infiltrations multiples sont les paramètres influant la céramique finale.

Les matériaux hôtes et les céramiques sont caractérisés par diffraction des rayons X à petits et à grands angles, par microscopie électronique en transmission et surtout par adsorption d'azote. Les résultats sont comparés de telle manière qu'à chaque fois, l'influence d'un seul paramètre est étudiée. Par exemple, l'influence de la concentration du précurseur est étudiée avec le même sol, avec le même template et sous les mêmes conditions. Par cette méthode, nous avons pu remonter à la meilleure combinaison de paramètres pour obtenir la surface spécifique la plus élevée et le volume poreux le plus important. La porosité la plus importante est obtenue à partir d'un hôte silicique de type mousse avec une solution diluée de nitrate de calcium et de triéthyle phosphite avec une calcination à basse température (400°C). La dissolution de la silice s'effectue par un traitement chimique à la soude. Il faut néanmoins faire un choix : les synthèses à partir de solutions diluées qui donnent un produit avec une surface spécifique élevée ont un rendement faible (en terme de masse d'hydroxyapatite par rapport à la masse du template). Par contre, les solutions concentrées conduisent à des rendements plus importants de céramiques à surface plus faible.

Discussion et conclusion

Les résultats sont ensuite discutés par rapport au contexte bibliographique. En conclusion de ce chapitre, il faut noter qu'aucune de nos expériences n'a mis en évidence un effet de réplique proprement dit. Les céramiques sont réellement mésoporeuses (contrairement à ce qui a été publié), mais leur porosité ne constitue pas une réplique exacte de la structure de l'hôte. En accord avec ce qui a été publié sur les phosphates de métaux de transition, qui résistent eux aussi à la réplique [125], nous concluons que la cinétique de condensation du système sol/gel en présence de l'hôte est trop rapide pour permettre la pénétration de la porosité. Le précurseur qui condense à l'extérieur de la porosité entraîne la formation de céramiques mal structurées. Pour améliorer la réplique, il faudra ralentir la vitesse de réaction.

Adsorption de protéines par l'hydroxyapatite poreux

Ce chapitre représente la deuxième partie de la thèse : l'étude de l'adsorption de protéines (modèles et facteurs de croissance) sur les céramiques poreuses synthétisées auparavant. Dans la partie bibliographie de ce chapitre, nous décrivons l'adsorption de protéines sur les phosphates de calcium et des matériaux mésoporeux, ainsi que des études associant les phosphates de calcium aux facteurs de croissance TGF et VEGF.

Les techniques courantes de quantification de protéines sont brièvement présentées. La partie expérimentale présente les méthodes d'adsorption et de relargage qui ont été utilisées pour ce travail. Les résultats de ces expériences sont ensuite décrits. La discussion compare les résultats avec les études publiées dans la littérature avant que la conclusion résume les résultats les plus marquants de l'étude d'adsorption et de relargage de protéines sur les céramiques poreuses.

Bibliographie

Quand un matériau est mis en contact avec un fluide biologique, les protéines et d'autres biomolécules sont les premières à s'adsorber sur sa surface. Ces biomolécules sont la base sur laquelle les cellules s'attachent et régulent l'interaction des cellules avec la surface. Une étude de l'adsorption de protéines sur un matériau qui est destiné à l'implantation est donc primordial pour prédire son comportement dans le corps du patient. Les phosphates de calcium et surtout l'hydroxyapatite sont couverts d'une couche d'hydratation qui contient des groupements - OH. En milieu aqueux, ces groupements se dissolvent partiellement ; la surface comporte par conséquent des sites riches en calcium et des sites riches en phosphates. Ces « sites C » [16] d'excès local de calcium interagissent avec les protéines acides qui sont chargées négativement à pH physiologique, alors que les protéines basiques s'absorbent de préférence sur les « sites P », possédant un excès de phosphate et chargées négativement. Dans un matériau poreux, l'adsorption de la protéine est sélective en taille : une grande protéine comme l'albumine ne peut pas pénétrer une mésoporosité fine. L'association de facteurs de croissance avec les phosphates de calcium est connue et un certain nombre de publications existent sur le sujet. Ces articles parlent d'études *in vivo* pour la plupart. Néanmoins, aucune étude n'a été publiée sur la combinaison de phosphates de calcium mésoporeux et de protéines. A ce jour, les phosphates de calcium mésoporeux ne sont pas encore disponibles en quantité suffisante.

Partie expérimentale et résultats

Dans un premier temps, la dissolution des céramiques dans le milieu de culture et leur potentiel ζ sont étudiés. Le potentiel ζ donne une estimation de la charge de surface de la céramique. Toutes les céramiques ont un potentiel négatif dans l'eau, le PBS et le DMEM (milieu de culture). Les essais d'adsorption et de relargage des protéines se déroulent en deux étapes : dans un premier temps, un protocole d'adsorption de BSA et de Cytochrome C est mis au point. Les concentrations de protéines adsorbées sur les céramiques sont déterminées par déplétion soit par absorbance UV/Vis directe (Cytochrome C) soit après révélation avec une solution Bradford (BSA). Dans un deuxième temps, l'adsorption des facteurs de croissance TGF et VEGF est étudiée. Les concentrations des facteurs de croissance étant trop faible pour une quantification classique, les concentrations dans le surnageant sont déterminées par ELISA (essais immunologiques spécifiques).

Discussion et conclusion

La BSA est la molécule la plus grande utilisée dans nos études. Nous avons observé qu'elle s'adsorbe uniquement à la surface et peut être éliminée par un simple rinçage. Cette faible adsorption est due à la charge négative de cette biomolécule acide, ce qui est défavorable pour l'adsorption sur une surface elle aussi négativement chargée. Le paramètre décisif pour son adsorption est la cristallinité de la céramique : plus la céramique est cristalline, plus la BSA s'adsorbe sur la surface.

Le comportement du Cytochrome C est plus proche de celui des facteurs de croissance. Vu sa taille plus petite, elle peut pénétrer dans la mésoporosité des céramiques. Le Cytochrome C s'adsorbe en plus grande quantité sur les céramiques à haute surface spécifique, mais l'adsorption est plus forte sur les échantillons mieux cristallisés.

Le TGF s'adsorbe sur les céramiques ayant une grande surface et un volume mésoporeux élevé. Son relargage est progressif et partiel, c'est-à-dire une partie de la protéine reste sur la céramique malgré une exposition prolongée au milieu de culture. Cette partie du facteur de croissance restera immobilisée dans la céramique jusqu'à la résorption de cette dernière après l'implantation.

Dans les expériences avec le VEGF, toutes les céramiques ont le même comportement : la protéine s'adsorbe rapidement et complètement sur la céramique et ne se relargue pas.

En conclusion des essais d'adsorption des protéines, il faut souligner que les résultats obtenus avec les protéines « modèles » ne permettent pas de prévoir le comportement des facteurs de croissance. Pour évaluer la capacité de rétention, il faut toujours travailler avec le facteur lui-même. L'adsorption forte des facteurs de croissance est favorable pour l'application : elle évite un relargage immédiat après l'implantation, ce qui peut avoir des effets nocifs. La poudre chargée peut alors servir de réservoir pour un relargage prolongé.

Conclusion générale

Cette thèse décrit pour la première fois la synthèse d'hydroxyapatite (HA) mésoporeuse à partir d'hôtes siliciques de type mousse. Contrairement au CMK-3, qui dispose d'une structure poreuse en forme de tubes, les mousses de silices ont un volume poreux plus important et une géométrie de pores plus adaptée à l'infiltration d'un précurseur liquide. Les produits résultants de cette réplique sont composés de nanograins agglomérés et ont une mésoporosité. La surface spécifique et le volume poreux dépendent du traitement thermique auquel le composite template/HA est soumis.

Le procédé le plus polyvalent pour la synthèse d'hydroxyapatite par réplique est la méthode sol-gel à partir de nitrate de calcium et de phosphate triéthylique. Ce procédé permet d'utiliser des solutions concentrées, limitant ainsi un effet de volume mort trop important. Le produit n'est que peu contaminé par des phases siliciques provenant du template. Les autres méthodes qui ont été testées soit ne conduisent pas à l'hydroxyapatite soit induisent forte contamination silicique.

Tout comme les produits décrits dans la littérature, nos produits ne montrent pas de

vrai effet de réplique : même si les produits sont mésoporeux, leur structure ne réplique pas la porosité de l'hôte. Ceci est dû à la condensation rapide du précurseur avant que la solution puisse pénétrer la porosité. Ce phénomène a déjà été décrit pour des phosphates de métaux de transition [125]. Nous pensons que cette limitation est propre aux hydroxyapatites mésoporeux synthétisées par une approche sol-gel.

Pourtant, dans le cas d'hôtes silicique en forme d'opale, un effet de réplique est mis en évidence. La céramique est composée de grains nanométriques qui se sont arrangés dans les cavités entre les billes de silice. Cette céramique dispose d'une méso- et d'une macroporosité, qui est particulièrement intéressante pour les applications dans l'implantation : la mésoporosité permet le stockage de facteurs de croissance pendant que la macroporosité assure la circulation de fluides corporels.

Ces céramiques ainsi que les hydroxyapatites obtenues par sol-gel (mis à disposition par le laboratoire LMI de Clermont-Ferrand) se prêtent bien à l'adsorption de protéines, notamment des facteurs de croissance TGF et VEGF. Nos expériences ont montré une différence importante entre les protéines modèles (BSA et Cytochrome C) et les facteurs de croissance. Cette différence est probablement en partie due à la gamme de concentration différente des facteurs de croissance et des protéines modèles. L'adsorption de la BSA est particulièrement défavorable : cette protéine est plus grande que les facteurs de croissance et ne pénètre pas la mésoporosité. Son adsorption est dirigée par la cristallinité de la surface de la céramique. Pour les autres protéines, la surface spécifique l'emporte sur la cristallinité. Contrairement au Cytochrome C et aux facteurs de croissance, la BSA est acide et négativement chargée à pH physiologique. Par conséquent, elle s'adsorbe difficilement sur les surfaces d'hydroxyapatite négativement chargées.

Il est donc judicieux d'utiliser les facteurs de croissance pour évaluer un matériau au lieu d'avoir recours à des protéines modèles.

L'adsorption des facteurs de croissance est rapide et forte. Le relargage des protéines (en particulier du VEGF) dépend de la dissolution de la matrice céramique dans le milieu biologique. La céramique représente donc un réservoir pour un relargage prolongé. Ceci est important pour l'application in vivo puisque un relargage immédiat doit être évité. Il a été observé que des doses fortes et localisées de VEGF peuvent entraîner des effets secondaires défavorables.

Perspectives

Evaluation biologique (suite du projet ANR)

Les céramiques sont soumises à différents tests in vitro et in vivo : l'équipe IBTH à Reims examine la capacité inflammatoire in vitro des poudres J, A, B et C. Pour cela, des monocytes humains sont cultivés en présence de ces poudres. L'expression des médiateurs vésiculaires est analysée dans le surnageant de culture. La production d'ARN messager est déterminée par PCR en temps réel sur les lysats des cellules. La première série de ces tests a montrée que la réponse des poudres A, B et C est équivalente. Seule la poudre J produit un effet inflammatoire plus important. Parmi les quatre poudres analysées,

seule la poudre C augmente la production de l'IL-10,² indiquant qu'elle pourrait avoir des effets anti-inflammatoires lors de l'implantation. Cette poudre semblerait la plus adaptée pour l'implantation.

En parallèle, les équipes de Bordeaux ont effectué des tests de culture cellulaire des cellules osseuses avec des extraits des poudres A, B et C. Les extraits ne montrent pas d'effet nocif sur les cellules. Des comprimés de la poudre J ont servis de support à la culture cellulaire de cellules ostéoprogénitrices. Le test live/dead ne montre pas de différence significative entre la pastille d'hydroxyapatite et le fond de la plaque de culture qui a été utilisé en tant que contrôle. La prolifération des cellules est moins importante sur les HA, mais la prolifération n'est pas complètement inhibée. Dans les conditions du test, les poudres ne sont pas cytotoxiques.

En ce moment, des tests d'ostéoinduction et d'ostéoconduction sont effectués à Bordeaux : les poudres JC et C sont mélangées au chlorure de sodium et implantées dans des condyles fémoraux de souris pour démontrer la capacité ostéoconductrice des céramiques. Parallèlement, des échantillons pressés en pastilles sont implantés sous la peau de souris. Ce test sert à analyser si la céramique peut induire la formation d'os dans un site non-osseux. Les résultats de ces tests ne sont pas encore disponibles.

La totalité de cette évaluation a pour but de déterminer la ou les poudres les plus appropriées à l'imprégnation avec les facteurs de croissance. Ces poudres chargées seront ensuite implantées dans des défauts crâniens et fémoraux de souris pour valider l'association des facteurs de croissance avec la céramique.

Améliorations possibles de la synthèse d'hydroxyapatite mésoporeux

A partir de nos expériences, nous concluons que la cinétique du système sol-gel est trop rapide pour permettre un effet de réplique. La condensation du système doit être ralentie pour améliorer la réplique de la porosité du matériau hôte. Dans la synthèse des zéolites, la condensation des précurseurs peut être ralentie par l'addition des ions fluorure à la réaction [125]. Dans notre cas, la haute affinité entre le calcium et le fluore entraînerait la formation de CaF_2 . Il faudra donc trouver d'autres additifs afin de ralentir la réaction.

Le même effet peut être obtenu grâce à l'utilisation des concentrations moins importantes. Cependant, comme nous l'avons montré, la dilution diminue le rendement de la réaction en termes de quantité d'HA qui peut être obtenue avec une quantité de template donnée. Il faudra donc faire une étude systématique avec des dilutions progressives pour trouver un équilibre entre une cinétique ralentie et un rendement raisonnable. Il sera nécessaire de combiner cette méthode avec des infiltrations multiples pour compenser le rendement faible.

Une autre possibilité pour réduire la vitesse de réaction est l'utilisation de précurseurs différents. Un premier pas dans cette direction a été la synthèse « sans solvant » à partir d'éthoxide de calcium et de différents phosphites organiques. Même si cette méthode n'a

²IL-10 (interleukine 10), connue aussi sous le nom du facteur humain inhibant la synthèse de cytokines, est une cytokine anti-inflammatoire.

pas abouti dans ce projet, elle mérite d'être poursuivie car elle mène à des cinétiques considérablement ralenties par rapport au système sol-gel aqueux.

La synthèse d'hydroxyapatite à partir de métaphosphates est prometteuse mais incompatible avec les templates siliciques. Il sera intéressant de poursuivre les expériences avec ce précurseur et un template inerte, par exemple du carbone. Les cinétiques de la réaction des métaphosphates sont différentes du système sol-gel et peut-être plus adaptées à la synthèse par réplique.

Dans le projet, il a été prévu de combiner des approches de nanoréplique et d'autoassemblage pour obtenir des céramiques avec une porosité hiérarchisée. Le matériau hôte le plus adapté pour cette combinaison est l'opale silicique, qui est le seul à avoir montré un effet de réplique. Il faudra infiltrer l'opale de silice avec une solution de précurseur qui contient un tensioactif. Après condensation du système, l'élimination du tensioactif doit se faire par extraction au lieu de calcination. Il a été démontré que l'élimination du tensioactif par extraction est une méthode plus efficace pour obtenir des céramiques à haute surface spécifique [133].